A THEORETICAL AND EXPERIMENTAL STUDY OF THERMAL AUTOFRETTAGE PROCESS

A Thesis Submitted in Partial Fulfillment of the Requirements
for the Degree of

DOCTOR OF PHILOSOPHY

by

Seikh Mustafa Kamal

(Roll No. 126103004)

Department of Mechanical Engineering
Indian Institute of Technology Guwahati
Guwahati–781039
INDIA

March 2016

Department of Mechanical Engineering
Indian Institute of Technology Guwahati
Guwahati- 781039
INDIA

CERTIFICATE

It is certified that the work contained in the thesis entitled "**A Theoretical and Experimental Study of Thermal Autofrettage Process**" submitted by **Mr. Seikh Mustafa Kamal** to the Indian Institute of Technology Guwahati for the award of the degree of Doctor of Philosophy has been carried out under my supervision in the Department of Mechanical Engineering, Indian Institute of Technology Guwahati. This work has not been submitted elsewhere for the award of any other degree or diploma.

(Dr. U. S. Dixit)
Professor
Department of Mechanical Engineering
Indian Institute of Technology Guwahati
Guwahati- 781039
INDIA

March 4, 2016

To

My dear parents

Kalamsha Seikh

&

Arifa Begum

for their love and support

Acknowledgement

I would like to express my sincere gratitude to people who have helped me during the tenure of my PhD work at IIT Guwahati. I take this opportunity to express my deep gratitude to all of them for their support and help during various phases of my PhD work.

First and foremost I am grateful for the guidance and advice of my supervisor Prof. U. S. Dixit. His constant motivation and support have been instrumental to the completion of this research work. He has helped me at various phases of my work with his valuable guidance and moral support. I would like to thank my doctoral committee members, Prof. S. K. Kakoty, Dr. P. Biswas and Prof. S. Natesan for their valuable suggestions and encouragement during the period of my research work. I am also grateful to the former and present heads of the mechanical engineering department, Prof. P. Mahanta and Prof. Anoop K. Dass for extending various facilities during the tenure of my doctoral program. I am very much thankful to Dr. Arun C. Borsaikia, Scientific Officer of civil engineering department, IIT Guwahati for helping me in conducting some experiments.

I gratefully acknowledge the financial assistance provided by the Engineering and Physical Sciences Research Council (UK) through grant EP/K028316/1 and Department of Science and Technology (India) through grant DST/RC-UK/14-AM/2012, project Modeling of Advanced Materials for Simulation of Transformative Manufacturing Processes (MAST). I also acknowledge the financial assistance provided by the Ministry of Human Resource Development, Government of India.

I express my sincere thanks to all the Workshop staff of mechanical engineering department. Specially, I would like to thank Mr. Mrinal Sarma, Mr. Upen Gohain, Mr. Dilip Chetri and Mr. Dhaneswar Khaklary for their help in fabricating the experimental set up. I also thank the technical staff of the department of mechanical engineering, especially, Mr. Sanjib Sarma, Mr. Jiten Basumatary, Mr. Nip Borah and Mr. Saiffuddin Ahmed for their direct or indirect help during my

Ph.D. I acknowledge the help and encouragement of Mr. Deva Kanta Rabha, Assistant Professor of mechanical engineering, Jorhat Engineering College. Thanks are also addressed to my friends Mr. Vinod Yadav, Mr. Saptarshi Karmakar and Mr. A. S. Pavan Kumar for their help and support during my PhD.

I shall always be grateful to my parents (Kalamsha Seikh and Arifa Begum) for their love and wishes. Their love and wishes have been the great source of inspiration for my life. I would also like to thank my siblings and all my well wishers for their moral support. I wish to thank Indian Institute of Technology Guwahati for providing a beautiful and serene residential campus.

Finally, I bow my head to the Almighty Allah in deepest gratitude and seek blessings.

4th March 2016

Seikh Mustafa Kamal
IIT Guwahati

Abstract

Thick-walled cylinders/hollow-disks find wide range of industrial applications to withstand very high pressure. Pressure vessels, gun barrels, fuel injection system in diesel engines, nuclear reactor and fastener holes are the typical examples. The cylinder may crack if the working internal pressure exceeds the yield strength of the material. The pressure carrying capacity and fatigue life of the thick-walled cylinders used for high pressure application can be significantly improved by inducing beneficial compressive residual stresses at and around the inner wall of the cylinder. This is achieved by employing a process called autofrettage, prior to their use in service condition. The most commonly employed autofrettage processes are hydraulic and swage autofrettage process. The hydraulic autofrettage is achieved by pressurizing the cylinders to an ultra-high hydraulic internal pressure. The swage autofrettage is achieved by pushing an oversized mandrel through the inside of the cylinder to plastically deform the inner wall and some portion beneath it. The autofrettage can also be achieved by detonating an explosive charge inside the vessel, which is called explosive autofrettage. All these existing processes have certain disadvantages. In order to avoid the difficulties associated with the existing methods of autofrettage, in the present thesis, a thermal autofrettage process is proposed. The proposed thermal autofrettage process is achieved by creating a radial thermal gradient across the wall thickness of a cylinder or hollow disk. The proposed thermal autofrettage process is very simple and easy to handle compared to the existing methods of autofrettage.

In this thesis, a theoretical and experimental study of the thermal autofrettage process is carried out. For the theoretical analysis, two analytical models— plane stress and generalized plane strain model have been developed. The plane stress model is applicable for the very short cylinders (thin disks) such as fastener holes and the generalized plane strain model is applicable for long cylinders such as gun barrels and pressure vessels. The models are based on the Tresca yield criterion and its associated flow rule. The strain hardening behaviour of the cylinders during autofrettage is studied. A three-dimensional finite element method (3-D FEM) modeling of the thermo-elasto-plastic stresses generated in the cylinder due to thermal gradient is also carried out in ABAQUS finite element package. The finite element results are compared with the stresses predicted by the plane stress and the generalized plane strain models. The main objective of this study is to develop a criterion for assessing the analytical models on the basis of the length to wall thickness ratio, $L/(b-a)$ of the cylinders.

An experimental setup has been developed for creating the desired temperature difference across the wall thickness of the cylinder to achieve thermal autofrettage. The experimental assessment of the residual stresses set up in the cylinders after thermal autofrettage are carried out using three different techniques—Sachs boring method, microhardness test and the measurement of opening angle as a result of cutting through the wall of the cylinders. All three experimental methods indicate the presence of beneficial compressive residual stresses at the inner wall of the thermally autofrettaged cylinders.

A comparative study of thermal and hydraulic autofrettage is also carried out. A parametric study is carried out for both thermal and hydraulic autofrettage and comparison is made. The thermal autofrettage process is also studied for the thick-walled cylinders subjected to high thermal gradient with or without pressure and is compared with the hydraulic autofrettage. Comparison shows that for cylinders subjected to high thermal gradient without pressure, the thermal autofrettage is superior to the hydraulic autofrettage. A methodology is proposed in this thesis for enhancing the pressure carrying capacity as well as the fatigue life of the thermally autofrettaged cylinder through shrink-fit. It is estimated that the pressure carrying capacity and the fatigue life of the thermally autofrettaged cylinder with shrink-fit significantly improves as compared to the corresponding thermally autofrettaged as well as non-autofrettaged single/monobloc cylinders.

The overall theoretical and experimental study of the thermal autofrettage process reveals that the process is a commercially viable and useful process. The simplicity of the process makes the process to be competitive with the existing methods of autofrettage.

Contents

List of Figures

List of Tables

Nomenclature

a	Inner radius of cylinder/disk
b	Outer radius of cylinder/disk
c, d, e, f	Interface radii between different zones
c_p	Specific heat of fluid at constant pressure
E	Young's modulus of elasticity
F_b	Cross-section of the original cylinder
F_r	Cross-section of the bored out cylinder
h	Convective heat transfer coefficient
K	Strain hardening coefficient
K_I	First mode of stress intensity factor
k	Thermal conductivity of the material
k_f	Thermal conductivity of fluid
k_1	Sign factor
L	Length of the cylinder/disk
l	Depth of crack
M	Bending moment acting over any radial cut across the wall thickness of the cylinder
$\dot{m}$	Mass flow rate
n	Strain hardening exponent
N_f	Fatigue life
N_u	Nusselt number
p_i	Internal working pressure
Pr	Prandtl number
p_{sh}	Contact pressure due to shrink-fit
$\overline{p}_Y$	Non-dimensional pressure
Q	Heat flow rate
r	Radius of cylinder/disk

Re	Reynolds number
T_a	Temperature at the inner surface of cylinder/disk
T_b	Temperature at the outer surface of cylinder/disk
T_f	Average temperature of fluid
T_i	Inlet temperature of fluid
T_o	Outlet temperature of fluid
u	Radial displacement
V	Velocity of fluid
W	Wall thickness ratio
w	Wall thickness of the cylinder/disk
z	Outer radius of the shrink-fitted cylindrical layer
α	Coefficient of thermal expansion
β	Opening angle
δ	Shrink-fit allowance
ε	Level of overstrain
ε_r, ε_θ, ε_0	Total radial, hoop and constant axial strain
ε_r^e, ε_θ^e, ε_0^e	Elastic components of radial, hoop and axial strain
ε_r^p, ε_θ^p, ε_0^p	Plastic part of radial, hoop and axial strain components
ε_{eq}^p	Equivalent plastic strain
μ	Coefficient of dynamic viscosity
ν	Poisson's ratio
ρ	Density
σ_{eq}	Equivalent stress
σ_r	Radial stress
σ_θ	Hoop stress
σ_z	Axial stress
$(\sigma_r)_{res}$	Residual radial stress
$(\sigma_\theta)_{res}$	Residual hoop stress
$(\sigma_z)_{res}$	Residual axial stress
σ_Y	Yield stress

θ and Λ	Strain parameters
θ_Y	Non-dimensional thermal gradient

Chapter 1

Introduction

1.1 The Autofrettage process

The thick-walled cylinder or hollow disk (very short cylinder) is one of the most important and widely used engineering components. It finds application in gun barrels, nuclear reactors, oil and chemical plants, rocket shells, water jet cutting, food sterilization, fuel injector lines in diesel engines, hydraulic chambers and fastener holes. In these applications, the thick-walled cylinder is subjected to very high internal pressure in service. However, the pressure that the cylinder can withstand is limited by the yield strength of the material, which must not exceed in normal use. If the working internal pressure exceeds the yield strength of the material, the cylinder material may crack at the inner wall where the hoop stress developed by the pressure is the highest. In order to increase the pressure carrying capacity as well as to increase the fatigue life, the thick-walled cylinders are subjected to a process called autofrettage prior to their use in service condition.

Autofrettage is a metal working process that induces compressive residual stresses at and around the inner wall of a thick walled cylinder by means of plastic deformation. The plastic deformation of the inner wall of the cylinder is caused by applying some loading. After achieving the desired deformation, when the applied load is released, the beneficial compressive residual stresses are generated at and around the inner wall of the cylinder. These compressive residual stresses offset the tensile hoop stresses, which are produced when the cylinder is subjected to internal pressure in the next stage of loading. Thus, the pressure carrying capacity of the cylinders is increased. The probability of crack initiation at the inner wall is also reduced due to the compressive residual stresses, which slows down the growth of cracks (Rogan, 1975; Stacey and Webster, 1988; Perl and Aroné, 1988). This enhances the fatigue life of the cylinder. The term 'autofrettage' is of the French origin, which means 'self-hooping'.

Depending upon the type of applied loading, autofrettage processes are mainly classified into two categories— hydraulic autofrettage and swage autofrettage. The hydraulic autofrettage utilizes an ultra-high hydraulic pressure at the inner wall of the cylinder to achieve the desired extent of plastic deformation. In swage autofrettage, the required plastic deformation is created by passing a tapered oversized mandrel through the inner wall axially. The autofrettage can also be achieved by detonating an explosive charge inside the vessel, which is called explosive autofrettage (Mote *et al.*, 1971; Ezra *et al.*, 1973; Taylor *et al.*, 2012). However, the process is not commonly practiced due to the involvement of explosive. Another promising way of achieving autofrettage is by means of thermal loading, termed as thermal autofrettage (Barbero and Wen, 2002; Hamilton *et al.*, 2015). This process is not well explored by the researchers.

In the present thesis, a method of achieving thermal autofrettage by creating radial thermal gradient in a thick-walled cylinder is proposed. Before introducing the proposed thermal autofrettage process, the hydraulic, swage and explosive autofrettage processes are briefly described in Sections 1.2, 1.3 and 1.4 respectively. Section 1.5 highlights the key issues to be considered in the analysis of autofrettage process. The thermal autofrettage process is introduced in Section 1.6 along with the scope and objective of the present thesis. Section 1.7 presents the organization of the thesis.

1.2 Hydraulic Autofrettage

The hydraulic autofrettage is the most popular and the oldest autofrettage method. The development of the process is credited to Jacob (1907), a French artillery officer. In hydraulic autofrettage, initially a single thick metallic cylinder of internal radius slightly less than the desired dimension is used. Then the thick walled cylindrical vessel is subjected to a high hydrostatic pressure, p_i, such that the equivalent stress at the inner wall of the cylinder exceeds the yield strength of the material. Thus, the material at and around the inner radius of the cylinder is subjected to plastic deformation. Pressure is further increased in order to achieve the desired depth of plastic deformation within the cylinder wall. The material near the outer wall of the cylinder deforms elastically. Generally, the cylinder is pressurized by hydraulic oil, pumped through a high pressure hydraulic pump. The ends of the cylinder are closed using rigid plugs or floating pistons to retain the oil inside the cylinder. A solid spacer is usually inserted into the centre of the cylinder to reduce the volume of the hydraulic oil that must be pumped into the cylinder to achieve autofrettage (Gibson, 2008).

When the pressurized oil is released from the cylinder, the outer portion of the material, which has undergone elastic deformation, attempts to return to its original dimension whilst the material at and around the inner wall, which has been deformed plastically, attempts to remain in the deformed state. This results in residual compressive stresses at and around the inner wall of the cylinder. Thus, when the cylinder is re-pressurized, the magnitude of the maximum stress reduces significantly enhancing its pressure carrying capacity. As the residual stresses are self-equilibrating, the portion of the cylinder from outer surface to some intermediate radial position will have tensile residual stresses, but this does not pose any problem as the working pressure produces relative smaller hoop stresses in the outer portion of the cylinder. A typical thick-walled cylinder undergoing hydraulic autofrettage is shown in Figure 1.1.

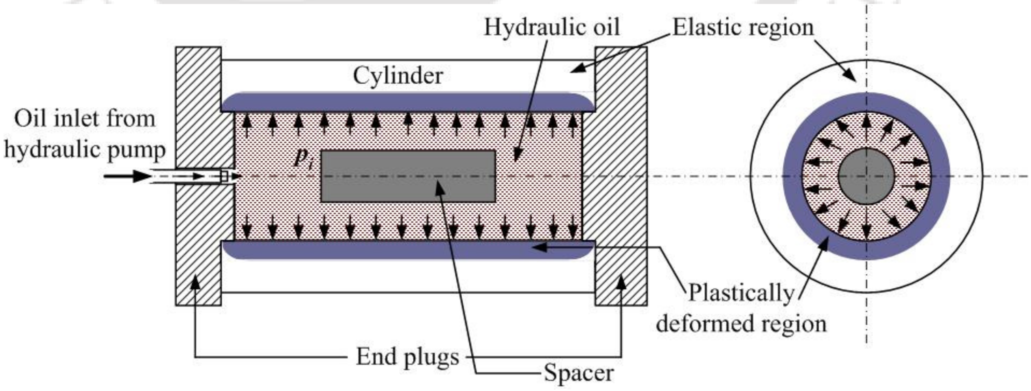

Figure 1.1 Hydraulic autofrettage of a thick-walled cylinder

In hydraulic autofrettage, the applied pressure is to be very carefully controlled to achieve the desired plastic deformation within the cylinder wall. This makes the process slow. Also, the arrangement of the plugs at the ends of the cylinder should be precisely made to contain the required pressure. The highly pressurized oil is dangerous if failure would occur during the process. Therefore, much care needs to be taken in applying the high hydraulic pressure. The process is also expensive due to the requirement of costly hydraulic power pack for pressurization. Moreover, any leakage of the hydraulic oil during the autofrettage process is harmful to the environment. Thus, it is not a greener manufacturing procedure.

1.3 Swage Autofrettage

To overcome the disadvantages associated with the cost and processing of the hydraulic autofrettage procedure, Davidson *et al.* (1962) developed a new approach for achieving autofrettage known as swage autofrettage. The swage autofrettage is achieved by the mechanical interference of an oversized tapered mandrel and the inner wall of a cylinder. The mandrels used in the swage autofrettage process typically consist of two conical sections connected by a short length of constant diameter. The schematic diagram of mandrel and swage autofrettage process is shown in Figure. 1.2. In Figure 1.2 (a), θ_F is the forward cone angle, θ_R is the rear cone angle and L_c is the length of the straight portion connecting the two cones in the mandrel. The mandrel is prepared in such way that the forward conical section has smaller slope than the rear section. The forward conical section controls the initial deformation of the cylinder and the rear conical section helps in subsequent unloading of the cylinder. The mandrel is pushed through the inner wall of the cylinder by means of pressure exerted by the ram of a hydraulic press. As a result, localized plastic deformation of the inner wall and some portion beneath it progresses keeping the outer wall in the elastic state. After unloading of the mandrel, the compressive residual stresses are generated at and around the inner wall.

In swage autofrettage process, when the mandrel travels through the inner wall of the cylinder, a lot of frictional force is generated between the mandrel and the cylinder. Therefore, the contact between the mandrel and the cylinder needs to be lubricated in order to reduce the sliding friction (O'Hara, 1992). The method also requires the use of a large and expensive hydraulic press and a mandrel of a material with excessively high compressive strength. The hydraulic pressure required to push the mandrel through the cylinder is much less in this process than that required by the conventional hydraulic autofrettage. However, the pressure required for driving the ram increases with the increase in the size of the mandrel (Iremonger and Kalsi, 2003).

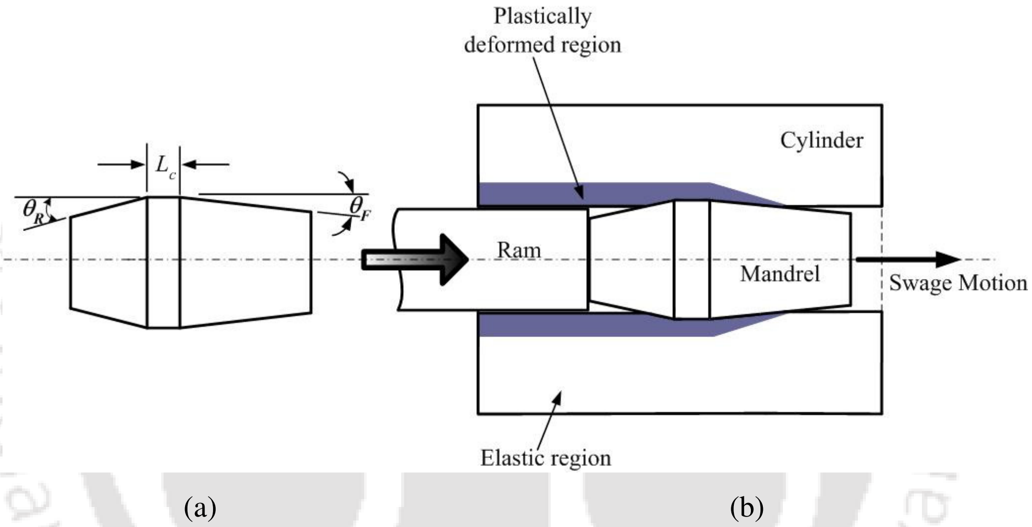

Figure 1.2 Schematic diagram of (a) mandrel and (b) swage autofrettage

1.4 Explosive Autofrettage

Explosive autofrettage is a dynamic way of introducing beneficial compressive residual stresses at and around the inner wall of a thick-walled cylinder. In this process, the inner wall of the cylinder is subjected to plastic deformation by detonating an explosive charge at the inside of the cylinder. A typical configuration for attempting dynamic autofrettage is shown in Figure 1.3. As shown in Figure 1.3, a rapid burning explosive charge is placed along the longitudinal axis of a ductile metal tube. This tube containing the explosive is termed as radial piston. The radial piston is then placed along the longitudinal axis of the thick-walled cylinder which is to be autofrettaged (Mote *et al*., 1971; Ezra *et al*., 1973). The region between radial piston and the thick-walled cylinder is filled with an energy transmitting medium such as water. The water is sealed axially with the help of end plugs and restraining fixtures. The explosive charge is then detonated by means of a blasting cap and the explosion gases operate to expand the radial piston. This greatly increases the pressure of the energy transmitting medium confined between the radial piston and the inner wall of the cylinder. With proper choice of the explosive charge and the correct dimension of the radial piston, the pressure can be increased to such a high value that the inner wall of the cylinder gets plastically deformed. Upon dissipation of the explosively created pressure, substantial residual compressive hoop stresses are generated at and around the inner wall of the cylinder.

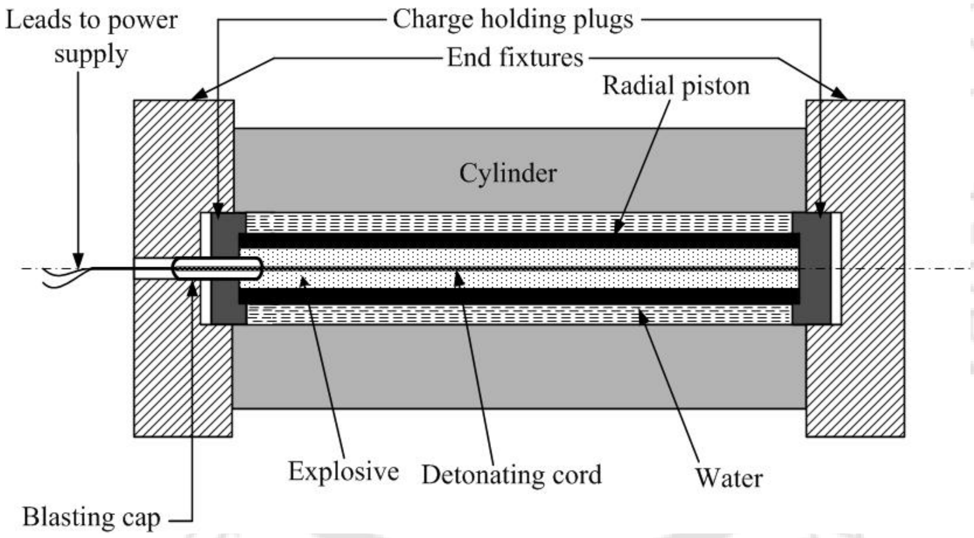

Figure 1.3 Schematic diagram of explosive autofrettage

The explosive autofrettage provides economic advantage over the hydraulic and swage autofrettage as the method does not require expensive capital investment in equipment such as hydraulic pumps or hydraulic presses. However, due to involvement of explosives, the control of the process requires skill. Also, in general, the residual compressive hoop stress level is smaller than those achieved by hydraulic and swage autofrettage. In order to produce the residual hoop stresses of the order of the hydraulic and swage autofrettage, the process requires a more sophisticated configuration of explosive tube. Moreover, the modeling of the process involves dynamic elasto-plasticity.

1.5 Key Issues in Autofrettage Processes

There are certain key issues that need to be addressed in the analysis of autofrettage processes. The prediction of the residual stresses, measurement of the level of overstrain and analysis of fatigue life of the autofrettaged cylinders are the important issues that need careful consideration in the analysis for practical realization of the process.

Residual stresses are the stresses that are present in a body without any external load. Such stresses are self-equilibrating and caused by incompatible internal strains due to removal of any external load. In autofrettage process, residual compressive stresses are generated at and around the inner wall of a thick-walled cylinder because of the difference between the plastic stresses and the elastic unloading stresses. The autofrettage induced residual stresses influence the pressure carrying capacity and fatigue life of cylinders used for high pressure application in industries. Thus, it is of significant industrial importance to predict the residual stresses either by theoretical or experimental methods in an autofrettage process. The correct modelling of the residual stresses depends on the suitability of the assumptions considered. The theoretical determination of residual stresses in autofrettaged cylinder has been carried out by many researchers considering different assumptions relating to yield criterion, material model (elastic-perfectly plastic, hardening), unloading behaviour and end conditions (Franklin and Morrison, 1960; Avitzur, 1994; Stacey and Webster, 1988; Huang and Cui, 2006; Gibson *et al.*, 2006). There are numerous experimental methods to quantify the residual stresses. Sachs boring method, hole drilling method, compliance method, neutron diffraction method, X-ray diffraction method (XRD) are the well-known experimental methods that have been used by researchers to determine residual stresses in autofrettaged cylinders (Stacey et al. 1985; George and Smith, 2000).

The level of overstrain in an autofrettaged cylinder is another important influencing factor that affects the residual stresses. Usually, the thick-walled cylinders are machined either at the inner or outer wall after autofrettage. Due to machining, the overstrain level in the cylinder changes. As the allowable pressure in the cylinder depends on the prevailing level of overstrain, its actual value needs to be determined (Perl, 2000). The level of overstrain is a function of the radial position up to which the plastic deformation is achieved by the autofrettage load at the inner portion of the cylinder, referred as the radius of elastic-plastic interface. The percentage level of overstrain in an autofrettaged cylinder is given by (Perl, 2000)

$$\varepsilon = \frac{c-a}{b-a} \times 100 , \tag{1.1}$$

where c is the radius of elastic-plastic interface, a is the inner radius and b is the outer radius of the cylinder.

Fatigue is a prime source of failure in almost all mechanical components. In general, fatigue failure in components takes place due to cyclic/fluctuating load. Many cylinders are designed to experience cyclic loading in service. The beneficial compressive residual stresses have profound effects in increasing the fatigue life of such cylinders and thereby limit the fatigue failure. Thus, the fatigue life analysis of autofrettaged cylinders is an important consideration. Many researchers have analyzed the fatigue life of autofrettaged cylinders using fracture-mechanics approach or finite element method (Rees, 1990; Thumser *et al.* 2002). Some researchers combined the autofrettage and shrink-fit of cylinders in order to achieve the maximum fatigue life (Parker, 2001; Parker and Kendall, 2003).

1.6 Scope and Objective of the Present Work: Thermal Autofrettage

It has been observed that there are certain disadvantages associated with the practicing methods of autofrettage. For example, the hydraulic autofrettage involves ultra-high hydraulic pressure and swage autofrettage involves a lot of friction. The explosive autofrettage needs sophisticated arrangement for explosion. To overcome these shortcomings, in the present thesis, a thermal autofrettage process is proposed.

The process is based on the generation of advantageous compressive residual stresses by creating a radial thermal gradient across the wall thickness of a thick-walled cylinder/disk.

The concept of thermal autofrettage is very recent. Barbero and Wen (2002) were the first to conceptualize the idea of thermal autofrettage for strengthening the composite metal-lined cryogenic pressure vessels by cooling the pipe to a temperature lower than the operating temperature using cryogenic fluids. The behaviour of the process was not analyzed in detail either theoretically or experimentally by the authors. Thermal autofrettage of thick-walled spherical pressure vessels under steady state thermal gradient has been studied by Kargarnovin *et al*. (2005). Recently, Hamilton *et al*. (2015) studied the thermal autofrettage of Titanium-Copper brazed joints by cooling the joint after brazing to induce plastic work in the joint, caused by the differential thermal contraction of the material. However, no researcher has studied the thermal autofrettage of thick-walled cylinder by creating radial thermal gradient across the wall thickness. The present thesis deals with the feasibility study of thermal autofrettage process due to radial thermal gradient.

A schematic diagram of the proposed thermal autofrettage process is shown in Figure 1.4. As shown in Figure 1.4, a thick-walled cylinder/disk is considered having inner radius a and outer radius b. The outer wall of the cylinder is heated externally using electrical heating element and subjected to a temperature, T_b. A flow of cold fluid *e.g*., cold water is continuously circulated through the cylinder to keep the inner wall at a lower temperature, T_a. Thus, the required temperature difference, (T_b-T_a) is created across the cylinder wall thickness. At a sufficiently large temperature difference between the outer and inner walls of the cylinder, the inner portion of the cylinder always yields first and it becomes plastic up to some intermediate radius, whilst the outer portion of the cylinder remains in the elastic state. This is so as long as the temperature difference is not large enough to cause the yielding of outer wall. As the temperature difference is increased further, after crossing a certain limit of (T_b-T_a), the outer wall of the cylinder begins to yield and the plastic deformation of both the inner and outer portion of the cylinder undergoes simultaneously. The intermediate portion of the cylinder remains in the elastic state provided the temperature difference is not large enough to cause the yielding of the whole cylinder. When the temperature difference across the wall thickness is released, *i.e.*, when the entire cylinder is cooled to room temperature, compressive residual stresses are generated at and around the inner wall of the cylinder in a similar way as in the case of hydraulic/swage autofrettage. The compressive residual stresses significantly reduce the magnitude of stress field at and around the inner wall of the cylinder or disk when it is subjected to loading by internal pressure. This enhances the pressure carrying capacity of the cylinder/disk.

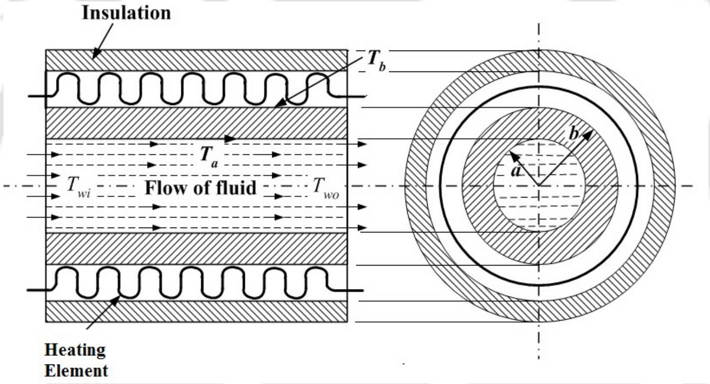

Figure 1.4 A schematic diagram of thermal autofrettage process

The thermal autofrettage process is simple and easy to handle compared to the existing methods of autofrettage. It does not involve any ultra-high hydraulic pressure or explosives, which makes the process inexpensive. Also, the friction is avoided as there is no moving part in the system. Moreover, the process utilizes heating element and cold fluid such as cold water to create the desired thermal gradient in the cylinder/disk, which is not harmful to the environment. This makes the process a greener manufacturing procedure.

The primary objective of the present thesis is to study the thermal autofrettage both theoretically and experimentally. The main focus of the study is to explore the feasibility of the process for its industrial exploitation. The analytical modeling of the process is carried out using both plane stress and generalized plane strain condition. A three-dimensional finite element modeling is carried out in order to define the applicability of the analytical models. An experimental setup is developed to achieve thermal autofrettage in thick-walled cylinders. The residual stresses induced in the thermally autofrettaged cylinders are assessed experimentally qualitatively and quantitatively using well-known methods such as Sachs boring. A comparison of the thermal autofrettage with the hydraulic autofrettage is carried out. Finally, a method for enhancing the performance of a thermally autofrettaged cylinder through shrink-fit is proposed.

The significance of the works presented in this thesis lies in the simplicity of the proposed thermal autofrettage process. The overall analysis indicates that the behavior of thermal autofrettage is easily predictable, a positive feature towards its industrial adaptation.

1.7 Organization of the Thesis

The thesis consists of nine chapters. The present chapter provides the introduction along with the scope and primary objective of the research work. The remaining chapters in the thesis are organized as follows:

- A brief review of literature on the autofrettage processes as well as on the different methods of residual stress measurement techniques and objectives of the present thesis are elaborated in Chapter 2.
- In Chapter 3, the plane stress modelling of the thermal autofrettage process is described for thick-walled hollow circular disk such as fastener holes. The modelling is based on the Tresca yield criterion and its associated flow rule. The effect of strain hardening of the material during plastic deformation is taken into account. Numerical simulations are carried out for different cylindrical geometries in order to envisage the feasibility of the process. A conceptual design for creating thermal gradient across the wall thickness of the disk is also presented.
- Chapter 4 presents the generalized plane strain modelling of the thermal autofrettage process for thick-walled hollow cylinders. The modelling involves Tresca yield criterion and its associated flow rule to analyze the

stress, strain and displacement fields in the cylinder under radial thermal gradient. The influence of strain hardening during plastic deformation is studied. Numerical simulations are carried out for typical cylinder geometries to study the feasibility of the thermal autofrettage of cylinders.

- In Chapter 5, a three-dimensional finite element method (3-D FEM) modelling of the thermo-elasto-plastic stresses in cylinders due to radial thermal gradient using ABAQUS finite element package is presented. The 3-D FEM results are compared with the plane stress and generalized plane strain analytical models. The comparison suggests the applicability of the analytical models on the basis of length to wall thickness ratio of cylinders.
- Chapter 6 deals with the experimental study of the thermal autofrettage process. The experimental setup developed for achieving thermal autofrettage is described. The experimental assessment of the residual stresses generated in the thermally autofrettaged cylinders is presented using three different techniques— Sachs boring, microhardness test and the measurement of opening angle due to single radial cut through the wall thickness of the cylinders. The experimental results are compared with the analytical results.
- Chapter 7 compares the thermal autofrettage with the conventional hydraulic autofrettage. A parametric study is carried out for both thermal and hydraulic autofrettage. The thermal autofrettage process is also studied for the thick-walled cylindrical vessels subjected to high thermal gradient with or without pressure and is compared with the hydraulic autofrettage.
- A methodology for enhancing the performance of thermally autofrettaged cylinders through shrink-fit is presented in Chapter 8. The performance analysis of the thermally autofrettaged cylinders with shrink-fit is carried out in order to increase the pressure carrying capacity as well as to increase the fatigue life of the cylinders.
- Conclusions and scope for future work are presented in Chapter 9 followed by references and appendices.

Chapter 2

Review of Literature

2.1 Introduction

Autofrettage or self-hooping is a metal working process that increases the elastic strength of a thick hollow cylinder. The autofrettage technology is an age old technique, the development of which was started with the refinement of the earliest form of gunpowder artillery called cannons. In ancient times the cannons were in the form of thick-walled cylindrical tube. The word ‘cannon’ is derived from the Latin origin ‘canna’ which means tube. Due to the poor sealing between the projectile and the tube wall and ineffective gunpowder, these were comparatively low pressure devices. In the mid-1800s, gun designers realized that if some inward force could be applied to the barrel the pressure carrying capacity of the barrel could be enhanced. As a consequence, barrels were ‘hooped’ to pre-compress the material at and around the inner radius of the barrel. For example, William Armstrong assembled compound cylinders from wrought iron tubes to achieve pre-compressing in 1854–55 (Bastable, 1992). In the early 1900s gun manufacturers envisaged that the barrel could be made to hoop itself by causing plastic expansion of the inner wall achieving similar pre-stressing to that developed by compound tubes. To this end, L. Jacob, a French artillery officer, suggested the process called ‘autofrettage’ for pre-stressing monobloc gun barrels by plastic expansion in 1907 (Jacob, 1907).

The most popular autofrettage processes are hydraulic and swage autofrettage. Both the processes are widely adopted in industries for setting up of beneficial compressive residual stresses in cylinders. The hydraulic autofrettage utilizes high hydrostatic pressure and swage autofrettage utilizes an oversized tapered mandrel to achieve the desired plastic deformation. The explosive autofrettage is not very popular due to the involvement of dynamic elasto-plasticity. The subject of the present thesis, the thermal autofrettage process for thick-walled cylinders is yet to be explored by the researchers both theoretically and experimentally.

In this chapter, a review of the existing literature in the area of autofrettage is presented. Section 2.2 discusses the theoretical modelling of hydraulic autofrettage process. Literature on the modelling of swage autofrettage process is discussed in Section 2.3. Section 2.4 presents the theoretical modelling on the explosive autofrettage process. A review on experimental determination of residual stresses in autofrettaged cylinders is presented in Section 2.5. Section 2.6 briefly reviews the works carried out by the researchers for analyzing the fatigue life of autofrettaged cylinders. In Section 2.7, research on autofrettaged and shrink-fitted compound cylinders is reviewed. A review of the analysis of thermo-elasto-plastic stresses is presented in Section 2.8. A few works reported on the study of thermal autofrettage is presented in Section 2.9. Research gap and detailed objectives of the present work have been presented in Section 2.10.

2.2 Modelling of Hydraulic Autofrettage Process

Researchers have used different analytical and numerical methods for theoretical modelling of the hydraulic autofrettage process. In order to get an approximate idea of the stresses generated during autofrettage, the analytical or numerical modelling of the process is essential. During mid 18th century, the modelling of cannons was based on well known Lamé's elastic solution (Lamé, 1852). The analysis of autofrettage process requires the consideration of plasticity. Lame's elastic solution provides the highest tensile stress at the inner radius of the cylinder and predicts the onset of yielding there. The problem of partial plastic deformation of internally pressurized thick-walled cylinders has drawn significant attention of the researchers as a means of achieving hydraulic autofrettage in cylinders. The analytical models substantially differ in their assumptions, *viz.*, stress-strain curve of material, yield criterion, compressibility of the material and end conditions. This section presents a review of the works carried out by the researchers on the theoretical modelling of the hydraulic autofrettage.

2.2.1 Analytical Models Assuming Elastic-perfectly Plastic Material

Most of the earlier solutions were based on the elastic-perfectly plastic material model devoid of strain hardening. Macrae (1930) carried out an early analytical analysis of the partially plastic thick-walled cylinders under internal pressure using Tresca yield criterion. Additional earlier contributions were made by Nádai (1931), MacGregor *et al*. (1948), Hill (1950), Allen and Sopwith (1951) and Steele (1952). The analytical solution of Nádai (1931) was based on von Mises yield criterion, plastic incompressibility and plane strain condition (ε_z=0), applicable to elastic-perfectly plastic material. The resulting solution introduces discontinuity in the longitudinal stress at the elastic-plastic boundary due the incorporation of plastic incompressibility. MacGregor *et al.* (1948) considered compressibility of the material in the plastic region. However, the modelling is based on von Mises yield criterion and the generalized plane strain condition (ε_z=constant). The generalized plane strain condition corresponds to the zero net axial force throughout the cylinder. The resulting solutions provide computation of stresses and strains in all directions and no discontinuities of stresses and strains are present at the radius of elastic-plastic boundary as arose in the solutions of Nádai (1931). A simple analytical model of hydraulic autofrettage assuming elastic-perfectly plastic material, von Mises yield criterion and the condition of incompressibility was given by Hill (1950). Allen and Sopwith (1951) assumed Tresca yield criterion and Hencky total strain theory which is an approximation of the Prandtl-Reuss theory. Authors obtained closed form expressions for closed-end condition, which are quite complicated and difficult to use for engineering design applications. Steele (1952) also assumed Tresca yield criterion and total strain theory of Hencky to derive closed form analytical expressions for elasto-plastic stresses in a thick-walled cylinder under internal pressure. Koiter (1953) adopted Tresca yield criterion and its associated flow rule to analyze the stresses in a thick-walled tube under internal pressure. He assumed that the axial stress is the intermediate principal stress. The assumption was shown to be valid for different end conditions (closed-end, open-end and hollow infinitely long cylinder). The solution was given for a non-hardening cylinder.

A series of analytical expressions for stress and displacement components in an open-ended cylinder were obtained by Davidson *et al*. (1963a) based on empirical relationship derived from experimental data. The expressions were based on von Mises yield criterion. Xiaoying and Gangling (1984) also formulated an analytical solution for the open-ended cylinder using von-Mises yield criterion. He derived closed form expressions for the pressure required to yield the inner wall as well as the pressure required to just bring the whole wall of the cylinder to plastic state. However, the formulation is not straight forward and involves lot of parameters to be evaluated to obtain the final solution. Later, the authors approximated their earlier solution provided by von Mises yield criterion, considering the regular twelve-angled prismatic surface, which is formed of the inner contact regular twelve polygons in the von Mises circle on the π-plane as the spatial yield surface (Gangling and Xiaoying, 1988). Avitzur (1994) assumed Tresca and von Mises yield criterion separately to investigate the elastic-plastic and residual stress field for a thick-walled cylinder undergoing hydraulic autofrettage. He presented the solutions for both plane stress and plane strain conditions considering elastic-perfectly plastic material. Author opined that multiplying the stress solution due to Tresca yield criterion in plane stress by a factor 2/√3, provides an upper bound solution for the radial stress at the elastic-plastic interface and throughout the plastic zone.

2.2.2 Large Strain Solutions

An exact large strain solution for the pressurized elasto-plastic thick-walled cylinder under the assumption of elastic incompressibility was given by Durban (1 979). The solution is valid for any strain hardening behaviour, which was based on von Mises flow rule and plane strain condition. In a later paper, Durban and Kubi (1992) provided a general solution of the problem employing Tresca yield criterion and its associated flow rule. The small strain version of the analysis for elastic-perfectly plastic solids was due to Koiter (1953). Author presented the solution using plane strain condition and arbitrary hardening of material accounting for elastic compressibility. An exact elasto-plastic analytical solution for large-strained internally pressurized cylinder was also given by Gao (1993). Their solution was based on the deformation theory of Hencky and von Mises yield criterion with closed-end condition applicable for elastic linear-hardening material.

2.2.3 Autofrettage Level after Machining

The autofrettage process is performed on the cylinders which are either rough machine forgings or centrifugal castings. It needs to be machined to its final dimensions both at the inner and outer surfaces after autofrettage. Moreover, in some cases the material is removed from the inner wall of the cylinder by broaching to make it rifled. As a result of these machining processes the level of autofrettage in the cylinder changes. The pressure carrying capacity as well as the fatigue life depends on the prevailing level of autofrettage. Thus, the value of autofrettage level after machining needs to be determined. Perl (2000) developed an analytical model for predicting the level of autofrettage following inner, outer or combined machining of a thick walled cylinder. The model is based on the Hill’s (1950) solution for the autofrettage residual stress field. Closed form simple algebraic expressions for the level of autofrettage resulting from the removal of material from the inner, outer or both sides of the cylinder was deduced in terms of the original level induced in the blank cylinder. Further, finite element simulation of the residual stresses in the machining process was carried out by an equivalent thermal load and compared with the analytical results.

2.2.4 Modelling considering Strain Hardening and Bauschinger Effect

The earlier analytical models neglect the effect of strain hardening and Bauschinger effect which may result inaccuracies in solutions for some materials. Many researchers incorporated the effect of strain hardening to model the hydraulic autofrettage of thick-walled cylinders. The elastic-perfectly plastic solution of Koiter (1953) was generalized by Bland (1956) to include strain hardening under internal and external pressures and temperature gradient. The elastic unloading of pressures and temperature difference and unloading with further plastic flow was considered to evaluate residual stresses. A numerical integration is necessary to obtain the solution as the analytical expressions are not in the closed form. Author assumed that the plane sections normal to the axis remain plane and the axial strain is same throughout the cylinder. Such hypothesis was not considered by Rees (1987), who obtained the theoretical general expressions using von Mises yield criterion, suitable for a numerical solution in the whole plastic zone. Author assumed closed-end condition taking into account work-hardening in the presence of small plastic strains based upon equivalent stress-strain data. The plastic strains were of the order of 10^{-2}. Comparison with experiments on carbon and alloy steels shows that author's solution provides more realistic predictions than a non-hardening theory.

Rees (1990) presented theories of hydraulic autofrettage for an open-ended thick-walled cylinder which predicts residual stress distribution in both strain hardening and non-hardening materials that deform by either von Mises or Tresca flow rule. The theories for hardening material do not provide the solution in closed form and a numerical integration is necessary. The von Mises theory was found to be more appropriate for open-end autofrettage practice in thick-walled cylinder of hardening material with diameter ratios greater than 2.96. The differences between the Tresca and von Mises solution was reported to be less severe for smaller diameter ratios with the maximum error of 15% in the bore hoop stress values. A general closed form analytical solution for the elasto-plastic stress, strain and displacement field for open-ended pressurized cylinder was given by Gao (1992) incorporating strain hardening. He obtained the solution using deformation theory of Hencky and von Mises yield criterion. He deduced a formula for the calculation of the plastic-limit pressure, which provides more reasonable theoretical basis for the design of an autofrettaged thick cylinder based on strength.

The Bauschinger effect is the reduction of the yield strength in compression as a result of prior tensile plastic overload. It is characterized by Bauschinger effect factor (BEF), given by the ratio of magnitude of true yield strength in compression to yield strength in tension (Parker *et al.*, 1999). It is a function of prior plastic strain in loading. The high compressive residual stress at the inner wall may cause reverse yielding of the cylinder. The reverse yielding may occur at a stress less than the tensile strength of the material due to Bauschinger effect. The Bauschinger effect is material dependent and thus, it is not predominant in all materials. Some high strength steels possess significant Bauschinger effect (Milligan *et al.*, 1966). Thus, for cylinders made of such materials, it is necessary to consider the Bauschinger effect in order to accurately predict the residual stress distribution due to autofrettage. Many researchers incorporated Bauschinger effect by defining a constant BEF for analyzing residual stress distribution in autofrettaged cylinders. Chen (1986) proposed a theoretical model for high strength steel and obtained a closed form solution of residual stresses with reverse yielding in autofrettaged cylinder. He studied the influence of the Bauschinger effect and hardening on the residual stress distribution. Author observed that both the hardening and Bauschinger effect affect the residual hoop stress distribution at the bore of the cylinder. Comparing the results for an 80% autofrettaged cylinder with wall ratio 2, author found that Koiter's model (1953) neglecting both the effects overestimates the residual hoop stress at the bore by 46% than the author's model. Stacey and Webster (1988) carried out analytical and numerical estimates of the residual stress distribution in hydraulically autofrettaged high-strength low-alloy steel cylinder with diameter ratio 2.07 by incorporating Bauschinger effect and strain hardening. The analysis was based on both Tresca and von Mises yield criterion. They observed a significant reduction in the residual hoop stresses at the inner wall with little alteration to the stress distribution elsewhere due to Bauschinger effect causing reverse yielding at the inner radius of the cylinder. Authors also observed that the calculated hoop stress distribution is sensitive to the assumed yield criterion irrespective of the material model used. The residual hoop stress predicted by Tresca criterion differs from the prediction of von Mises criterion by approximately 15%. Megahed and Abbas (1991) also developed a model using a material model capable of describing the observed reverse yielding and subsequent non-linear hardening during unloading to investigate the elasto-plastic and residual stresses of hydraulically autofrettaged cylinder. Numerical simulations for high strength medium alloy steel shows the reduction of compressive residual stresses due to

Bauschinger effect. However, the model proposed by the authors is physically unacceptable for many materials that require a specific analytical form.

The percentage plastic strain varies from a maximum value at the bore of the autofrettaged cylinder to zero at the radius of elastic-plastic interface and so does the BEF. Assumption of constant BEF may provide inaccuracies in the resulting residual stress distributions due to reverse yielding. Some researchers analyzed the influence of Bauschinger effect on residual stresses in autofrettaged cylinder considering variable BEF, which provides better accuracy than the models considering constant BEF. For example, Jahed and Dubey (1997) presented a method of predicting residual stress distribution in autofrettaged cylinder based on actual material curve, isotropic and kinematic hardening models and variable Bauschinger effect factor (BEF). They used linear elastic solution of an axisymmetric boundary value problem as a basis to generate the inelastic solution. The method treats the material parameters as a field variable and obtained the residual stress distribution following an iterative procedure. Authors observed significant changes to residual hoop stress near the bore of the cylinder for low level autofrettage than the high level autofrettage due to consideration of the variable BEF on plastic strain. Parker and Underwood (1998) also assumed variable BEF through the wall thickness to address the influence of Bauschinger effect on the residual stress distribution in cylinders undergoing hydraulic autofrettage. A parametric study was conducted by the authors to identify the optimum value of BEF at the inner radius for which the compressive residual hoop stress at the inner wall reaches a maximum value at the overstrain level corresponding to the onset of reversed yielding. The models of Jahed and Dubey (1997) and Parker and Underwood (1998) assumed a bilinear unloading behaviour of material to assess the Bauschinger effect. Parker *et al.* (1999) extended the method of Jahed and Dubey (1997) assuming the true nonlinear unloading profile of the material. They presented typical residual hoop stress distribution based upon Tresca yield criterion and plane stress condition for autofrettage of a cylinder with wall thickness ratio of 2. The results were compared with the results predicted by elastic-perfectly plastic behaviour without Bauschinger effect. Authors observed a reduction in the residual compressive hoop stress at the inner wall. They also observed that the Bauschinger effect penetrates much deeper into the cylinder than previous attempts at modeling typical gun steels have suggested (Chen, 1986; Parker and Underwood, 1998). Parker (2001a) further extended the works of Parker *et al*. (1999) to include the von Mises yield criterion combined with generalized plane strain condition for the cylinders with wall thickness ratio in the range 1.1–3. The results were compared with the ASME Pressure Vessel code (1997) and have been incorporated in ASME Boiler and Pressure Vessel code (2004). A general analytical solution applicable to various end conditions assuming von Mises yield criterion under similar conditions was given by Hosseinian *et al*. (2009).

In general, the autofrettage theories assume elastic-perfectly plastic, linear hardening or power law hardening stress-strain behaviour for modelling the process. Huang (2005) proposed an autofrettage model that does not need prior assumption of stress-strain behaviour, but depends on the actual tensile–compressive stress–strain curve of the material. Author assumed von Mises yield criterion, material incompressibility, and the plane strain condition and incorporated the Bauschinger effect. Analytical expressions for the residual stress distribution were derived. A similar analytical model was also proposed by Huang and Cui (2006) modifying the yield criterion. The authors modified the yield criterion for the cylinder incorporating a parameter α as $\sigma_{eq}=(\sqrt{3}/2)\alpha\sigma_Y$, where $1<\alpha<2/\sqrt{3}$. Authors found that the model provides more accurate prediction of the residual stresses in the cylinder for $\alpha=1.11$. Although the use of plane stain and incompressibility criterion makes model of Huang (2005) and Huang and Cui (2006) more restrictive, but the models provide reliable means for validating numerical as well as experimental results. Parker (2005) modified the model of Huang (2005) for open-end and generalized plane strain condition and proposed a pragmatic solution procedure using the plane strain solution of Huang (2005). An analytical solution for autofrettage considering Young's modulus and the reverse yield stress dependent on the prior plasticity based on actual tensile-compressive curve of the material and von Mises yield criterion was proposed by Huang and Moan (2009). They incorporated variable BEF and variation of unloading modulus as a function of prior plastic strain. A fixed nonlinear unloading profile was assumed for the analysis. Darijani *et al.* (2009) derived closed form analytical expressions for residual stresses in autofrettaged cylinders, considering Bauschinger effect and different slopes for forward and reversed loading based on Tresca yield criterion. They provided a simple analytical expression for determining the best autofrettage pressure with known cylindrical dimension. Also, the minimum acceptable thickness was determined for known working pressure and inner radius.

Recently, Aliakbari and Farhangdoost (2014) presented a mathematical model to study the behaviour of autofrettaged DIN1.0406 steel cylinder used in fuel injection system of diesel engine. They studied the influence of plastic deformation on the loading-unloading behaviour of the steel cylinder considering Bauschinger effect. A comparison of the behaviour of DIN1.0406 steel was carried out with DIN1.6959, HY 180 and PH 13-8Mo steel grades and it was found that the Bauschinger effect factor is not as great as the other three steel grades. Most recently, Alexandrov *et al.* (2016) provided exact analytical solutions for the residual stresses and strains in a thick-walled cylinder subjected to hydraulic autofrettage. The work is an extension of the seminal work of Bland (1956), who formulated analytical solution for isotropic hardening material. However, Alexandrov *et al.* (2016) extended it to kinematic hardening to take into account the Bauschinger effect. The solution was based on the Tresca yield criterion and its associated flow rule. Authors assumed closed-end condition and plane strain case for the analysis. A variable elastic range and different rates under forward and reversed deformation were assumed. Although the solution is analytic in practice, a numerical technique is required to solve the transcendental equations.

2.2.5 Modelling Based on Strain Gradient Plasticity Theory

An analytical model capable of predicting the stress, strain and displacement components in a hydraulically autofrettaged cylinder in closed form was given by Gao (2003) for strain-hardening material using plane strain condition based on a strain gradient plasticity theory. To describe the constitutive behavior of the material subjected to plastic deformation author assumed Hencky's deformation theory, the modified von Mises yield criterion and the power law hardening model. The classical-plasticity based solution for the same cylinder problem was recovered from the gradient-plasticity based solution. Numerical results for the maximum effective stress in the cylinder wall were presented in order to compare the classical-plasticity based solution and gradient-plasticity based solution. It was found that the gradient plasticity solution differs significantly from the classical plasticity solution for cylinders with very small inner radius, less than 200 microns. For cylinders with inner radius 200 microns or above, the gradient plasticity solution approaches to that of the classical plasticity solution. Gao (2007) presented another similar analytical solution based on strain gradient plasticity theory for elastic linear-hardening plastic material to construct improved expanding cavity models that incorporate both the strain-hardening and indentation size effects. Recently, Gao *et al*. (2015) generalized the two earlier strain gradient plasticity solutions (Gao, 2003 and 2007) based on a unified yield criterion and applied the resulting solutions to perform autofrettage analyses of thick-walled cylinders.

2.2.6 Finite Element Method and Finite Difference Method Based Models

Many researchers have employed numerical techniques such as finite element method (FEM) or finite difference method (FDM) for studying the stress behaviour induced in hydraulic autofrettage. At the earliest, Hill *et al*. (1947, 1951) developed a finite difference method of solution assuming plane strain condition for hydraulically autofrettaged closed-end cylinder. They considered Tresca yield criterion and Prandtl-Reuss plastic stress-strain law for the analysis. The model assumes compressibility of materials within the plastic region. Comparing the solution with the theories neglecting elastic strains in the plastic region, they observed a discontinuity in the axial stress at the elastic-plastic boundary radius. The difference between the two solutions increases as the elastic-plastic boundary radius increases. An error of greater than 60% in the axial stress was observed on the assumption of zero elastic strain in the plastic region for all ratios of outer to inner radii. A finite difference numerical solution of hydraulic autofrettage of open-ended thick cylinder of wall ratio 2:1 was carried out by Thomas (1953). The solution was based on the Prandtl-Reuss incremental stress-strain relations, together with the Tresca yield criterion. The author compared his solutions with the previously available solutions of Allen and Sopwith (1951) and Steele (1952). A stiffness method involving finite difference solution for elastic-plastic problems using the incremental Prandtl-Reuss equations was suggested by Marcal (1965). The method assumes that the laws of plasticity are linear over an increment. Author tested the method for the closed-end thick-walled cylinder subjected to internal pressure. The results of Marcal (1965) agree with the results of Hill *et al*. (1951) for a cylinder with a diameter ratio of 2:1. Chen (1972) developed the incremental tangent-modulus approach of the finite element formulation together with the computer program for the generalized plane-strain case in the thick-walled cylinders subjected to internal pressure, external pressure and end force. The material model was assumed to be elastic-plastic strain-hardening, obeying the von Mises yield criterion and the Prandtl-Reuss flow theory. Later, the author proposed a finite difference approach for the problem (Chen, 1980). The numerical procedure uses an incremental approach and does not involve any iteration for each increment. The accuracy of the problem depends on the grid size and load increments.

In late 90's and early 21st century, several researchers used FEM modeling of the hydraulic autofrettage process to study residual stress distribution, optimum autofrettage pressure, post machining effects on the distribution of residual stresses. Feng *et al*. (1998) carried out the analysis of stresses and strains induced by low temperature hydraulic autofrettage of AISI 304 steel cylinder by using FEM method. They investigated the influences of the autofrettage pressure, temperature, work hardening and reverse yielding on the residual stresses generated in the cylinder. The finite element calculation showed that more beneficial residual stress can be generated by autofrettage at low temperature than at room temperature. This may be due to the fact that at low temperature, the yield stress of the material is higher and the thermal strains accumulated during warm up to room temperature add to the autofrettage pre-compression. Authors found that the optimal autofrettage pressure and temperature of the cylinder were about 4000 bar and –90 °C, respectively. A 3-D FEM analysis of the autofrettaged cylinders with cross-bore was carried out by

Badr *et al*. (1999). They analyzed elastic-plastic and residual stress and strain fields including Bauschinger effect. The FEM results were compared with the analytically developed solution based on the strain energy density method. The strain energy density method provides relatively simple and reasonably accurate estimate of cross-bore intersection stresses and strains than the expensive and time consuming elastic-plastic FEM analysis. Hameed *et al*. (2004) also carried out a 3-D FEM analysis to evaluate the effect of radial cross-bore qualitatively in an autofrettaged cylinder using ANSYS finite element package. They observed that there is a severe localized change in the residual stress profile in the vicinity of the cross-bore. Authors carried out the analysis for variable cross-bore diameter and observed that by increasing the diameter of the radial hole, the residual hoop stress at the inner wall reduces, whilst it increases at the outer wall.

Gibson *et al*. (2006) presented a series of finite element models to predict the residual stress distribution in hydraulically autofrettaged cylinders for a range of end conditions— plane stress, plane strain and generalized plane strain. They assumed bilinear strain hardening material model including Bauschinger effect. Authors compared the results with an alternative numerical model (Parker, 2001) and Huang's (2005) analytical model.

A multi-linear kinematic two-dimensional FEM model incorporating Bauschinger effect was developed by Hameed *et al*. (2003) using commercial ANSYS package to assess the post machining effects in a hydraulically autofrettaged gun barrel. They studied the effect of machining both at the inside and at the outside diameter on the depth of yield, maximum firing pressure and final residual stress distribution in the barrel. The FEM results were validated with experimental results. Authors observed that the reduction in the maximum compressive hoop stress is more sensitive to internal machining than external machining. They also observed that the depth of yield remains stable and there is no movement of the radius of elastic-plastic interface, relative to its location before material removal. The maximum firing pressure is not affected, if the internal machining removes material in which reverse yield has occurred. The post machining residual stress distribution in a hydraulically autofrettaged cylinder was also studied by Bähre and Brünnet (2011) by using finite element analysis in ABAQUS and they made the similar observations.

Majzoobi *et al.* (2003) investigated the effect of autofrettage process on high pressure cylinders using finite element numerical simulation. They performed numerical simulation using finite element package NISA with an axisymmetric analysis. Authors incorporated kinematic hardening model for the analysis. The burst pressure of the cylinder was evaluated using von Mises yield criterion. Experiments were also conducted to compare the numerical results. Authors observed that the best autofrettage pressure for strain hardened material is the pressure which brings the outer surface of the cylinder to the yield point. Any pressure higher than that will result in reduction of bursting pressure of the cylinder. The value of autofrettage pressure obtained by finite element simulation and experiments closely agrees with the Xiaoying and Gangling (1984) analytical solutions.

A finite element analysis was carried out by Alegre *et al*. (2006) to obtain the residual stress distribution after the autofrettage of a 15–15 PH stainless steel incorporating Bauschinger effect. The finite element simulations were carried out considering an elastic-perfectly plastic behaviour of the material for the loading phase and a Ramberg–Osgood behaviour for the unloading phase, with its power coefficients depending on the previous equivalent plastic strain reached during the loading process. Authors observed a reduction of the residual stresses of about 25% due to the Bauschinger effect. They also observed that if an autofrettage pressure value is exceeded, the residual stresses increase only slightly, whereas the plastic strains achieved during the autofrettage loading increase exponentially. Shim *et al.* (2010) studied the Bauschinger effect in hydraulic autofrettage of SNCM8 high strength steel cylinder and observed that this effect is significant under some conditions. The tensile and uniaxial Bauschinger effect tests of SNCM8 were performed to evaluate BEF, and then this constant was used in calculating the residual stress distribution by analytical and finite element analysis.

Recently, Parker *et al.* (2012) carried out a finite element stress analysis of hydraulic autofrettage incorporating a material model whose unloading behaviour varies with radius and Bauschinger effect. The finite element analysis was carried out by two methods— using a user programmable feature within a non-linear finite element analysis and using an elastic modulus and Poisson’s ratio adjustment procedure within a linear effective finite element analysis. Authors showed that both these two methods are in agreement with each other.

A finite difference method (FDM) was used by Perry and Aboudi (2003) to study hydraulic autofrettage of a thick-walled cylinder. The analysis was based on von Mises yield criterion, isotropic strain hardening in plastic region and Prandtl-Reuss theory. Authors assumed plane stress condition and accounted for Bauschinger effect during pressure release. The stresses were evaluated incrementally by FDM. The effect of machining of the cylinder after autofrettage on residual stresses was also studied. It was observed that strain hardening does not affect the residual stress distribution significantly, but Bauschinger effect does. A three-dimensional (3-D) finite difference numerical solution for hydraulic autofrettage incorporating the Bauschinger effect, using an accurate numerical representation of the experimentally measured material behaviour was given by Perl and Perry (2006). A 3-D computer code was developed for determining the stresses, strains and displacements throughout the autofrettage process. The analysis can also predict residual stress field in swage autofrettage process.

2.2.7 Optimization of Autofrettage Pressure

An analytical model to obtain the optimum radius of elasto-plastic interface and optimum autofrettage pressure in a hydraulically autofrettaged cylinder was given by Zhu and Yang (1998). They derived simple analytical expressions to evaluate optimum radius of elastic-plastic interface and optimum autofrettage pressure based on Tresca and von Mises yield criterion considering elastic-perfectly plastic material model. Authors studied the influence of autofrettage on stress distribution in a cylinder. Majzoobi and Ghomi (2006) used sequential quadratic programming (SQP) technique to obtain the optimum radius of elastic-plastic interface and the optimum autofrettage pressure. Wahi *et al.* (2011) presented an analytical procedure for hydraulic autofrettage to predict the optimum autofrettage pressure and the radius of elastic-plastic interface. They reported that the optimum autofrettage pressure and radius of elastic-plastic interface increases with operating pressure.

A theoretical modelling of a strain hardening cylinder undergoing hydraulic autofrettage was carried out by Hojjati and Hassani (2007) to investigate the optimum autofrettage pressure and the optimum radius of the elastic-plastic boundary in plane stress and plane strain condition. They assumed von-Mises yield criterion and isotropic hardening material model for the analysis. Authors also carried out a finite element analysis using commercial finite element package ANSYS to model the cases (plane stress and plane strain). They optimized the parameters based on minimizing the maximum equivalent von Mises stress. The finite element results were compared with the analytical results. They observed the maximum error of 0.3% in the optimum radius of elastic-plastic boundary and 0.7% in the optimum autofrettage pressure between the analytical and the finite element results. Comparing the optimum autofrettage pressure in plane-stress and plane-strain for various working pressures authors observed that the difference of optimum autofrettage pressure in these two different conditions is negligible with the maximum deviation of 1.6%. It was also observed that increase of the strain hardening exponent, *n*, and the ratio of outer to inner radii of the cylinder leads to an increase in the optimum autofrettage pressure. A similar analysis in ANSYS was also carried out by Ali *et al.* (2010). They calculated the optimum autofrettage pressure and the optimum radius of elastic-plastic junction on the basis of von Mises yield criterion and bi-linear elasto-plastic behaviour of the material. Authors observed that the optimum autofrettage pressure increases along with the working pressures. They concluded that cylinder material having higher slope of strain hardening segment provides better benefits in the autofrettage process. It is due to the reduction of the resultant von Mises stress as the slope of the strain hardening segment increases. Ayob *et al.* (2009) used two dimensional FEM simulations with ABAQUS package to investigate optimum autofrettage pressure and elastic-plastic radius of interface. They also provided analytical solutions and validated with the FEM model. Authors studied the effects of autofrettage level parameters on the pressure carrying capacity of cylinders. Using Tresca's yield criterion, with the assumption of an elastic-plastic material together with an autofrettage level parameter, they developed a precise solution for residual stress distribution.

2.3 Modelling of Swage Autofrettage Process

The swage autofrettage process is less investigated by the researchers. The theoretical models for swage autofrettage are mostly based on the numerical methods. The analytical modelling of swage autofrettage process is difficult due to its localized and transient nature of the process. Nevertheless, Clark (1982) predicted the residual stresses induced by swage autofrettage of a gun barrel in a simplified manner considering the cylinder under internal pressure while the mandrel is pushed through the cylinder. A similar approach was followed for the analysis as in the hydraulic autofrettage assuming elastic-perfectly plastic material model and open-end condition. An empirical relation based on experimental observation was used by the author as yield criterion, which is given by

$$\sigma_\theta - \sigma_r = 1.08\sigma_Y, \qquad (2.1)$$

where σ_θ, σ_r correspond to the hoop and radial stresses and σ_Y is the yield stress of the material. A simple analysis of the swage autofrettage process was also reported by Chen (1988a) providing analytical solutions expressed in closed-form. He considered a simplified plane-strain problem of the mandrel-tube assembly. The analysis was based on Tresca's yield criterion and its associated flow rule. For the analysis author assumed elastic-perfectly plastic material model for the cylinder and an elastic mandrel. He obtained the deformation and stress distribution during swaging by solving the shrink-fit problem beyond the elastic limit. After swaging, the permanent bore enlargement and residual stresses were calculated by an unloading analysis taking into account the Bauschinger effect and the strain-hardening.

Many researchers have carried out numerical modelling of the swage autofrettage process based on either finite difference method (FDM) or finite element method (FEM). A nonlinear FEM analysis to calculate residual stress and deformation time history of a swage autofrettaged thick walled cylinder was carried out by Till and Rammerstorfer (1983). The influence of friction at the interface between the moving mandrel and the inside surface of the cylinder was taken into account for the analysis. Authors presented a comparison of the process with the hydraulic autofrettage. A significant amount of axial stresses was observed in the swage autofrettage than the hydraulic autofrettage process. These axial stresses lead to smaller plastic regions in swage autofrettage compared to hydraulic autofrettage. Also, the residual stresses generated in the swage autofrettaged cylinder were found to be slightly smaller than in the hydraulically autofrettaged cylinder. Chen (1988b) carried out both one and two-dimensional FEM analyses of the swage autofrettage of a thick-walled cylinder using non-linear finite element program in ABAQUS. They presented the numerical results for the displacements, strains, and stresses in the cylinder during and after swage autofrettage. Approximate solutions were obtained for both one and two-dimensional cylinders pressed by rigid or elastic mandrels. By comparing the results between the one and two-dimensional models, authors observed that the difference of the residual stress distribution obtained by the two models is negligible. The process was also investigated by O'Hara (1992) using finite element ABAQUS code. The residual stress distribution was calculated from a conventional theoretical solution for 83% overstrain for plane stress case and was compared with the finite element solution taken from the contour plots. Authors observed reasonable agreement of the residual stresses at the inner and outer radii of the cylinder, whereas the distribution within the cylinder wall is rather different. O'Hara (1992) presented the swage autofrettage solution for elastic-perfectly plastic material without Bauschinger effect. Later, Parker *et al.* (2003) modified the results presented in O'Hara (1992) incorporating Bauschinger effect. Available experimental evidence was used by the authors to assess the validity of the resulting modified stress distribution.

A non-linear finite difference based numerical analysis of the swage autofrettage of a gun barrel by forcing an oversize mandrel through the barrel was carried out by Iremonger and Kalsi (2003). They conducted analyses on a single pass as well as on a two pass swaging procedure in which two separate swages are driven through the barrel. The analysis was based on elastic-perfectly plastic material model and von Mises yield criterion. The ram driving force required along with the resulting barrel deformations and stresses in both single and two pass swaging are analyzed. The effects of changes to swage geometry for single pass swaging are also considered. Authors found that the two pass swaging process provides greater reduction of driving force than single pass swaging. The mandrel shape modification was investigated and found that only an increase in the slope of the rear of the mandrel leads to a meaningful reduction in the driving force but this is at the price of a reduced enlargement of the bore radius. This is caused by the more reduction in contact area between the barrel and the mandrel. Gibson *et al.* (2012) also investigated driving force variation during swage autofrettage using finite element analysis in ANSYS. They observed a close match between the driving force predicted by their ANSYS model and the experimentally known value quoted in Iremonger and Kalsi (2003). A detailed analysis of the effect of double pass swaging in order to study the influence on the resulting stress distribution in swage autofrettage of cylinders was also carried out by Barbáchano *et al.* (2011) using finite element simulation, assessing the advantages and drawbacks as opposed to the single pass swaging. They used a combined isotropic and kinematic hardening model incorporating Bauschinger effect for the analysis. The analyses were carried out with mandrels of varying sizes to analyze the effect of a rigid mandrel compared to a linear elastic one. Authors observed that the double pass swaging in opposite directions generates greater compressive stresses and reduces the edge effect. Also, a rigid mandrel with corrected interference instead of an elastic one provides more accurate distribution of radial and hoop stresses.

Bihamta *et al.* (2007) carried out two dimensional axisymmetric and three dimensional FEM analyses to investigate the effects of workpiece and mandrel geometry on the forming load and part quality in swage autofrettage process. The FEM results were validated with experiments. Authors observed that the forming load is increased with increasing the mandrel cone angle. Mandrel with larger cone angle creates smaller radial stresses and may provide a longer life. They also concluded that increasing the length of the constant cross-section of the mandrel causes better dimensional stability of the product, but it results in an increase of forming load. A similar analysis was also carried out by Alinezhad and Bihamta (2012) using commercial finite element package ABAQUS to assess the effect of various tool design parameters (mandrel angle and sizing zone length) on the swage autofrettage process.

A 3-D axisymmetric model for solving the residual stress field due to swage autofrettage in terms of both the radial and axial displacements was presented by Perry and Perl (2008). A finite difference approach was used to approximate the axisymmetric equilibrium equations. The resulting equations were then solved by Gauss-Seidel method. Authors developed a computer code to evaluate the stresses, strains, displacements and forces in the process and validated the numerical results with a full-scale instrumented swage autofrettage experiment. Rees (2011) presented a classical elastic-plastic theory for swaging of thin discs. The theory was based upon material hardening model under plane stress and plane strain conditions considering both Tresca and von Mises yield criterion. The solution of the analytical expressions requires a numerical integration procedure. The obtained numerical solutions were close to the solutions of non-hardening material. He also provided an experimental assessment of the theory.

The influence of the coefficient of friction on residual stresses and plastic radius in swage autofrettage was investigated by Chang *et al.* (2013) using a finite element method. The method involves Coulomb friction model and plane strain condition for the analysis. Authors observed that the coefficient of friction does not affect the residual stress and plastic radius. They deduced the formula of plastic radius, stress and strain in the swage autofrettaged cylinder, utilizing all equations of the spatial axisymmetric problem, boundary condition and continuity condition of swaging. A finite element modelling of the swage autofrettage process was developed by Gibson *et al.* (2014) in ANSYS to investigate the mechanism of deformation and residual stresses. A parametric study was carried out by them considering various properties such as mandrel slope angle, parallel section length and coefficient of friction to study the influence of these parameters on the residual stress distribution. Hu and Penumarthy (2014) carried out an axisymmetric FEM modelling of swage autofrettage of thick-walled cylinders considering elasto-plastic material model with non-linear strain-hardening and kinematic hardening. They analyzed the residual stresses induced by swage autofrettage process and compared the results with the experimental results available from the literature. Authors optimized the radial interference of the mandrel with the cylinder and obtained the maximum percentage reduction of the von Mises stress in the swage autofrettaged thick-walled cylinder under elastic-limit working pressure. Recently, Dewangan and Panigrahi (2015) analyzed the swage autofrettage in the gun barrel by varying the percentage of interaction between the mandrel and the barrel interference. They used commercially available ANSYS package to study the deformation effects caused by the mandrel and the geometrical variation of the mandrel on the gun barrel. Authors concluded that a proper design of the geometry of the mandrel is necessary in order to determine the after effects in the swaging process.

2.4 Modelling of Explosive Autofrettage Process

The realistic modelling of the explosive autofrettage is complex due to the dynamic nature of the problem. Limited literature analyzed the behaviour of the explosive autofrettage. Mote *et al.* (1971) studied the feasibility of the explosive autofrettage process for cannon barrels. The study involved determining the applicability of, the reliability of and the scaling laws associated with the process. The analytical study developed the scaling laws and similitude requirements for scale model testing. A mathematical model of the plastic response of a thick-walled cylinder subjected to an internal impulse was also developed. Authors assumed an isotropic, incompressible, elastic-perfectly plastic material devoid of Bauschinger defect for the modelling involving dynamic elasto-plasticity. The axial and tangential velocities and displacements were assumed to be negligible in the analysis.

A non-linear FEM analysis of explosive autofrettage of a thick-walled cylinder made of 43CrNiZMoVA steel was carried out by Ren-rui *et al.* (1999). The analysis was based on the explosive pressure curve, dynamic mechanical property and constructive relationship of the material. The stress distribution, displacement, velocity of different position and the size of the plastic zone versus the time were obtained for different explosive pressure.

2.5 Experimental Measurement of Residual Stresses in Autofrettage processes

The experimental assessment of the residual stresses induced by autofrettage process is necessary for understanding the physical viability of the process. Researchers have used different experimental methods to quantify the residual stresses induced by autofrettage process in a thick-walled cylinder. The methods are destructive or non-destructive in nature. The most widely used destructive methods by the researchers for measuring the residual stresses in autofrettaged cylinders are Sachs boring method (Sachs, 1927), hole drilling method (Mathar, 1934; Beaney and Proctor, 1974), compliance method (Cheng and Fannie, 1986) and slitting method (Vaidyanathan and Finnie, 1971). The popular non-destructive methods include X-Ray diffraction (XRD) technique (Hughes, 1967) and neutron diffraction technique (Allen *et al*., 1981).

The most popular destructive method is the Sachs boring method for experimental measurement of residual stresses in autofrettaged cylinders. In its usual form, the method involves fixing strain gauges in the circumferential and axial directions on the outer periphery of the cylinder. The layers of material from the inside of the cylinder are then bored out incrementally and the relaxed strains are measured after removal of each layer of material. The measured strains are then used to evaluate the residual stresses using Sachs boring equations (Sachs, 1927). Faupel (1955) evaluated the residual stress distribution in autofrettaged steel cylinder using Sachs boring method and compared the results with the theoretical prediction. Author observed the maximum deviation of about 25% between the Sachs boring and the theoretical prediction of the residual hoop stress at the bore of the cylinder. Stacey *et al*. (1985) measured the residual stresses in high strength low alloy steel autofrettaged cylinder using Sachs boring method. They also quantified the residual stresses using neutron diffraction method and compared the stress distribution with the Sachs boring technique. Authors observed a close agreement of the residual stresses predicted by the two methods. Stacey and Webster (1988) carried out the experimental determination of the residual stresses in the hydraulically autofrettaged AISI 4333M4 steel cylinder by the Sachs boring method and neutron diffraction method to verify the analytically obtained stress distribution based on both Tresca and von Mises yield criterion. Authors observed that except close to the inner radius, the experimental data lie between the results predicted by considering von Mises and Tresca criteria irrespective of the material model employed. The determination of the residual stresses in the hydraulically autofrettaged steel cylinders using Sachs boring method was carried out by Venter *et al.* (2000). In addition, they used neutron diffraction and the compliance method and carried out a comparison among them. They reported that results from the Sachs boring and neutron diffraction techniques compare favorably across large portion of the cylinder wall, while the results of the compliance method showed different features. Perry and Aboudi (2003) also conducted Sachs boring experiment to verify the residual stresses predicted by the finite difference model developed by them.

Davidson *et al.* (1962) were the first to determine the residual stresses experimentally in swage autofrettaged cylinder using Sachs boring method. In a later paper, Davidson *et al.* (1963b) also used Sachs boring method to determine residual stresses as a function of the magnitude of overstrain and its effect on elastic strength characteristics in swage autofrettaged cylinders. They carried out the test for different diameter ratios ranging from 1.5 to 2.3 with different level of overstrains. Authors found that for optimum overstrain conditions, the tangential residual stress distribution and the increase in elastic response of cylinders autofrettaged by swaging are comparable to those of the hydraulic autofrettage behaviour. A substantial axial residual stress exists in the swage autofrettaged cylinders as the result of an axial shearing stress due to the tapered mandrel. They also observed that the axial residual stress increases with increased overstrain with a resultant decrease in the residual hoop stress. Underwood *et al.* (2007) measured the residual hoop stress induced by swage autofrettage in thick-walled cylinder using neutron diffraction method and compared the results to measurements of residual hoop stress of a similar cylinder due to hydraulic autofrettage. Results from neutron diffraction measurements showed a significantly shallower depth of overstrain in a swage autofrettaged tube compared with those predicted from hydraulically autofrettaged cylinder for the same amount of total bore hoop strain. The Sachs boring method was used by Ezra *et al*. (1973) and Ren-rui *et al*. (1999) for experimental evaluation of residual stresses induced by explosive autofrettage. Taylor *et al*. (2012) carried out experimental measurement of residual stresses in an explosively clad cylindrical pressure vessel using neutron diffraction and slitting method.

George and Smith (2000) measured the residual stresses using the deep-hole technique in a hydraulically autofrettaged steel tube. Their measurement results are in good agreement with residual stresses predicted by a finite element simulation of the autofrettage process. The results show a deviation of about 19.5% in the maximum hoop stress at the inner radius. The hoop and radial residual stress distribution in an autofrettaged high strength steel cylinder was measured by Jahed *et al*. (2012) using hole drilling technique. For the measurement, a ring sample cut from an autofrettaged cylinder was used and relieved strains due to hole-drilling were measured by rosettes of three strain gauges fixed on the surface of the ring. The measured strains were then transformed to residual stresses using calibration constants and mathematical relations of elasticity based on ASTM standard recommendations (ASTM E 837-08, 2008). Authors compared their measurements with the predicted residual stress using the method of Jahed and Dubey (1997).

Clark (1984) used X-ray diffraction (XRD) technique to measure residual stresses in autofrettaged cylinder. Ring specimens of 25.4 mm thick were cut from the central section of the cylinders. Mechanical polishing and electro-polishing were then carried out on one face of the specimens in order to remove all mechanical damage from the prior cutting operations. X-ray measurements of the residual hoop stress were obtained at a number of points along a radius on each ring. Zerari *et al*. (2013) also used XRD method to evaluate residual stresses in cylinders induced by the hydraulic autofrettage. Lee *et al*. (1992) carried out X-ray residual stress distribution analysis in swage autofrettaged steel cylinder to characterize the effects of axial mid-wall channels and investigated the effect of spatial resolution on stress determination and obtained X-ray beam images to determine the effective beam spread. An optimized partial beam technique was used to take experimental measurements in the channel root areas, where high stress gradients were found. The experimental stress distribution was compared with a model based on Tresca's yield criterion for a solid cylinder under internal pressure.

Microhardness test can be used as a qualitative test for inferring residual stresses in components (Kokubo, 1932; Pharr *et al*., 1994; Tosha, 2002). Researchers observed that the surface microhardness increases due to presence of compressive residual stresses, whilst the surface microhardness decreases due to presence of tensile residual stresses. Another qualifying test for envisaging the presence of residual stresses in an autofrettaged cylinder is the measurement of opening angle due to radial cut through the wall of the cylinders (Parker *et al*., 1983; Parker and Underwood, 1998). When a radial cut is made through the wall of the autofrettaged cylinder, the cylinder opens by an angle which is a direct measure of pure bending moment ‘locked-in’ to the cylinder. It can be demonstrated that the experimentally measured opening angle matches with the released bending moments locked into the cylinder based upon stress analysis and thus confirming the presence of residual stresses.

2.6 Fatigue Life Analysis of Autofrettaged Cylinders

In the design of thick-walled cylinders, one of the prime objectives is to increase their fatigue life. Several researchers have analyzed the fatigue life of autofrettaged cylinders in order to provide a safe and reliable design while operating under cyclic loading. Parker and Farrow (1981) presented approximate solutions for the opening mode stress intensity factor in a radially cracked autofrettaged thick cylinder, with or without internal pressure. The solutions can be used for the prediction of fatigue life of the cylinder under cyclic pressurization. Parker *et al.* (1983) predicted fatigue life using the stress intensity factor solution of Parker and Farrow (1981) for straight-fronted radial crack in a thick-walled cylinder subjected to autofrettage. Rees (1990) predicted the fatigue life of both autofrettaged and non-autofrettaged cylinders with diameter ratio 2 under open-end conditions considering non-hardening as well as hardening material model. For this purpose, the stress intensity factor calibration of Parker and Farrow (1981) was used and the stress intensity factor of Bowie and Freese (1972) was modified to account for the presence of the residual stresses. The stress intensity factor was calculated for straight as well as elliptical fronted longitudinal crack and the fatigue life was evaluated using Paris law (Paris and Erdogan, 1963). Results were compared with the available experimentally determined fatigue lives. It was observed that the non-hardening material model provides acceptable results. Rees (1991a) also carried out the fatigue life prediction of autofrettaged cylinder for closed-end conditions modifying number of available stress intensity factors (Underwood, 1972; Bowie and Freese, 1972; Pu and Hussain, 1979; Throop, 1970; Parker and Farrow, 1981) and then incorporating in Paris law. Author considered elliptical crack geometry for the analysis and in order to incorporate the crack geometry, the available stress intensity factors were modified accordingly. Comparing the results with the fatigue life of non-autofrettaged cylinder, author observed a significant increase in the fatigue life of autofrettaged cylinder for a range of working pressures. Also, comparing the results with experiments, author found that the result provided by modified stress intensity factor of Bowie and Freese (1972) is more consistent with the fatigue life observed in autofrettaged cylinders. In a later paper, Rees (1991b) combined the stress intensity factors of Bowie and Freese (1972) and Banks-Sills and Marmur (1989) to calculate the fatigue lives of plain and rifled-bored cylinders for both non-autofrettaged and autofrettaged conditions in a similar manner considering the straight-fronted and elliptical-fronted longitudinal crack.

A fracture mechanics-based fatigue life analysis was developed by Underwood and Parker (1995) for pressurized thick-walled autofrettaged cylinders with one or several semi-elliptical-shaped axial grooves at the inner radius. The fatigue life for a crack initiating at the root of the groove was calculated for various cylinder, groove and crack configurations and for different material yielding conditions. Authors compared their result with laboratory life of A723 thick-walled cylinders resulting from cyclic hydraulic pressurization.

Koh (1996) carried out a finite element fatigue test simulation of autofrettaged thick-walled cylinders with an external groove under pulsating pressure. Life estimations of the cylinders were made by using a local strain approach, which is based on a local strain calculation and a fatigue damage relation.

Author observed that the estimated fatigue lives were within factors of 2–4, compared with the experimental fatigue lives determined from the simulation fatigue tests. The fatigue life design of thick-walled autofrettaged pressure vessel with external groove using computer aided engineering techniques was carried out by Koh *et al*. (1997). He carried out the shape optimization of the external grooves and fatigue life estimation of the vessel using ANSYS finite element package. Koh (2000) also predicted the fatigue life of cross-bored autofrettaged cylinder using linear elastic finite element analysis. The fatigue analysis of autofrettaged components using FEM was carried out by Thumser *et al*. (2002) incorporating strain dependent Bauschinger effect. The calculated residual stress field was used to evaluate the endurance limit of the component. Authors calculated the necessary stress intensity factors due to loading and residual stresses using the weight function method.

Parker and Underwood (1998) studied the effect of fatigue lives in autofrettaged cylinders, which they have corrected for the Bauschinger effect. Considering the analysis of Parker and Underwood (1998) further, Troiano *et al*. (2003) estimated the fatigue lives for all cylinders using Paris law. They observed that the higher strength material always provides longer fatigue life. The fatigue life analysis of autofrettaged cylinders based on experimental loading-unloading stress-strain characteristic was carried out by Jahed *et al*. (2006a). A longitudinal surface crack emanating from the bore was assumed for the analysis. Authors employed weight function method developed by Bueckner (1970) and Rice (1972) to evaluate the stress intensity factor. The stress intensity factor was then used in Paris law to estimate the fatigue life. It was observed that the fatigue life is increased by a factor of 2.11 at 10% autofrettage to 4.96 at 90% autofrettage. Farhangdoost and Aliakbari (2011) carried out a comparison of the fatigue lives of autofrettaged and non-autofrettaged aluminum cylinder with outer to inner radii ratio 2. They conducted experiments and carried out numerical simulation in ABAQUS to estimate the fatigue lives. Authors observed that the fatigue life of the autofrettaged cylinder is more than the non-autofrettaged cylinder for a range of working pressures. Recently, Ma *et al*. (2015) studied the influence of Bauschinger effect on the stress intensity factors of a semi-elliptical crack in determining the fatigue life of autofrettaged cylinders.

2.7 Study of the Autofrettage Process Combined with Shrink-fit

Both shrink-fit and autofrettage are generally employed in order to generate beneficial compressive residual stresses in cylinders. The shrink-fit of cylinders alone generates less compressive residual stress compared to autofrettage process at and around the inner wall of a cylinder. The combination of both shrink-fit and autofrettage may provide a more suitable residual stress distribution increasing the performance of the compound cylinder than the autofrettaged monobloc cylinder. Researchers have studied the combination of autofrettage and shrink-fit to enhance the residual stress distribution and thereby to improve the fatigue life. Kapp et *al*. (1998) proposed a multilayer design procedure incorporating shrink-fit of cylindrical layers on a previously autofrettaged monobloc cylinder in order to achieve a very long fatigue life. A Bauschinger effect design procedure by adding material through shrink-fit to an autofrettaged tube was proposed by Parker (2001b). Parker’s method (2001b) was based on an earlier method (Parker *et al*., 1999) where the removal of material from the inside of the cylinder achieved a similar reduction of the Bauschinger effect. Parker and Kendall (2003) presented a design methodology for combination of autofrettage and shrink-fit which is different from Parker (2001b). Their procedure consists of a sequence involving shrink-fit of two cylinders followed by autofrettage. The procedure reduces the near-bore plastic strain by approximately 50% compared to that occurs in the monobloc autofrettaged cylinder, thereby reducing the impact of Bauschinger effect. The authors achieved an increase of 41% in the fatigue lifetime of the cylinder.

Majzoobi *et al*. (2004) simulated aluminum shrink-fit cylinders with different shrink-fit radii for different shrink-fit pressures. They investigated the optimum shrink-fit radius when the shrink-fitted cylinder is subjected to autofrettaged pressures. Authors obtained the best shrink-fit radius corresponding to the situation when the maximum von Mises stress at the inner radii of both the inner and outer cylinders become equal.

A methodology for design optimization of a three-layered cylindrical vessel for achieving the maximum fatigue life under the combined effects of autofrettage and shrink-fit was presented by Jahed *et al.* (2006b) based on actual material behaviour. They determined the optimum values of the layer thicknesses, shrink-fitting pressures and autofrettage percentages with a proper sequence of steps. Simplex search method was employed to obtain optimum size of each layer and to optimize the initial stress distribution. For predicting the residual stress induced by autofrettage process, authors employed the method of Jahed and Dubey (1997). Authors observed that with proper combination of operations, a significant enhancement in the fatigue lifetime of the cylinder can be achieved. Lee et *al.* (2009) studied the combined effect of shrink-fit and autofrettage process for cylinders based on elastic-perfectly plastic and the strain hardening material models. They investigated the effect of shrink-fit tolerance for different overstrain percentages of the autofrettage on the residual hoop strain. Authors found that the residual compressive stress due to strain hardening model can be considerably improved by increasing overstrain level up to 80%. They concluded that the increase of shrink-fit tolerance is detrimental to the combined process.

Some recent studies on the combination of autofrettage and shrink-fit of cylinders have been carried out by Gexia and Hongzhao (2012), Abdelsalam and Sedaghati (2013) and Bhatnagar (2013). Gexia and Hongzhao (2012) presented analytical solutions for residual stresses in shrink-fit two-layer cylinders after autofrettage based on the actual tensile-compressive stress-strain curve of the material, von Mises yield criterion and plane strain condition. Similar to Huang and Cui's model (2006), they assumed a fixed material behavior during autofrettaged unloading and shrink-fitting. Abdelsalam and Sedaghati (2013) presented a design optimization methodology to identify optimal configurations of a two-layer cylinder subjected to different combinations of shrink-fit and autofrettage processes using genetic algorithm and sequential quadratic programming (SQP) optimization techniques. They optimized the thickness of each layer, autofrettage pressure and radial interference for each shrink-fit and autofrettage combination in order to achieve the maximum fatigue life of the compound cylinder. The modelling of autofrettage and shrink-fit compound cylinder using Huang's model (2005) including reverse yielding due to Bauschinger effect was carried out by Bhatnagar (2013). The autofrettage and post autofrettage machining was validated using FEM on ANSYS. The author concluded that the compounded cylinder provides a high maximum safe pressure, good fatigue life and manufacturing economy in terms of reduced autofrettage pressure leading to the reduction in the maintenance of a hydraulic autofrettage plant.

2.8 Elasto-plastic Thermal Stress Analysis

The thermal loading in a cylindrical body produces thermal stresses. Under sufficiently high thermal loading, the thermal stresses may cause elasto-plastic deformation in the wall of the cylinder. Removal of the thermal loading has the potential to generate the residual stresses. This is the basis of the present research work. Thus, for its relevant importance, works analyzing the elasto-plastic thermal stresses in cylindrical bodies have been reviewed in this section.

The classical solution of elastic thermal stresses in thick-walled cylinders under steady state temperature distribution due to thermal gradient is well known (Noda *et al.*, 2003). Numerous papers exist analyzing the thermo-elastic stresses in cylinders under steady or transient temperature distributions (Poritsky, 1934; Sinha, 1978; Ootao *et al.*, 1991; Obata and Noda, 1994; Kandil *et al.*, 1995; Lee *et al.*, 2001). Recently, Baishya *et al.* (2014) carried out optimization of pressure vessel under thermo-elastic condition. They considered the combined effect of internal pressure and steady-state temperature gradient. Authors minimized the total cost and the maximum shear stress simultaneously using genetic algorithm.

There have been only a few papers analyzing the elasto-plastic stresses in thick-walled cylinders under thermal loading. The elastic-plastic deformation of a solid cylinder subjected to radially distributed heat source, lateral pressure and axial force was studied by Kammash *et al.* (1960). The study was based on the Tresca yield criterion and its associated flow rule considering a linear work hardening law. They provided the solution of thermal stresses in closed form in terms of the exponential integral and the incomplete gamma function and found to exhibit three stages of plastic deformation. In stage I, the plastic domain consists of two concentric and adjacent zones separated by an interface radius with different stress fields which expand outward from the centre of the cylinder. The outer region of the cylinder refers to the elastic domain. In stage II, the elastic domain vanishes, while the inner plastic zone continues to propagate. In stage III, a third plastic zone is formed at the outer radius which propagates inward to a certain interface boundary. Authors found that the boundaries of the inner plastic zone and outer plastic zone never meet but approach limit values as the temperature tends to infinity.

Orçan and Gamer (1991) determined the elasto-plastic stress, displacement and plastic strains occurring in a centrally heated cylinder for different ratios of hot core diameter and outer diameter of the cylinder considering plane strain condition. The temperature was assumed constant in the core of the cylinder and in its outer part, dropping to reference temperature at the surface. The authors assumed elastic-perfectly plastic material obeying Tresca yield criterion and its associated flow rule for the analysis. Their analysis also suggested that for small radii of the hot core, a plastic region consisting of two adjacent concentric zones exists at the center and expands towards the surface of the cylinder with increasing core temperature. However, depending on the core radius, two plastic regions in a similar fashion with two adjacent zones developed one after the other or simultaneously, in the core and at the surface. The two plastic regions merge in the fully plastic state. In a later paper, Orçan (1994) derived the expressions for elasto-plastic thermal stresses in a solid cylindrical rod with uniform internal heat generation under the similar assumption for generalized plane strain condition. For this case, yielding first initiates at the surface and outer plastic zones emerge simultaneously and propagate inwards. When the internal heat generation is increased beyond a critical value, simultaneous plastic deformation takes place at the centre and at the outer surface, resulting into two outer plastic zones and two inner plastic zones separated by an intermediate elastic zone. Orçan (1995) extended this problem to analyze the residual stress distribution in the rod when the internal heat generation rate is decreased gradually to zero.

Bland (1956) developed a thermo-mechanical model for hollow thick-walled cylinders under steady state thermal gradient, internal and external pressures. An elasto-plastic analysis of elastic-perfectly plastic hollow cylinder subjected to time dependant internal temperature field and pressure internal heating and pressure was carried out by Wong and Simionescu (1996). The analysis was based on yield criterion of Tresca and plane strain condition. However, Bland (1956) and Wong and Simionescu (1996) suggested that cylinder wall undergoes plastic deformation only at the inner radius and propagates outwards under the temperature field and internal pressure. There is no plastic deformation at the outer wall of the cylinder. Orçan and Gulgec (2000) carried out thermo-elasto-plastic stress analysis in an internal heat generating hollow cylinder with free ends, where they have considered similar nature of plastic deformation as reported in an earlier paper of Orçan (1994). Further yielding of the cylinder wall with increased thermal load was considered to analyze the fully plastic state. For the analysis, authors assumed temperature dependent yield stress of the material. Later, Orçan and Eraslan (2001) reported that for internal heat generating cylinders with fixed ends and an insulated inner surface, beyond a critical thermal load the cylinder is composed of an outer elastic region and an inner plastic region that propagates outwards. Sadeghian and Toussi (2012, 2014) carried out an axisymmetric thermal elasto-plastic stress analysis in cylindrical vessels made of functionally graded material.

Some literatures exist analyzing the thermo-elasto-plastic stresses in spherical shells. Spherical shells are also subjected to a second zone of yielding initiated at the outer surface and spreads radially inwards under thermal gradient as observed by some researchers in the case of cylinders (Orçan, 1994; Orçan and Gulgec, 2000). Cowper (1960) obtained an exact solution for the behavior of an ideal elasto-plastic hollow sphere which is thermally stressed by a slowly increasing temperature difference between the inner and outer surfaces. Some other contributions are made by Johnson and Mellor (1962), Durban (1981, 1983), Kargarnovin *et al.* (2005) and Darijani *et al.* (2009) to study the thermo-elasto-plastic behaviour of spherical shells.

2.9 Study of Thermal Autofrettage

The idea of achieving autofrettage by thermal loading has been conceptualized in the early 21st century. Barbero and Wen (2002) outlined an idea of thermal autofrettage for strengthening the composite metal-lined cryogenic pressure vessels. They proposed to cool the cylinder with metal liner to a temperature lower than the operating temperature so that the thermally induced plastic deformation sets the liner in compression. Authors suggested liquid nitrogen, liquid helium or a mixture of the two as the cooling medium for achieving thermal autofrettage. However, they did not carry out any analysis of the process either theoretically or experimentally.

Kargarnovin *et al.* (2005) carried out the elasto-plastic stress analysis in thick-walled spheres due to combined pressure and thermal gradient, thermal loading and unloading using the concept of thermal autofrettage as a strengthening mechanism. They did not provide any experimental appraisal of the thermal autofrettage process for spheres. A study of thermal autofrettage of Titanium-Copper brazed joints by cooling the joint after brazing was carried out recently by Hamilton *et al.* (2015). The cooling of the joint induces plastic work in the joint due to the differential thermal contraction of the material. Authors carried out finite element modelling of the process. An experimental determination of the residual stresses generated in the brazed joint after thermal autofrettage was also carried out using X-ray diffraction (XRD) technique. They found that the thermal autofrettage of dissimilar material brazed joint potentially reduce the damaging tensile residual stresses present after the joining process.

2.10 Research Gap and Detailed Objectives of the Present Thesis

The extensive literature review on the existing autofrettage processes reveals that a lot of works have been carried out by the researchers on the hydraulic autofrettage process. The swage autofrettage process is less investigated compared to hydraulic autofrettage process by the researchers. Nevertheless, the process has got adequate attention of the researchers to investigate the process numerically and experimentally. Explosive autofrettage is not well recognized in the research community due its dynamic elasto-plastic behaviour. Only, a few researchers attempted the study of the explosive autofrettage process. Although, the hydraulic and swage autofrettage process is widely practiced in industries, the processes have certain disadvantages associated with the cost and safety of the processes. There are processing complexities in carrying out these processes. The explosive autofrettage also involves complexity in detonating explosives and needs extra care. Moreover, all these processes are not greener manufacturing practices due to involvement of hydraulic oil or explosive. On the other hand, the thermal autofrettage process is a promising way of achieving autofrettage without any involvement of oil or explosive. The potentiality of the process is not well explored by the researchers. Few researchers have attempted to study the process for spherical shell (Kargarnovin *et al*., 2005) or brazed joints (Hamilton *et al*., 2015). The study of Kargarnovin *et al*. (2005) was based on only theoretical analysis. They did not provide any experimental evidence of the thermal autofrettage in spherical shells. Barbero and Wen (2002) only gave an idea for achieving autofrettage in composite metal-lined cryogenic cylinders by cooling to cryogenic temperatures without any theoretical or experimental analysis. Other than this, there is no literature available on the study of thermal autofrettage for thick-walled cylinders. This provides enormous scope to study the thermal autofrettage for thick-walled cylinders analyzing its behaviour both theoretically and experimentally.

It is very well-recognized in the research community that thermal gradient in a body generates residual stresses. The basis of any autofrettage process for a thick-walled cylinder is the generation of beneficial residual stresses at and around the inner wall of the cylinder. All the well-established autofrettage methods are based on the generation of residual stresses in the cylinder by applying hydraulic pressure, explosive or mechanical swaging. However, the feasibility of the autofrettage process by creating thermal gradient in a thick-walled cylinder has not been studied. In the present work, a method of achieving thermal autofrettage in thick-walled cylinders is proposed by creating radial thermal gradient across the wall thickness of the cylinder. At sufficiently high thermal gradient, the wall of the cylinder is subjected to non-homogeneous plastic deformation. Afterwards, when the thermal gradient is released, *i.e*., when the cylinder is cooled to room temperature, beneficial compressive residual stresses are generated at and around the inner wall of the cylinder. The feasibility of the process is studied in detail by carrying out both theoretical and experimental analysis for its industrial adaptation. The detailed objectives of the present thesis are as follows:

1. **Analytical modelling of thermal autofrettage process:** In order to study the behaviour of the proposed thermal autofrettage process, the analytical modelling of the process will be carried out. The analysis considers steady-state temperature distribution under a radial thermal gradient. Two analytical models have been developed considering the plane stress and generalized plane strain condition. The plane stress model assumes the absence of axial stress and the generalized plane strain model assumes a constant axial strain. Both the models are based on the Tresca yield criterion and its associated flow rule. The effect of strain hardening is incorporated in the analysis considering Ludwik’s hardening law.
2. **Three-dimensional finite element modelling of thermal autofrettage process:** It is recognized that plane stress model is suitable for the autofrettage analysis of very short cylinders (thin hollow disks) such as fastener holes. The generalized plane strain model is applicable in general for long thick-walled cylindrical vessels used in industries. However, there is no quantification of the length of the cylinders upto which these models are valid. Therefore, in order to define a criterion for the analytical models on the basis of length to wall thickness ratio of the cylinders, a three-dimensional finite element modelling of the process will be carried out using commercially available finite element package ABAQUS.
3. **Experimental study of thermal autofrettage process:** A detailed experimental study of the thermal autofrettage process for thick-walled cylinders will be carried out in the present thesis. An experimental setup has been developed to create desired temperature

difference across the wall thickness of the cylinder for achieving thermal autofrettage. Several experiments have been conducted for different materials in order to see the industrial feasibility of the process. After achieving thermal autofrettage in the experimental setup, the residual stresses generated in the thermal autofrettage of thick-walled cylinders were measured using Sachs boring technique. In addition, two other methods, *viz*., microhardness test and measurement of opening angle due to a single radial cut across the wall thickness of the cylinder have been carried out for the qualitative analysis of the residual stresses induced in the cylinder. All these experimental methods are well established. However, this will be the first rigorous experimental study on thermal autofrettage process.

4. **Comparison of thermal autofrettage with hydraulic autofrettage:** The conventional hydraulic autofrettage process is the most widely used autofrettage process. The process has certain disadvantages. On the other hand the proposed thermal autofrettage process has some edge over this existing method. It could be a competent process in industries for increasing the pressure carrying capacity as well as to enhance the fatigue life of cylindrical vessels. Therefore, in order to assess the acceptability of the thermal autofrettage process, a detailed comparison of the process with the hydraulic autofrettage process will be presented considering different aspects.
5. **Enhancing the performance of thermally autofrettaged cylinder through shrink-fit:** The maximum achievable pressure carrying capacity in thermally autofrettaged cylinders is dependent on the temperature difference induced across the wall thickness. The maximum temperature difference across the wall thickness is limited by the maximum temperature upto which the material of the cylinder can be subjected to without any significant change in material properties. In order achieve more increase in the pressure carrying capacity than that achieved by only thermal autofrettage; a

methodology will be presented combining the thermal autofrettage of thick-walled cylinders with shrink-fit. The fatigue life of the combined thermal autofrettage and shrink-fitted compound cylinder will also be investigated.

The research plan is presented in the form of flow chart in Figure 2.1.

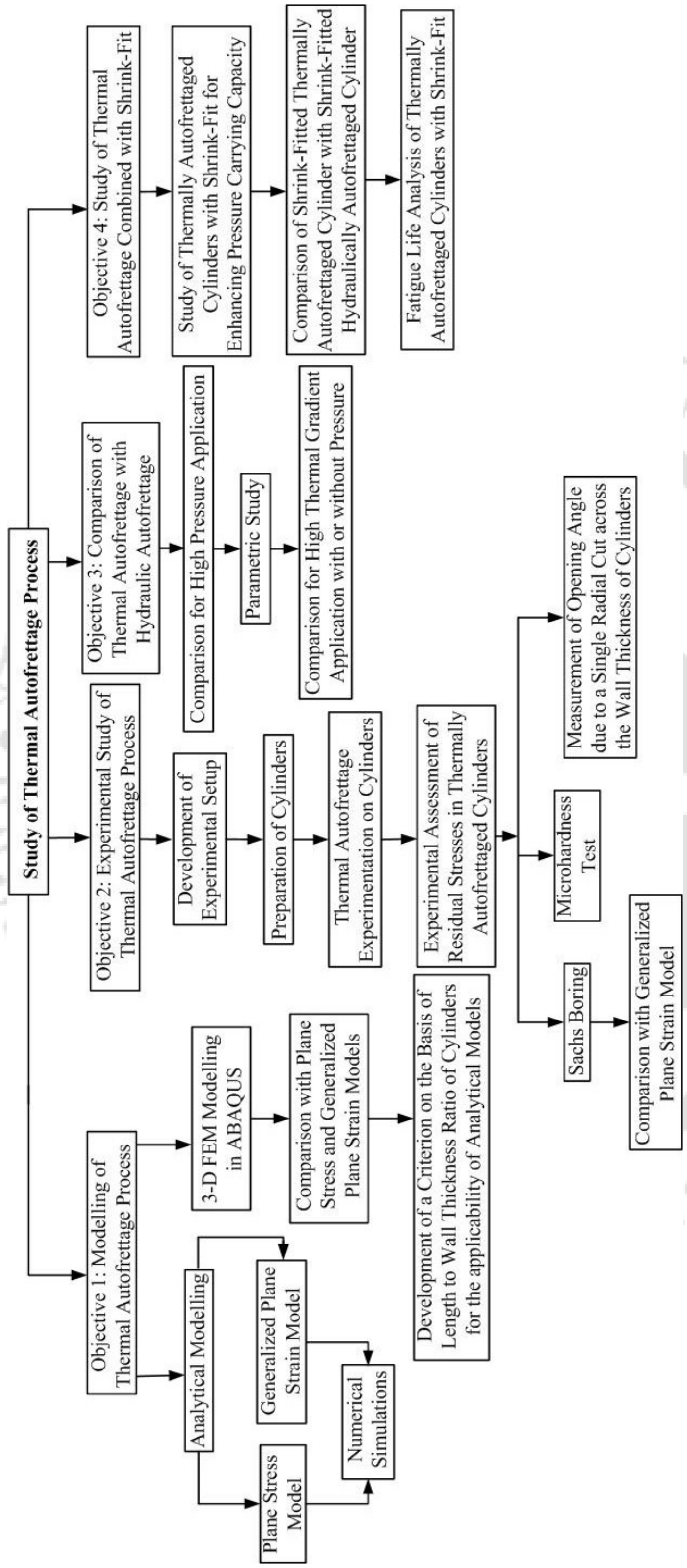

Figure 2.1 Research plan in the form of flow Chart

Chapter 3

The Plane Stress Model of Thermal Autofrettage

3.1 Introduction

Autofrettage is a metal fabrication technique which applies to components subjected to very high pressure. The most common ways of achieving autofrettage are by applying ultra-high hydraulic internal pressure known as the hydraulic autofrettage and by pushing an oversized mandrel through the bore of the cylinder known as swage autofrettage. Many researchers widely investigated the hydraulic as well as the swage autofrettage process (Gao 1992; Avitzur, 1994; Jahed and Dubey, 1997; Parker, 2001; Hameed *et al*., 2003; Parker *et al.* 2012; Perl and Perry 2006; Davidson *et al*., 1962; Chen, 1988; Iremonger and Kalsi, 2003). A few researchers suggested a method for achieving autofrettage by detonating an explosive charge inside the cylinder, called explosive autofrettage (Mote *et al*., 1971; Ezra *et al*., 1973). The autofrettage process produces the compressive residual stresses at and around the inner side of the cylinder, enabling the cylinder to withstand higher working pressure. The autofrettage induced compressive residual stresses at and around the inner wall of the cylinder also enhances its fatigue life. The existing methods of autofrettage have certain difficulties. The hydraulic autofrettage requires costly hydraulic power pack to generate ultra-high pressure for achieving autofrettage. The swage autofrettage also requires costly equipment and involves a lot of friction during autofrettage. Due to the involvement of high hydraulic pressure/explosive, the hydraulic and explosive autofrettage becomes dangerous at times.

The basis of autofrettage process is generating residual stresses in the thick-walled cylinder due to non-homogeneous plastic deformation. This effect can also be achieved by thermal loading, termed as thermal autofrettage. The thermal autofrettage process is a promising process offering many advantages over the conventional hydraulic and swage autofrettage processes. However, there have been limited number of studies on thermal autofrettage (Barbero and Wen, 2002; Kargarnovin *et al*., 2005 and Hamilton *et al*., 2015). None of the existing literature studies the thermal autofrettage of thick-walled cylinders or disks either theoretically or experimentally. Only, Barbero and Wen (2002) suggested thermal autofrettage for the composite metal-lined cryogenic pressure vessels by cooling the vessel with metal liner below its operating temperature, which did not provide any theoretical modelling or experimental appraisal of the process. The residual stresses can be generated by creating a radial thermal gradient in cylindrical bodies. The present work proposes a thermal autofrettage process based on the generation of compressive residual stresses by inducing a radial thermal gradient between the outer and inner wall of a thick-walled cylinder or hollow disk. The process has been described in Section 1.6. In this process, the outer wall of the cylinder/disk is heated and the inner wall is cooled simultaneously. The thermal gradient across the wall thickness generates thermal stresses. Sufficiently high thermal stresses can cause plastic deformation in some portion of the wall of the cylinder or disk. After unloading, *i.e*., after the removal of the thermal gradient, the residual stresses are set in. The proposed method is very simple and easy to handle compared to the existing methods of autofrettage. It requires no pressure and is expected to be inexpensive due to elimination of costly hydraulic power pack and/or explosives.

In order to understand the mechanics of thermal autofrettage, an analytical model assuming the plane stress condition is developed in this chapter. The plane stress condition will provide reasonable solution for thick-walled hollow circular disks such as fastener holes. The analysis is based on the Tresca yield criterion and its associated flow rule. The solutions for stress, strain and displacement components are derived in closed form during the elasto-plastic deformation under a steady state radial thermal gradient. The effect of strain hardening is incorporated during plastic deformation using Ludwik's hardening law. A conceptual design for creating desired thermal gradient across the wall of a hollow disk is also presented. Numerical simulations are carried out for typical hollow disks to see the feasibility of the thermal autofrettage process for its industrial exploitation.

3.2 Thermal Stress Analysis in the Disk

Consider an open ended thin hollow circular disk (σ_z=0) of homogeneous material with inner radius a and outer radius b as shown in Figure 3.1. The disk is subjected to Dirichlet temperature boundary conditions. The outer wall of the disk is maintained at temperature T_b and the inner wall is maintained at temperature T_a such that $T_b>T_a$. The steady-state temperature distribution in the disk is given by (Chakrabarty, 2006)

$$T = T_b + \left(T_a - T_b\right)\frac{\ln\left(\frac{b}{r}\right)}{\ln\left(\frac{b}{a}\right)}. \tag{3.1}$$

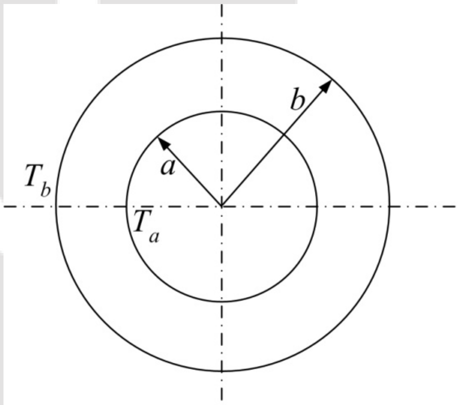

Figure 3.1 Cross-section of the disk with Dirichlet temperature boundary conditions

For a low temperature gradient (T_b–T_a), which is not sufficient to cause the yielding of the wall of the disk, the entire wall thickness (b–a) is in the elastic state. When (T_b–T_a) is increased further, at a certain threshold temperature gradient, the inner wall of the disk yields first and upon crossing this temperature gradient the wall deforms plastically to some intermediate radial position. When the temperature gradient (T_b–T_a) reaches a second threshold, the outer wall begins to yield simultaneously with the inner wall. Upon crossing the second threshold, the disk-wall gets divided into an inner plastic, intermediate elastic and outer plastic zone. In this work, it is assumed that the material yields as per Tresca criterion. The yielding behaviour of the most metals is close to von Mises criterion. However, it is not uncommon to correct the residual stresses obtained using Tresca criterion by multiplying them by a factor of 1.15 corresponding to von Mises case (Parker, 2001a). In the following sections solution for thermal stresses for elastic and different stages of elasto-plastic deformation are discussed.

3.2.1 Solution for Thermo-elastic Stresses

With zero temperature as a reference and using generalized Hook's law, the radial and hoop strains under plane stress condition for a purely elastic body at temperature T are given as (Noda *et al.*, 2003)

$$\varepsilon_r = \frac{1}{E}\left(\sigma_r - \nu\sigma_\theta\right) + \alpha T, \tag{3.2}$$

$$\varepsilon_\theta = \frac{1}{E}\left(\sigma_\theta - \nu\sigma_r\right) + \alpha T, \tag{3.3}$$

where σ_r is the radial stress, σ_θ is the hoop stress, ν is the Poisson's ratio, E is the Young's modulus of elasticity and α is the coefficient of thermal expansion. For radial displacement u as a function of r, the radial and hoop strains are given by (Chakrabarty, 2006)

$$\varepsilon_r = \frac{\mathrm{d}u}{\mathrm{d}r}, \quad \varepsilon_\theta = \frac{u}{r}. \tag{3.4}$$

Hence, the strain compatibility in cylindrical polar co-ordinate system can be written as (Chakrabarty, 2006)

$$\varepsilon_r - \varepsilon_\theta = r\frac{\mathrm{d}\varepsilon_\theta}{\mathrm{d}r}. \tag{3.5}$$

The stresses are governed by the equilibrium equation given by (Chakrabarty, 2006)

$$\sigma_\theta - \sigma_r = r\frac{\mathrm{d}\sigma_r}{\mathrm{d}r}. \tag{3.6}$$

Using Eqs. (3.2, 3.3) in Eq. (3.5) and solving it along with Eq. (3.6), provides the following differential equation:

$$\frac{\mathrm{d}}{\mathrm{d}r}\left\{\frac{1}{r}\frac{\mathrm{d}}{\mathrm{d}r}\left(r^2\sigma_r\right)\right\} + E\alpha\frac{\mathrm{d}T}{\mathrm{d}r} = 0, \tag{3.7}$$

where T is given by Eq. (3.1). The solution of Eq. (3.7) provides

$$\sigma_r = A - \frac{B}{r^2} + \frac{E\alpha\left(T_b - T_a\right)}{2\ln\left(\dfrac{b}{a}\right)}\left\{\frac{1}{2} - \ln\left(\frac{r}{a}\right)\right\}, \tag{3.8}$$

where *A* and *B* are constants. Using Eq. (3.8) in Eq. (3.6) the solution for hoop stress is given by

$$\sigma_\theta = A + \frac{B}{r^2} - \frac{E\alpha\left(T_b - T_a\right)}{2\ln\left(\dfrac{b}{a}\right)}\left\{\frac{1}{2} + \ln\left(\frac{r}{a}\right)\right\}. \tag{3.9}$$

Using the boundary condition of vanishing radial stress at inner and outer radii *i.e.* at *r*=*a* and *r*=*b*, $\sigma_r = 0$ in Eq. (3.8) yields

$$A = -\frac{1}{2}\frac{E\alpha\left(T_b - T_a\right)}{2\ln\left(\dfrac{b}{a}\right)} - \left(\frac{b^2}{a^2 - b^2}\right)\frac{E\alpha\left(T_b - T_a\right)}{2}, \tag{3.10}$$

$$B = -\left(\frac{a^2 b^2}{a^2 - b^2}\right)\frac{E\alpha\left(T_b - T_a\right)}{2}. \tag{3.11}$$

Inserting Eqs. (3.10) and (3.11) in Eqs. (3.8) and (3.9), the elastic radial and hoop stresses are obtained as (Noda *et al.*, 2003)

$$\sigma_r = \frac{E\alpha}{2}\left(T_b - T_a\right)\left\{-\frac{\ln\left(\dfrac{r}{a}\right)}{\ln\left(\dfrac{b}{a}\right)} + \left(1 - \frac{a^2}{r^2}\right)\frac{b^2}{b^2 - a^2}\right\}, \tag{3.12}$$

$$\sigma_\theta = \frac{E\alpha}{2}\left(T_b - T_a\right)\left\{-\frac{1 + \ln\left(\dfrac{r}{a}\right)}{\ln\left(\dfrac{b}{a}\right)} + \left(1 + \frac{a^2}{r^2}\right)\frac{b^2}{b^2 - a^2}\right\}. \tag{3.13}$$

3.2.2 The Thermo-elasto-plastic Behaviour of the Hollow Disk

A typical distribution of elastic stresses as a function of radial position given by Eqs. (3.12) and (3.13) is shown in Figure 3.2 for an aluminum disk with a=10 mm, b=20 mm, E=69 GPa, (T_b-T_a)=40°C and α=22.2×10^{-6}/°C. Figure 3.2 suggests that the thermal stresses are distributed according to the inequality $\sigma_\theta>\sigma_r>\sigma_z$ at and around inner radius of the disk. At and around the outer radius the stresses are distributed such that $\sigma_r>\sigma_z>\sigma_\theta$. The difference $|\sigma_\theta-\sigma_z|$ at inner radius is always greater than the difference $|\sigma_r-\sigma_\theta|$ at outer radius. Hence, for increasing thermal gradient the yielding of the disk begins first at the inner radius of the disk as per Tresca yield criterion. For initiation of yielding at the inner radius, $r=a$, Tresca yield criterion provides

$$\left(\sigma_\theta-\sigma_z\right)\Big|_{r=a}=k_1\sigma_Y, \tag{3.14}$$

where σ_Y is the yield stress and k_1 is a sign factor that can be +1 or −1 depending on whether $T_b>T_a$ or $T_b<T_a$. As σ_z=0, evaluating σ_θ at $r=a$ from Eq. (3.13) and substituting it into Eq. (3.14), the temperature difference required for initial yielding at inner radius is given by

$$\left(T_b-T_a\right)_{Y_i}=\frac{2k_1\sigma_Y}{E\alpha\left\{\dfrac{\ln\left(\dfrac{b}{a}\right)-1}{\ln\left(\dfrac{b}{a}\right)}+\left(\dfrac{a^2}{b^2-a^2}\right)\left(\dfrac{b^2}{a^2}+1\right)\right\}}. \tag{3.15}$$

Eq. (3.15) shows that for materials having large E and α and low yield stress, a small temperature difference can cause yielding at the inner radius.

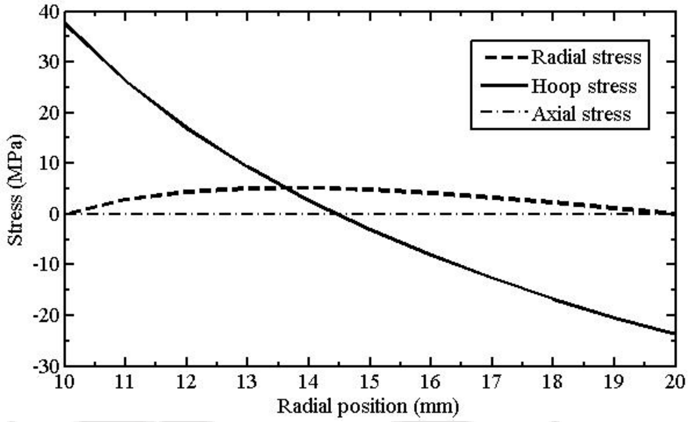

Figure 3.2 A typical thermo-elastic stress distributions in aluminum disk

If the temperature difference (T_b–T_a) exceeds the temperature difference required for initial yielding at the inner radius given by Eq. (3.15), but is lesser than the temperature difference required for yielding the outer wall, the first stage of elasto-plastic deformation takes place. During first stage of elasto-plastic deformation, a portion of the inner wall of the disk becomes plastic up to a radius c and beyond c the outer wall remains in the elastic state. Thus, an inner plastic zone $a \leq r \leq c$ and an outer elastic zone $c \leq r \leq b$ are formed within the disk. When the temperature difference keeps on increasing further, at some temperature difference, the yielding commences at the outer radius of the disk. Upon exceeding this temperature difference, the wall of the disk undergoes second stage of elasto-plastic deformation forming an inner plastic zone $a \leq r \leq c$ and an outer plastic zone $d \leq r \leq b$ separated by an intermediate elastic zone $c \leq r \leq d$. The second stage of elasto-plastic deformation remains in the wall of the disk as long as the temperature difference is not large enough to cause the plastic deformation of the whole wall. The different zones developed within the wall of the disk as a result of elasto-plastic deformation in general are shown schematically in Figure 3.3. In the following subsections, the analysis of different zones during first and second stage of elasto-plastic deformation is carried out.

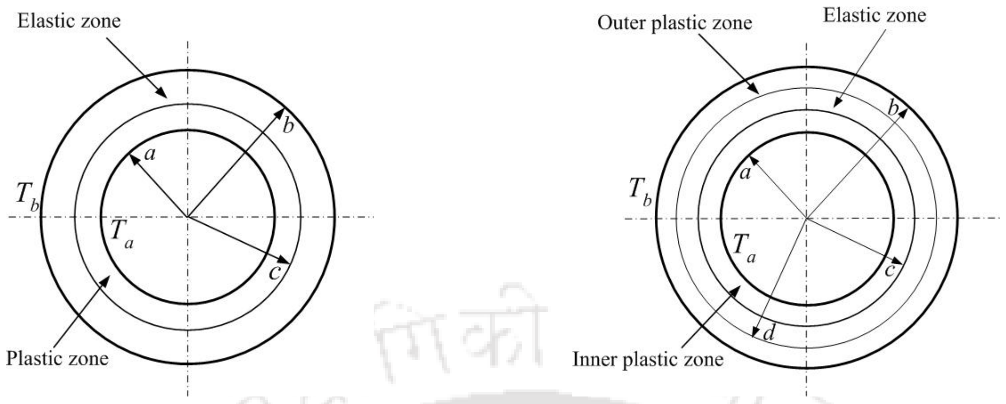

(a) (b)

Figure 3.3 The elastic and plastic zones in the disk during (a) first stage and (b) second stage of elasto-plastic deformation

3.2.3 Analysis of the First Stage of Elasto-plastic Deformation

During first stage of elasto-plastic deformation, an inner plastic zone propagates outwards to a radius *c*. Thus the inner plastic zone $a \le r \le c$ is surrounded by an outer elastic zone $c \le r \le b$ within the wall of the disk. The radius *c* is known as the radius of elastic-plastic interface. The inner plastic and outer elastic zones are analyzed as follows:

3.2.3.1 Elastic zone: $c \le r \le b$

For the outer elastic zone $c \le r \le b$ the solution for thermal stresses are still given by Eqs. (3.8) and (3.9). Using boundary condition of vanishing radial stress at the outer radius and $(\sigma_\theta)_{r=c} = k_1\sigma_Y$ in Eqs. (3.8) and (3.9) the constants *A* and *B* are evaluated and the expressions for radial and hoop stresses are given by

$$\sigma_r = \frac{E\alpha(T_b - T_a)}{2\ln\left(\frac{b}{a}\right)}\left[\ln\left(\frac{b}{r}\right) + \left(\frac{c^2}{b^2+c^2}\right)\left(1-\frac{b^2}{r^2}\right)\left\{1-\ln\left(\frac{b}{c}\right)\right\}\right] + \frac{c^2k_1\sigma_Y}{b^2+c^2}\left(1-\frac{b^2}{r^2}\right), \qquad (3.16)$$

$$\sigma_\theta = \frac{E\alpha(T_b - T_a)}{2\ln\left(\frac{b}{a}\right)}\left[\ln\left(\frac{b}{r}\right) - 1 + \left(\frac{c^2}{b^2+c^2}\right)\left(1+\frac{b^2}{r^2}\right)\left\{1-\ln\left(\frac{b}{c}\right)\right\}\right] + \frac{c^2k_1\sigma_Y}{b^2+c^2}\left(1+\frac{b^2}{r^2}\right). \qquad (3.17)$$

The radial displacement component, *u* in the outer elastic zone is obtained using Eqs. (3.16) and (3.17) in Eq. (3.3) and second relation of Eq. (3.4) as

$$u=\frac{\alpha(T_b-T_a)}{2\ln\left(\frac{b}{a}\right)}\left[\begin{array}{l}(1-\nu)r\ln\left(\frac{b}{r}\right)-r+(1-\nu)r\left(\frac{c^2}{b^2+c^2}\right)\left\{1-\ln\left(\frac{b}{c}\right)\right\}\\+\left(\frac{c^2}{b^2+c^2}\right)\left\{1-\ln\left(\frac{b}{c}\right)\right\}\left\{(1-\nu)r+(1+\nu)\frac{b^2}{r}\right\}\end{array}\right] \tag{3.18}$$

$$+\frac{c^2k_1\sigma_Y}{E\left(b^2+c^2\right)}\left\{(1-\nu)r+(1+\nu)\frac{b^2}{r}\right\}+r\alpha T.$$

3.2.3.2 Plastic zone: *a≤r≤c*

For the plastic zone (*a≤r≤c*), the effect of strain hardening of the material is taken into account. When the material strain hardens, Tresca yield criterion in the inner plastic zone becomes

$$\sigma_\theta=k_1\sigma_{eq}, \tag{3.19}$$

where σ_{eq} ($>\sigma_Y$) is the equivalent stress in uniaxial tension or compression. It is assumed that the hardening of the disk material follows the Ludwik's hardening law (Dixit and Dixit, 2008) given by

$$\sigma_{eq}=\sigma_Y+K\left(\varepsilon_{eq}^p\right)^n, \tag{3.20}$$

where *K* is the hardening coefficient and *n* is the strain hardening exponent. Using Eq. (3.19) in Eq. (3.6)

$$\frac{\mathrm{d}}{\mathrm{d}r}\left(r\sigma_r\right)=k_1\left\{\sigma_Y+K\left(\varepsilon_{eq}^p\right)^n\right\}. \tag{3.21}$$

Integrating Eq. (3.21) in the plastic zone from *r* to *r=c* and using the boundary condition, σ_r at *r=c* from elastic zone (Eq. 3.16), the solution for radial thermal stress in the plastic zone is obtained as

$$\sigma_r=k_1\sigma_Y\left\{1-\left(\frac{2b^2}{b^2+c^2}\right)\left(\frac{c}{r}\right)\right\}+\left(\frac{c}{r}\right)\frac{E\alpha(T_b-T_a)}{2\ln\left(\frac{b}{a}\right)}\left[\ln\left(\frac{b}{c}\right)+\left(\frac{c^2}{b^2+c^2}\right)\left(1-\frac{b^2}{c^2}\right)\left\{1-\ln\left(\frac{b}{c}\right)\right\}\right] \tag{3.22}$$

$$-k_1\frac{K}{r}\int_r^c\left(\varepsilon_{eq}^p\right)^n\mathrm{d}r_1\ ,$$

where r_1 is a dummy variable. The thermal hoop stress in the plastic zone is given by Eq. (3.19).

In the plastic zone, the total strain is composed of elastic and plastic strains. Hence,

$$\varepsilon_r = \frac{\mathrm{d}u}{\mathrm{d}r} = \varepsilon_r^e + \varepsilon_r^p, \quad \varepsilon_\theta = \frac{u}{r} = \varepsilon_\theta^e + \varepsilon_\theta^p. \tag{3.23}$$

The elastic components ε_θ^e and ε_r^e are given by Eqs. (3.2) and (3.3). In view of Tresca's associated flow rule (Chakrabarty, 2006), $\mathrm{d}\varepsilon_r^p = 0$, $\mathrm{d}\varepsilon_\theta^p = -\mathrm{d}\varepsilon_z^p$. Hence, ε_r is entirely elastic. Substituting Eq. (3.23) in Eqs. (3.2) and (3.3):

$$\sigma_r = \frac{E}{1-\nu^2}\left\{\frac{\mathrm{d}u}{\mathrm{d}r} + \nu\left(\frac{u}{r} - \varepsilon_\theta^p\right) - \alpha T(1+\nu)\right\}, \tag{3.24}$$

$$\sigma_\theta = \frac{E}{1-\nu^2}\left\{\left(\frac{u}{r} - \varepsilon_\theta^p\right) + \nu\frac{\mathrm{d}u}{\mathrm{d}r} - \alpha T(1+\nu)\right\}. \tag{3.25}$$

Inserting Eqs. (3.24) and (3.25) in Eq. (3.6), the following differential equation is obtained:

$$\frac{\mathrm{d}}{\mathrm{d}r}\left\{\frac{1}{r}\frac{\mathrm{d}}{\mathrm{d}r}(ur)\right\} = \nu\frac{\mathrm{d}\varepsilon_\theta^p}{\mathrm{d}r} + \alpha(1+\nu)\frac{\mathrm{d}T}{\mathrm{d}r} - \left(\frac{1-\nu}{r}\right)\varepsilon_\theta^p. \tag{3.26}$$

For the plastic zone, the total strain compatibility condition (Eq. 3.5) may be written as

$$r\frac{\mathrm{d}}{\mathrm{d}r}\left(\varepsilon_\theta^e + \varepsilon_\theta^p\right) = \left(\varepsilon_r^e - \varepsilon_\theta^e\right) - \varepsilon_\theta^p. \tag{3.27}$$

Putting ε_r^e and ε_θ^e from Eqs. (3.2) and (3.3) the following differential equation is obtained:

$$\frac{1}{E}\frac{\mathrm{d}\sigma_\theta}{\mathrm{d}r} + \frac{1}{E}\frac{\mathrm{d}\sigma_r}{\mathrm{d}r} + \alpha\frac{\mathrm{d}T}{\mathrm{d}r} + \frac{\mathrm{d}\varepsilon_\theta^p}{\mathrm{d}r} = -\frac{\varepsilon_\theta^p}{r}. \tag{3.28}$$

Substituting ε_θ^p / r from Eq. (3.28) in Eq. (3.26) and then integrating:

$$\frac{1}{r}\frac{\mathrm{d}}{\mathrm{d}r}(ur)=\frac{1-\nu}{E}(\sigma_\theta+\sigma_r)+2\alpha\left\{T_a+(T_b-T_a)\frac{\ln\left(\frac{r}{a}\right)}{\ln\left(\frac{b}{a}\right)}\right\}+\varepsilon_\theta^p+C, \tag{3.29}$$

where C is integration constant. To determine the constant C in Eq. (3.29), the right and left hand side expressions are evaluated at $r=c$ by taking the corresponding values from the elastic zone. Equations (3.16) and (3.17) provide σ_r and σ_θ at $r=c$ and Eq. (3.18) provides

$$\begin{aligned}\left.\frac{\mathrm{d}}{\mathrm{d}r}(ur)\right|_{r=c}&=\frac{\alpha(T_b-T_a)}{2\ln\left(\frac{b}{a}\right)}\left[\begin{aligned}&2(1-\nu)c\ln\left(\frac{b}{c}\right)-c(1-\nu)\\&+2(1-\nu)\left(\frac{c^3}{b^2+c^2}\right)\left\{1-\ln\left(\frac{b}{c}\right)\right\}+4c\ln\left(\frac{c}{a}\right)\end{aligned}\right]\\&+\frac{2(1-\nu)}{E}\left(\frac{c^3k_1\sigma_Y}{b^2+c^2}\right)+2cT_a\alpha.\end{aligned} \tag{3.30}$$

Also,

$$\left.\varepsilon_\theta^p\right|_{r=c}=0. \tag{3.31}$$

Insertion of all expressions in Eq. (3.29) provides C=0. Substituting C in Eq. (3.29) and integrating it in the plastic domain from r to $r=c$ gives

$$\begin{aligned}\left.u\right|_{r=c}c-ur&=\left(\frac{1-\nu}{E}\right)\left(c^2\left.\sigma_r\right|_{r=c}-r^2\sigma_r\right)+\alpha T_a\left(c^2-r^2\right)\\&+\frac{\alpha(T_b-T_a)}{\ln\left(\frac{b}{a}\right)}\left[\left\{c^2\ln\left(\frac{c}{a}\right)-r^2\ln\left(\frac{r}{a}\right)\right\}-\frac{1}{2}\left(c^2-r^2\right)\right]+\int_r^c r_1\varepsilon_\theta^p dr_1\end{aligned} \tag{3.32}$$

Evaluating $\left.u\right|_{r=c}$ from Eq. (18) and $\left.\sigma_r\right|_{r=c}$ from Eq. (3.16) and then inserting these into Eq. (3.32) provides total hoop strain component as

$$\frac{u}{r}=\frac{\alpha(T_b-T_a)}{2\ln\left(\frac{b}{a}\right)}\left[\left\{\frac{2c^2b^2}{r^2\left(b^2+c^2\right)}\right\}\left\{1-\ln\left(\frac{b}{c}\right)\right\}+2\ln\left(\frac{r}{a}\right)-1\right]$$
$$+\frac{2}{E}\frac{k_1c^2b^2\sigma_Y}{r^2\left(b^2+c^2\right)}+\frac{1-\nu}{E}\sigma_r+\alpha T_a-\frac{1}{r^2}\int_r^c r_1\varepsilon_\theta^p\mathrm{d}r_1. \tag{3.33}$$

The plastic hoop strain field ε_θ^p is given by

$$\varepsilon_\theta^p=\frac{u}{r}-\varepsilon_\theta^e. \tag{3.34}$$

Inserting *u/r*, from Eq. (3.33), ε_θ^e from Eq. (3.3) and using Eqs. (3.19) and (3.22), the plastic hoop strain component is obtained as

$$\varepsilon_\theta^p=\frac{\alpha(T_b-T_a)}{2\ln\left(\frac{b}{a}\right)}\left[\begin{array}{l}\left\{\frac{2c^2b^2}{r^2\left(b^2+c^2\right)}\right\}\left\{1-\ln\left(\frac{b}{c}\right)\right\}-1+\frac{c}{r}\ln\left(\frac{b}{c}\right)\\+\left\{\frac{c^3}{r\left(b^2+c^2\right)}\right\}\left(1-\frac{b^2}{c^2}\right)\left\{1-\ln\left(\frac{b}{c}\right)\right\}\end{array}\right]+\frac{2}{E}\frac{k_1c^2b^2\sigma_Y}{r^2\left(b^2+c^2\right)}$$
$$+\frac{k_1c^3\sigma_Y}{Er\left(b^2+c^2\right)}\left(1-\frac{b^2}{c^2}\right)-\frac{k_1\sigma_Y}{E}\left(\frac{c}{r}\right)-k_1\frac{K}{Er}\int_r^c\left(\varepsilon_{eq}^p\right)^n\mathrm{d}r_1-\frac{1}{r^2}\int_r^c r_1\varepsilon_\theta^p\mathrm{d}r_1-k_1\frac{K}{E}\left(\varepsilon_{eq}^p\right)^n. \tag{3.35}$$

The equivalent plastic strain field ε_{eq}^p for the present case is given as

$$\varepsilon_{eq}^p=\frac{2}{\sqrt{3}}\varepsilon_\theta^p. \tag{3.36}$$

Thus, Eq. (3.35) becomes

$$\varepsilon_\theta^p = \frac{\alpha(T_b - T_a)}{2\ln\left(\dfrac{b}{a}\right)}\left[\begin{array}{l}\left\{\dfrac{2c^2b^2}{r^2\left(b^2+c^2\right)}\right\}\left\{1-\ln\left(\dfrac{b}{c}\right)\right\}-1+\dfrac{c}{r}\ln\left(\dfrac{b}{c}\right)\\ +\left\{\dfrac{c^3}{r\left(b^2+c^2\right)}\right\}\left(1-\dfrac{b^2}{c^2}\right)\left\{1-\ln\left(\dfrac{b}{c}\right)\right\}\end{array}\right]+\frac{2}{E}\frac{k_1c^2b^2\sigma_Y}{r^2\left(b^2+c^2\right)}$$

$$+\frac{k_1c^3\sigma_Y}{Er\left(b^2+c^2\right)}\left(1-\frac{b^2}{c^2}\right)-\frac{k_1\sigma_Y}{E}\left(\frac{c}{r}\right)-k_1\left(\frac{2}{\sqrt{3}}\right)^n\frac{K}{Er}\int_r^c\left(\varepsilon_\theta^p\right)^n \mathrm{d}r_1-\frac{1}{r^2}\int_r^c r_1\varepsilon_\theta^p \mathrm{d}r_1 \qquad (3.37)$$

$$-k_1\left(\frac{2}{\sqrt{3}}\right)^n\frac{K}{E}\left(\varepsilon_\theta^p\right)^n.$$

Eq. (3.37) can be solved for ε_θ^p at any radial positions in the plastic domain. An iterative approach may be employed for this.

3.2.4 Analysis of the Second Stage of Elasto-plastic Deformation

During the second stage of elasto-plastic deformation, the wall of the disk consists of three zones: an inner plastic zone $a \le r \le c$, an outer plastic zone $d \le r \le b$ and an intermediate elastic zone $c \le r \le d$. The radii, c and d are the radii of elastic-plastic interface. The elasto-plastic zones during second stage of elasto-plastic deformation are analyzed as follows:

3.2.4.1 Intermediate elastic zone: $c \le r \le d$

Using the boundary conditions $(\sigma_\theta)_{r=c} = k_1\sigma_Y$ and $(\sigma_\theta - \sigma_r)_{r=d} = -k_1\sigma_Y$, in Eq. (3.9) the constants A and B are evaluated. Then substituting A and B in Eqs. (3.8) and (3.9), the stresses in the elastic zone $c \le r \le d$ are obtained as

$$\sigma_r = \frac{E\alpha\left(T_b - T_a\right)}{2\ln\left(\dfrac{b}{a}\right)}\left\{1+\ln\left(\frac{c}{r}\right)-\frac{d^2}{2c^2}-\frac{d^2}{2r^2}\right\}+k_1\sigma_Y\left(1+\frac{d^2}{2c^2}+\frac{d^2}{2r^2}\right), \qquad (3.38)$$

$$\sigma_\theta = \frac{E\alpha\left(T_b - T_a\right)}{2\ln\left(\dfrac{b}{a}\right)}\left\{\ln\left(\frac{c}{r}\right)-\frac{d^2}{2c^2}+\frac{d^2}{2r^2}\right\}+k_1\sigma_Y\left(1+\frac{d^2}{2c^2}-\frac{d^2}{2r^2}\right). \qquad (3.39)$$

The displacement component for this elastic zone is obtained using Eqs. (3.38) and (3.39) in Eq. (3.3) and second relation of Eq. (3.4) as

$$u=\frac{\alpha\left(T_b-T_a\right)}{2\ln\left(\dfrac{b}{a}\right)}\left\{(1+\nu)\frac{d^2}{2r}-(1-\nu)\frac{d^2r}{2c^2}+(1-\nu)r\ln\left(\frac{c}{r}\right)-\nu r\right\}$$

$$+\frac{k_1\sigma_Y}{E}\left\{\left(1-\nu\right)r+\left(1-\nu\right)\frac{d^2r}{2c^2}-\left(1+\nu\right)\frac{d^2}{2r}\right\}+\alpha r\left\{T_a+\left(T_b-T_a\right)\frac{\ln\left(\dfrac{r}{a}\right)}{\ln\left(\dfrac{b}{a}\right)}\right\}. \tag{3.40}$$

3.2.4.2 Inner plastic zone: *a≤r≤c*

To find out the solution for radial thermal stress in the inner plastic zone (*a≤r≤c*), the differential Eq. (3.21) is used. Integrating Eq. (3.21) and using the boundary condition, σ_r at *r=c* from elastic zone *c≤r≤d* (Eq. 3.38), the expression for radial thermal stress is obtained as

$$\sigma_r=\left(\frac{c}{r}\right)\frac{E\alpha\left(T_b-T_a\right)}{2\ln\left(\dfrac{b}{a}\right)}\left(1-\frac{d^2}{c^2}\right)+k_1\sigma_Y\left(1+\frac{d^2}{cr}\right)-k_1\frac{K}{r}\int_r^c\left(\varepsilon_{eq}^p\right)^n\mathrm{d}r_1. \tag{3.41}$$

The hoop stress component is given by Eq. (3.19).

For evaluating the total hoop strain component Eq. (3.29) is utilized. In Eq. (3.29), the constant *C* is obtained by evaluating the right and left hand side expressions at *r* = *c*. For this the values of σ_r and σ_θ at *r=c* is evaluated from Eqs. (3.38) and (3.39) and using Eq. (3.40),

$$\left\{\frac{1}{r}\frac{\mathrm{d}}{\mathrm{d}r}\left(ur\right)\right\}\Bigg|_{r=c}=\frac{\alpha\left(T_b-T_a\right)}{2\ln\left(\dfrac{b}{a}\right)}\left\{(1-\nu)-(1-\nu)\frac{d^2}{c^2}+4\ln\left(\frac{c}{a}\right)\right\}$$

$$+\frac{k_1\sigma_Y}{E}\left\{2\left(1-\nu\right)+\left(1-\nu\right)\frac{d^2}{c^2}\right\}+2\alpha T_a. \tag{3.42}$$

Substitution of all these expressions along with Eq. (3.31) in Eq. (3.29) provides *C* = 0. Inserting *C* in Eq. (3.29) and integrating it in the plastic domain from *r* to *r=c* provides Eq. (3.32). Evaluating $u\big|_{r=c}$ from Eq. (3.40) and $\sigma_r\big|_{r=c}$ from Eq. (3.38) and then substituting these in Eq. (3.32) gives

$$\varepsilon_\theta = \frac{u}{r} = \frac{\alpha\left(T_b - T_a\right)}{2\ln\left(\dfrac{b}{a}\right)}\left\{\frac{d^2}{r^2} - 1 + 2\ln\left(\frac{r}{a}\right)\right\} - \frac{k_1\sigma_Y}{E}\frac{d^2}{r^2} + \left(\frac{1-\nu}{E}\right)\sigma_r$$
$$+\alpha T_a - \frac{1}{r^2}\int_r^c r_1\varepsilon_\theta^p dr_1. \tag{3.43}$$

Inserting *u/r* from Eq. (3.43), ε_θ^e from Eq. (3.3) in Eq. (3.34) and using Eqs. (3.19), (3.41) and (3.36) the plastic part of hoop strain is obtained as

$$\varepsilon_\theta^p = \frac{\alpha\left(T_b - T_a\right)}{2\ln\left(\dfrac{b}{a}\right)}\left\{\frac{d^2}{r^2} - 1 + \left(\frac{c}{r}\right)\left(1 - \frac{d^2}{c^2}\right)\right\} + \frac{k_1\sigma_Y}{E}\left(\frac{d^2}{cr} - \frac{d^2}{r^2}\right)$$
$$-\frac{1}{r^2}\int_r^c r_1\varepsilon_\theta^p \mathrm{d}r_1 - k_1\left(\frac{2}{\sqrt{3}}\right)^n \frac{K}{rE}\int_r^c \left(\varepsilon_\theta^p\right)^n \mathrm{d}r_1 - k_1\left(\frac{2}{\sqrt{3}}\right)^n \frac{K}{E}\left(\varepsilon_\theta^p\right)^n. \tag{3.44}$$

3.2.4.3 Outer plastic zone: *d≤r≤b*

For the plastic zone (*d≤r≤b*), considering the effect of strain hardening of the material Tresca yield criterion is given by

$$\sigma_\theta - \sigma_r = -k_1\sigma_{eq} \tag{3.45}$$

where σ_{eq} is given by Eq. (3.20). Using Eq. (3.45) and Eq.(3.6),

$$\frac{\mathrm{d}\sigma_r}{\mathrm{d}r} = -k_1\left\{\frac{\sigma_Y}{r} + \frac{K}{r}\left(\varepsilon_{eq}^p\right)^n\right\}. \tag{3.46}$$

Integrating Eq. (3.46) in the plastic domain from *r=d* to *r* and using the boundary condition, σ_r at *r=d* from elastic zone *c≤r≤d* (Eq. 3.38), the solution for radial thermal stress is given by

$$\sigma_r = \frac{E\alpha\left(T_b - T_a\right)}{2\ln\left(\dfrac{b}{a}\right)}\left\{\frac{1}{2} + \ln\left(\frac{c}{d}\right) - \frac{d^2}{2c^2}\right\} + k_1\sigma_Y\left\{\frac{3}{2} + \frac{d^2}{2c^2} - \ln\left(\frac{r}{d}\right)\right\} + k_1 K\int_r^d \frac{1}{r_1}\left(\varepsilon_{eq}^p\right)^n \mathrm{d}r_1. \tag{3.47}$$

Inserting Eq. (3.47) in Eq. (3.45), the solution for hoop stress is given by

$$\sigma_\theta = \frac{E\alpha\left(T_b - T_a\right)}{2\ln\left(\dfrac{b}{a}\right)}\left\{\frac{1}{2}+\ln\left(\frac{c}{d}\right)-\frac{d^2}{2c^2}\right\}+k_1\sigma_Y\left\{\frac{1}{2}+\frac{d^2}{2c^2}-\ln\left(\frac{r}{d}\right)\right\}$$

$$+k_1K\int_r^d \frac{1}{r_1}\left(\varepsilon_{eq}^p\right)^n \mathrm{d}r_1 - k_1K\left(\varepsilon_{eq}^p\right)^n . \tag{3.48}$$

In the outer plastic zone, the stresses are such that $\sigma_\theta<\sigma_z<\sigma_r$. Thus in view of Tresca's associated flow rule, $\mathrm{d}\varepsilon_z^p = 0,\ \mathrm{d}\varepsilon_\theta^p = -\mathrm{d}\varepsilon_r^p$. Hence, plastic incompressibility gives $\varepsilon_r^p + \varepsilon_\theta^p = 0$. The total strain in the plastic zone is composed of both elastic and plastic strain components and thus,

$$\varepsilon_r + \varepsilon_\theta = \varepsilon_r^e + \varepsilon_r^p + \varepsilon_\theta^e + \varepsilon_\theta^p = \varepsilon_r^e + \varepsilon_\theta^e \tag{3.49}$$

The elastic strain components in Eq. (3.49) are given by Eqs. (3.2) and (3.3). Using Eq. (3.4) and inserting Eqs. (3.2) and (3.3) in Eq. (3.49), the following differential equation is obtained:

$$\frac{\mathrm{d}}{\mathrm{d}r}(ur) = 2\alpha\left\{T_a + \left(T_b - T_a\right)\frac{\ln\left(\dfrac{r}{a}\right)}{\ln\left(\dfrac{b}{a}\right)}\right\}r + \frac{1}{E}(1-\nu)\frac{\mathrm{d}}{\mathrm{d}r}\left(r^2\sigma_r\right) \tag{3.50}$$

Integration of Eq. (3.50) provides,

$$ur = \alpha T_a r^2 + 2\alpha\frac{\left(T_b - T_a\right)}{\ln\left(\dfrac{b}{a}\right)}\left\{\ln\left(\frac{r}{a}\right)\frac{r^2}{2} - \frac{r^2}{4}\right\} + \frac{1}{E}(1-\nu)r^2\sigma_r + D \tag{3.51}$$

where, *D* is an integration constant. To find out the constant *D*, the left and right hand side of Eq. (3.51) are evaluated at *r*=*c*. For this σ_r and *u* at *r*=*c*, are evaluated using Eqs. (3.38) and (3.40) and are inserted into Eq. (3.51). This provides

$$D = \frac{\alpha\left(T_b - T_a\right)}{2\ln\left(\dfrac{b}{a}\right)}d^2 - \frac{k_1\sigma_Y}{E}d^2 . \tag{3.52}$$

Substituting the value of D from Eq. (3.52) in Eq. (3.51), the total hoop strain component in the plastic zone $d \le r \le b$ is obtained as

$$\frac{u}{r} = \alpha T_a + \frac{\alpha(T_b - T_a)}{2\ln\left(\frac{b}{a}\right)}\left\{2\ln\left(\frac{r}{a}\right) - 1 + \frac{d^2}{r^2}\right\} + \frac{1}{E}(1-\nu)\sigma_r - \frac{k_1\sigma_Y}{E}\frac{d^2}{r^2}. \tag{3.53}$$

Inserting u/r from Eq. (3.53) and ε_θ^e from Eq. (3.3) in Eq. (3.34) and using Eqs. (3.47, 3.48 and 3.36), the plastic part of hoop strain is obtained as

$$\varepsilon_\theta^p = \frac{\alpha(T_b - T_a)}{2\ln\left(\frac{b}{a}\right)}\left\{\frac{d^2}{r^2} - 1\right\} + \frac{k_1\sigma_Y}{E}\left(1 - \frac{d^2}{r^2}\right) + \frac{k_1 K}{E}\left(\frac{2}{\sqrt{3}}\right)^n \left(\varepsilon_\theta^p\right)^n. \tag{3.54}$$

3.3 Residual Thermal Stresses

When the temperature difference induced in the hollow disk vanishes due to cooling, residual thermal stresses are generated in the disk. It is assumed that the unloading process is completely elastic and linear devoid of Bauschinger effect. In the following subsections residual thermal stresses generated in different zones within the wall of the disk during the first and second stage of elasto-plastic deformation are given.

3.3.1 Residual Stresses During the First Stage of Elasto-plastic Deformation

As the unloading process is entirely elastic, the expressions for the residual radial and hoop stresses in the outer elastic zone ($c \le r \le b$), are obtained by subtracting Eqs. (3.12) and (3.13) from Eqs. (3.16) and (3.17) as

$$\begin{aligned}(\sigma_r)_{res} = {} & \frac{E\alpha(T_b - T_a)}{2\ln\left(\frac{b}{a}\right)}\left[\left(\frac{c^2}{b^2+c^2}\right)\left(1 - \frac{b^2}{r^2}\right)\left\{1 - \ln\left(\frac{b}{c}\right)\right\} + \left(\frac{a^2}{b^2-a^2}\right)\ln\left(\frac{b}{a}\right)\left(\frac{b^2}{r^2} - 1\right)\right] \\ & + \frac{c^2 k_1\sigma_Y}{b^2+c^2}\left(1 - \frac{b^2}{r^2}\right),\end{aligned} \tag{3.55}$$

$$\left(\sigma_\theta\right)_{res} = \frac{E\alpha\left(T_b - T_a\right)}{2\ln\left(\dfrac{b}{a}\right)}\left[\left(\frac{c^2}{b^2+c^2}\right)\left(1+\frac{b^2}{r^2}\right)\left\{1-\ln\left(\frac{b}{c}\right)\right\} - \left(\frac{a^2}{b^2-a^2}\right)\ln\left(\frac{b}{a}\right)\left(1+\frac{b^2}{r^2}\right)\right] + \frac{c^2 k_1 \sigma_Y}{b^2+c^2}\left(1+\frac{b^2}{r^2}\right). \tag{3.56}$$

Similarly, the residual stresses in the inner plastic zone ($a \le r \le c$) are obtained by subtracting Eqs. (3.12) and (3.13) from Eqs. (3.22) and (3.19) and are given by

$$\begin{aligned}\left(\sigma_r\right)_{res} &= k_1\sigma_Y\left\{1-\left(\frac{2b^2}{b^2+c^2}\right)\left(\frac{c}{r}\right)\right\} - k_1\frac{K}{r}\int_r^c \left(\varepsilon_{eq}^p\right)^n \mathrm{d}r \\ &\quad + \frac{E\alpha\left(T_b-T_a\right)}{2\ln\left(\dfrac{b}{a}\right)}\left[\begin{array}{l}\left(\dfrac{c}{r}\right)\ln\left(\dfrac{b}{c}\right)+\left(\dfrac{c^2}{b^2+c^2}\right)\left(\dfrac{c}{r}\right)\left(1-\dfrac{b^2}{r^2}\right)\left\{1-\ln\left(\dfrac{b}{c}\right)\right\} \\ -\ln\left(\dfrac{b}{r}\right)-\left(\dfrac{a^2}{b^2-a^2}\right)\ln\left(\dfrac{b}{a}\right)\left(\dfrac{b^2}{r^2}-1\right)\end{array}\right],\end{aligned} \tag{3.57}$$

$$\left(\sigma_\theta\right)_{res} = k_1\left\{\sigma_Y + K\left(\varepsilon_{eq}^p\right)^n\right\} + \frac{E\alpha\left(T_b-T_a\right)}{2\ln\left(\dfrac{b}{a}\right)}\left\{1+\ln\left(\frac{r}{a}\right)-\left(1+\frac{a^2}{r^2}\right)\ln\left(\frac{b}{a}\right)\left(\frac{b^2}{b^2-a^2}\right)\right\}. \tag{3.58}$$

3.3.2 Residual Stresses During the Second Stage of Elasto-plastic Deformation

The expressions for the residual stresses for elastic zone ($c \le r \le d$), are obtained by subtracting Eqs. (3.12) and (3.13) from Eqs. (3.38) and (3.39) as

$$\left(\sigma_r\right)_{res} = \frac{E\alpha\left(T_b-T_a\right)}{2\ln\left(\dfrac{b}{a}\right)}\left\{1+\ln\left(\frac{c}{a}\right)-\frac{d^2}{2c^2}-\frac{d^2}{2r^2}-\left(1-\frac{a^2}{r^2}\right)\ln\left(\frac{b}{a}\right)\left(\frac{b^2}{b^2-a^2}\right)\right\} + k_1\sigma_Y\left\{1+\frac{d^2}{2c^2}+\frac{d^2}{2r^2}\right\}, \tag{3.59}$$

$$(\sigma_\theta)_{res} = \frac{E\alpha(T_b - T_a)}{2\ln\left(\frac{b}{a}\right)}\left\{1 + \ln\left(\frac{c}{a}\right) - \frac{d^2}{2c^2} + \frac{d^2}{2r^2} - \left(1 + \frac{a^2}{r^2}\right)\ln\left(\frac{b}{a}\right)\left(\frac{b^2}{b^2 - a^2}\right)\right\}$$
$$+ k_1\sigma_Y\left\{1 + \frac{d^2}{2c^2} - \frac{d^2}{2r^2}\right\}. \tag{3.60}$$

The residual radial thermal stress in the inner plastic zone (*a*≤*r*≤*c*), is obtained by subtracting Eq. (3.12) from Eq. (3.41) as

$$(\sigma_r)_{res} = \left(\frac{c}{r}\right)\frac{E\alpha(T_b - T_a)}{2\ln\left(\frac{b}{a}\right)}\left\{\frac{c}{r} - \frac{d^2}{cr} + \ln\left(\frac{r}{a}\right) - \left(1 - \frac{a^2}{r^2}\right)\ln\left(\frac{b}{a}\right)\left(\frac{b^2}{b^2 - a^2}\right)\right\}$$
$$+ k_1\sigma_Y\left(1 + \frac{d^2}{cr}\right) - k_1\frac{K}{r}\int_r^c \left(\varepsilon_{eq}^p\right)^n \mathrm{d}r, \tag{3.61}$$

The residual thermal hoop stress in this zone is given by Eq. (3.58).

In the outer plastic zone (*d*≤*r*≤*b*), the residual thermal stresses are obtained by subtracting Eqs. (3.12) and (3.13) from Eqs. (3.47) and (3.48) as

$$(\sigma_r)_{res} = \frac{E\alpha(T_b - T_a)}{2\ln\left(\frac{b}{a}\right)}\left\{\frac{1}{2} + \ln\left(\frac{c}{d}\right) - \frac{d^2}{2c^2} + \ln\left(\frac{r}{a}\right) - \left(1 - \frac{a^2}{r^2}\right)\ln\left(\frac{b}{a}\right)\left(\frac{b^2}{b^2 - a^2}\right)\right\}$$
$$+ k_1\sigma_Y\left\{\frac{3}{2} + \frac{d^2}{2c^2} - \ln\left(\frac{r}{d}\right)\right\} + k_1 K\int_r^d \frac{1}{r_1}\left(\varepsilon_{eq}^p\right)^n \mathrm{d}r_1, \tag{3.62}$$

$$(\sigma_\theta)_{res} = \frac{E\alpha(T_b - T_a)}{2\ln\left(\frac{b}{a}\right)}\left\{\frac{3}{2} + \ln\left(\frac{c}{d}\right) - \frac{d^2}{2c^2} + \ln\left(\frac{r}{a}\right) - \left(1 + \frac{a^2}{r^2}\right)\ln\left(\frac{b}{a}\right)\left(\frac{b^2}{b^2 - a^2}\right)\right\}$$
$$+ k_1\sigma_Y\left\{\frac{1}{2} + \frac{d^2}{2c^2} - \ln\left(\frac{r}{d}\right)\right\} + k_1 K\int_r^d \frac{1}{r_1}\left(\varepsilon_{eq}^p\right)^n \mathrm{d}r_1 - k_1 K\left(\varepsilon_{eq}^p\right)^n. \tag{3.63}$$

3.4 Solution Methodology

During first stage of elasto-plastic deformation, the radius of elastic-plastic interface, *c* is unknown. The elastic-plastic interface radii, *c* and *d* are the unknowns during second stage of elasto-plastic deformation. The boundary condition of vanishing radial stress at the inner radius during the first stage of elasto-plastic deformation provides

$$k_1\sigma_Y\left\{1-\left(\frac{2b^2}{b^2+c^2}\right)\left(\frac{c}{a}\right)\right\}+\left(\frac{c}{a}\right)\frac{E\alpha\left(T_b-T_a\right)}{2\ln\left(\frac{b}{a}\right)}\left[\ln\left(\frac{b}{c}\right)+\left(\frac{c^2}{b^2+c^2}\right)\left(1-\frac{b^2}{c^2}\right)\left\{1-\ln\left(\frac{b}{c}\right)\right\}\right]$$
$$-k_1\frac{K}{a}\int_a^c\left(\varepsilon_{eq}^p\right)^n \mathrm{d}r_1=0. \tag{3.64}$$

Solution of Eq. (3.64) will provide the value of the unknown radius *c*. The boundary conditions of vanishing radial stress both at inner and outer radius during the second stage of elasto-plastic deformation gives

$$\left(\frac{c}{a}\right)\frac{E\alpha\left(T_b-T_a\right)}{2\ln\left(\frac{b}{a}\right)}\left(1-\frac{d^2}{c^2}\right)+k_1\sigma_Y\left(1+\frac{d^2}{ca}\right)-k_1\frac{K}{a}\int_a^c\left(\varepsilon_{eq}^p\right)^n \mathrm{d}r_1=0, \tag{3.65}$$

$$\frac{E\alpha\left(T_b-T_a\right)}{2\ln\left(\frac{b}{a}\right)}\left\{\frac{1}{2}+\ln\left(\frac{c}{d}\right)-\frac{d^2}{2c^2}\right\}+k_1\sigma_Y\left\{\frac{3}{2}+\frac{d^2}{2c^2}-\ln\left(\frac{b}{d}\right)\right\}+k_1K\int_b^d\frac{1}{r_1}\left(\varepsilon_{eq}^p\right)^n \mathrm{d}r_1=0. \tag{3.66}$$

To find out the values of unknown radii *c* and *d*, Eqs. (3.65) and (3.66) needs to be solved simultaneously. The Eqs. (3.64–3.66) are nonlinear in nature. To evaluate *c* or *c* & *d*, from Eq. (3.64) or Eqs. (3.65) & (3.66), a numerical solution methodology as described in the following is adopted.

Step 1: For the first stage of elasto-plastic deformation, the initial estimate for radius of elastic-plastic interface, *c* is obtained by making *K*=0 in Eq. (3.64) and solving it using FZERO function (based on bisection method) in MATLAB. The bisection method for solving non-linear equation is described in Appendix A. However, during second stage of elasto-plastic deformation, the initial estimates for *c* & *d*, are obtained by making *K*=0 in Eqs. (3.65) and (3.66) and solving them for *c* & *d* using FSOLVE function (the least square method of solving simultaneous nonlinear equations) in MATLAB. The initial guess value of ε_θ^p is taken as zero.

Step 2: The updated plastic strain field ε_θ^p at different radial positions is found out from Eq. (3.37) during the first stage of elasto-plastic deformation and from Eqs. (3.44) and (3.54) during second stage of elasto-plastic deformation. For the fixed *c*, in Eq. (3.37) and for the fixed values of *c* & *d*, in Eqs. (3.44) and (3.54), values of ε_θ^p is updated further and this process is repeated till convergence in ε_θ^p is achieved. This basically amounts to solving for ε_θ^p using fixed point iteration method (Gerald and Wheatley, 1994). The integrations involved in Eqs. (3.37), (3.44) and (3.54) are evaluated numerically using trapezoidal rule. Using Eq. (3.36), the updated estimate of ε_{eq}^p is obtained.

Step 3: Now, using the values of ε_θ^p at different radial positions in the corresponding plastic zones the integral terms in Eqs. (3.64), (3.65) and (3.66) are evaluated and the expressions are solved for new estimated values of *c* or *c* & *d*. If the new estimated values of *c* or *c* & *d* are same as the previous estimated values, go to step 4. Otherwise go to Step 2 and repeat the process till the convergence for *c* or *c* & *d* is achieved.

Step 4: Using the latest updated values of ε_θ^p, *c* or *c* & *d*, the radial and hoop stresses in the plastic zones for the corresponding cases are calculated from Eqs. (3.22), (3.19), (3.41), (3.47) and (3.48). The thermal residual stresses are estimated using the relevant equations derived in Section 3.3.

3.5 Conceptual Design of a System for Creation of Thermal Gradient in the Disk

For achieving the thermal autofrettage of a hollow disk, a certain amount of temperature difference across the wall of the disk needs to be created. The desired temperature difference between the outer and inner wall of the disk can be created by heating the outer wall and cooling the inner wall simultaneously. The outer wall of the disk can be heated externally by using electrical heating element providing proper insulation in order to prevent heat loss to the environment. The heat transfer takes place from outer to inner wall of the disk in radial direction. An arrangement for cooling the inner wall of the disk can be made by flowing cold fluid *e.g.*, cold water, which will carry away the heat from the inner surface. Thus, heat transfer takes place from outer to inner wall by conduction and then by convection from inner wall to the cold fluid.

Heat flow rate is given by

$$Q = 2\pi kL\frac{\left(T_b - T_a\right)}{\ln\left(\frac{b}{a}\right)} = 2\pi aLh(T_a - T_f)\,, \tag{3.67}$$

where L is the length of the disk, h is the convective heat transfer coefficient of the fluid, k is the thermal conductivity of the material of the disk and T_f is the average temperature of fluid flowing inside the disk. The average temperature can be taken as the mean of inlet temperature T_i and outlet temperature T_o of the fluid. The temperature difference required for achieving autofrettage, (T_b–T_a), can be fixed for a particular material. From Eq. (3.67),

$$T_a - T_f = \frac{k\left(T_b - T_a\right)}{ah\ln\left(\frac{b}{a}\right)} \tag{3.68}$$

The heat flow rate Q is also expressed by

$$Q = \dot{m}c_p\left(T_o - T_i\right), \tag{3.69}$$

where c_p is the specific heat of fluid at constant pressure. The convective heat transfer coefficient, h can be calculated from the Nusselt number, Nu, defined as

$$\mathrm{Nu} = \frac{hD}{k_f}\ , \tag{3.70}$$

where k_f is the thermal conductivity of fluid at T_f and D is the inside diameter of the disk. For the present problem, D=2a. The Nusselt number can be calculated by using Gnielinski correlation (Incropera and Dewitt, 1996) given by

$$Nu = \frac{\left(f/8\right)\left(\mathrm{Re}-1000\right)\mathrm{Pr}}{1+12.7\left(f/8\right)^{1/2}\left\{\left(\mathrm{Pr}\right)^{2/3}-1\right\}}, \tag{3.71}$$

where

$$f = \left\{0.790\ln\left(\mathrm{Re}\right)-1.64\right\}^{-2}. \tag{3.72}$$

This relation is valid for $3000<\mathrm{Re}<5\times10^{6}$ and $0.5<\mathrm{Pr}<2000$. The Reynolds number of flow, Re and Prandtl number, Pr are evaluated using the following relations

$$\mathrm{Re} = \frac{\rho VD}{\mu}, \quad \mathrm{Pr} = \frac{\mu c_p}{k_f}, \tag{3.73}$$

where V is the velocity of fluid, ρ is the density and μ is the coefficient of dynamic viscosity of fluid at T_f. The value of h can be calculated using Eqs. (3.69–3.73) and the temperature of the inner surface T_a can be estimated from Eq. (3.68).

An example

A hollow disk of SS316 steel with inner radius a=10 mm, outer radius b=30 mm and length L=20 mm is considered. It is heated externally and a temperature difference, (T_b-T_a) = 150 ℃ is maintained for achieving autofrettage. The thermal conductivity, k of SS316 is taken as 13.4 W/m ℃ (Incropera and Dewitt, 1996). It is decided to use cold water as the fluid. Using Eq. (3.67), the amount of heat transfer Q is calculated as

$$Q = 229.91\ \mathrm{W}.$$

Taking $\dot{m}$ = 1 kg/s and c_p = 4.18 kJ/kg-K, the temperature difference between outlet and inlet of the cold water flowing through the disk (T_o-T_i) is obtained from Eq. (3.69) as

$$(T_o-T_i) = 0.05°\mathrm{C}.$$

Assuming the temperature of the water at the inlet as T_i= 25 ºC, the temperature at the outlet is estimated as T_o = 25.05°C. Thus, the average temperature of the water flowing inside the disk is

$$T_f = \frac{T_i + T_o}{2} = 25.025 \ ^\circ\text{C}.$$

Properties of water at 25.025 ºC are $\rho = 997$ kg/m^3, $\mu = 0.899 \times 10^{-3}$ Ns/m^2, k_f=0.606 W/m ºC (Incropera and Dewitt, 1996). The velocity of flow is calculated as

$$V = \frac{\dot{m}}{\rho \left(\pi/4 \right) D^2} = 3.19 \text{ m/s}$$

.

Using Eq. (3.73) provides

$$\text{Re} = 70{,}754.83, \quad \text{Pr} = 6.20.$$

Hence, from Eq. (3.71),

$$\text{Nu} = 420.46.$$

Putting Nu in Eq. (3.70) the value of heat transfer coefficient, h is obtained as

$$h = 12{,}740 \text{ W/m}^2 \, ^\circ\text{C}.$$

Using the value of h in Eq. (3.68), the inner wall temperature T_a is estimated as 39.38 °C. As the difference in temperature between the inner and outer wall of the disk is 150 ºC, the value of outer wall temperature T_b is 189.38 ºC.

3.6 Numerical Simulations

The proposed autofrettage process is simulated numerically using the equations developed in Subsections 3.2.3, 3.2.4, 3.3.1 and 3.3.2. For this purpose two cases are considered. The corresponding equations are solved following the methodology discussed in Section 3.4. The simulated results are discussed in the following subsections.

3.6.1 Case of Aluminum Disk

An aluminum disk is considered with inner radius, a=10 mm and outer radius, b=20 mm. The material properties of aluminum are as follows: Young's modulus of elasticity, E=69 GPa, yield stress, σ_Y=50.3 MPa and coefficient of thermal expansion, α=22.2×10^{-6}/ºC. The temperature difference required for initial yielding at inner wall of the disk is calculated using Eq. (3.15) and is obtained as 53.66 ºC. For achieving autofrettage in the aluminum disk, two temperature differences are considered— a temperature difference of 80 ºC to cause the first stage of elasto-plastic deformation and a temperature difference of 100 ºC to cause the second stage of elasto-plastic deformation in the wall of the disk. The radius of elastic-plastic interface, c is obtained as 11.21 mm when the temperature difference is 80 ºC. The estimates of c and d are obtained as 11.86 mm and 18.89 mm when the temperature difference is 100 ºC. The hardening coefficient K and strain hardening exponent n for the disk material are taken as 58.18 MPa and 0.48 in Ludwik's hardening law given by Eq. (3.20). The various stresses generated in the disk due to thermal autofrettage are simulated and are shown as a function of radial position.

3.6.1.1 Elasto-plastic thermal stress pattern

The elasto-plastic thermal stresses for 80 °C temperature difference are obtained using Eqs. (3.16), (3.17), (3.19) and (3.22). For the temperature difference of 100 °C, the elasto-plastic stresses are estimated using Eqs. (3.38), (3.39), (3.41), (3.19), (3.47) and (3.48). The resulting elasto-plastic stress distribution for temperature difference of 80 °C and 100 °C is shown in Figure 3.4. It is observed that the magnitude of radial stresses is quite small compared to hoop stresses. The radial stresses are always tensile, whilst the hoop stresses change from tensile to compressive along the positive radial direction. This trend gets reversed when the temperature difference is removed. It is also observed that strain hardening effect is not very significant in the present case.

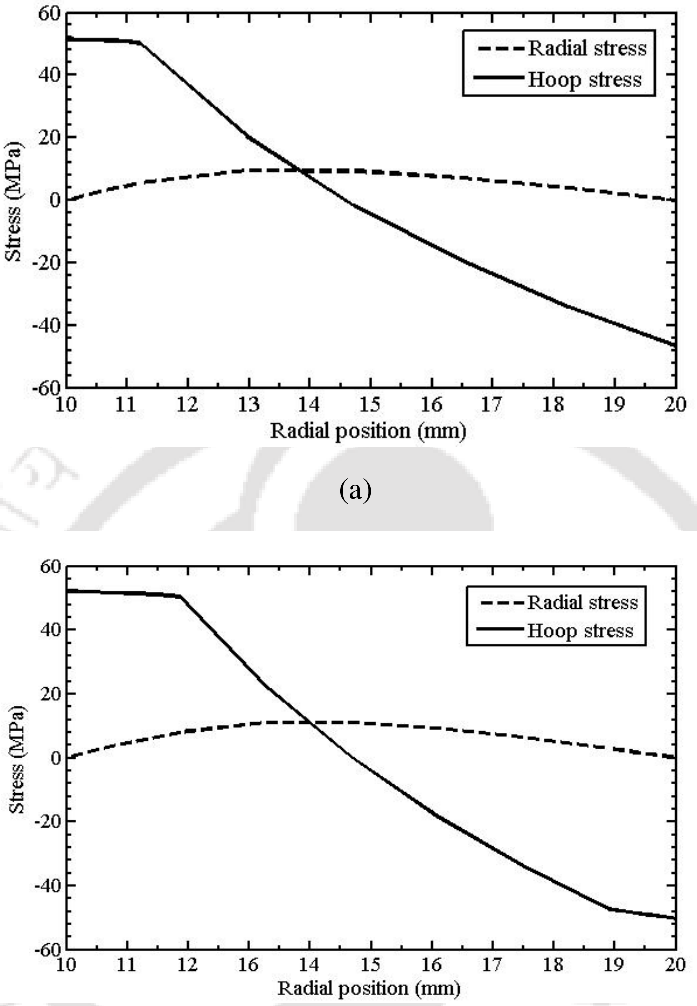

(a)

(b)

Figure 3.4 Elasto-plastic stress distributions in aluminum disk for (a) $(T_b – T_a)$=80 °C and (b) $(T_b – T_a)$=100 °C

3.6.1.2 Residual stress pattern

On removal of the temperature difference, residual thermal stresses are generated in the disk. The residual stress variation with the radial position is shown in Figure 3.5 for the temperature differences of 80 °C and 100 °C. It is observed that the residual compressive hoop stresses are generated at and around the inner wall of the disk, whilst residual tensile stresses are generated at the outer region of the disk. For the temperature difference of 100 °C, the magnitudes of compressive residual stresses are higher compared to the case of temperature difference of 80 °C. The maximum magnitude of residual stress for the temperature difference of 80 °C is about 23 MPa (compressive), generated at the inner radius of the disk. For the case of 100 °C temperature difference, this magnitude is about 42 MPa (compressive). Hence, when the disk is subjected to loading by inducing internal pressure, then the resulting residual compressive stress leads to decrease in the maximum value of stress occurring in the disk.

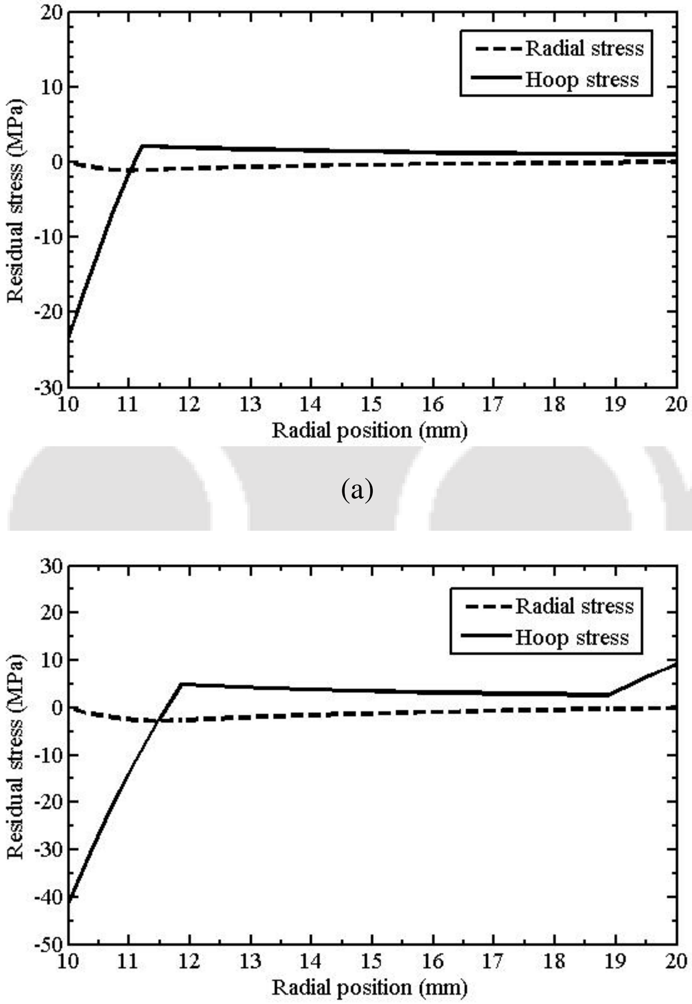

(a)

(b)

Figure 3.5 Residual stress distributions in aluminum disk for (a) $(T_b{-}T_a)$=80 °C and (b) $(T_b{-}T_a)$=100 °C

The magnitudes of residual tensile stresses at the outer portion of the disk are small compared to residual compressive stresses for the case of 80 °C. For the 100 °C temperature difference, the magnitudes of tensile residual stresses show an increasing trend at the outer plastic zone. For the temperature difference of 80 °C, the maximum tensile residual stress is generated at the elastic-plastic interface (at r=c). For the temperature difference of 100 °C, the maximum tensile residual stress occurs at the outer radius. Moreover, its magnitude is larger in comparison to 80 °C temperature difference case. In corrosive environment, the larger tensile residual stress at the outer radius may cause stress corrosion cracking. Therefore, autofrettage by 100 °C temperature difference is not desirable in corrosive environment.

3.6.1.3 Overall stresses with and without autofrettage

Assume that the aluminum disk which is autofrettaged by inducing temperature difference between inner and outer wall is subjected to an internal working pressure of 18 MPa for both the temperature difference case. The overall stresses are then obtained by adding stresses due to internal working pressure to the residual thermal stresses. The stresses that occur in the disk due to internal working pressure are given by well-known Lame's equations (Chakrabarty, 2006).

$$\sigma_r = \frac{p_i a^2}{b^2 - a^2}\left(1 - \frac{b^2}{r^2}\right), \tag{3.74}$$

$$\sigma_\theta = \frac{p_i a^2}{b^2 - a^2}\left(1 + \frac{b^2}{r^2}\right), \tag{3.75}$$

where p_i is the internal working pressure. If the same disk is considered only under the condition of internal working pressure without autofrettage, then the elastic stresses generated in the disk are given by Eqs. (3.74) and (3.75) only.

The resulting stresses with and without autofrettage for the case of 80 °C temperature difference is shown in Figure 3.6 (a). For 100 °C temperature difference, they are shown in Figure 3.6 (b). The equivalent Tresca stress ($|\sigma_\theta - \sigma_r|/2$, in the present cases) is the maximum at the elastic-plastic interface (r=c), in the autofrettaged disk during pressurization. Therefore, for the autofrettaged disk, yielding will first take place at the elastic-plastic interface (r=c).

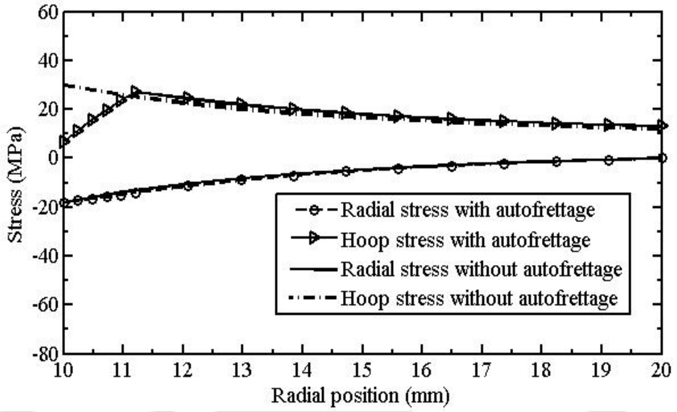

(a)

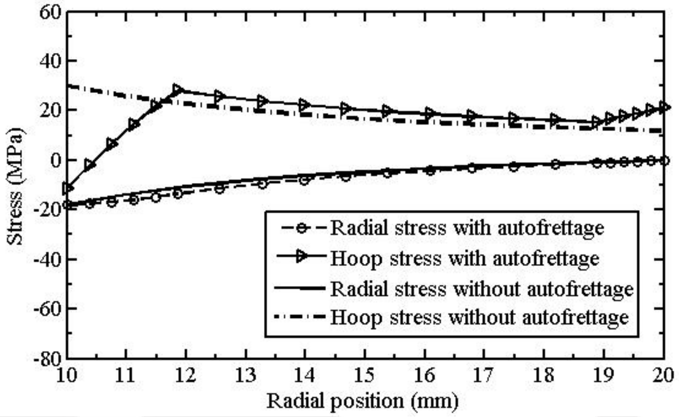

(b)

Figure 3.6 Comparison of stresses with and without autofrettage in aluminum disk for (a) (T_b−T_a)=80 °C and (b) (T_b−T_a)=100 °C at working pressure of 18 MPa

When the temperature difference is 80 °C, the autofrettaged disk can withstand the maximum pressure of 22.2 MPa without yielding. The disk which is autofrettaged with 100 °C temperature difference can withstand the maximum pressure carrying capacity of 22.5 MPa. On the other hand, the non-autofrettaged disk can withstand a maximum pressure of 18 MPa. It is observed that the maximum equivalent Tresca stress is reduced by 13.85% in the disk when it is autofrettaged by inducing temperature difference of 80 °C as compared to the disk without autofrettage at a working pressure of 18 MPa. For the temperature difference of 100

°C this reduction is observed to be 13.25%. It is always preferred to perform partial thermal autofrettage of disks in order avoid stress corrosion cracking as in the present case. Underwood and Miller (1988) have also advocated partial autofrettage even in the case of hydraulic autofrettage to circumvent the problem of stress corrosion cracking. Nevertheless, compared to hydraulic autofrettage, the level of thermal autofrettage is limited, because the maximum temperature needs to be kept well below the recrystallization temperature of the material.

It is to be noted that the wall thickness ratio b/a and temperature difference (T_b−T_a) across the wall thickness affect the pressure carrying capacity of the disk. The effect of these parameters in thermal autofrettage for the present case is discussed in appendix B.

3.6.2 Case of Mild Steel Disk

A mild steel disk with inner radius, a=10 mm and outer radius, b=30 mm is simulated when it undergoes autofrettage process due to a temperature difference between the outer and inner surface. Material properties considered for steel are as follows: Young's modulus of elasticity, E=200 GPa, yield stress, σ_Y=324 MPa, coefficient of thermal expansion, $\alpha=13\times10^{-6}$/°C. The temperature difference required for initial yielding at the inner wall of the disk for this case is 186 °C which is much lower than the recrystallization temperature of mild steel. However, a large temperature difference is required to cause the yielding of the outer wall of the disk. The large temperature difference may greatly change the material properties. Therefore, it is not advisable to induce such a large temperature difference that will cause the yielding of both the inner and outer wall of the disk for achieving autofrettage. Hence, the disk is simulated for a temperature difference of 270 °C for achieving autofrettage. At 270 °C temperature difference, the wall of the disk undergoes first phase of elasto-plastic deformation. The radius of elastic-plastic interface, c is obtained as 11.709 mm. The hardening coefficient K and strain hardening exponent n for the disk are taken as 226.98 MPa and 0.43. The stresses generated in the disk as a result of autofrettage are shown as a function of radial position.

3.6.2.1 Elastic-plastic thermal stress pattern

The elastic-plastic thermal stresses for the disk are obtained using Eqs. (3.16), (3.17), (3.19) and (3.22). The similar trend, as obtained in the case of aluminum disk with 80 °C of temperature-difference, is observed. The results are shown in Figure 3.7. Here also, the strain hardening is not significant.

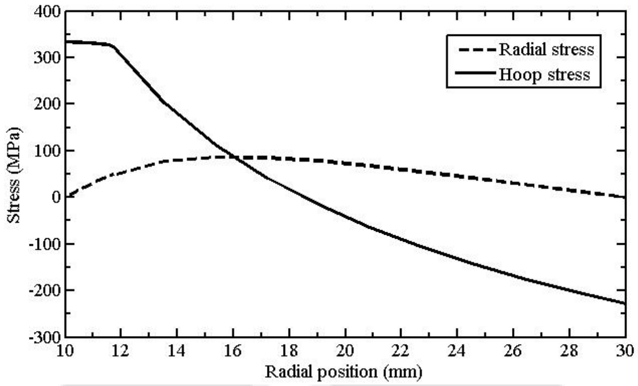

Figure 3.7 Elasto-plastic stresses in mild steel disk

3.6.2.2 Residual stress pattern

The residual stress pattern for the autofrettaged steel disk is shown in Figure 3.8. It is observed that a significant amount of compressive residual hoop stresses are generated in and around the inner radius of the disk and hence it reduces the magnitude of resultant stress when it is subjected to internal working pressure. The magnitudes of tensile residual stresses generated at the outer region of the disk are very small.

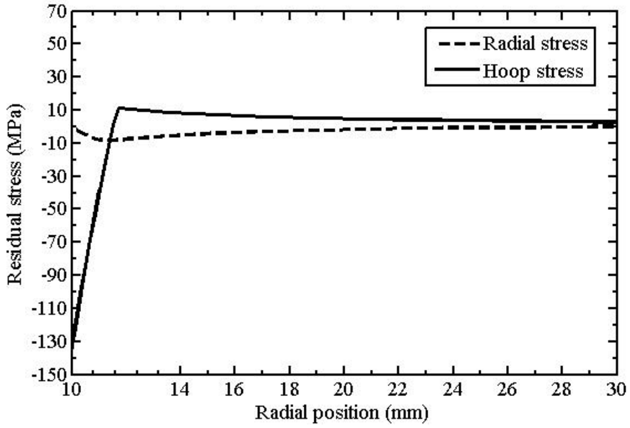

Figure 3.8 Residual stresses in mild steel disk

3.6.2.3 Overall stresses with and without autofrettage

The autofrettaged steel disk is subjected to an internal working pressure of 100 MPa and the resultant stress pattern is shown in Figure 3.9. The corresponding stresses without autofrettage are also shown using Eqs. (3.74) and (3.75). In case of the autofrettaged disk, the magnitude of the maximum equivalent Tresca stress is found to be 18.82% less than that in case of the disk without autofrettage during pressurization. The maximum equivalent Tresca stress exists at the radius of elastic-plastic interface for the autofrettaged case. Therefore, yielding of the disk during pressurization will first take place at the elastic-plastic interface. The maximum pressure carrying capacity of the autofrettaged disk in this case is 186 MPa. The non-autofrettaged disk can withstand a maximum pressure of 144 MPa only.

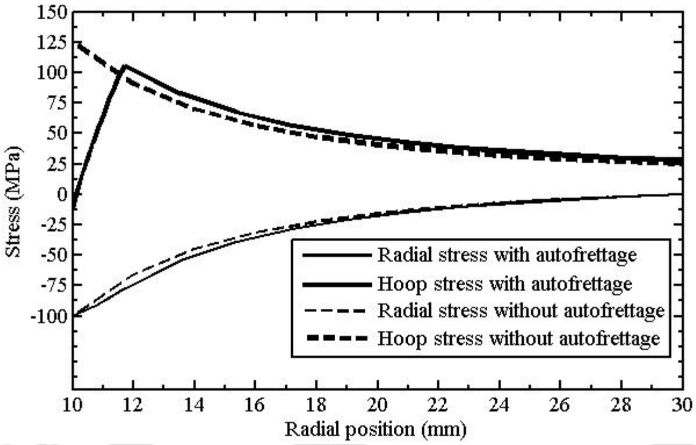

Figure 3.9 Comparison of stresses with and without autofrettage in mild steel disk at a working pressure of 100 MPa

3.7 Summary

In this chapter, a theoretical model for thermal autofrettage considering plane stress assumption is presented. The model is suitable for the thermal autofrettage of thick-walled short cylinders or thin hollow disks. The analysis is based on the Tresca yield criterion and its associated flow rule. The strain hardening of the material has been taken into account during plastic deformation. The closed form theoretical solutions of stresses have been numerically simulated for aluminum and mild steel disks. The overall simulation results show that in thermal autofrettage, removal of thermal gradient generates substantial amount of compressive residual stresses at and around the inner wall of the disk in a similar way as in the case of hydraulic or swage autofrettage process. Compared to hydraulic and swage autofrettage, the achievable level of autofrettage is limited by the maximum allowable temperature at the outer wall of the disk. However, the simplicity of the process has potential to make it a competitive process.

Chapter 4

The Generalized Plane Strain Model of Thermal Autofrettage

4.1 Introduction

The autofrettage process is widely practiced for strengthening the thick-walled cylinders. It finds application in industries for the manufacture of gun barrels, pressure vessels, high pressure piping and fuel injection systems for diesel engines. The process increases the operating pressure of thick-walled cylinders. The process also increases the fatigue life of the cylinders and achieves a safe (leak-before-break) failure mode (Perl and Aroné, 1988; Parker and Kendall, 2003). Many researchers investigated the process of well-known hydraulic and swage autofrettage processes either analytically or numerically considering different assumptions. Most of the modelling is based on either Tresca or von Mises yield criterion considering plane stress, plane strain and generalized plane strain conditions (Nádai, 1931; Avitzur, 1994; Jahed and Dubey, 1997; Parker *et al.*, 1999; Gibson *et al.* 2006; Perry and Aboudi, 2003; O'Hara 1992).

The thermal autofrettage process is based on the non-homogeneous plastic deformation due to thermal loading. Barbero and Wen (2002) conceptualized an idea of thermal autofrettage for the composite metal-lined cryogenic pressure vessels. For achieving thermal autofrettage, they suggested cooling of the cylinder with metal liner using cryogenic fluids to a temperature lower than the operating temperature so that the thermally induced plastic deformation sets the liner in compression. They did not carry out any analytical or experimental study for the process they conceived. Kargarnovin *et al.* (2005) analyzed the elasto-plastic stresses in thick-walled spherical vessels due to combined pressure and thermal gradient, thermal loading and unloading using the concept of thermal autofrettage. A recent study on the thermal autofrettage of titanium-copper brazed joints was carried out by Hamilton *et al.* (2015) using finite element method (FEM). They achieved thermal autofrettage by cooling of the joint, which induces plastic work in the joint due to the differential thermal contraction of the material. Authors determined the residual stresses generated in the brazed joint after thermal autofrettage experimentally using X-ray diffraction (XRD) technique compared with the FEM results. The study of the present thesis is on the thermal autofrettage, where the beneficial compressive residual stresses at and around the inner wall of the cylinder is proposed to generate by means of thermal gradient. There is no study of the thermal autofrettage for thick-walled cylinders in the literature analysing its feasibility due to thermal gradient.

The thermal autofrettage process based on the plastic deformation by the thermal gradient for hollow circular disks has been described in Chapter 3 assuming plane stress condition. The analysis presented in Chapter 3 is not valid for long cylinders as the analysis considers that the axial stress in the cylinder is zero under thermal gradient (plane stress condition). In cylinders, the axial stress component in cylinders is not zero under thermal gradient. This motivates the modelling of thermal autofrettage for thick-walled cylinders considering generalized plane strain condition. The generalized plane strain condition leads to the state of constant axial strain with zero net axial force. The consideration of generalized plane strain condition also corresponds to a thick-walled cylinder with free ends.

In this chapter, the thermal autofrettage process is analyzed theoretically for thick-walled cylinders considering generalized plane strain condition. The thermo-elasto-plastic stresses, strain components and residual stresses are derived in closed form when the cylinder is subjected to a steady-state radial thermal gradient. The solutions are based on Tresca yield criterion and its associated flow rule. The analysis considers both non-hardening and strain hardening of the cylinders during plastic deformation. To represent the strain hardening during plastic deformation, Ludwik's hardening law is used. The analytical solutions are simulated numerically for typical aluminum and SS304 cylinders to ensure the practical reliability of the thermal autofrettage process. A numerical comparison of thermo-elasto-plastic stresses are also carried out with and without strain hardening to study the effect of strain hardening.

4.2 Thermal stress analysis

Thermal elastic-plastic stress analysis in cylinders and other structures has been the subject of study by many researchers. However, it has not been used for studying the autofrettage in cylinders. For example, Orçan (1994) studied elastic-plastic deformation in cylindrical rods with uniform internal heat generation under generalized plane strain condition. Orçan did not carry out the analysis for hollow cylinders. Here, the analysis is carried out for hollow thick-cylinders subjected to a thermal gradient across the wall of the cylinder. The residual stresses generated after the removal of thermal gradient are estimated for exploring the feasibility of thermal autofrettage process.

A thick-walled long cylinder with free ends under radial thermal gradient is considered. If a and b are the inner and outer radius of the cylinder and T_a and T_b are the temperature at the inner and outer wall of the cylinder, then the steady state temperature distribution in the cylinder is given by Eq. (3.1).

Due to thermal gradient induced in the cylinder, there exist three different situations of deformations. Elastic deformation of entire wall of the cylinder takes place for small temperature difference. When the temperature difference crosses the first threshold, the inner wall yields and undergoes the first stage of elasto-plastic deformation. It is assumed that the material deforms according to Tresca yield criterion. In this case, the cylinder wall consists of three zones (Figure 4.1 a), *viz*., plastic zone I: $a \le r \le c$, plastic zone II: $c \le r \le d$ and outer elastic zone: $d \le r \le b$. These two plastic zones correspond to different sides of Tresca yield locus. In von-Mises criterion, the yield locus is smooth (without having any corner) and hence there is no need to assume two different plastic zones. The plastic flow of the outer wall commences in the cylinder when the temperature difference crosses the second threshold. Thus, the second stage of elasto-plastic deformation occurs in the cylinder. During the second stage of elasto-plastic deformation, besides the two inner plastic zones, additional plastic zones at the outer wall (Figure 4.1 b), *viz*., plastic zone III: $f \le r \le b$ and plastic zone IV: $e \le r \le f$ are formed. In between there an intermediate elastic zone: $d \le r \le e$. The analytical modelling of the thermal stresses is based on the assumption that the maximum allowable temperature, T_b, in the cylinder is below the recrystallization temperature (homologous temperature ≈ 0.4) of the material to avoid phase transformation. For most of the materials, the material properties do not vary much at such a low temperature and the percentage change is below 10%. It is also to be noted that the temperature rapidly drops from outer to inner surface of the cylinder and limiting the outer surface up to recrystallization temperature does not alter overall mechanical and metallurgical properties. In this section, the thermal stress analysis is carried out without strain hardening. Most of the cylinders are cold worked during their manufacturing and thus already strain hardened. Therefore, the effect of strain hardening can be neglected during the autofrettage of cold worked cylinders. The effect of strain hardening is incorporated in Section 4.5. In the present work, the small strain plasticity is assumed and after the analysis, it was verified that the maximum plastic strain is of the order of 10^{-4}.

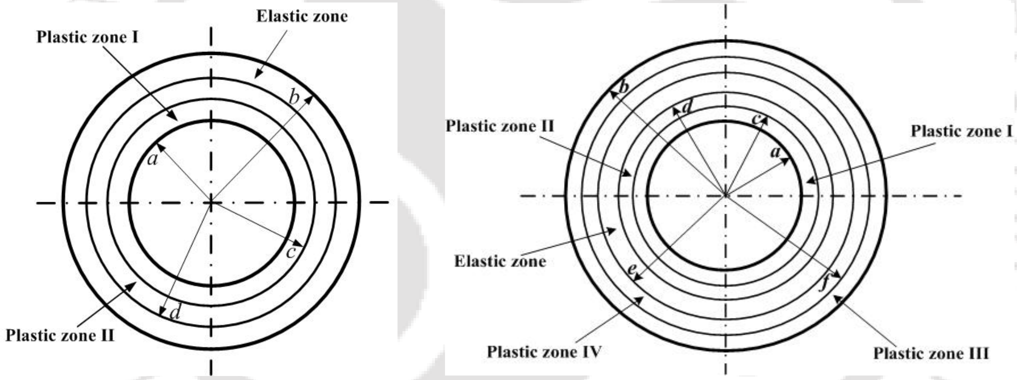

(a) (b)

Figure 4.1 The elastic and plastic zones in the cylinder during (a) first and (b) second stage of elasto-plastic deformation

4.2.1 Solution for thermo-elastic stresses

With zero temperature as a reference, the generalized Hook's law in cylindrical co-ordinate gives the radial, hoop and axial strain as (Chakrabarty, 2006)

$$\varepsilon_r = \frac{1}{E}\left\{\sigma_r - \nu\left(\sigma_\theta + \sigma_z\right)\right\} + \alpha T, \tag{4.1}$$

$$\varepsilon_\theta = \frac{1}{E}\left\{\sigma_\theta - \nu\left(\sigma_r + \sigma_z\right)\right\} + \alpha T, \tag{4.2}$$

$$\varepsilon_z = \frac{1}{E}\left\{\sigma_z - \nu\left(\sigma_r + \sigma_\theta\right)\right\} + \alpha T, \tag{4.3}$$

where T is given by Eq. (3.1). Using generalized plane strain condition (ε_z=constant=ε_0), Eq. (4.3) can be written as

$$\sigma_z = \nu\left(\sigma_r + \sigma_\theta\right) - \alpha E T + E\varepsilon_0 \tag{4.4}$$

Substitution of Eq. (4.4) in Eq. (4.1) and (4.2) provides

$$\varepsilon_r = \frac{1-\nu^2}{E}\left(\sigma_r - \frac{\nu}{1-\nu}\sigma_\theta\right) + \left(1+\nu\right)\alpha T - \nu\varepsilon_0 \tag{4.5}$$

$$\varepsilon_\theta = \frac{1-\nu^2}{E}\left(\sigma_\theta - \frac{\nu}{1-\nu}\sigma_r\right) + \left(1+\nu\right)\alpha T - \nu\varepsilon_0 \tag{4.6}$$

Substituting Eqs. (4.5) and (4.6) in strain-displacement relations given by Eq. (3.4) and using strain compatibility Eq. (3.5) and equilibrium Eq. (3.6), the solution for radial and hoop stresses are given by

$$\begin{aligned}\sigma_r = {} & \frac{-E\alpha}{2\left(1-\nu\right)}T_a - \frac{E\alpha}{2\left(1-\nu\right)}\frac{\left(T_b - T_a\right)}{\ln\left(\frac{b}{a}\right)}\left\{\ln\left(\frac{r}{a}\right) - \frac{1}{2}\right\} + \frac{E}{\left(1+\nu\right)\left(1-2\nu\right)}C_1 - \frac{E}{\left(1+\nu\right)}\frac{C_2}{r^2} \\ & + \frac{E}{\left(1+\nu\right)\left(1-2\nu\right)}\nu\varepsilon_0,\end{aligned} \tag{4.7}$$

$$\begin{aligned}\sigma_\theta = {} & -\frac{E\alpha}{2\left(1-\nu\right)}T_a - \frac{E\alpha}{2\left(1-\nu\right)}\frac{\left(T_b - T_a\right)}{\ln\left(\frac{b}{a}\right)}\left\{\ln\left(\frac{r}{a}\right) + \frac{1}{2}\right\} + \frac{E}{\left(1+\nu\right)\left(1-2\nu\right)}C_1 + \frac{E}{\left(1+\nu\right)}\frac{C_2}{r^2} \\ & + \frac{E}{\left(1+\nu\right)\left(1-2\nu\right)}\nu\varepsilon_0.\end{aligned} \tag{4.8}$$

In Eqs. (4.7) and (4.8) C_1 and C_2 are integration constants. The boundary conditions of vanishing radial stress at the inner and outer radius provides the constants C_1 and C_2 as

$$C_1 = \frac{(1+\nu)(1-2\nu)}{E}\left\{\left(\frac{b^2}{b^2-a^2}\right)\frac{E\alpha(T_b-T_a)}{2(1-\nu)} - \frac{E\alpha}{4(1-\nu)}\frac{(T_b-T_a)}{\ln\left(\frac{b}{a}\right)} + \frac{E\alpha}{2(1-\nu)}T_a - \frac{E}{(1+\nu)(1-2\nu)}\nu\varepsilon_0\right\}, \tag{4.9}$$

$$C_2 = \frac{(1+\nu)}{E}\left(\frac{a^2b^2}{b^2-a^2}\right)\frac{E\alpha(T_b-T_a)}{2(1-\nu)}. \tag{4.10}$$

Substituting the values of C_1 and C_2 from Eqs. (4.9) and (4.10) in Eqs. (4.7) and (4.8) the solution for thermo-elastic radial and hoop stresses are obtained as (Noda *et al.*, 2003)

$$\sigma_r = \frac{E\alpha}{2(1-\nu)}(T_b-T_a)\left\{-\frac{\ln\left(\frac{r}{a}\right)}{\ln\left(\frac{b}{a}\right)} + \left(1-\frac{a^2}{r^2}\right)\frac{b^2}{b^2-a^2}\right\} \tag{4.11}$$

$$\sigma_\theta = \frac{E\alpha}{2(1-\nu)}(T_b-T_a)\left\{-\frac{1+\ln\left(\frac{r}{a}\right)}{\ln\left(\frac{b}{a}\right)} + \left(1+\frac{a^2}{r^2}\right)\frac{b^2}{b^2-a^2}\right\} \tag{4.12}$$

Using Eq. (4.4), the axial stress distribution is given by

$$\sigma_z = -\alpha E T_a + \frac{E\alpha}{2(1-\nu)}(T_b-T_a)\left\{-\frac{\nu+2\ln\left(\frac{r}{a}\right)}{\ln\left(\frac{b}{a}\right)} + \frac{2\nu b^2}{b^2-a^2}\right\} + E\varepsilon_0. \tag{4.13}$$

The constant axial strain ε_0 can be determined from the free end condition (zero total axial force) given by

$$\int_a^b \sigma_z 2\pi r \mathrm{d}r = 0. \tag{4.14}$$

Using Eq. (4.13) in Eq. (4.14), the constant axial strain is obtained as

$$\varepsilon_0 = \alpha T_a - \frac{\alpha\left(T_b - T_a\right)}{2\left(1-\nu\right)}\left\{-\frac{\nu}{\ln\left(\dfrac{b}{a}\right)} - 2\frac{b^2}{\left(b^2-a^2\right)} + \frac{1}{\ln\left(\dfrac{b}{a}\right)} + 2\nu\frac{b^2}{\left(b^2-a^2\right)}\right\}. \tag{4.15}$$

Substituting Eq. (4.15) in Eq. (4.13), the solution for elastic axial stress in the cylinder is obtained as (Noda *et al.*, 2003)

$$\sigma_z = \frac{E\alpha}{2\left(1-\nu\right)}\left(T_b - T_a\right)\left\{-\frac{1+2\ln\left(\dfrac{r}{a}\right)}{\ln\left(\dfrac{b}{a}\right)} + \frac{2b^2}{b^2-a^2}\right\}. \tag{4.16}$$

Using Eqs. (4.11) and (4.12) and the second relation of Eq. (3.4) in Eq. (4.6), the radial displacement component *u* is obtained as (Noda *et al.*, 2003)

$$u = \alpha r T_a + \left(\frac{1+\nu}{1-\nu}\right)\alpha\left(T_b - T_a\right) r\left\{\frac{\ln\left(\dfrac{r}{a}\right)}{2\ln\left(\dfrac{b}{a}\right)} + \left(\frac{1-3\nu}{1+\nu} + \frac{a^2}{r^2}\right)\frac{b^2}{2\left(b^2-a^2\right)} - \frac{1-\nu}{1+\nu}\,\frac{1}{2\ln\left(\dfrac{b}{a}\right)}\right\}. \tag{4.17}$$

4.2.2 Initiation of Yielding

The distribution of the thermo-elastic stresses given by Eqs. (4.11), (4.12) and (4.16) for a typical aluminum cylinder with a=10 mm, b=20 mm, E=69 GPa, $(T_b - T_a)$=30°C, ν=0.25 and $\alpha=22.2\times10^{-6}$/°C is shown in Figure 4.2. The distribution suggests that the initiation of yielding takes place first at the inner radius of the cylinder as per Tresca yield criterion when the temperature difference across the wall thickness is increased. The temperature difference required for initial yielding at the inner radius can be obtained by using Tresca yield criterion at the inner radius given by

$$\left(\sigma_\theta - \sigma_r\right)\Big|_{r=a} = k_1\sigma_Y \quad \text{or} \quad \left(\sigma_z - \sigma_r\right)\Big|_{r=a} = k_1\sigma_Y, \tag{4.18}$$

where σ_Y is the yield stress of the material and k_1 is a sign factor that can be 1 or −1 depending on whether $T_b > T_a$ or $T_b < T_a$. The present analysis is carried out for $T_b > T_a$. Thus, k_1 is equal to 1. By evaluating the corresponding stresses from Eqs (4.11), (4.12) and (4.16) in Eq. (4.18) at *r*=*a*, the temperature difference required for initiation of yielding at the inner radius is obtained as

$$(T_b - T_a)_{Y_i} = \frac{2(1-\nu)k_1\sigma_Y}{E\alpha\left\{-\dfrac{1}{\ln\left(\dfrac{b}{a}\right)} + \dfrac{2b^2}{b^2-a^2}\right\}}. \tag{4.19}$$

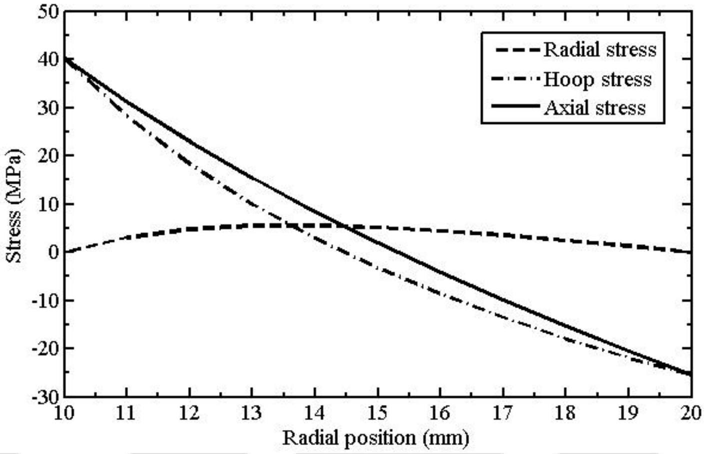

Figure 4.2 Typical thermo-elastic stress distributions in aluminum cylinder

When the temperature difference exceeds the temperature difference given by Eq. (4.19), the cylinder undergoes first stage of elasto-plastic deformation as described in Section 4.2.

4.2.3 Analysis of the First Stage of Elasto-plastic Deformation

In the first stage of elasto-plastic deformation the thick-walled cylinder is composed of two plastic zones— plastic zone I: $a \le r \le c$ and plastic zone II: $c \le r \le d$. The plastic zone I and plastic zone II propagate outwards as per Tresca yield criterion given by Eqs. (4.18) & (4.19), respectively. The outer region, $d \le r \le b$ remains in the elastic state. The radius *c* can be called as plastic-plastic interface and the radius *d* is the radius of elastic-plastic interface. The thermal stresses generated in different zones during first stage of elasto-plastic deformation are discussed in the following subsections.

4.2.3.1 Plastic zone I: $a \le r \le c$

The state of stress at the inner radius of the cylinder is $\sigma_\theta = \sigma_z > \sigma_r$. Thus, the Tresca yield criterion for a non-hardening cylinder provides

$$\sigma_\theta - \sigma_r = k_1 \sigma_Y, \quad \sigma_z - \sigma_r = k_1 \sigma_Y, \tag{4.20}$$

Using Eq. (4.20) in equilibrium equation (Eq. 3.6), the radial thermal stress in the plastic zone I is obtained as

$$\sigma_r = k_1 \sigma_Y \ln r + C_3, \tag{4.21}$$

where C_3 is an integration constant. From Eq. (4.20), the thermal hoop and axial stresses are obtained as

$$\sigma_\theta = \sigma_z = k_1 \sigma_Y \left(1 + \ln r\right) + C_3. \tag{4.22}$$

The plastic incompressibility provides

$$\varepsilon_\theta^p + \varepsilon_r^p + \varepsilon_0^p = 0. \tag{4.23}$$

Thus, the sum of the total radial, hoop and axial strains are given by the sum of their elastic parts only. Hence,

$$\varepsilon_\theta + \varepsilon_r + \varepsilon_0 = \varepsilon_\theta^e + \varepsilon_r^e + \varepsilon_0^e. \tag{4.24}$$

The elastic components of strains are given by generalized Hook's law and thus Eq. (4.24) provides

$$E\left(\varepsilon_\theta + \varepsilon_r + \varepsilon_0\right) = \left(1 - 2\nu\right)\left(\sigma_r + \sigma_\theta + \sigma_z\right) + 3E\alpha T. \tag{4.25}$$

Using Eq. (3.4) in Eq. (4.25), the following differential equation is obtained:

$$\frac{\mathrm{d}u}{\mathrm{d}r} + \frac{u}{r} = \frac{1 - 2\nu}{E}\left(\sigma_r + \sigma_\theta + \sigma_z\right) + 3\alpha T - \varepsilon_0. \tag{4.26}$$

Inserting Eqs. (4.21) and (4.22) in Eq. (4.26) and then solving it, the solution for radial displacement is obtained as

$$u=\frac{1-2\nu}{E}\left\{\frac{k_1\sigma_Y}{2}r\left(\frac{1}{2}+3\ln r\right)+\frac{3}{2}C_3r\right\}+\frac{3}{2}\alpha T_a r+\frac{3\alpha\left(T_b-T_a\right)}{\ln\left(\frac{b}{a}\right)}\frac{r}{2}\left\{\ln\left(\frac{r}{a}\right)-\frac{1}{2}\right\}-\frac{r}{2}\varepsilon_0+\frac{C_4}{r}. \tag{4.27}$$

where C_4 is an integration constant.

Knowing the expression of u, the expression for total hoop and radial strain component can easily be obtained by using strain-displacement relations (Eq. 3.4). Thus, the expression for total hoop and radial strains are obtained as

$$\varepsilon_\theta=\frac{u}{r}=\frac{1-2\nu}{E}\left[\frac{k_1\sigma_Y}{2}\left(\frac{1}{2}+3\ln r\right)+\frac{3}{2}C_3\right]+\frac{3}{2}\alpha T_a+\frac{3\alpha\left(T_b-T_a\right)}{2\ln\left(\frac{b}{a}\right)}\left\{\ln\left(\frac{r}{a}\right)-\frac{1}{2}\right\}-\frac{1}{2}\varepsilon_0+\frac{C_4}{r^2}, \tag{4.28}$$

$$\varepsilon_r=\frac{\mathrm{d}u}{\mathrm{d}r}=\frac{1-2\nu}{E}\left[\frac{k_1\sigma_Y}{2}\left\{\frac{7}{2}+3\ln r\right\}+\frac{3}{2}C_3\right]+\frac{3}{2}\alpha T_a+\frac{3\alpha\left(T_b-T_a\right)}{2\ln\left(\frac{b}{a}\right)}\left\{1+\ln\left(\frac{r}{a}\right)-\frac{1}{2}\right\}-\frac{1}{2}\varepsilon_0-\frac{C_4}{r^2}. \tag{4.29}$$

The plastic part of the strain components are evaluated by subtracting the elastic and thermal parts from the total strain components. The elastic and thermal parts of strain components are given by generalized Hook's law. Thus,

$$\varepsilon_\theta^p=\varepsilon_\theta-\varepsilon_\theta^e=\varepsilon_\theta-\frac{1}{E}\left\{\sigma_\theta-\nu\left(\sigma_r+\sigma_z\right)\right\}-\alpha T_a-\alpha\left(T_b-T_a\right)\frac{\ln\left(\frac{r}{a}\right)}{\ln\left(\frac{b}{a}\right)}, \tag{4.30}$$

$$\varepsilon_r^p=\varepsilon_r-\varepsilon_r^e=\varepsilon_r-\frac{1}{E}\left\{\sigma_r-\nu\left(\sigma_\theta+\sigma_z\right)\right\}-\alpha T_a-\alpha\left(T_b-T_a\right)\frac{\ln\left(\frac{r}{a}\right)}{\ln\left(\frac{b}{a}\right)}, \tag{4.31}$$

$$\varepsilon_z^p=\varepsilon_0^p=\varepsilon_0-\varepsilon_z^e=\varepsilon_0-\frac{1}{E}\left\{\sigma_z-\nu\left(\sigma_r+\sigma_\theta\right)\right\}-\alpha T_a-\alpha\left(T_b-T_a\right)\frac{\ln\left(\frac{r}{a}\right)}{\ln\left(\frac{b}{a}\right)}. \tag{4.32}$$

Substituting the stress components, σ_r, σ_θ and σ_z from Eqs. (4.21) and (4.22) in Eqs. (4.30)–(4.32), the resulting plastic part of strain components in the plastic zone I are obtained as

$$\varepsilon_\theta^p = \frac{1-2\nu}{E}\left\{\frac{1}{2}\left(k_1\sigma_Y \ln r + C_3\right)\right\} - \frac{3-2\nu}{4E}k_1\sigma_Y + \frac{1}{2}\alpha T_a + \frac{\alpha\left(T_b-T_a\right)}{2\ln\left(\frac{b}{a}\right)}\left\{\ln\left(\frac{r}{a}\right) - \frac{3}{2}\right\} - \frac{1}{2}\varepsilon_0 + \frac{C_4}{r^2}, \tag{4.33}$$

$$\varepsilon_r^p = \frac{1-2\nu}{E}\left\{\frac{1}{2}\left(k_1\sigma_Y \ln r + C_3\right)\right\} + \frac{7-6\nu}{4E}k_1\sigma_Y + \frac{1}{2}\alpha T_a + \frac{\alpha\left(T_b-T_a\right)}{2\ln\left(\frac{b}{a}\right)}\left\{\ln\left(\frac{r}{a}\right) + \frac{3}{2}\right\} - \frac{1}{2}\varepsilon_0 - \frac{C_4}{r^2}, \tag{4.34}$$

$$\varepsilon_z^p = \varepsilon_0^p = \varepsilon_0 - \frac{1-2\nu}{E}\left\{k_1\sigma_Y \ln r + C_3\right\} - \frac{1-\nu}{E}k_1\sigma_Y - \alpha T_a - \alpha\left(T_b - T_a\right)\frac{\ln\left(\frac{r}{a}\right)}{\ln\left(\frac{b}{a}\right)}. \tag{4.35}$$

4.2.3.2 Plastic zone II: c≤r≤d

According to the inequality $\sigma_z > \sigma_\theta > \sigma_r$, plastic zone II: $c \le r \le d$ is developed within the wall of the cylinder simultaneously with the plastic zone I. The radius d is known as the radius of elastic-plastic interface. In this case, the Tresca's yield criterion takes the form

$$\sigma_z - \sigma_r = k_1\sigma_Y. \tag{4.36}$$

From Tresca's associated flow rule,

$$\mathrm{d}\varepsilon_r^p = -\mathrm{d}\varepsilon_{0,}^p \quad \mathrm{d}\varepsilon_\theta^p = 0. \tag{4.37}$$

Hence, hoop strain component is entirely elastic, *i.e.*, $\varepsilon_\theta = \varepsilon_\theta^e$. The radial strain component is given by

$$\varepsilon_r = \varepsilon_r^e + \varepsilon_0^e - \varepsilon_0. \tag{4.38}$$

The strain compatibility relation (Eq. 3.5) can be expressed as

$$\varepsilon_r^e + \varepsilon_0^e - \varepsilon_0 = \frac{\mathrm{d}}{\mathrm{d}r}\left(\varepsilon_\theta^e r\right). \tag{4.39}$$

The elastic part of strains is given by the generalized Hook's law. Using Eq. (4.36), in the generalized Hook's law and inserting it into Eq. (4.39) one obtains

$$\frac{2\sigma_r}{E} - \frac{2\nu}{E}\left\{\sigma_\theta + \sigma_r - \frac{\mathrm{d}}{\mathrm{d}r}(r\sigma_r)\right\} - \frac{\sigma_\theta}{E} - \frac{r}{E}\frac{\mathrm{d}\sigma_\theta}{\mathrm{d}r} + \frac{1}{E}k_1\sigma_Y = \varepsilon_0 - \alpha T_a - \alpha(T_b - T_a)\frac{\ln\left(\frac{r}{a}\right)}{\ln\left(\frac{b}{a}\right)} + \alpha\frac{(T_b - T_a)}{\ln\left(\frac{b}{a}\right)}. \tag{4.40}$$

Using equilibrium equation (Eq. 3.6) in Eq. (4.40), the following differential equation is obtained:

$$\frac{r^2}{E}\frac{\mathrm{d}^2\sigma_r}{\mathrm{d}r^2} + \frac{3r}{E}\frac{\mathrm{d}\sigma_r}{\mathrm{d}r} - \frac{1-2\nu}{E}\sigma_r = \frac{1}{E}k_1\sigma_Y + \alpha T_a + \alpha(T_b - T_a)\frac{\ln\left(\frac{r}{a}\right)}{\ln\left(\frac{b}{a}\right)} - \alpha\frac{(T_b - T_a)}{\ln\left(\frac{b}{a}\right)} - \varepsilon_0. \tag{4.41}$$

Eq. (4.41) is a second order linear non-homogeneous differential equation with varying coefficients in σ_r. The procedure for obtaining the solution of Eq. (4.41) is described in Appendix C, which provides the radial stress distributions in the plastic zone II as

$$\sigma_r = C_5 r^{-1+\sqrt{2(1-\nu)}} + C_6 r^{-1-\sqrt{2(1-\nu)}} + \frac{k_1\sigma_Y}{(2\nu-1)} + \frac{E\alpha T_a}{(2\nu-1)} + \frac{E\alpha(T_b - T_a)}{(2\nu-1)\ln\left(\frac{b}{a}\right)}\left\{\ln\left(\frac{r}{a}\right) - \frac{2\nu+1}{2\nu-1}\right\} - \frac{E\varepsilon_0}{(2\nu-1)}, \tag{4.42}$$

where C_5 and C_6 are constants. Using equilibrium equation (Eq. 3.6), the hoop stress distribution is obtained as

$$\sigma_\theta = C_5\sqrt{2(1-\nu)}\,r^{\sqrt{2(1-\nu)}-1} - C_6\sqrt{2(1-\nu)}\,r^{-\sqrt{2(1-\nu)}-1} + \frac{k_1\sigma_Y}{(2\nu-1)} + \frac{E\alpha T_a}{(2\nu-1)} + \frac{E\alpha(T_b - T_a)}{(2\nu-1)\ln\left(\frac{b}{a}\right)}\left\{\ln\left(\frac{r}{a}\right) - \frac{2}{2\nu-1}\right\} - \frac{E\varepsilon_0}{(2\nu-1)}. \tag{4.43}$$

Knowing the expression for σ_r from Eq. (4.42), the solution for axial stress can be obtained using Tresca's yield criterion (Eq. 4.36) as

$$\sigma_z = C_5 r^{-1+\sqrt{2(1-\nu)}} + C_6 r^{-1-\sqrt{2(1-\nu)}} + \left(\frac{2\nu}{2\nu-1}\right) k_1 \sigma_Y + \frac{E\alpha T_a}{(2\nu-1)} + \frac{E\alpha (T_b - T_a)}{(2\nu-1)\ln\left(\frac{b}{a}\right)} \left\{ \ln\left(\frac{r}{a}\right) - \frac{2\nu+1}{2\nu-1} \right\} - \frac{E\varepsilon_0}{(2\nu-1)}. \qquad (4.44)$$

The radial plastic strain field is given by

$$\varepsilon_r^p = -\varepsilon_0^p = \varepsilon_0^e - \varepsilon_0. \qquad (4.45)$$

In Eq. (4.45), ε_0^e is given by Eq. (4.3). Using ε_0^e in Eq. (4.45) and inserting σ_r, σ_θ, σ_z from Eqs. (4.42)– (4.44) in the resulting expression, the plastic part of radial strain component is obtained as

$$\varepsilon_r^p = \frac{C_5}{E} r^{-1+\sqrt{2(1-\nu)}} \left\{ 1-\nu-\nu\sqrt{2(1-\nu)} \right\} + \frac{C_6}{E} r^{-1-\sqrt{2(1-\nu)}} \left\{ 1-\nu+\nu\sqrt{2(1-\nu)} \right\} + \frac{\alpha (T_b - T_a)}{\ln\left(\frac{b}{a}\right)} \frac{(1+\nu)}{(2\nu-1)}. \qquad (4.46)$$

4.2.3.3 Elastic zone: $d \le r \le b$

The elastic radial, hoop and axial stress distributions in the elastic zone, $d \le r \le b$ are represented by Eqs. (4.7), (4.8) and (4.4), respectively. The constants C_1 and C_2 in Eqs. (4.7) and (4.8) are evaluated using the following boundary conditions:

The yielding condition at the elastic-plastic interface $r = d$,

$$\left(\sigma_z - \sigma_r\right)\Big|_{r=d} = k_1 \sigma_Y \qquad (4.47)$$

and the vanishing radial stress at the outer radius, *i.e.*,

$$\left(\sigma_r\right)_{r=b} = 0. \qquad (4.48)$$

The use of boundary conditions given by Eqs. (4.47) and (4.48) provides the constants C_1 and C_2 as

$$\begin{aligned}
C_1 = {} & \frac{\alpha(1+\nu)(1-2\nu)}{2(1-\nu)}T_a + \frac{\alpha(1+\nu)(1-2\nu)}{2(1-\nu)}\frac{(T_b-T_a)}{\ln\left(\frac{b}{a}\right)}\left\{\ln\left(\frac{b}{a}\right)-\frac{1}{2}\right\} \\
& -\nu\varepsilon_0 + \frac{(1+\nu)(1-2\nu)}{E}\left\{\frac{d^2}{b^2+d^2(2\nu-1)}\right\}k_1\sigma_Y \\
& +(1+\nu)(1-2\nu)\left\{\frac{d^2}{b^2+d^2(2\nu-1)}\right\}\alpha T_a-(1+\nu)(1-2\nu)\left\{\frac{d^2}{b^2+d^2(2\nu-1)}\right\}\varepsilon_0 \\
& -\frac{\alpha(1+\nu)(1-2\nu)}{2(1-\nu)}\frac{(T_b-T_a)}{\ln\left(\frac{b}{a}\right)}\left\{\frac{d^2}{b^2+d^2(2\nu-1)}\right\}\left\{\ln\left(\frac{b}{a}\right)(2\nu-1)-\nu-\ln\left(\frac{d}{a}\right)\right\},
\end{aligned} \tag{4.49}$$

$$\begin{aligned}
C_2 = {} & \frac{(1+\nu)}{E}\left\{\frac{b^2d^2}{b^2+d^2(2\nu-1)}\right\}k_1\sigma_Y+(1+\nu)\left\{\frac{b^2d^2}{b^2+d^2(2\nu-1)}\right\}\alpha T_a-(1+\nu)\left\{\frac{b^2d^2}{b^2+d^2(2\nu-1)}\right\}\varepsilon_0 \\
& -\frac{\alpha(1+\nu)}{2(1-\nu)}\frac{(T_b-T_a)}{\ln\left(\frac{b}{a}\right)}\left\{\frac{b^2d^2}{b^2+d^2(2\nu-1)}\right\}\left\{\ln\left(\frac{b}{a}\right)(2\nu-1)-\nu-\ln\left(\frac{d}{a}\right)\right\}.
\end{aligned} \tag{4.50}$$

Substituting the values of C_1 and C_2 in Eqs. (4.7) and (4.8), the resulting elastic radial and hoop stress distributions in the elastic zone are obtained as

$$\begin{aligned}
\sigma_r = {} & \frac{E\alpha}{2(1-\nu)}\frac{(T_b-T_a)}{\ln\left(\frac{b}{a}\right)}\left[\ln\left(\frac{b}{r}\right)-\left\{\frac{d^2}{b^2+d^2(2\nu-1)}\right\}\left\{\ln\left(\frac{b}{a}\right)(2\nu-1)-\nu-\ln\left(\frac{d}{a}\right)\right\}\left(1-\frac{b^2}{r^2}\right)\right] \\
& +\left\{\frac{d^2}{b^2+d^2(2\nu-1)}\right\}k_1\sigma_Y\left(1-\frac{b^2}{r^2}\right)+\left\{\frac{d^2}{b^2+d^2(2\nu-1)}\right\}E\alpha T_a\left(1-\frac{b^2}{r^2}\right) \\
& -\left\{\frac{d^2}{b^2+d^2(2\nu-1)}\right\}E\varepsilon_0\left(1-\frac{b^2}{r^2}\right),
\end{aligned} \tag{4.51}$$

$$\begin{aligned}
\sigma_\theta = {} & \frac{E\alpha}{2(1-\nu)}\frac{(T_b-T_a)}{\ln\left(\frac{b}{a}\right)}\left[\ln\left(\frac{b}{r}\right)-1-\left\{\frac{d^2}{b^2+d^2(2\nu-1)}\right\}\left\{\ln\left(\frac{b}{a}\right)(2\nu-1)-\nu-\ln\left(\frac{d}{a}\right)\right\}\left(1+\frac{b^2}{r^2}\right)\right] \\
& +\left\{\frac{d^2}{b^2+d^2(2\nu-1)}\right\}k_1\sigma_Y\left(1+\frac{b^2}{r^2}\right)+\left\{\frac{d^2}{b^2+d^2(2\nu-1)}\right\}E\alpha T_a\left(1+\frac{b^2}{r^2}\right) \\
& -\left\{\frac{d^2}{b^2+d^2(2\nu-1)}\right\}E\varepsilon_0\left(1+\frac{b^2}{r^2}\right),
\end{aligned} \tag{4.52}$$

Using Eqs. (4.51) and (4.52) in Eq. (4.4), the axial stress distribution is obtained as

$$\sigma_z = \frac{E\alpha\nu}{2(1-\nu)}\frac{(T_b-T_a)}{\ln\left(\frac{b}{a}\right)}\left[2\ln\left(\frac{b}{r}\right)-1-\left\{\frac{2d^2}{b^2+d^2(2\nu-1)}\right\}\left\{\ln\left(\frac{b}{a}\right)(2\nu-1)-\nu-\ln\left(\frac{d}{a}\right)\right\}\right]$$
$$+\left\{\frac{2\nu d^2}{b^2+d^2(2\nu-1)}\right\}k_1\sigma_Y+\left\{\frac{d^2-b^2}{b^2+d^2(2\nu-1)}\right\}E\alpha T_a-\left\{\frac{d^2-b^2}{b^2+d^2(2\nu-1)}\right\}E\varepsilon_0-E\alpha(T_b-T_a)\frac{\ln\left(\frac{r}{a}\right)}{\ln\left(\frac{b}{a}\right)}. \tag{4.53}$$

The constant axial strain ε_0 for generalized plane strain involved in the different equations of stresses and strains during first stage of elasto-plastic deformation can be determined from the condition that the total axial force is zero. The constants involved in the equations, C_3, C_4, C_5 and C_6 can be determined using the boundary conditions. The determination of ε_0 and the constants is provided in Section 4.2.5.

4.2.4 Residual Stress Distribution in the First Stage of Elasto-plastic Deformation

Residual thermal stresses are set up in the cylinder when the temperature gradient between the outer and inner wall of the cylinder is released. The unloading process is assumed to be completely elastic. Thus, the residual thermal stresses in different zones are obtained by subtracting Eqs. (4.11), (4.12) and (4.16) from the respective equations of radial, hoop and axial stresses in different zones. The expressions for residual thermal stresses in different zones are given as follows:

Elastic zone, $d \leq r \leq b$:

$$(\sigma_r)_{res} = \frac{E\alpha}{2(1-\nu)}\frac{(T_b-T_a)}{\ln\left(\frac{b}{a}\right)}\left[\ln\left(\frac{b}{a}\right)-\ln\left(\frac{b}{a}\right)\left(1-\frac{a^2}{r^2}\right)\frac{b^2}{b^2-a^2}-\left\{\frac{d^2}{b^2+d^2(2\nu-1)}\right\}\left\{\ln\left(\frac{b}{a}\right)(2\nu-1)-\nu-\ln\left(\frac{d}{a}\right)\right\}\left(1-\frac{b^2}{r^2}\right)\right] \tag{4.54}$$
$$+\left\{\frac{d^2}{b^2+d^2(2\nu-1)}\right\}k_1\sigma_Y\left(1-\frac{b^2}{r^2}\right)+\left\{\frac{d^2}{b^2+d^2(2\nu-1)}\right\}E\alpha T_a-\left\{\frac{d^2}{b^2+d^2(2\nu-1)}\right\}E\varepsilon_0\left(1-\frac{b^2}{r^2}\right),$$

$$(\sigma_\theta)_{res} = \frac{E\alpha}{2(1-\nu)}\frac{(T_b-T_a)}{\ln\left(\frac{b}{a}\right)}\left[\ln\left(\frac{b}{a}\right)-\ln\left(\frac{b}{a}\right)\left(1+\frac{a^2}{r^2}\right)\frac{b^2}{b^2-a^2}-\left\{\frac{d^2}{b^2+d^2(2\nu-1)}\right\}\left\{\ln\left(\frac{b}{a}\right)(2\nu-1)-\nu-\ln\left(\frac{d}{a}\right)\right\}\left(1+\frac{b^2}{r^2}\right)\right] \tag{4.55}$$
$$+\left\{\frac{d^2}{b^2+d^2(2\nu-1)}\right\}k_1\sigma_Y\left(1+\frac{b^2}{r^2}\right)+\left\{\frac{d^2}{b^2+d^2(2\nu-1)}\right\}E\alpha T_a\left(1+\frac{b^2}{r^2}\right)-\left\{\frac{d^2}{b^2+d^2(2\nu-1)}\right\}E\varepsilon_0\left(1+\frac{b^2}{r^2}\right),$$

$$(\sigma_z)_{res}=\frac{E\alpha}{2(1-\nu)}\frac{(T_b-T_a)}{\ln\left(\frac{b}{a}\right)}\left[1+2\ln\left(\frac{r}{a}\right)-\ln\left(\frac{b}{a}\right)\frac{2b^2}{b^2-a^2}+2\nu\ln\left(\frac{b}{r}\right)-\nu-\left\{\frac{2\nu d^2}{b^2+d^2(2\nu-1)}\right\}\left\{\ln\left(\frac{b}{a}\right)(2\nu-1)-\nu-\ln\left(\frac{d}{a}\right)\right\}\right]$$
$$+\left\{\frac{2\nu d^2}{b^2+d^2(2\nu-1)}\right\}k_1\sigma_Y+\left\{\frac{d^2-b^2}{b^2+d^2(2\nu-1)}\right\}E\alpha T_a-\left\{\frac{d^2-b^2}{b^2+d^2(2\nu-1)}\right\}E\varepsilon_0-E\alpha(T_b-T_a)\frac{\ln\left(\frac{r}{a}\right)}{\ln\left(\frac{b}{a}\right)}. \tag{4.56}$$

Plastic zone I, *a≤r≤c:*

$$(\sigma_r)_{res}=k_1\sigma_Y\ln r+C_3+\frac{E\alpha(T_b-T_a)}{2(1-\nu)\ln\left(\frac{b}{a}\right)}\left\{\ln\left(\frac{r}{a}\right)-\ln\left(\frac{b}{a}\right)\left(1-\frac{a^2}{r^2}\right)\frac{b^2}{b^2-a^2}\right\}, \tag{4.57}$$

$$(\sigma_\theta)_{res}=k_1\sigma_Y(1+\ln r)+C_3+\frac{E\alpha(T_b-T_a)}{2(1-\nu)\ln\left(\frac{b}{a}\right)}\left\{1+\ln\left(\frac{r}{a}\right)-\ln\left(\frac{b}{a}\right)\left(1+\frac{a^2}{r^2}\right)\frac{b^2}{b^2-a^2}\right\}, \tag{4.58}$$

$$(\sigma_z)_{res}=k_1\sigma_Y(1+\ln r)+C_3+\frac{E\alpha(T_b-T_a)}{2(1-\nu)\ln\left(\frac{b}{a}\right)}\left\{1+2\ln\left(\frac{r}{a}\right)-\ln\left(\frac{b}{a}\right)\frac{2b^2}{b^2-a^2}\right\}. \tag{4.59}$$

Plastic zone II, *c≤r≤d:*

$$(\sigma_r)_{res}=C_5r^{-1+\sqrt{2(1-\nu)}}+C_6r^{-1-\sqrt{2(1-\nu)}}+\frac{k_1\sigma_Y}{(2\nu-1)}+\frac{E\alpha T_a}{(2\nu-1)}+\frac{E\alpha(T_b-T_a)}{(2\nu-1)\ln\left(\frac{b}{a}\right)}\left\{\ln\left(\frac{r}{a}\right)-\frac{2\nu+1}{2\nu-1}\right\}$$
$$-\frac{E\varepsilon_0}{(2\nu-1)}+\frac{E\alpha(T_b-T_a)}{2(1-\nu)\ln\left(\frac{b}{a}\right)}\left\{\ln\left(\frac{r}{a}\right)-\ln\left(\frac{b}{a}\right)\left(1-\frac{a^2}{r^2}\right)\frac{b^2}{b^2-a^2}\right\}, \tag{4.60}$$

$$(\sigma_\theta)_{res}=C_5\sqrt{2(1-\nu)}\,r^{\sqrt{2(1-\nu)}-1}-C_6\sqrt{2(1-\nu)}\,r^{-\sqrt{2(1-\nu)}-1}+\frac{k_1\sigma_Y}{(2\nu-1)}$$
$$+\frac{E\alpha T_a}{(2\nu-1)}+\frac{E\alpha(T_b-T_a)}{(2\nu-1)\ln\left(\frac{b}{a}\right)}\left\{\ln\left(\frac{r}{a}\right)-\frac{2}{2\nu-1}\right\}$$
$$-\frac{E\varepsilon_0}{(2\nu-1)}+\frac{E\alpha(T_b-T_a)}{2(1-\nu)\ln\left(\frac{b}{a}\right)}\left\{1+\ln\left(\frac{r}{a}\right)-\ln\left(\frac{b}{a}\right)\left(1+\frac{a^2}{r^2}\right)\frac{b^2}{b^2-a^2}\right\}, \tag{4.61}$$

$$
\begin{aligned}
(\sigma_z)_{res} &= C_5 r^{-1+\sqrt{2(1-\nu)}} + C_6 r^{-1-\sqrt{2(1-\nu)}} + \left(\frac{2\nu}{2\nu-1}\right) k_1 \sigma_Y + \frac{E\alpha T_a}{(2\nu-1)} + \frac{E\alpha(T_b-T_a)}{(2\nu-1)\ln\left(\frac{b}{a}\right)}\left\{\ln\left(\frac{r}{a}\right) - \frac{2\nu+1}{2\nu-1}\right\} \\
&\quad - \frac{E\varepsilon_0}{(2\nu-1)} + \frac{E\alpha(T_b-T_a)}{2(1-\nu)\ln\left(\frac{b}{a}\right)}\left\{1 + 2\ln\left(\frac{r}{a}\right) - \ln\left(\frac{b}{a}\right)\frac{2b^2}{b^2-a^2}\right\}.
\end{aligned} \tag{4.62}
$$

4.2.5 Evaluation of Constants and Solution Methodology for the First Stage of Elasto-plastic Deformation

The interface radii *c* & *d* and constant axial strain ε_0 are unknown in the first stage of elasto-plastic deformation. Also, the constants— C_3, C_4, C_5 and C_6 are not known. The constants can be evaluated by using the boundary conditions:

(i) At the radius of elastic-plastic interface, $r=d$

$$\sigma_r^{(\text{plastic zone II})} = \sigma_r^{(\text{elastic zone})}, \quad \varepsilon_r^{p(\text{plastic zone II})} = 0. \tag{4.63}$$

(ii) At $r=c$,

$$\sigma_r^{(\text{plastic zone I})} = \sigma_r^{(\text{plastic zone II})}, \quad \varepsilon_\theta^{p(\text{plastic zone I})} = \varepsilon_\theta^{p(\text{plastic zone II})}. \tag{4.64}$$

Substituting Eqs. (4.42), (4.51) and (4.46) in boundary conditions given by Eq. (4.63) and solving them together provides

$$C_5 = Q + \frac{2\nu b^2}{(2\nu-1)\left\{b^2 + d^2(2\nu-1)\right\}} d^{1-\sqrt{2(1-\nu)}} \left\{\frac{1-\nu+\nu\sqrt{2(1-\nu)}}{2\nu\sqrt{2(1-\nu)}}\right\} E\varepsilon_0, \tag{4.65}$$

$$C_6 = P - \frac{2\nu b^2}{(2\nu-1)\left\{b^2 + d^2(2\nu-1)\right\}} \left\{\frac{1-\nu-\nu\sqrt{2(1-\nu)}}{d^{-1-\sqrt{2(1-\nu)}}\, 2\nu\sqrt{2(1-\nu)}}\right\} E\varepsilon_0, \tag{4.66}$$

where

$$\begin{aligned}P=&\frac{E\alpha(T_b-T_a)}{(2\nu-1)\ln\left(\frac{b}{a}\right)}\left\{\frac{1-\nu-\nu\sqrt{2(1-\nu)}}{d^{-1-\sqrt{2(1-\nu)}}2\nu\sqrt{2(1-\nu)}}\right\}\left\{\ln\left(\frac{d}{a}\right)-\frac{2\nu+1}{2\nu-1}-\frac{(1+\nu)}{1-\nu-\nu\sqrt{2(1-\nu)}}\right\}\\&-\frac{E\alpha}{2(1-\nu)}\frac{(T_b-T_a)}{\ln\left(\frac{b}{a}\right)}\left\{\frac{1-\nu-\nu\sqrt{2(1-\nu)}}{d^{-1-\sqrt{2(1-\nu)}}2\nu\sqrt{2(1-\nu)}}\right\}\left[\ln\left(\frac{b}{d}\right)+\left\{\frac{b^2-d^2}{b^2+d^2(2\nu-1)}\right\}\left\{\ln\left(\frac{b}{a}\right)(2\nu-1)-\nu-\ln\left(\frac{d}{a}\right)\right\}\right]\\&+\frac{2\nu b^2}{(2\nu-1)\{b^2+d^2(2\nu-1)\}}\left\{\frac{1-\nu-\nu\sqrt{2(1-\nu)}}{d^{-1-\sqrt{2(1-\nu)}}2\nu\sqrt{2(1-\nu)}}\right\}k_1\sigma_Y+\frac{2\nu b^2}{(2\nu-1)\{b^2+d^2(2\nu-1)\}}\left\{\frac{1-\nu-\nu\sqrt{2(1-\nu)}}{d^{-1-\sqrt{2(1-\nu)}}2\nu\sqrt{2(1-\nu)}}\right\}E\alpha T_a,\end{aligned}\tag{4.67}$$

and

$$Q=-Pd^{-2\sqrt{2(1-\nu)}}\left\{\frac{1-\nu+\nu\sqrt{2(1-\nu)}}{1-\nu-\nu\sqrt{2(1-\nu)}}\right\}-\frac{E\alpha(T_b-T_a)}{(2\nu-1)\ln\left(\frac{b}{a}\right)}\frac{(1+\nu)}{d^{-1+\sqrt{2(1-\nu)}}\left\{1-\nu-\nu\sqrt{2(1-\nu)}\right\}}.\tag{4.68}$$

Using Eqs. (4.21) and (4.42) in the first condition of Eq. (4.64) gives

$$C_3=R+\left[\begin{aligned}&\frac{2\nu b^2c^{-1+\sqrt{2(1-\nu)}}}{(2\nu-1)\{b^2+d^2(2\nu-1)\}}d^{1-\sqrt{2(1-\nu)}}\left\{\frac{1-\nu+\nu\sqrt{2(1-\nu)}}{2\nu\sqrt{2(1-\nu)}}\right\}\\&-\frac{2\nu b^2c^{-1-\sqrt{2(1-\nu)}}}{(2\nu-1)\{b^2+d^2(2\nu-1)\}}\left\{\frac{1-\nu-\nu\sqrt{2(1-\nu)}}{d^{-1-\sqrt{2(1-\nu)}}2\nu\sqrt{2(1-\nu)}}\right\}-\frac{1}{(2\nu-1)}\end{aligned}\right]E\varepsilon_0,\tag{4.69}$$

where

$$\begin{aligned}R=&Qc^{-1+\sqrt{2(1-\nu)}}-k_1\sigma_Y\ln c+Pc^{-1-\sqrt{2(1-\nu)}}+\frac{k_1\sigma_Y}{(2\nu-1)}+\frac{E\alpha T_a}{(2\nu-1)}\\&+\frac{E\alpha(T_b-T_a)}{(2\nu-1)\ln\left(\frac{b}{a}\right)}\ln\left(\frac{c}{a}\right)-\frac{2E\alpha(T_b-T_a)}{(2\nu-1)^2\ln\left(\frac{b}{a}\right)}-\frac{E\alpha(T_b-T_a)}{(2\nu-1)\ln\left(\frac{b}{a}\right)},\end{aligned}\tag{4.70}$$

Using Eq. (4.33) and second relation of Eq. (4.37) in the second condition of Eq. (4.64), the constant C_4 is obtained as

$$C_4 = \frac{1-2\nu}{E}\left[-\frac{c^2}{2}\left(k_1\sigma_Y \ln c + C_3\right)\right] + \frac{3-2\nu}{4E}c^2 k_1\sigma_Y - \frac{1}{2}c^2\alpha T_a - \frac{\alpha\left(T_b - T_a\right)}{2\ln\left(\frac{b}{a}\right)}\left\{c^2\ln\left(\frac{c}{a}\right) - \frac{3c^2}{2}\right\} + \frac{c^2}{2}\varepsilon_0. \tag{4.71}$$

The constant axial strain ε_0 is obtained by using free end condition (zero total axial force) given by

$$\left[\int_a^c \sigma_z^{\text{(plastic zone I)}} r\mathrm{d}r + \int_c^d \sigma_z^{\text{(plastic zone II)}} r\mathrm{d}r + \int_d^b \sigma_z^{\text{(elastic zone)}} r\mathrm{d}r\right] = 0. \tag{4.72}$$

Inserting the expressions of σ_z from first plastic I, plastic zone II and elastic zone in Eq. (4.72), the constant axial strain during first stage of elasto-plastic deformation is obtained as

$$\begin{aligned}
\varepsilon_0 = {} & \frac{k_1\sigma_Y}{AE}\left\{\ln c\frac{c^2}{2} - \ln a\frac{a^2}{2} + \frac{1}{4}\left(c^2 - a^2\right) + \frac{\nu\left(d^2 - c^2\right)}{2\nu - 1} + \frac{\nu d^2\left(b^2 - d^2\right)}{b^2 + d^2\left(2\nu - 1\right)}\right\} + \frac{R}{AE}\left(\frac{c^2 - a^2}{2}\right) \\
& + \frac{Q}{AE}\left\{\frac{d^{1+\sqrt{2(1-\nu)}} - c^{1+\sqrt{2(1-\nu)}}}{1+\sqrt{2(1-\nu)}}\right\} + \frac{P}{AE}\left\{\frac{d^{1-\sqrt{2(1-\nu)}} - c^{1-\sqrt{2(1-\nu)}}}{1-\sqrt{2(1-\nu)}}\right\} + \frac{\alpha T_a}{A}\left[\frac{d^2 - c^2}{2(2\nu - 1)} - \frac{\left(b^2 - d^2\right)^2}{2\left\{b^2 + d^2\left(2\nu - 1\right)\right\}}\right] \\
& + \frac{\alpha\left(T_b - T_a\right)}{\left(2\nu - 1\right)\ln\left(\frac{b}{a}\right)A}\left\{\ln\left(\frac{d}{a}\right)\frac{d^2}{2} - \ln\left(\frac{c}{a}\right)\frac{c^2}{2} - \frac{1}{2}\left(d^2 - c^2\right)\frac{6\nu + 1}{2\left(2\nu - 1\right)}\right\} \\
& + \frac{\alpha}{2(1-\nu)}\frac{\left(T_b - T_a\right)}{\ln\left(\frac{b}{a}\right)A}\left[\begin{array}{l} -\nu d^2\ln\left(\frac{b}{d}\right) - \left\{\frac{\nu d^2\left(b^2 - d^2\right)}{b^2 + d^2\left(2\nu - 1\right)}\right\}\left\{\ln\left(\frac{b}{a}\right)\left(2\nu - 1\right) - \nu - \ln\left(\frac{d}{a}\right)\right\} \\ -2(1-\nu)\left\{\ln\left(\frac{b}{a}\right)\frac{b^2}{2} - \ln\left(\frac{d}{a}\right)\frac{d^2}{2} - \frac{1}{4}\left(b^2 - d^2\right)\right\} \end{array}\right],
\end{aligned} \tag{4.73}$$

where

$$
\begin{aligned}
A = {} & \frac{d^2 - c^2}{2(2\nu - 1)} - \frac{\left(b^2 - d^2\right)^2}{2\left\{b^2 + d^2(2\nu - 1)\right\}} \\
& -\left(\frac{c^2 - a^2}{2}\right)\left\{\frac{2\nu b^2}{(2\nu - 1)\left\{b^2 + d^2(2\nu - 1)\right\}2\nu\sqrt{2(1-\nu)}}\left(\begin{array}{l}\left(\frac{c}{d}\right)^{-1+\sqrt{2(1-\nu)}}\left(1-\nu+\nu\sqrt{2(1-\nu)}\right) \\ -\left(\frac{c}{d}\right)^{-1-\sqrt{2(1-\nu)}}\left(1-\nu-\nu\sqrt{2(1-\nu)}\right)\end{array}\right) - \frac{1}{(2\nu - 1)}\right\} \\
& -\left\{\frac{d^{1+\sqrt{2(1-\nu)}} - c^{1+\sqrt{2(1-\nu)}}}{1+\sqrt{2(1-\nu)}}\right\}\frac{2\nu b^2}{(2\nu - 1)\left\{b^2 + d^2(2\nu - 1)\right\}}d^{1-\sqrt{2(1-\nu)}}\left\{\frac{1-\nu+\nu\sqrt{2(1-\nu)}}{2\nu\sqrt{2(1-\nu)}}\right\} \\
& +\left\{\frac{d^{1-\sqrt{2(1-\nu)}} - c^{1-\sqrt{2(1-\nu)}}}{1-\sqrt{2(1-\nu)}}\right\}\frac{2\nu b^2}{(2\nu - 1)\left\{b^2 + d^2(2\nu - 1)\right\}}\left\{\frac{1-\nu-\nu\sqrt{2(1-\nu)}}{d^{-1-\sqrt{2(1-\nu)}}2\nu\sqrt{2(1-\nu)}}\right\}.
\end{aligned}
\tag{4.74}
$$

To find out the values of the boundary radii, *c* and *d*, the boundary conditions of vanishing radial stress at the inner radius and $\sigma_\theta^{(\text{plastic zone II})} = \sigma_z^{(\text{plastic zone II})}$ at *r*=*c* are used. These provide

$$k_1\sigma_Y \ln a + C_3 = 0, \tag{4.75}$$

$$C_5 c^{\sqrt{2(1-\nu)}-1}\left\{\sqrt{2(1-\nu)}-1\right\} - C_6 c^{-\sqrt{2(1-\nu)}-1}\left\{\sqrt{2(1-\nu)}-1\right\} + \frac{E\alpha\left(T_b - T_a\right)}{(2\nu - 1)\ln\left(\frac{b}{a}\right)} - k_1\sigma_Y = 0, \tag{4.76}$$

The Eqs. (4.75) and (4.76) are solved simultaneously using FSOLVE function in MATLAB to obtain the values of *c* and *d*.

4.2.6 Analysis of the Second Stage of Elasto-plastic Deformation

The second stage of elasto-plastic flow commences at the outer radius when the temperature difference crosses the second threshold. In this stage of elasto-plastic deformation, besides the inner plastic zones, two additional plastic zones— plastic zone III: $f \le r \le b$ and plastic zone IV: $e \le r \le f$ exists at the outer region of the cylinder. The intermediate zone, $d \le r \le e$ remains in the elastic state. The analysis of the plastic zone I and plastic zone II are same as described for the case of first stage of elasto-plastic deformation in Section 4.2.3. Only the value of constants C_3, C_4, C_5 and C_6 will change due to change of boundary conditions.

4.2.6.1 Elastic zone: d≤r≤e

The elastic stresses are given by equations (4.7), (4.8) and (4.4). In the elastic zone, *d≤r≤e*, using the boundary conditions:

$$\left.\left(\sigma_z-\sigma_r\right)\right|_{r=d}=k_1\sigma_Y, \tag{4.77}$$

and

$$\left.\left(\sigma_\theta-\sigma_r\right)\right|_{r=e}=-k_1\sigma_Y, \tag{4.78}$$

the constants C_1 and C_2 involved in Eqs. (4.7) and (4.8) are obtained as

$$C_1=-\frac{\alpha(1+\nu)}{2(1-\nu)}T_a-\frac{\alpha(1+\nu)(T_b-T_a)}{2(1-\nu)\ln\left(\dfrac{b}{a}\right)}\left\{\ln\left(\frac{d}{a}\right)+\frac{1}{2}-\frac{e^2}{2d^2}\right\}-\frac{(1+\nu)}{E}k_1\sigma_Y\left(1+\frac{e^2}{2d^2}\right)+\varepsilon_0, \tag{4.79}$$

$$C_2=\left(\frac{e^2}{2}\right)\frac{\alpha(1+\nu)(T_b-T_a)}{2(1-\nu)\ln\left(\dfrac{b}{a}\right)}-\frac{(1+\nu)}{E}\left(\frac{e^2}{2}\right)k_1\sigma_Y. \tag{4.80}$$

Substituting the expressions of C_1 and C_2 in Eqs. (4.7) and (4.8), the resulting elastic radial and hoop stresses are obtained as

$$\begin{aligned}\sigma_r={}&\frac{E\alpha}{(2\nu-1)}T_a+\frac{E\alpha(T_b-T_a)}{2(1-\nu)\ln\left(\dfrac{b}{a}\right)}\left[\frac{1}{(2\nu-1)}\left\{\ln\left(\frac{d}{a}\right)+\frac{1}{2}-\frac{e^2}{2d^2}\right\}-\ln\left(\frac{r}{a}\right)+\frac{1}{2}-\frac{e^2}{2r^2}\right]\\&+\frac{k_1\sigma_Y}{2\nu-1}\left(1+\frac{e^2}{2d^2}\right)+\frac{e^2}{2r^2}k_1\sigma_Y+\frac{E\varepsilon_0}{(1-2\nu)},\end{aligned} \tag{4.81}$$

$$\begin{aligned}\sigma_\theta={}&\frac{E\alpha}{(2\nu-1)}T_a+\frac{E\alpha(T_b-T_a)}{2(1-\nu)\ln\left(\dfrac{b}{a}\right)}\left[\frac{1}{(2\nu-1)}\left\{\ln\left(\frac{d}{a}\right)+\frac{1}{2}-\frac{e^2}{2d^2}\right\}-\ln\left(\frac{r}{a}\right)-\frac{1}{2}+\frac{e^2}{2r^2}\right]\\&+\frac{k_1\sigma_Y}{2\nu-1}\left(1+\frac{e^2}{2d^2}\right)-\frac{e^2}{2r^2}k_1\sigma_Y+\frac{E\varepsilon_0}{(1-2\nu)}.\end{aligned} \tag{4.82}$$

Using Eqs. (4.81) and (4.82) in Eq. (4.4), the axial stress distribution is given by

$$\sigma_z=\frac{E\alpha}{(2\nu-1)}T_a+\frac{E\alpha(T_b-T_a)}{2(1-\nu)\ln\left(\frac{b}{a}\right)}\left[\frac{2\nu}{(2\nu-1)}\left\{\ln\left(\frac{d}{a}\right)+\frac{1}{2}-\frac{e^2}{2d^2}\right\}-2\ln\left(\frac{r}{a}\right)\right]$$
$$+\frac{2\nu}{2\nu-1}k_1\sigma_Y\left(1+\frac{e^2}{2d^2}\right)+\frac{E\varepsilon_0}{(1-2\nu)}. \tag{4.83}$$

4.2.6.2 Plastic zone III: $f\leq r\leq b$

In this outermost plastic zone, Tresca's yield criterion takes the form

$$\sigma_\theta-\sigma_r=-k_1\sigma_Y,\qquad \sigma_z-\sigma_r=-k_1\sigma_Y. \tag{4.84}$$

Now, following the same procedure as in Subsection 4.2.3.1, the radial, hoop and axial stress distributions in the plastic zone III are given by

$$\sigma_r=-k_1\sigma_Y\ln r+C_7, \tag{4.85}$$

$$\sigma_\theta=\sigma_z=-k_1\sigma_Y(1+\ln r)+C_7, \tag{4.86}$$

where C_7 is an integration constant.

Using the differential Eq. (4.26), the radial displacement, u is obtained as

$$u=\frac{1-2\nu}{E}\left[-\frac{k_1\sigma_Y}{2}r\left(\frac{1}{2}+3\ln r\right)+\frac{3}{2}C_7r\right]+\frac{3}{2}\alpha T_ar+\frac{3\alpha(T_b-T_a)}{\ln\left(\frac{b}{a}\right)}\frac{r}{2}\left\{\ln\left(\frac{r}{a}\right)-\frac{1}{2}\right\}-\frac{r}{2}\varepsilon_0+\frac{C_8}{r}, \tag{4.87}$$

where C_8 is an integration constant. Following a similar procedure as in Subsection 4.2.3.1, the plastic part of hoop, radial and axial strain are obtained as

$$\varepsilon_\theta^p=\frac{1-2\nu}{E}\left[\frac{1}{2}(C_7-k_1\sigma_Y\ln r)\right]+\frac{3-2\nu}{4E}k_1\sigma_Y+\frac{1}{2}\alpha T_a+\frac{\alpha(T_b-T_a)}{2\ln\left(\frac{b}{a}\right)}\left\{\ln\left(\frac{r}{a}\right)-\frac{3}{2}\right\}-\frac{1}{2}\varepsilon_0+\frac{C_8}{r^2}, \tag{4.88}$$

$$\varepsilon_r^p=\frac{1-2\nu}{E}\left[\frac{1}{2}(C_7-k_1\sigma_Y\ln r)\right]-\frac{7-6\nu}{4E}k_1\sigma_Y+\frac{1}{2}\alpha T_a+\frac{\alpha(T_b-T_a)}{2\ln\left(\frac{b}{a}\right)}\left\{\ln\left(\frac{r}{a}\right)+\frac{3}{2}\right\}-\frac{1}{2}\varepsilon_0-\frac{C_8}{r^2}, \tag{4.89}$$

$$\varepsilon_z^p = \varepsilon_0^p = \varepsilon_0 - \frac{1-2\nu}{E}\left\{-k_1\sigma_Y \ln r + C_7\right\} + \frac{1-\nu}{E}k_1\sigma_Y - \alpha T_a - \alpha\left(T_b - T_a\right)\frac{\ln\left(\dfrac{r}{a}\right)}{\ln\left(\dfrac{b}{a}\right)}. \quad (4.90)$$

4.2.6.3 Plastic zone IV: e≤r≤f

Tresca's yield criterion provides

$$\sigma_\theta - \sigma_r = -k_1\sigma_Y. \quad (4.91)$$

Using Eq. (4.91) in Eq. (3.6) and then integrating it:

$$\sigma_r = \left(\sigma_r\right)\Big|_{r=e} - k_1\sigma_Y \ln\left(\frac{r}{e}\right). \quad (4.92)$$

The value of $\left(\sigma_r\right)\Big|_{r=e}$ in Eq. (4.92) can be evaluated from the radial stress equation of elastic zone, *d≤r≤e* (Eq. 4.81). Thus, from Eq. (4.92), the radial stress distribution in the plastic zone IV is obtained as

$$\begin{aligned}\sigma_r = {} & \frac{E\alpha}{(2\nu-1)}T_a + \frac{E\alpha\left(T_b - T_a\right)}{2(1-\nu)\ln\left(\dfrac{b}{a}\right)}\left[\frac{1}{(2\nu-1)}\left\{\ln\left(\frac{d}{a}\right) + \frac{1}{2} - \frac{e^2}{2d^2}\right\} - \ln\left(\frac{e}{a}\right)\right] \\ & + k_1\sigma_Y\left\{\frac{1}{2\nu-1}\left(1 + \frac{e^2}{2d^2}\right) + \frac{1}{2} - \ln\left(\frac{r}{e}\right)\right\} + \frac{E\varepsilon_0}{(1-2\nu)}.\end{aligned} \quad (4.93)$$

Once the solution for σ_r is known, the expression for hoop stress, σ_θ can be obtained from Eq. (4.91) as

$$\begin{aligned}\sigma_\theta = {} & \frac{E\alpha}{(2\nu-1)}T_a + \frac{E\alpha\left(T_b - T_a\right)}{2(1-\nu)\ln\left(\dfrac{b}{a}\right)}\left[\frac{1}{(2\nu-1)}\left\{\ln\left(\frac{d}{a}\right) + \frac{1}{2} - \frac{e^2}{2d^2}\right\} - \ln\left(\frac{e}{a}\right)\right] \\ & + \left\{\frac{1}{2\nu-1}\left(1 + \frac{e^2}{2d^2}\right) - \frac{1}{2} - \ln\left(\frac{r}{e}\right)\right\}k_1\sigma_Y + \frac{E\varepsilon_0}{(1-2\nu)}.\end{aligned} \quad (4.94)$$

In view of Tresca's associated flow rule, $\mathrm{d}\varepsilon_\theta^p = -\mathrm{d}\varepsilon_r^p, \mathrm{d}\varepsilon_z^p = 0$. Hence, the axial strain is composed of only elastic and thermal parts. This provides

$$\sigma_z = \nu\left(\sigma_r + \sigma_\theta\right) + E\varepsilon_0 - E\alpha T_a - E\alpha\left(T_b - T_a\right)\frac{\ln\left(\frac{r}{a}\right)}{\ln\left(\frac{b}{a}\right)}. \tag{4.95}$$

Inserting the expressions of σ_r and σ_θ from Eqs. (4.93) and (4.94) in Eq. (4.95), the axial stress distribution is obtained as

$$\begin{aligned}\sigma_z = {} & \frac{E\alpha}{(2\nu-1)}T_a + \frac{E\alpha\left(T_b - T_a\right)}{2(1-\nu)\ln\left(\frac{b}{a}\right)}\left[\frac{2\nu}{(2\nu-1)}\left\{\ln\left(\frac{d}{a}\right)+\frac{1}{2}-\frac{e^2}{2d^2}\right\}+2\nu\ln\left(\frac{r}{e}\right)-2\ln\left(\frac{r}{a}\right)\right] \\ & + k_1\sigma_Y\left\{\frac{2\nu}{2\nu-1}\left(1+\frac{e^2}{2d^2}\right)-2\nu\ln\left(\frac{r}{e}\right)\right\}+\frac{E\varepsilon_0}{(1-2\nu)}.\end{aligned} \tag{4.96}$$

The plastic incompressibility provides

$$\varepsilon_r^p + \varepsilon_\theta^p = 0. \tag{4.97}$$

Thus,

$$\varepsilon_r + \varepsilon_\theta = \varepsilon_r^e + \varepsilon_\theta^e. \tag{4.98}$$

Using the strain-displacement relation (Eq. 3.4) and generalized Hook's law (Eqs. 4.1 and 4.2), the following differential equation is obtained:

$$\frac{\mathrm{d}}{\mathrm{d}r}(ur) = \frac{1}{E}(1-\nu)\frac{\mathrm{d}}{\mathrm{d}r}\left(r^2\sigma_r\right) - \frac{2\nu}{E}r\sigma_z + 2\alpha T_a r + 2\alpha\left(T_b - T_a\right)r\frac{\ln\left(\frac{r}{a}\right)}{\ln\left(\frac{b}{a}\right)}. \tag{4.99}$$

Solving Eq. (4.99), the radial displacement u is obtained as

$$\begin{aligned}u = {} & \frac{\alpha\left(T_b - T_a\right)r}{2(1-\nu)\ln\left(\frac{b}{a}\right)}\left[2\ln\left(\frac{r}{a}\right)-1-(1+\nu)\left\{\ln\left(\frac{d}{a}\right)+\frac{1}{2}-\frac{e^2}{2d^2}\right\}-(1-\nu)\ln\left(\frac{e}{a}\right)-2\nu^2\left\{\ln\left(\frac{r}{e}\right)-\frac{1}{2}\right\}\right] \\ & + \frac{r}{E}\left[(1-\nu)\left\{\frac{1}{2}-\ln\left(\frac{r}{e}\right)\right\}-(1+\nu)\left(1+\frac{e^2}{2d^2}\right)+2\nu^2\left\{\ln\left(\frac{r}{e}\right)-\frac{1}{2}\right\}\right]k_1\sigma_Y + \varepsilon_0 r + \frac{C_9}{r},\end{aligned} \tag{4.100}$$

where C_9 is an integration constant. The total hoop strain is u/r. The plastic part of the hoop strain component is obtained by subtracting the elastic part from the total hoop strain component and is given by

$$\varepsilon_\theta^p = -\varepsilon_r^p = \frac{\alpha\left(T_b - T_a\right)}{2\left(1-\nu\right)\ln\left(\dfrac{b}{a}\right)}\left(\nu^2 - 1\right) + \left(1-\nu^2\right)\frac{k_1\sigma_Y}{E} + \frac{C_9}{r^2}. \tag{4.101}$$

4.2.7 Residual Stress Distribution in the Second Stage of Elasto-plastic Deformation

The residual stresses set up in the cylinder in different zones during second stage of elasto-plastic deformation are evaluated similar way as in Section 4.2.4. The expressions of residual stresses for both the inner plastic zone is same as in Section 4.2.4, except that the values of the constants are different. The expressions for residual stresses in the elastic zone and two outer plastic zones are given as follows:

Elastic zone, $d \leq r \leq e$:

$$\begin{aligned}\left(\sigma_r\right)_{res} = {} & \frac{E\alpha}{\left(2\nu-1\right)}T_a + \frac{E\alpha\left(T_b - T_a\right)}{2\left(1-\nu\right)\ln\left(\dfrac{b}{a}\right)}\left[\frac{1}{\left(2\nu-1\right)}\left\{\ln\left(\frac{d}{a}\right) + \frac{1}{2} - \frac{e^2}{2d^2}\right\} + \frac{1}{2} - \frac{e^2}{2r^2} - \ln\left(\frac{b}{a}\right)\left(1 - \frac{a^2}{r^2}\right)\frac{b^2}{b^2 - a^2}\right] \\ & + \frac{k_1\sigma_Y}{2\nu-1}\left(1 + \frac{e^2}{2d^2}\right) + \frac{e^2}{2r^2}k_1\sigma_Y + \frac{E\varepsilon_0}{\left(1-2\nu\right)},\end{aligned} \tag{4.102}$$

$$\begin{aligned}\sigma_\theta = {} & \frac{E\alpha}{\left(2\nu-1\right)}T_a + \frac{E\alpha\left(T_b - T_a\right)}{2\left(1-\nu\right)\ln\left(\dfrac{b}{a}\right)}\left[\frac{1}{\left(2\nu-1\right)}\left\{\ln\left(\frac{d}{a}\right) + \frac{1}{2} - \frac{e^2}{2d^2}\right\} + \frac{1}{2} + \frac{e^2}{2r^2} - \ln\left(\frac{b}{a}\right)\left(1 + \frac{a^2}{r^2}\right)\frac{b^2}{b^2 - a^2}\right] \\ & + \frac{k_1\sigma_Y}{2\nu-1}\left(1 + \frac{e^2}{2d^2}\right) - \frac{e^2}{2r^2}k_1\sigma_Y + \frac{E\varepsilon_0}{\left(1-2\nu\right)},\end{aligned} \tag{4.103}$$

$$\begin{aligned}\sigma_z = {} & \frac{E\alpha}{\left(2\nu-1\right)}T_a + \frac{E\alpha\left(T_b - T_a\right)}{2\left(1-\nu\right)\ln\left(\dfrac{b}{a}\right)}\left[\frac{2\nu}{\left(2\nu-1\right)}\left\{\ln\left(\frac{d}{a}\right) + \frac{1}{2} - \frac{e^2}{2d^2}\right\} + 1 - \ln\left(\frac{b}{a}\right)\frac{2b^2}{b^2 - a^2}\right] \\ & + \frac{2\nu}{2\nu-1}k_1\sigma_Y\left(1 + \frac{e^2}{2d^2}\right) + \frac{E\varepsilon_0}{\left(1-2\nu\right)}.\end{aligned} \tag{4.104}$$

Plastic zone III, f≤r≤b:

$$(\sigma_r)_{res} = -k_1\sigma_Y \ln r + C_7 + \frac{E\alpha(T_b - T_a)}{2(1-\nu)\ln\left(\frac{b}{a}\right)}\left\{\ln\left(\frac{r}{a}\right) - \ln\left(\frac{b}{a}\right)\left(1 - \frac{a^2}{r^2}\right)\frac{b^2}{b^2 - a^2}\right\}, \tag{4.105}$$

$$(\sigma_\theta)_{res} = -k_1\sigma_Y (1 + \ln r) + C_7 + \frac{E\alpha(T_b - T_a)}{2(1-\nu)\ln\left(\frac{b}{a}\right)}\left\{1 + \ln\left(\frac{r}{a}\right) - \ln\left(\frac{b}{a}\right)\left(1 + \frac{a^2}{r^2}\right)\frac{b^2}{b^2 - a^2}\right\}, \tag{4.106}$$

$$(\sigma_z)_{res} = -k_1\sigma_Y (1 + \ln r) + C_7 + \frac{E\alpha(T_b - T_a)}{2(1-\nu)\ln\left(\frac{b}{a}\right)}\left\{1 + 2\ln\left(\frac{r}{a}\right) - \ln\left(\frac{b}{a}\right)\frac{2b^2}{b^2 - a^2}\right\}. \tag{4.107}$$

Plastic zone IV, e≤r≤f:

$$\begin{aligned}(\sigma_r)_{res} ={}& \frac{E\alpha}{(2\nu-1)}T_a + \frac{E\alpha(T_b - T_a)}{2(1-\nu)\ln\left(\frac{b}{a}\right)}\left[\frac{1}{(2\nu-1)}\left\{\ln\left(\frac{d}{a}\right) + \frac{1}{2} - \frac{e^2}{2d^2}\right\} + \ln\left(\frac{r}{e}\right) - \ln\left(\frac{b}{a}\right)\left(1 - \frac{a^2}{r^2}\right)\frac{b^2}{b^2 - a^2}\right] \\ &+ k_1\sigma_Y\left\{\frac{1}{2\nu-1}\left(1 + \frac{e^2}{2d^2}\right) + \frac{1}{2} - \ln\left(\frac{r}{e}\right)\right\} + \frac{E\varepsilon_0}{(1-2\nu)},\end{aligned} \tag{4.108}$$

$$\begin{aligned}(\sigma_\theta)_{res} ={}& \frac{E\alpha}{(2\nu-1)}T_a + \frac{E\alpha(T_b - T_a)}{2(1-\nu)\ln\left(\frac{b}{a}\right)}\left[\frac{1}{(2\nu-1)}\left\{\ln\left(\frac{d}{a}\right) + \frac{1}{2} - \frac{e^2}{2d^2}\right\} + 1 + \ln\left(\frac{r}{e}\right) - \ln\left(\frac{b}{a}\right)\left(1 + \frac{a^2}{r^2}\right)\frac{b^2}{b^2 - a^2}\right] \\ &+ \left\{\frac{1}{2\nu-1}\left(1 + \frac{e^2}{2d^2}\right) - \frac{1}{2} - \ln\left(\frac{r}{e}\right)\right\}k_1\sigma_Y + \frac{E\varepsilon_0}{(1-2\nu)},\end{aligned} \tag{4.109}$$

$$\begin{aligned}(\sigma_z)_{res} ={}& \frac{E\alpha}{(2\nu-1)}T_a + \frac{E\alpha(T_b - T_a)}{2(1-\nu)\ln\left(\frac{b}{a}\right)}\left[\frac{2\nu}{(2\nu-1)}\left\{\ln\left(\frac{d}{a}\right) + \frac{1}{2} - \frac{e^2}{2d^2}\right\} + 2\nu\ln\left(\frac{r}{e}\right) + 1 - \ln\left(\frac{b}{a}\right)\frac{2b^2}{b^2 - a^2}\right] \\ &+ k_1\sigma_Y\left\{\frac{2\nu}{2\nu-1}\left(1 + \frac{e^2}{2d^2}\right) - 2\nu\ln\left(\frac{r}{e}\right)\right\} + \frac{E\varepsilon_0}{(1-2\nu)}.\end{aligned} \tag{4.110}$$

4.2.8 Evaluation of Constants and Solution Methodology for the Second Stage of Elasto-plastic Deformation

In the second stage of elasto-plastic deformation, the radii of plastic-plastic interface, *c* & *f* and radii of elastic-plastic interface, *d* & *e* are unknown. The constant axial strain, ε_0 is also to be evaluated. The constants— C_3, C_4, C_5, C_6, C_7,

C_8 and C_9 are also not known and these are evaluated using boundary conditions. Using the boundary conditions from Eq. (4.63) the constants C_5 and C_6 are obtained as

$$\begin{aligned} C_6 = {} & \frac{E\alpha(T_b - T_a)}{(2\nu-1)\ln\left(\frac{b}{a}\right)} \left\{ \frac{1-\nu-\nu\sqrt{2(1-\nu)}}{d^{-1-\sqrt{2(1-\nu)}}\, 2\nu\sqrt{2(1-\nu)}} \right\} \left\{ \ln\left(\frac{d}{a}\right) - \frac{2\nu+1}{2\nu-1} - \frac{(1+\nu)}{1-\nu-\nu\sqrt{2(1-\nu)}} \right\} \\ & - \frac{E\alpha(T_b - T_a)}{2(1-\nu)\ln\left(\frac{b}{a}\right)} \left\{ \frac{1-\nu-\nu\sqrt{2(1-\nu)}}{d^{-1-\sqrt{2(1-\nu)}}\, 2\nu\sqrt{2(1-\nu)}} \right\} \left[\frac{1}{(2\nu-1)} \left\{ \ln\left(\frac{d}{a}\right) + \frac{1}{2} - \frac{e^2}{2d^2} \right\} - \ln\left(\frac{d}{a}\right) + \frac{1}{2} - \frac{e^2}{2d^2} \right] \\ & - \left\{ \frac{1-\nu-\nu\sqrt{2(1-\nu)}}{d^{-1-\sqrt{2(1-\nu)}}\, 2\nu\sqrt{2(1-\nu)}} \right\} \left(\frac{2\nu}{2\nu-1} \right) k_1 \sigma_Y \frac{e^2}{2d^2}, \end{aligned} \tag{4.111}$$

$$C_5 = -C_6 d^{-2\sqrt{2(1-\nu)}} \left\{ \frac{1-\nu+\nu\sqrt{2(1-\nu)}}{1-\nu-\nu\sqrt{2(1-\nu)}} \right\} - \frac{E\alpha(T_b - T_a)}{(2\nu-1)\ln\left(\frac{b}{a}\right)} \frac{(1+\nu)}{d^{-1+\sqrt{2(1-\nu)}} \left\{ 1-\nu-\nu\sqrt{2(1-\nu)} \right\}}, \tag{4.112}$$

where C_6 is given by Eq. (4.111). Using the first condition of Eq. (4.64), the constant C_3 is obtained as

$$C_3 = N + \frac{E\varepsilon_0}{(1-2\nu)}, \tag{4.113}$$

where

$$N = C_5 c^{-1+\sqrt{2(1-\nu)}} + C_6 c^{-1-\sqrt{2(1-\nu)}} + \frac{k_1\sigma_Y}{(2\nu-1)} + \frac{E\alpha T_a}{(2\nu-1)} + \frac{E\alpha(T_b - T_a)}{(2\nu-1)\ln\left(\frac{b}{a}\right)} \left\{ \ln\left(\frac{c}{a}\right) - \frac{2\nu+1}{2\nu-1} \right\} - k_1\sigma_Y \ln c. \tag{4.114}$$

The constant C_4 is given by Eq. (4.71), where C_3, C_5 and C_6 are given by Eqs. (4.113), (4.112) and (4.111). To find out the constant C_7, the boundary condition, at $r{=}f$, $\sigma_r^{(\text{plastic zone III})} = \sigma_r^{(\text{plastic zone IV})}$ is used. This gives

$$C_7 = M + \frac{E\varepsilon_0}{(1-2\nu)}, \tag{4.115}$$

where

$$M=\frac{E\alpha}{(2\nu-1)}T_a+\frac{E\alpha(T_b-T_a)}{2(1-\nu)\ln\left(\frac{b}{a}\right)}\left[\frac{1}{(2\nu-1)}\left\{\ln\left(\frac{d}{a}\right)+\frac{1}{2}-\frac{e^2}{2d^2}\right\}-\ln\left(\frac{e}{a}\right)\right]$$
$$+\left\{\frac{1}{2\nu-1}\left(1+\frac{e^2}{2d^2}\right)+\frac{1}{2}-\ln\left(\frac{f}{e}\right)+\ln f\right\}k_1\sigma_Y. \quad (4.116)$$

The constant C_9 is obtained from the boundary condition: at $r=e$, $\varepsilon_\theta^{p(\text{plastic zone IV})}=0$. This provides

$$C_9=-\frac{e^2\alpha(T_b-T_a)}{2(1-\nu)\ln\left(\frac{b}{a}\right)}\left(\nu^2-1\right)-e^2\left(1-\nu^2\right)\frac{k_1\sigma_Y}{E}. \quad (4.117)$$

At $r=f$, $\varepsilon_\theta^{p(\text{plastic zone III})}=\varepsilon_\theta^{p(\text{plastic zone IV})}$. This provides the constant C_8 as

$$C_8=\frac{f^2\alpha(T_b-T_a)}{2(1-\nu)\ln\left(\frac{b}{a}\right)}\left(\nu^2-1\right)+\left(1-\nu^2\right)\frac{k_1\sigma_Y}{E}f^2+C_9-\frac{1-2\nu}{E}\left[\frac{f^2}{2}\left(C_7-k_1\sigma_Y\ln f\right)\right]$$
$$-\frac{3-2\nu}{4E}f^2k_1\sigma_Y-\frac{1}{2}f^2\alpha T_a-\frac{\alpha(T_b-T_a)}{2\ln\left(\frac{b}{a}\right)}f^2\left\{\ln\left(\frac{f}{a}\right)-\frac{3}{2}\right\}+\frac{f^2}{2}\varepsilon_0, \quad (4.118)$$

Using free end condition given by

$$\left[\int_a^c\sigma_z^{(\text{plastic zone I})}r\mathrm{d}r+\int_c^d\sigma_z^{(\text{plastic zone II})}r\mathrm{d}r+\int_d^e\sigma_z^{(\text{elastic zone})}r\mathrm{d}r+\int_e^f\sigma_z^{(\text{plastic zone IV})}r\mathrm{d}r+\int_f^b\sigma_z^{(\text{plastic zone III})}r\mathrm{d}r\right]=0, \quad (4.119)$$

the constant axial strain ε_0 is obtained as

$$\begin{aligned}\varepsilon_0 = \frac{k_1\sigma_Y}{BE}&\left[\begin{array}{l}\ln c\left(\dfrac{c^2}{2}\right)-\ln a\left(\dfrac{a^2}{2}\right)+\dfrac{1}{4}\left(c^2-a^2\right)+\dfrac{\nu}{2\nu-1}\left(d^2-c^2\right)+\dfrac{\nu}{2\nu-1}\left(1+\dfrac{e^2}{2d^2}\right)\left(f^2-d^2\right)\\ -\nu\left\{\ln\left(\dfrac{f}{e}\right)f^2-\dfrac{1}{2}\left(f^2-e^2\right)\right\}-\dfrac{1}{4}\left(b^2-f^2\right)-\ln b\left(\dfrac{b^2}{2}\right)+\ln f\left(\dfrac{f^2}{2}\right)\end{array}\right]\\ &+\frac{N}{2BE}\left(c^2-a^2\right)+\frac{C_5}{BE}\left\{\frac{d^{1+\sqrt{2(1-\nu)}}-c^{1+\sqrt{2(1-\nu)}}}{1+\sqrt{2(1-\nu)}}\right\}+\frac{C_6}{BE}\left\{\frac{d^{1-\sqrt{2(1-\nu)}}-c^{1-\sqrt{2(1-\nu)}}}{1-\sqrt{2(1-\nu)}}\right\}+\frac{\alpha T_a}{2(2\nu-1)B}\left(f^2-c^2\right)\\ &+\frac{\alpha\left(T_b-T_a\right)}{(2\nu-1)\ln\left(\dfrac{b}{a}\right)B}\left\{\ln\left(\frac{d}{a}\right)\frac{d^2}{2}-\ln\left(\frac{c}{a}\right)\frac{c^2}{2}-\frac{3}{4}\left(d^2-c^2\right)-\frac{d^2-c^2}{2\nu-1}\right\}+\frac{M}{2BE}\left(b^2-f^2\right)\\ &+\frac{\alpha\left(T_b-T_a\right)}{2(1-\nu)\ln\left(\dfrac{b}{a}\right)B}\left[\begin{array}{l}\dfrac{\nu}{(2\nu-1)}\left\{\ln\left(\dfrac{d}{a}\right)+\dfrac{1}{2}-\dfrac{e^2}{2d^2}\right\}\left(f^2-d^2\right)-\left\{\ln\left(\dfrac{e}{a}\right)e^2-\ln\left(\dfrac{d}{a}\right)d^2-\dfrac{1}{2}\left(e^2-d^2\right)\right\}\\ +\nu\left\{\ln\left(\dfrac{f}{e}\right)f^2-\dfrac{1}{2}\left(f^2-e^2\right)\right\}-\left\{\ln\left(\dfrac{f}{a}\right)f^2-\ln\left(\dfrac{e}{a}\right)e^2-\dfrac{1}{2}\left(f^2-e^2\right)\right\}\end{array}\right],\end{aligned} \tag{4.120}$$

where

$$B=\left\{\frac{b^2-a^2}{2\left(2\nu-1\right)}\right\}. \tag{4.121}$$

Using the boundary conditions of vanishing radial stress at the outer radius and $\sigma_\theta^{(\text{plastic zone IV})}=\sigma_z^{(\text{plastic zone IV})}$, at $r=f$ provides

$$-k_1\sigma_Y\ln b+C_7=0, \tag{4.122}$$

$$\begin{aligned}&\frac{E\alpha\left(T_b-T_a\right)}{2(1-\nu)\ln\left(\dfrac{b}{a}\right)}\left[\ln\left(\frac{d}{a}\right)+\frac{1}{2}-\frac{e^2}{2d^2}+2\nu\ln\left(\frac{f}{e}\right)+\ln\left(\frac{e}{a}\right)-2\ln\left(\frac{f}{a}\right)\right]\\ &+\left\{1+\frac{e^2}{2d^2}+\frac{1}{2}+(1-2\nu)\ln\left(\frac{f}{e}\right)\right\}k_1\sigma_Y=0\end{aligned} \tag{4.123}$$

Eqs. (4.75), (4.76), (4.122) and (4.123) are solved simultaneously using FSOLVE function in MATLAB to obtain the interface radii *c*, *d*, *e* and *f*.

4.3 Conceptual Design of a System for Creation of Thermal Gradient in the Cylinder: An Example

A conceptual design as described in Section 3.5 can be employed for creating the desired thermal gradient across the wall thickness of the cylinder to achieve thermal autofrettage. Here, the design procedure is explained for a typical cylinder as follows:

A cylinder of SS304 with inner radius a=10 mm, outer radius b=30 mm and length L=60 mm is considered. It is heated externally and a temperature difference, $(T_b - T_a) = 120$ ºC is maintained for achieving autofrettage. The thermal conductivity, k of SS304 is taken as 14.9 W/m ºC (Incropera and Dewitt, 1996). It is decided to use cold water as the fluid. Using Eq. (3.67), the amount of heat transfer Q is calculated as

$$Q = 613.55 \text{ W}.$$

Taking $\dot{m} = 1$ kg/s and $c_p = 4.18$ kJ/kg-K, the temperature difference between outlet and inlet of the cold water flowing through the cylinder $(T_o - T_i)$ is obtained from Eq. (3.69) as

$$(T_o - T_i) = 0.15°\text{C}.$$

Assuming the temperature of the water at the inlet as T_i= 25 ºC, the temperature at the outlet is estimated as T_o = 25.15°C. Thus, the average temperature of the water flowing inside the cylinder is

$$T_f = \frac{T_i + T_o}{2} = 25.08\,°\text{C}.$$

Properties of water at 25.08 ºC are $\rho = 997$ kg/m^3, $\mu = 0.891 \times 10^{-3}$ Ns/m^2, k_f=0.607 W/m ºC (Incropera and Dewitt, 1996). The velocity of flow is calculated as

$$V = \frac{\dot{m}}{\rho\left(\pi/4\right)D^2} = 3.19 \text{ m/s}.$$

Using Eq. (3.73) provides

$$\mathrm{Re}= 71390.12,\ \mathrm{Pr} = 6.14.$$

Hence, from Eq. (3.71),

$$\mathrm{Nu} = 417.88.$$

Putting Nu in Eq. (3.70), the value of heat transfer coefficient, h is obtained as

$$h= 12682.66\ \mathrm{W/m^2\,°C}.$$

Using the value of h in Eq. (3.68), the inner surface temperature T_a is estimated as 37.91°C. As the difference in temperature between the inner and outer surface of the cylinder is 120 ºC, the value of outer surface temperature T_b is 157.91 ºC.

4.4 Numerical Simulations

The stress equations developed in Section 3 are numerically simulated to see the feasibility of thermal autofrettage process. The solution methodology for the different cases of elasto-plastic deformation is described in Sections 4.2.5 and 4.2.8. The simulations are carried out for the case of aluminum and SS304 cylinder and the results are discussed in the following Subsections.

4.4.1 Case of aluminum cylinder

An aluminum cylinder with free ends is considered. The inner radius, a and outer radius, b of the cylinder are considered as 10 mm and 20 mm. The material properties of aluminum are as follows: Young's modulus of elasticity, E = 69 GPa, yield stress, σ_Y =50.3 MPa, Poisson's ratio, ν =0.3, coefficient of thermal expansion, $\alpha = 22.2\times10^{-6}$/ºC. For achieving autofrettage in the aluminum cylinder a temperature difference of 70 ºC is considered. At a temperature difference of 70 ºC, the cylinder undergoes second stage of elasto-plastic deformation. The interface radii c, d, e and f are obtained as 11.4071 mm, 11.8562 mm, 18.8182 mm and 19.3612 mm. It is assumed that the inner wall of the cylinder is maintained at a temperature, T_a=25 ºC. The simulation results are discussed in the following subsections. The stress distributions are shown as a function of radial position.

4.4.1.1 Elastic-plastic thermal stress distribution

At a temperature difference of 70 ºC, the outer surface gets yielded and the corresponding stress distributions in different zones are obtained by using the stress equations developed in Section 4.2.6. The elastic-plastic stress distribution is shown in Figure 4.3.

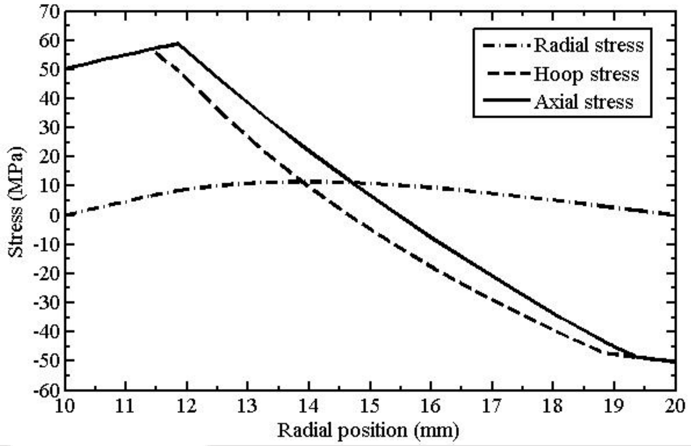

Figure 4.3 Elastic-plastic stress distributions in aluminum cylinder

It is observed that the magnitude of radial stresses is quite small compared to the magnitude of hoop and axial stresses in the cylinder. The magnitude of hoop and axial stresses are same in plastic zone I and plastic zone III. Along the positive radial direction the hoop and axial stresses change from tensile to compressive. The radial stresses are always tensile in nature. This trend gets reversed on the removal of the induced temperature gradient. The strains in the plastic zones as a function of radial position are evaluated using the relevant equations of Subsections 4.2.3.1, 4.2.3.2, 4.2.6.2 and 4.2.6.3 and it is observed that the maximum plastic strain is in the order of 10^{-4}.

4.4.1.2 Residual thermal stress distribution

When the induced temperature gradient in the cylinder is released, then residual thermal stresses are generated in the cylinder. The residual thermal stresses generated in the cylinder are estimated by using equations developed in Section 4.2.7 and the simulated result is shown in Figure 4.4. It is observed that the residual radial thermal stress becomes compressive with smaller magnitude. The magnitudes of residual hoop and axial stresses are higher and compressive in nature at and around the inner radius of the cylinder, whilst they become tensile at and around the outer radius. The maximum magnitude of residual hoop and axial stress is 43.44 MPa (compressive) generated at the inner radius of the cylinder. This large magnitude of residual compressive stresses leads to the decrease in the maximum value of stress generated in the cylinder when it is subjected to internal pressure loading.

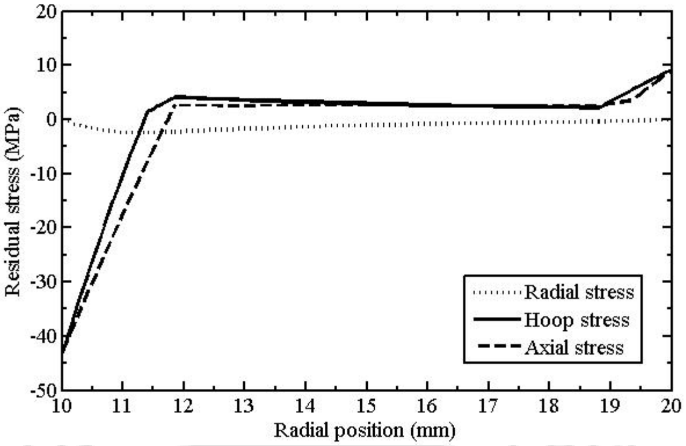

Figure 4.4 Residual stresses in the aluminum cylinder

The residual tensile hoop and axial stresses at and around the outer radius does not pose any problem during autofrettage as long as their magnitudes are small. The higher magnitude of tensile residual stresses at the outer radius of the cylinder may cause stress corrosion cracking. Thus, in order to keep the tensile stresses of smaller magnitude, the induced temperature gradient in the cylinder needs to be controlled. In the present case, it is observed that the magnitude of tensile residual hoop and axial stresses follow an increasing trend in the outer plastic zones and maximum at the outer radius. However, this magnitude is small.

4.4.1.3 Overall stress distribution with and without autofrettage

After setting up the residual thermal stresses in the cylinder, it is now subjected to internal pressure loading to see the effect of autofrettage. The aluminum cylinder which is autofrettaged by temperature difference of 70 ºC is subjected to an internal pressure of 18 MPa. The stress distribution in the cylinder due to internal pressure loading is given by Lamé’s equations (Eqs. 3.74 and 3.75). Due to free end condition, the axial stress is zero. The resulting stress distribution in the autofrettaged cylinder is obtained by adding residual stresses to the stresses due to internal pressure. For non-autofrettaged cylinder, the stress distribution in the cylinder is only given by Lamé’s equations. The resulting stress distribution for autofrettaged and non-autofrettaged cylinder is shown in Figure 4.5.

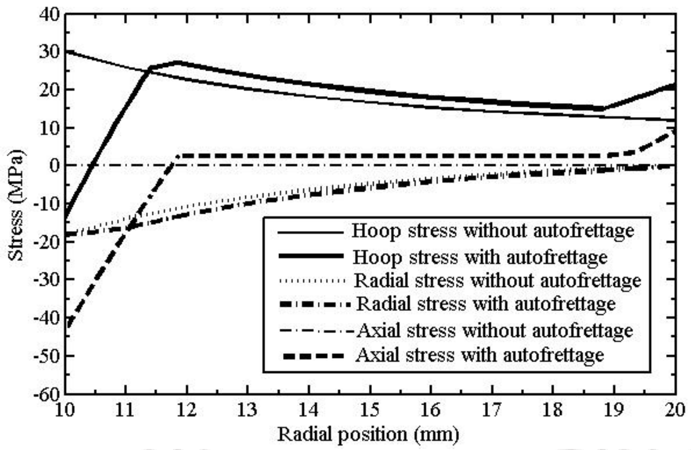

Figure 4.5 Stress distributions in the aluminum cylinder with and without autofrettage

It is observed that the maximum equivalent Tresca stress ($|\sigma_\theta - \sigma_r|/2$, in the present case) is generated at the radius of plastic-plastic interface ($r=c$) in the autofrettaged cylinder. For a non-autofrettaged cylinder the maximum equivalent Tresca stress occurs at the inner radius ($r=a$). The reduction in the maximum equivalent Tresca stress in the autofrettaged cylinder is observed to be 15.14% in the present case compared to the non-autofrettaged cylinder.

4.4.2 Case of SS304 cylinder

A cylinder of SS304 with inner radius, *a*=10 mm and outer radius, *b*=30 mm with free ends is considered for autofrettage by inducing temperature gradient. The material properties of SS304 are as follows: Young's modulus of elasticity, *E*=193 GPa, yield stress, σ_Y=205 MPa, Poisson's ratio, ν=0.3, coefficient of thermal expansion, $\alpha=17.2\times10^{-6}$/°C. A temperature difference of 120 °C is considered for achieving thermal autofrettage in the cylinder. The inner wall of the cylinder is maintained at 25 °C. At 120 °C, the cylinder undergoes first stage of elasto-plastic deformation. For this case, the interface radii, *c* and *d* are obtained as 11.9775 mm and 12.9193 mm. In the following subsections the various stress distributions in the SS304 cylinder for a temperature difference of 120 °C are discussed. The stress distributions are shown as a function of radial position.

4.4.2.1 Elastic-plastic thermal stress distribution

The elastic-plastic thermal stresses in different zones in the SS304 cylinder for 120 °C temperature difference are shown in Figure 4.6. These are obtained by numerical simulation of equations developed in Section 4.2.3. A similar trend for the stresses is obtained as in the case of aluminum cylinder.

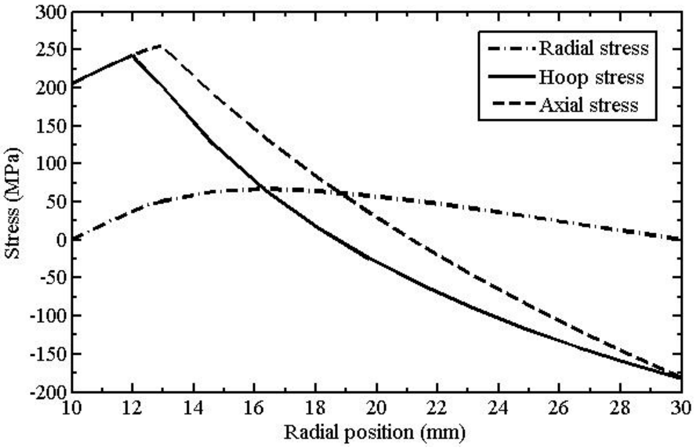

Figure 4.6 Elastic-plastic stress distributions in SS304 cylinder

4.4.2.2 Residual thermal stress distribution

On cooling to room temperature, a significant amount of compressive residual thermal hoop and axial stresses are generated at and around the inner radius of the SS304 cylinder. The resulting residual thermal stress distribution is evaluated using the equations developed in Section 4.2.4 and is shown in Figure 4.7. At the outer elastic zone, tensile residual hoop and axial stresses of small magnitude are generated. The compressive residual thermal radial stresses are significantly small.

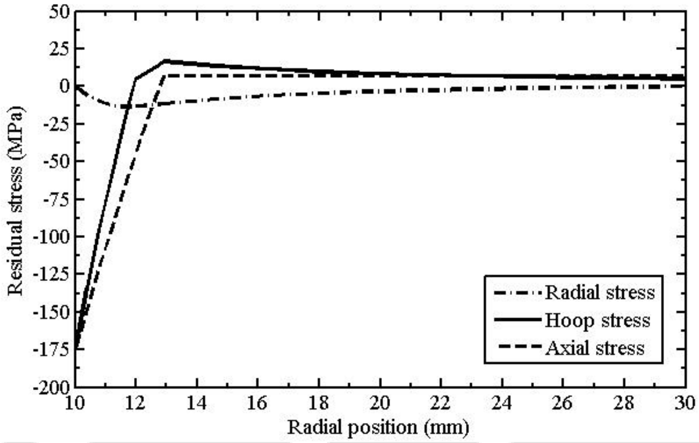

Figure 4.7 Residual stresses in SS304 cylinder

Table 4.1 Compressive stress at the inner wall for steel cylinders with medium and high values of σ_Y

Material of the cylinder	E (GPa)	σ_Y (MPa)	α (/°C)	ν	$(T_b – T_a)$ (°C)	Compressive stress at the inner wall (MPa)
S17700 annealed steel	200	450	17.1×10^{-6}	0.3	200	204.60 (45% of yield stress)
					250	368.20 (82% of yield stress)
SNCM 8 high strength steel	202.2	1129	17.5×10^{-6}	0.3	340	19.53 (1.7% of yield stress)
					360	90.06 (8 % of yield stress)

It is observed in the present case that the compressive residual stress generated at the inner wall is 176.20 MPa which is about 86% of the yield stress. However, it is found that for steels with higher values of yield strength the compressive residual stress at the inner wall is reduced. This is illustrated in Table 4.1 by taking the examples of S17700 annealed steel and SNCM 8 high strength steel cylinders under thermal gradient. The dimension of the cylinder is taken as same as in the case of SS304. The cylinders do not undergo second stage of elasto-plastic deformation due to the limitation on (T_b–T_a) *i.e.*, the maximum temperature T_b does not cross the recrystallization temperature of the material. Here, T_a has been taken as 25 °C. One can further reduce it to some extent for increasing the temperature difference. However, the present method will surely have some limitation for high strength material compared to hydraulic autofrettage.

4.4.2.3 Overall stress distribution with and without autofrettage

Due to large magnitude of compressive residual stresses set up at and around the inner radius, the SS304 cylinder is now able to withstand a high internal pressure. The tensile hoop stress due to internal pressure loading gets added to the compressive residual hoop stress generated at and around the inner radius and the resulting stress becomes smaller in magnitude. This leads to the reduction of equivalent maximum stress in the cylinder. Thus, the pressure carrying capacity of the SS304 cylinder is increased. It is assumed that the thermally autofrettaged SS304 cylinder by 120 ºC temperature difference is subjected to an internal pressure of 90 MPa. The resulting stress pattern with and without autofrettage for this case is shown Figure 4.8.

In the autofrettaged cylinder, for an internal pressure of 90 MPa, the maximum Tresca stress is reduced by 23.89% in comparison with the non-autofrettaged cylinder. The maximum equivalent stress occurs at the plastic-plastic interface (r=c) during pressurization in the autofrettaged cylinder. Hence, reyielding due to internal pressure is expected to occur first at the radius of plastic-plastic interface.

From the numerical simulation of residual thermal stresses for aluminum and SS304 cylinders it is observed that considerable amount of compressive residual stresses are generated at and around the inner radius of the cylinder. This reduces the maximum stress generated within the cylinder wall during loading by internal pressure. Thus, autofrettage have been achieved by creating thermal gradient in the cylinders. The proposed thermal autofrettage is advantageous over the conventional hydraulic autofrettage process in terms of its simplicity. However, it is necessary to carry out a quantitative analysis to know how much pressure carrying capacity of the cylinders is increased by thermal autofrettage as compared to hydraulic autofrettage. A quantitative comparison of the maximum pressure carrying capacity of cylinders in thermal autofrettage with hydraulic autofrettage will be carried out in Section 7.2.

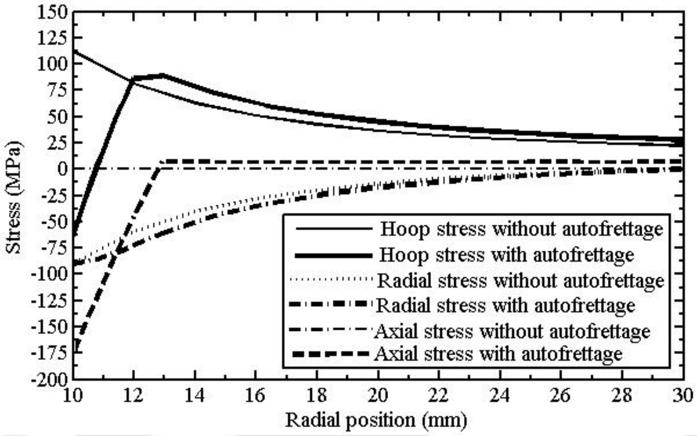

Figure 4.8 Stress distributions in SS304 cylinder with and without autofrettage

4.5 Influence of Strain Hardening

In plastic deformation, the material of the cylinder may strain harden. In Section 4.2, the analysis of the thermal autofrettage is provided without strain hardening during plastic deformation. In this section, the thermal autofrettage is analyzed considering strain hardening. The strain hardening during plastic deformation is represented by the Ludwik's hardening law given by Eq. (3.20). In the following sections, the analysis for the first and second stage of elasto-plastic deformation in thermal autofrettage is discussed incorporating strain hardening.

4.5.1 Strain Hardening in First stage of Elasto-plastic Deformation

When the material strain hardens, in the first stage of elasto-plastic deformation, the plastic zone I, $a \le r \le c$ propagate according to the Tresca criterion,

$$\sigma_\theta - \sigma_r = k_1 \sigma_{eq}, \quad \sigma_z - \sigma_r = k_1 \sigma_{eq}, \tag{4.124}$$

where σ_{eq} is the equivalent yield stress in uniaxial tension or compression, which is a function of equivalent plastic strain, ε_{eq}^{p}. Here, the equivalent yield stress is represented by the Ludwik's hardening law (Eq. 3.20). Using first condition of Eq. (4.124) in equilibrium equation (Eq. 3.6), the integration of the resulting equation provides the radial stress as

$$\sigma_r = k_1 \sigma_Y \ln r + k_1 K \int_a^r \frac{\left(\varepsilon_{eq}^{p}\right)^n}{r_1} \mathrm{d}r_1 + C_3, \tag{4.125}$$

where ε_{eq}^{p} is a function of radius and r_1 is a dummy variable. From Eq. (4.124),

$$\sigma_\theta = \sigma_z = k_1 \sigma_Y \left(1 + \ln r\right) + k_1 K \left(\varepsilon_{eq}^{p}\right)^n + k_1 K \int_a^r \frac{\left(\varepsilon_{eq}^{p}\right)^n}{r_1} \mathrm{d}r_1 + C_3. \tag{4.126}$$

Following the similar procedure as described in Subsection 4.2.3.1, the plastic part of the strain components are given by

$$\begin{aligned} \varepsilon_\theta^{p} = {} & \frac{1-2\nu}{E}\left[\frac{1}{2}\left(k_1\sigma_Y \ln r + C_3\right) + \frac{2k_1K}{r^2}\int_a^r r_1\left(\varepsilon_{eq}^{p}\right)^n \mathrm{d}r_1 - k_1K\int_a^r \frac{\left(\varepsilon_{eq}^{p}\right)^n}{r_1}\mathrm{d}r_1 + \frac{3k_1K}{r^2}\int_a^r\left\{r_2\int_a^{r_2}\frac{\left(\varepsilon_{eq}^{p}\right)^n}{r_1}\mathrm{d}r_1\right\}\mathrm{d}r_2\right] \\ & - \frac{3-2\nu}{4E}k_1\sigma_Y - \frac{1-\nu}{E}k_1K\left(\varepsilon_{eq}^{p}\right)^n + \frac{1}{2}\alpha T_a + \frac{\alpha\left(T_b - T_a\right)}{2\ln\left(\frac{b}{a}\right)}\left\{\ln\left(\frac{r}{a}\right) - \frac{3}{2}\right\} - \frac{1}{2}\varepsilon_0 + \frac{C_4}{r^2}, \end{aligned} \tag{4.127}$$

$$\begin{aligned}\varepsilon_r^p = & \frac{1-2\nu}{E}\left[\frac{1}{2}\left(k_1\sigma_Y \ln r + C_3\right) + 2k_1K\int_a^r \frac{\left(\varepsilon_{eq}^p\right)^n}{r_1}\mathrm{d}r_1 - \frac{2k_1K}{r^2}\int_a^r r_1\left(\varepsilon_{eq}^p\right)^n \mathrm{d}r_1 - \frac{3k_1K}{r^2}\int_a^r\left\{r_2\int_a^{r_2}\frac{\left(\varepsilon_{eq}^p\right)^n}{r_1}\mathrm{d}r_1\right\}\mathrm{d}r_2\right] \\ & + \frac{7-6\nu}{4E}k_1\sigma_Y + \frac{2(1-\nu)}{E}k_1K\left(\varepsilon_{eq}^p\right)^n + \frac{1}{2}\alpha T_a + \frac{\alpha\left(T_b-T_a\right)}{2\ln\left(\frac{b}{a}\right)}\left\{\ln\left(\frac{r}{a}\right)+\frac{3}{2}\right\} - \frac{1}{2}\varepsilon_0 - \frac{C_4}{r^2},\end{aligned} \tag{4.128}$$

$$\begin{aligned}\varepsilon_0^p = & \varepsilon_0 - \frac{1-2\nu}{E}\left\{k_1\sigma_Y \ln r + C_3 + k_1K\int_a^r \frac{\left(\varepsilon_{eq}^p\right)^n}{r_1}\mathrm{d}r_1\right\} - \frac{1-\nu}{E}k_1\sigma_Y - \frac{1-\nu}{E}k_1K\left(\varepsilon_{eq}^p\right)^n \\ & - \alpha T_a - \alpha\left(T_b - T_a\right)\frac{\ln\left(\frac{r}{a}\right)}{\ln\left(\frac{b}{a}\right)},\end{aligned} \tag{4.129}$$

where r_1 and r_2 are dummy variables. The equivalent plastic strain in the plastic zone I is given by

$$\varepsilon_{eq}^p = \sqrt{\frac{2}{3}\left\{\left(\varepsilon_r^p\right)^2 + \left(\varepsilon_\theta^p\right)^2 + \left(\varepsilon_0^p\right)^2\right\}}. \tag{4.130}$$

The plastic zone II, $c \le r \le d$ is formed according to the Tresca criterion, $\sigma_z - \sigma_r = k_1\sigma_{eq}$. Following the similar procedure as described in Subsection 4.2.3.2, the resulting expressions for stresses and plastic part of strains are given by

$$\begin{aligned}\sigma_r = & C_5 r^{-1+\sqrt{2(1-\nu)}} + C_6 r^{-1-\sqrt{2(1-\nu)}} + \frac{k_1\sigma_Y}{(2\nu-1)} + \frac{k_1K r^{-1+\sqrt{2(1-\nu)}}\left\{1-\nu+\nu\sqrt{2(1-\nu)}\right\}}{2\sqrt{2(1-\nu)}}\int_c^r r_1^{-\sqrt{2(1-\nu)}}\left(\varepsilon_{eq}^p\right)^n \mathrm{d}r_1 \\ & - \frac{k_1K r^{-1-\sqrt{2(1-\nu)}}\left\{1-\nu-\nu\sqrt{2(1-\nu)}\right\}}{2\sqrt{2(1-\nu)}}\int_c^r r_1^{\sqrt{2(1-\nu)}}\left(\varepsilon_{eq}^p\right)^n \mathrm{d}r_1 + \frac{E\alpha T_a}{(2\nu-1)} + \frac{E\alpha\left(T_b-T_a\right)}{(2\nu-1)}\frac{\ln\left(\frac{r}{a}\right)}{\ln\left(\frac{b}{a}\right)} \\ & - \frac{2E\alpha\left(T_b-T_a\right)}{(2\nu-1)^2\ln\left(\frac{b}{a}\right)} - \frac{E\alpha\left(T_b-T_a\right)}{(2\nu-1)\ln\left(\frac{b}{a}\right)} - \frac{E\varepsilon_0}{(2\nu-1)},\end{aligned} \tag{4.131}$$

$$\begin{aligned}\sigma_\theta ={}& C_5\sqrt{2(1-\nu)}r^{\sqrt{2(1-\nu)}-1}-C_6\sqrt{2(1-\nu)}r^{-\sqrt{2(1-\nu)}-1}+\frac{k_1\sigma_Y}{(2\nu-1)}+\frac{E\alpha T_a}{(2\nu-1)}+\frac{E\alpha(T_b-T_a)}{(2\nu-1)}\frac{\ln\left(\frac{r}{a}\right)}{\ln\left(\frac{b}{a}\right)}\\ &-\frac{2E\alpha(T_b-T_a)}{(2\nu-1)^2\ln\left(\frac{b}{a}\right)}-\frac{E\varepsilon_0}{(2\nu-1)}+\frac{k_1K\sqrt{2(1-\nu)}r^{\sqrt{2(1-\nu)}-1}\left\{1-\nu+\nu\sqrt{2(1-\nu)}\right\}}{2\sqrt{2(1-\nu)}}\int_c^r r_1^{-\sqrt{2(1-\nu)}}\left(\varepsilon_{eq}^p\right)^n\mathrm{d}r_1\\ &+\frac{k_1K\sqrt{2(1-\nu)}r^{-\sqrt{2(1-\nu)}-1}\left\{1-\nu-\nu\sqrt{2(1-\nu)}\right\}}{2\sqrt{2(1-\nu)}}\int_c^r r_1^{\sqrt{2(1-\nu)}}\left(\varepsilon_{eq}^p\right)^n\mathrm{d}r_1+\nu k_1K\left(\varepsilon_{eq}^p\right)^n.\end{aligned} \tag{4.132}$$

Knowing the expression for σ_r, the expression for σ_z can be obtained from Tresca yield criterion.

$$\begin{aligned}\varepsilon_r^p ={}& -\varepsilon_\theta^p=\frac{C_5}{E}r^{-1+\sqrt{2(1-\nu)}}\left\{1-\nu-\nu\sqrt{2(1-\nu)}\right\}+\frac{C_6}{E}r^{-1-\sqrt{2(1-\nu)}}\left\{1-\nu+\nu\sqrt{2(1-\nu)}\right\}\\ &+\frac{k_1Kr^{-1+\sqrt{2(1-\nu)}}\left\{1-\nu-\nu\sqrt{2(1-\nu)}\right\}\left\{1-\nu+\nu\sqrt{2(1-\nu)}\right\}}{2\sqrt{2(1-\nu)}E}\int_c^r r_1^{-\sqrt{2(1-\nu)}}\left(\varepsilon_{eq}^p\right)^n\mathrm{d}r_1\\ &-\frac{k_1Kr^{-1-\sqrt{2(1-\nu)}}\left\{1-\nu+\nu\sqrt{2(1-\nu)}\right\}\left\{1-\nu-\nu\sqrt{2(1-\nu)}\right\}}{2\sqrt{2(1-\nu)}E}\int_c^r r_1^{\sqrt{2(1-\nu)}}\left(\varepsilon_{eq}^p\right)^n\mathrm{d}r_1\\ &+\left(1-\nu^2\right)\frac{k_1K}{E}\left(\varepsilon_{eq}^p\right)^n+\frac{\alpha(T_b-T_a)}{\ln\left(\frac{b}{a}\right)}\frac{(1+\nu)}{(2\nu-1)}.\end{aligned} \tag{4.133}$$

The equivalent plastic strain field in the plastic zone II is given by

$$\varepsilon_{eq}^p=\frac{2}{\sqrt{3}}\varepsilon_r^p. \tag{4.134}$$

The different constants involved in the equations of first stage of plastic deformation with strain hardening can be evaluated using the conditions explained in Section 4.2.5. The resultant expressions of C_5 and C_6 are still given by Eqs. (4.65) and (4.66), where

$$
\begin{aligned}
P=&\frac{E\alpha\left(T_b-T_a\right)}{(2\nu-1)\ln\left(\dfrac{b}{a}\right)}\left\{\frac{1-\nu-\nu\sqrt{2(1-\nu)}}{d^{-1-\sqrt{2(1-\nu)}}2\nu\sqrt{2(1-\nu)}}\right\}\left\{\ln\left(\frac{d}{a}\right)-\frac{2\nu+1}{2\nu-1}-\frac{(1+\nu)}{1-\nu-\nu\sqrt{2(1-\nu)}}\right\}\\
&+k_1K\left\{\frac{1-\nu-\nu\sqrt{2(1-\nu)}}{2\sqrt{2(1-\nu)}}\right\}\int_c^d r_1^{\sqrt{2(1-\nu)}}\left(\varepsilon_{eq}^p\right)^n \mathrm{d}r_1\\
&-\frac{E\alpha}{2(1-\nu)}\frac{\left(T_b-T_a\right)}{\ln\left(\dfrac{b}{a}\right)}\left\{\frac{1-\nu-\nu\sqrt{2(1-\nu)}}{d^{-1-\sqrt{2(1-\nu)}}2\nu\sqrt{2(1-\nu)}}\right\}\left[\ln\left(\frac{b}{d}\right)+\left\{\frac{b^2-d^2}{b^2+d^2(2\nu-1)}\right\}\left\{\ln\left(\frac{b}{a}\right)(2\nu-1)-\nu-\ln\left(\frac{d}{a}\right)\right\}\right]\\
&+\frac{2\nu b^2}{(2\nu-1)\left\{b^2+d^2(2\nu-1)\right\}}\left\{\frac{1-\nu-\nu\sqrt{2(1-\nu)}}{d^{-1-\sqrt{2(1-\nu)}}2\nu\sqrt{2(1-\nu)}}\right\}k_1\sigma_Y\\
&+\frac{2\nu b^2}{(2\nu-1)\left\{b^2+d^2(2\nu-1)\right\}}\left\{\frac{1-\nu-\nu\sqrt{2(1-\nu)}}{d^{-1-\sqrt{2(1-\nu)}}2\nu\sqrt{2(1-\nu)}}\right\}E\alpha T_a,
\end{aligned}
\tag{4.135}
$$

$$
\begin{aligned}
Q=&-Pd^{-2\sqrt{2(1-\nu)}}\left\{\frac{1-\nu+\nu\sqrt{2(1-\nu)}}{1-\nu-\nu\sqrt{2(1-\nu)}}\right\}+\frac{k_1K\left\{1-\nu+\nu\sqrt{2(1-\nu)}\right\}}{2\sqrt{2(1-\nu)}}\int_c^d r_1^{-\sqrt{2(1-\nu)}}\left(\varepsilon_{eq}^p\right)^n \mathrm{d}r_1\\
&-\frac{k_1Kd^{-2\sqrt{2(1-\nu)}}\left\{1-\nu+\nu\sqrt{2(1-\nu)}\right\}}{2\sqrt{2(1-\nu)}}\int_c^d r_1^{\sqrt{2(1-\nu)}}\left(\varepsilon_{eq}^p\right)^n \mathrm{d}r_1\\
&-\frac{E\alpha\left(T_b-T_a\right)}{(2\nu-1)\ln\left(\dfrac{b}{a}\right)}\frac{(1+\nu)}{d^{-1+\sqrt{2(1-\nu)}}\left\{1-\nu-\nu\sqrt{2(1-\nu)}\right\}}.
\end{aligned}
\tag{4.136}
$$

The constant C_3 is given by Eq. (4.69), with a change in the value of the term, R which is given by

$$
\begin{aligned}
R=&Qc^{-1+\sqrt{2(1-\nu)}}-k_1\sigma_Y\ln c-k_1K\int_a^c\frac{\left(\varepsilon_{eq}^p\right)^n}{r_1}\mathrm{d}r_1+Pc^{-1-\sqrt{2(1-\nu)}}+\frac{k_1\sigma_Y}{(2\nu-1)}+\frac{E\alpha T_a}{(2\nu-1)}\\
&+\frac{E\alpha\left(T_b-T_a\right)}{(2\nu-1)\ln\left(\dfrac{b}{a}\right)}\ln\left(\frac{c}{a}\right)-\frac{2E\alpha\left(T_b-T_a\right)}{(2\nu-1)^2\ln\left(\dfrac{b}{a}\right)}-\frac{E\alpha\left(T_b-T_a\right)}{(2\nu-1)\ln\left(\dfrac{b}{a}\right)}.
\end{aligned}
\tag{4.137}
$$

The resulting expression for C_4 is given by

$$C_4=\frac{1-2\nu}{E}\left[-\frac{c^2}{2}\left(k_1\sigma_Y\ln c+C_3\right)-2k_1K\int_a^c r_1\left(\varepsilon_{eq}^p\right)^n \mathrm{d}r_1+k_1Kc^2\int_a^c\frac{\left(\varepsilon_{eq}^p\right)^n}{r_1}\mathrm{d}r_1-3k_1K\int_a^c\left\{r_2\int_a^{r_2}\frac{\left(\varepsilon_{eq}^p\right)^n}{r_1}\mathrm{d}r_1\right\}\mathrm{d}r_2\right]$$
$$+\frac{3-2\nu}{4E}c^2k_1\sigma_Y+\frac{(1-\nu)}{E}c^2k_1K\left(\varepsilon_{eq}^p\Big|_{r=c}\right)^n-\frac{1}{2}c^2\alpha T_a-\frac{\alpha\left(T_b-T_a\right)}{2\ln\left(\frac{b}{a}\right)}\left\{c^2\ln\left(\frac{c}{a}\right)-\frac{3c^2}{2}\right\}+\frac{c^2}{2}\varepsilon_0. \tag{4.138}$$

The resulting expression for constant axial strain, ε_0 is obtained as

$$\varepsilon_0=\frac{k_1\sigma_Y}{AE}\left\{\ln c\frac{c^2}{2}-\ln a\frac{a^2}{2}+\frac{1}{4}\left(c^2-a^2\right)+\frac{\nu\left(d^2-c^2\right)}{2\nu-1}+\frac{\nu d^2\left(b^2-d^2\right)}{b^2+d^2\left(2\nu-1\right)}\right\}$$
$$+\frac{k_1K}{AE}\int_a^c\left\{r\int_a^r\frac{\left(\varepsilon_{eq}^p\right)^n}{r_1}\mathrm{d}r_1\right\}\mathrm{d}r+\frac{R}{AE}\left(\frac{c^2-a^2}{2}\right)+\frac{k_1K}{AE}\int_a^c r\left(\varepsilon_{eq}^p\right)^n\mathrm{d}r+\frac{Q}{AE}\left\{\frac{d^{1+\sqrt{2(1-\nu)}}-c^{1+\sqrt{2(1-\nu)}}}{1+\sqrt{2(1-\nu)}}\right\}$$
$$+\frac{P}{AE}\left\{\frac{d^{1-\sqrt{2(1-\nu)}}-c^{1-\sqrt{2(1-\nu)}}}{1-\sqrt{2(1-\nu)}}\right\}+\frac{k_1K\left\{1-\nu+\nu\sqrt{2(1-\nu)}\right\}}{2\sqrt{2(1-\nu)}AE}\int_c^d\left[r^{\sqrt{2(1-\nu)}}\int_c^r r_1^{-\sqrt{2(1-\nu)}}\left(\varepsilon_{eq}^p\right)^n\mathrm{d}r_1\right]\mathrm{d}r$$
$$-\frac{k_1K\left\{1-\nu-\nu\sqrt{2(1-\nu)}\right\}}{2\sqrt{2(1-\nu)}AE}\int_c^d\left[r^{-\sqrt{2(1-\nu)}}\int_c^r r_1^{\sqrt{2(1-\nu)}}\left(\varepsilon_{eq}^p\right)^n\mathrm{d}r_1\right]\mathrm{d}r+\frac{\alpha T_a}{A}\left[\frac{d^2-c^2}{2(2\nu-1)}-\frac{\left(b^2-d^2\right)^2}{2\left\{b^2+d^2\left(2\nu-1\right)\right\}}\right]$$
$$+\frac{\alpha\left(T_b-T_a\right)}{(2\nu-1)\ln\left(\frac{b}{a}\right)A}\left\{\ln\left(\frac{d}{a}\right)\frac{d^2}{2}-\ln\left(\frac{c}{a}\right)\frac{c^2}{2}-\frac{1}{2}\left(d^2-c^2\right)\frac{6\nu+1}{2(2\nu-1)}\right\}+\frac{k_1K}{AE}\int_c^d r\left(\varepsilon_{eq}^p\right)^n\mathrm{d}r$$
$$+\frac{\alpha}{2(1-\nu)}\frac{\left(T_b-T_a\right)}{\ln\left(\frac{b}{a}\right)A}\left[\begin{matrix}-\nu d^2\ln\left(\frac{b}{d}\right)-\left\{\frac{\nu d^2\left(b^2-d^2\right)}{b^2+d^2\left(2\nu-1\right)}\right\}\left\{\ln\left(\frac{b}{a}\right)(2\nu-1)-\nu-\ln\left(\frac{d}{a}\right)\right\}\\-2(1-\nu)\left\{\ln\left(\frac{b}{a}\right)\frac{b^2}{2}-\ln\left(\frac{d}{a}\right)\frac{d^2}{2}-\frac{1}{4}\left(b^2-d^2\right)\right\}\end{matrix}\right], \tag{4.139}$$

where A is given by Eq. (4.74).

To evaluate the unknown boundary radii, c and d, a numerical procedure needs to be used. The procedure involves an iterative approach to estimate the values of c and d. The numerical solution procedure is described as follows:

The initial estimates for c and d can be obtained from non-hardening case by solving Eqs. (4.75) and (4.76) simultaneously using FSOLVE function in MATLAB. The initial guess value of ε_{eq}^p is taken as zero everywhere in the plastic zones I and II. With these values of c and d, the values of $\varepsilon_\theta^p, \varepsilon_r^p$ and ε_0^p are updated from Eqs. (4.127)–(4.129) for plastic zone I. Eq. (4.130) provides the updated values of ε_{eq}^{p} at any radial position in the plastic zone I. Similarly, using Eq. (4.133), the values of ε_{r}^{p} at different radial positions in the plastic zone II are updated. The updated values of ε_{eq}^{p} at different radial positions in the plastic zone II are obtained from Eq. (4.134). The values of ε_{eq}^{p} is updated further for fixed *c* and *d* in both the plastic zones and the procedure is repeated till the convergence in ε_{eq}^{p} is achieved. The integral terms involved in the expressions can be evaluated numerically by using two-Gauss-point formula. The two-Gauss-point formula for numerical integration is provided in Appendix D. Now, using the converged values of ε_{eq}^{p}, the boundary conditions of vanishing radial stress at the inner radius and at *r*=*c*, $\sigma_{\theta}^{\text{(plastic zone II)}} = \sigma_{z}^{\text{(plastic zone II)}}$ are solved to get the new estimates of *c* and *d*. If these new estimates of *c* and *d* are same as the previously estimated values of *c* and *d* the procedure is stopped, otherwise the whole procedure is repeated till the convergence for *c* and *d* is achieved.

4.5.2 Strain Hardening in Second stage of Elasto-plastic Deformation

The stress and strain expressions with strain hardening for the plastic zones I and II during the second stage of elasto-plastic deformation are still given by the expressions provided in Section 4.5.1. The stress and strain components in the plastic zone III and plastic zone IV incorporating strain hardening will be provided in this section.

Considering strain hardening, the Tresca yield criterion at the outer wall is given by

$$\sigma_{\theta} - \sigma_{r} = -k_{1}\sigma_{eq}, \qquad \sigma_{z} - \sigma_{r} = -k_{1}\sigma_{eq}. \qquad (4.140)$$

The plastic zone III, *f*≤*r*≤*b* from outer wall propagates inwards according to Eq. (4.140). The expressions for the stresses and the plastic strain components in this zone can be derived in a similar way as discussed in Subsection 4.2.6.2 and they are given by

$$\sigma_r = -k_1\sigma_Y \ln r - k_1 K \int_f^r \frac{\left(\varepsilon_{eq}^p\right)^n}{r_1} \mathrm{d}r_1 + C_7, \tag{4.141}$$

$$\sigma_\theta = \sigma_z = -k_1\sigma_Y \left(1+\ln r\right) - k_1 K \left(\varepsilon_{eq}^p\right)^n - k_1 K \int_f^r \frac{\left(\varepsilon_{eq}^p\right)^n}{r_1} \mathrm{d}r_1 + C_7, \tag{4.142}$$

$$\begin{aligned}\varepsilon_\theta^p = {} & \frac{1-2\nu}{E}\left[\frac{1}{2}\left(C_7 - k_1\sigma_Y \ln r\right) - \frac{2k_1K}{r^2}\int_f^r r_1\left(\varepsilon_{eq}^p\right)^n \mathrm{d}r_1 + k_1K\int_f^r \frac{\left(\varepsilon_{eq}^p\right)^n}{r_1}\mathrm{d}r_1 - \frac{3k_1K}{r^2}\int_f^r\left\{r_2\int_f^{r_2}\frac{\left(\varepsilon_{eq}^p\right)^n}{r_1}\mathrm{d}r_1\right\}\mathrm{d}r_2\right] \\ & + \frac{3-2\nu}{4E}k_1\sigma_Y + \frac{1-\nu}{E}k_1K\left(\varepsilon_{eq}^p\right)^n + \frac{1}{2}\alpha T_a + \frac{\alpha\left(T_b - T_a\right)}{2\ln\left(\frac{b}{a}\right)}\left\{\ln\left(\frac{r}{a}\right) - \frac{3}{2}\right\} - \frac{1}{2}\varepsilon_0 + \frac{C_8}{r^2},\end{aligned} \tag{4.143}$$

$$\begin{aligned}\varepsilon_r^p = {} & \frac{1-2\nu}{E}\left[\frac{1}{2}\left(C_7 - k_1\sigma_Y \ln r\right) - 2k_1K\int_f^r \frac{\left(\varepsilon_{eq}^p\right)^n}{r_1}\mathrm{d}r_1 + \frac{2k_1K}{r^2}\int_f^r r_1\left(\varepsilon_{eq}^p\right)^n \mathrm{d}r_1 + \frac{3k_1K}{r^2}\int_f^r\left\{r_2\int_f^{r_2}\frac{\left(\varepsilon_{eq}^p\right)^n}{r_1}\mathrm{d}r_1\right\}\mathrm{d}r_2\right] \\ & - \frac{7-6\nu}{4E}k_1\sigma_Y - \frac{2\left(1-\nu\right)}{E}k_1K\left(\varepsilon_{eq}^p\right)^n + \frac{1}{2}\alpha T_a + \frac{\alpha\left(T_b - T_a\right)}{2\ln\left(\frac{b}{a}\right)}\left\{\ln\left(\frac{r}{a}\right) + \frac{3}{2}\right\} - \frac{1}{2}\varepsilon_0 - \frac{C_8}{r^2},\end{aligned} \tag{4.144}$$

$$\begin{aligned}\varepsilon_0^p = {} & \varepsilon_0 - \frac{1-2\nu}{E}\left\{-k_1\sigma_Y \ln r + C_7 - k_1K\int_f^r \frac{\left(\varepsilon_{eq}^p\right)^n}{r_1}\mathrm{d}r_1\right\} + \frac{1-\nu}{E}k_1\sigma_Y + \frac{1-\nu}{E}k_1K\left(\varepsilon_{eq}^p\right)^n \\ & - \alpha T_a - \alpha\left(T_b - T_a\right)\frac{\ln\left(\frac{r}{a}\right)}{\ln\left(\frac{b}{a}\right)}.\end{aligned} \tag{4.145}$$

The equivalent plastic strain component in the plastic zone III is given by Eq. (4.130).

The plastic zone IV, *e*≤*r*≤*f* is developed as per the Tresca yield criterion, $\sigma_\theta - \sigma_r = -k_1\sigma_{eq}$. Deriving the equations for the stress and the plastic strain components as described in Subsection 4.2.6.3, the resulting expressions with strain hardening are given by

$$\sigma_r = \frac{E\alpha}{(2\nu-1)}T_a + \frac{E\alpha(T_b - T_a)}{2(1-\nu)\ln\left(\frac{b}{a}\right)}\left[\frac{1}{(2\nu-1)}\left\{\ln\left(\frac{d}{a}\right)+\frac{1}{2}-\frac{e^2}{2d^2}\right\}-\ln\left(\frac{e}{a}\right)\right]$$
$$+\left\{\frac{1}{2\nu-1}\left(1+\frac{e^2}{2d^2}\right)+\frac{1}{2}-\ln\left(\frac{r}{e}\right)\right\}k_1\sigma_Y + \frac{E\varepsilon_0}{(1-2\nu)} - k_1K\int_e^r \frac{\left(\varepsilon_{eq}^p\right)^n}{r_1}\mathrm{d}r_1, \tag{4.146}$$

$$\sigma_z = \frac{E\alpha}{(2\nu-1)}T_a + \frac{E\alpha(T_b - T_a)}{2(1-\nu)\ln\left(\frac{b}{a}\right)}\left[\frac{2\nu}{(2\nu-1)}\left\{\ln\left(\frac{d}{a}\right)+\frac{1}{2}-\frac{e^2}{2d^2}\right\}+2\nu\ln\left(\frac{r}{e}\right)-2\ln\left(\frac{r}{a}\right)\right]$$
$$+\left\{\frac{2\nu}{2\nu-1}\left(1+\frac{e^2}{2d^2}\right)-2\nu\ln\left(\frac{r}{e}\right)\right\}k_1\sigma_Y + \frac{E\varepsilon_0}{(1-2\nu)} - 2\nu k_1K\int_e^r \frac{\left(\varepsilon_{eq}^p\right)^n}{r_1}\mathrm{d}r_1 - \nu k_1K\left(\varepsilon_{eq}^p\right)^n. \tag{4.147}$$

The expression for σ_z can be obtained from the Tresca yield criterion with strain hardening.

$$\varepsilon_\theta^p = -\varepsilon_r^p = \frac{\alpha(T_b - T_a)}{2(1-\nu)\ln\left(\frac{b}{a}\right)}\left(\nu^2-1\right)+\left(1-\nu^2\right)\frac{k_1\sigma_Y}{E}+\frac{4\nu^2}{Er^2}k_1K\int_e^r\left\{r_2\int_e^{r_2}\frac{\left(\varepsilon_{eq}^p\right)^n}{r_1}\mathrm{d}r_1\right\}\mathrm{d}r_2$$
$$+\frac{2\nu^2}{Er^2}k_1K\int_e^r r_1\left(\varepsilon_{eq}^p\right)^n\mathrm{d}r_1+\left(1-\nu^2\right)\frac{k_1K}{E}\left(\varepsilon_{eq}^p\right)^n-\frac{2\nu^2k_1K}{E}\int_e^r\frac{\left(\varepsilon_{eq}^p\right)^n}{r_1}\mathrm{d}r_1+\frac{C_9}{r^2}. \tag{4.148}$$

In all the above expressions, r_1 and r_2 are dummy variables. The equivalent plastic strain component is given by Eq. (3.36). The various constants involved in the expressions can be evaluated using the conditions provided in Section 4.2.8. The resulting expressions for the constants C_5 and C_6 are given by

$$C_5 = -C_6 d^{-2\sqrt{2(1-\nu)}}\left\{\frac{1-\nu+\nu\sqrt{2(1-\nu)}}{1-\nu-\nu\sqrt{2(1-\nu)}}\right\}+\frac{k_1K\left\{1-\nu+\nu\sqrt{2(1-\nu)}\right\}}{2\sqrt{2(1-\nu)}}\int_c^d r_1^{-\sqrt{2(1-\nu)}}\left(\varepsilon_{eq}^p\right)^n\mathrm{d}r_1$$
$$-\frac{k_1Kd^{-2\sqrt{2(1-\nu)}}\left\{1-\nu+\nu\sqrt{2(1-\nu)}\right\}}{2\sqrt{2(1-\nu)}}\int_c^d r_1^{\sqrt{2(1-\nu)}}\left(\varepsilon_{eq}^p\right)^n\mathrm{d}r_1-\frac{E\alpha(T_b-T_a)}{(2\nu-1)\ln\left(\frac{b}{a}\right)}\frac{(1+\nu)}{d^{-1+\sqrt{2(1-\nu)}}\left\{1-\nu-\nu\sqrt{2(1-\nu)}\right\}}, \tag{4.149}$$

$$
\begin{aligned}
C_6 = {} & \frac{E\alpha\left(T_b - T_a\right)}{\left(2\nu - 1\right)\ln\left(\dfrac{b}{a}\right)}\left\{\frac{1-\nu-\nu\sqrt{2\left(1-\nu\right)}}{d^{-1-\sqrt{2(1-\nu)}}\,2\nu\sqrt{2\left(1-\nu\right)}}\right\}\left\{\ln\left(\frac{d}{a}\right)-\frac{2\nu+1}{2\nu-1}-\frac{\left(1+\nu\right)}{1-\nu-\nu\sqrt{2\left(1-\nu\right)}}\right\} \\
& + k_1 K\left\{\frac{1-\nu-\nu\sqrt{2\left(1-\nu\right)}}{2\sqrt{2\left(1-\nu\right)}}\right\}\int_c^d r_1^{\sqrt{2(1-\nu)}}\left(\varepsilon_{eq}^{p}\right)^n \mathrm{d}r_1 - \left\{\frac{1-\nu-\nu\sqrt{2\left(1-\nu\right)}}{d^{-1-\sqrt{2(1-\nu)}}\,2\nu\sqrt{2\left(1-\nu\right)}}\right\}\left(\frac{2\nu}{2\nu-1}\right)k_1\sigma_Y\frac{e^2}{2d^2} \\
& - \frac{E\alpha\left(T_b - T_a\right)}{2\left(1-\nu\right)\ln\left(\dfrac{b}{a}\right)}\left\{\frac{1-\nu-\nu\sqrt{2\left(1-\nu\right)}}{d^{-1-\sqrt{2(1-\nu)}}\,2\nu\sqrt{2\left(1-\nu\right)}}\right\}\left[\frac{1}{\left(2\nu-1\right)}\left\{\ln\left(\frac{d}{a}\right)+\frac{1}{2}-\frac{e^2}{2d^2}\right\}-\ln\left(\frac{d}{a}\right)+\frac{1}{2}-\frac{e^2}{2d^2}\right],
\end{aligned}
\tag{4.150}
$$

The constants C_3 and C_7 are expressed by the Eqs. (4.113) and (4.115), where the terms N and M are given by

$$
\begin{aligned}
N = {} & C_5 c^{-1+\sqrt{2(1-\nu)}} + C_6 c^{-1-\sqrt{2(1-\nu)}} + \frac{k_1\sigma_Y}{\left(2\nu-1\right)} + \frac{E\alpha T_a}{\left(2\nu-1\right)} + \frac{E\alpha\left(T_b - T_a\right)}{\left(2\nu-1\right)\ln\left(\dfrac{b}{a}\right)}\left\{\ln\left(\frac{c}{a}\right)-\frac{2\nu+1}{2\nu-1}\right\} \\
& - k_1\sigma_Y \ln c - k_1 K\int_a^c \frac{\left(\varepsilon_{eq}^{p}\right)^n}{r_1}\mathrm{d}r_1,
\end{aligned}
\tag{4.151}
$$

$$
\begin{aligned}
M = {} & \frac{E\alpha}{\left(2\nu-1\right)}T_a + \frac{E\alpha\left(T_b - T_a\right)}{2\left(1-\nu\right)\ln\left(\dfrac{b}{a}\right)}\left[\frac{1}{\left(2\nu-1\right)}\left\{\ln\left(\frac{d}{a}\right)+\frac{1}{2}-\frac{e^2}{2d^2}\right\}-\ln\left(\frac{e}{a}\right)\right] \\
& \left\{\frac{1}{2\nu-1}\left(1+\frac{e^2}{2d^2}\right)+\frac{1}{2}-\ln\left(\frac{f}{e}\right)+\ln f\right\}k_1\sigma_Y - k_1 K\int_e^f \frac{\left(\varepsilon_{eq}^{p}\right)^n}{r_1}\mathrm{d}r_1.
\end{aligned}
\tag{4.152}
$$

The expression for C_4 is still given by Eq. (4.138). The final expression for C_8 is obtained as

$$
\begin{aligned}
C_8 = {} & \frac{\alpha f^2\left(T_b - T_a\right)}{2\left(1-\nu\right)\ln\left(\dfrac{b}{a}\right)}\left(\nu^2-1\right)+\left(1-\nu^2\right)f^2\frac{k_1\sigma_Y}{E}+\frac{4\nu^2}{E}k_1 K\left(\frac{2}{\sqrt{3}}\right)^n\int_e^f\left\{r_2\int_e^{r_2}\frac{\left(\varepsilon_{eq}^{p}\right)^n}{r_1}\mathrm{d}r_1\right\}\mathrm{d}r_2 \\
& + \frac{2\nu^2}{E}k_1 K\int_e^f r_1\left(\varepsilon_{eq}^{p}\right)^n \mathrm{d}r_1 + \left(1-\nu^2\right)f^2\frac{k_1 K}{E}\left(\varepsilon_{eq}^{p}\right)^n\Big|_{r=f} - \frac{2\nu^2 k_1 K}{E}f^2\int_e^f\frac{\left(\varepsilon_{eq}^{p}\right)^n}{r_1}\mathrm{d}r_1 + C_9 \\
& - \frac{\left(1-2\nu\right)}{E}\left[\frac{f^2}{2}\left(C_7 - k_1\sigma_Y\ln f\right)\right]-\frac{3-2\nu}{4E}f^2 k_1\sigma_Y - \frac{1-\nu}{E}f^2 k_1 K\left(\varepsilon_{eq}^{p}\right)^n\Big|_{r=f} - \frac{f^2}{2}\alpha T_a \\
& - \frac{\alpha\left(T_b - T_a\right)}{2\ln\left(\dfrac{b}{a}\right)}f^2\left\{\ln\left(\frac{f}{a}\right)-\frac{3}{2}\right\}+\frac{f^2}{2}\varepsilon_0.
\end{aligned}
\tag{4.153}
$$

The constant C_9 is same as expressed by Eq. (4.117). The resulting expression of the constant axial strain, ε_0 is obtained as

$$
\begin{aligned}
\varepsilon_0 = {} & \frac{k_1\sigma_Y}{BE}\left[\begin{array}{l} \ln c\left(\dfrac{c^2}{2}\right)-\ln a\left(\dfrac{a^2}{2}\right)+\dfrac{1}{4}\left(c^2-a^2\right)+\dfrac{\nu}{2\nu-1}\left(d^2-c^2\right)+\dfrac{\nu}{2\nu-1}\left(1+\dfrac{e^2}{2d^2}\right)\left(f^2-d^2\right) \\ -\nu\left\{\ln\left(\dfrac{f}{e}\right)f^2-\dfrac{1}{2}\left(f^2-e^2\right)\right\}-\dfrac{1}{4}\left(b^2-f^2\right)-\ln b\left(\dfrac{b^2}{2}\right)+\ln f\left(\dfrac{f^2}{2}\right) \end{array}\right] \\
& +\frac{N}{2BE}\left(c^2-a^2\right)+\frac{C_5}{BE}\left\{\frac{d^{1+\sqrt{2(1-\nu)}}-c^{1+\sqrt{2(1-\nu)}}}{1+\sqrt{2(1-\nu)}}\right\}+\frac{C_6}{BE}\left\{\frac{d^{1-\sqrt{2(1-\nu)}}-c^{1-\sqrt{2(1-\nu)}}}{1-\sqrt{2(1-\nu)}}\right\}+\frac{\alpha T_a}{2(2\nu-1)B}\left(f^2-c^2\right) \\
& +\frac{\alpha\left(T_b-T_a\right)}{(2\nu-1)\ln\left(\dfrac{b}{a}\right)B}\left\{\ln\left(\frac{d}{a}\right)\frac{d^2}{2}-\ln\left(\frac{c}{a}\right)\frac{c^2}{2}-\frac{3}{4}\left(d^2-c^2\right)-\frac{d^2-c^2}{2\nu-1}\right\} \\
& +\frac{\alpha\left(T_b-T_a\right)}{2(1-\nu)\ln\left(\dfrac{b}{a}\right)B}\left[\begin{array}{l} \dfrac{\nu}{(2\nu-1)}\left\{\ln\left(\dfrac{d}{a}\right)+\dfrac{1}{2}-\dfrac{e^2}{2d^2}\right\}\left(f^2-d^2\right)-\left\{\ln\left(\dfrac{e}{a}\right)e^2-\ln\left(\dfrac{d}{a}\right)d^2-\dfrac{1}{2}\left(e^2-d^2\right)\right\} \\ +\nu\left\{\ln\left(\dfrac{f}{e}\right)f^2-\dfrac{1}{2}\left(f^2-e^2\right)\right\}-\left\{\ln\left(\dfrac{f}{a}\right)f^2-\ln\left(\dfrac{e}{a}\right)e^2-\dfrac{1}{2}\left(f^2-e^2\right)\right\} \end{array}\right] \\
& +\frac{M}{2BE}\left(b^2-f^2\right)+k_1K\int_a^c r\left(\varepsilon_{eq}^p\right)^n \mathrm{d}r+\frac{k_1K\left\{1-\nu+\nu\sqrt{2(1-\nu)}\right\}}{2BE\sqrt{2(1-\nu)}}\int_c^d\left[r^{\sqrt{2(1-\nu)}}\int_c^r r_1^{-\sqrt{2(1-\nu)}}\left(\varepsilon_{eq}^p\right)^n \mathrm{d}r_1\right]\mathrm{d}r \\
& -\frac{k_1K\left\{1-\nu-\nu\sqrt{2(1-\nu)}\right\}}{2BE\sqrt{2(1-\nu)}}\int_c^d\left[r^{-\sqrt{2(1-\nu)}}\int_c^r r_1^{\sqrt{2(1-\nu)}}\left(\varepsilon_{eq}^p\right)^n \mathrm{d}r_1\right]\mathrm{d}r+\frac{k_1K}{BE}\int_c^d r\left(\varepsilon_{eq}^p\right)^n \mathrm{d}r-\frac{2\nu k_1K}{BE}\int_e^f\left\{r\int_e^r\frac{\left(\varepsilon_{eq}^p\right)^n}{r_1}\mathrm{d}r_1\right\}\mathrm{d}r \\
& -\frac{\nu k_1K}{BE}\int_e^f r\left(\varepsilon_{eq}^p\right)^n \mathrm{d}r-\frac{k_1K}{BE}\int_f^b r\left(\varepsilon_{eq}^p\right)^n \mathrm{d}r-\frac{k_1K}{BE}\int_f^b\left\{r\int_f^r\frac{\left(\varepsilon_{eq}^p\right)^n}{r_1}\mathrm{d}r_1\right\}\mathrm{d}r+\frac{k_1K}{BE}\int_a^c\left\{r\int_a^r\frac{\left(\varepsilon_{eq}^p\right)^n}{r_1}\mathrm{d}r_1\right\}\mathrm{d}r,
\end{aligned}
\tag{4.154}
$$

where B is given by Eq. (4.121).

The unknown boundary radii, c, d, e and f can be obtained following the similar numerical procedure as explained for the first stage of elasto-plastic deformation in Section 4.5.1.

4.5.3 Numerical Comparison of Stresses with and without Strain Hardening

To study the effect of strain hardening numerically, a numerical comparison of the stresses with and without strain hardening is carried out for SS304 and aluminum cylinders. The SS304 and aluminum cylinders are considered under temperature difference of 130 °C and 75 °C, respectively. The SS304 cylinder undergoes first stage of elasto-plastic deformation for the temperature difference of 130 °C. The aluminum cylinder undergoes second stage of elasto-plastic deformation for 75 °C of temperature difference.

The elasto-plastic stresses generated in the cylinders are simulated numerically for both non-hardening and strain hardening case. In the case of strain hardening, the K and n values for the SS304 cylinder are taken as 1425 MPa & 0.70 and that for aluminum are taken as 58.18 MPa & 0.48 in Ludwik's hardening law. In SS304 cylinder, the plastic zones at the inner wall propagate outwards to a radial position of 13.3243 mm for the non-hardening case, whilst in strain hardening the plastic zones propagate to a radial position of 13.2690 mm. In aluminum cylinder, the inner plastic zones propagate outwards to a radial position of 12.0385 mm and the outer plastic zones propagate inwards to a radial position of 18.3630 mm in the non-hardening case. In the case of strain hardening, the inner plastic zones propagate outwards to a radial position of 12.0215 mm and the outer plastic zones propagate inwards to a radial position of 19.0966 mm. The resulting elasto-plastic stress distribution with and without strain hardening for both the cylinders are shown in Figure 4.9 as a function of radial position.

It is observed that the effect of strain hardening in SS304 as well as in aluminum cylinder is not very significant. Due to strain hardening, the stresses in the plastic zones are little higher than the stresses without strain hardening. The maximum deviation between the hoop and axial stresses is observed to be at the inner radius. In the case of SS304 cylinder, the maximum deviation of the stresses is only 8.34% and that in the aluminum cylinder is only 4.51% with respect to the non-hardening case.

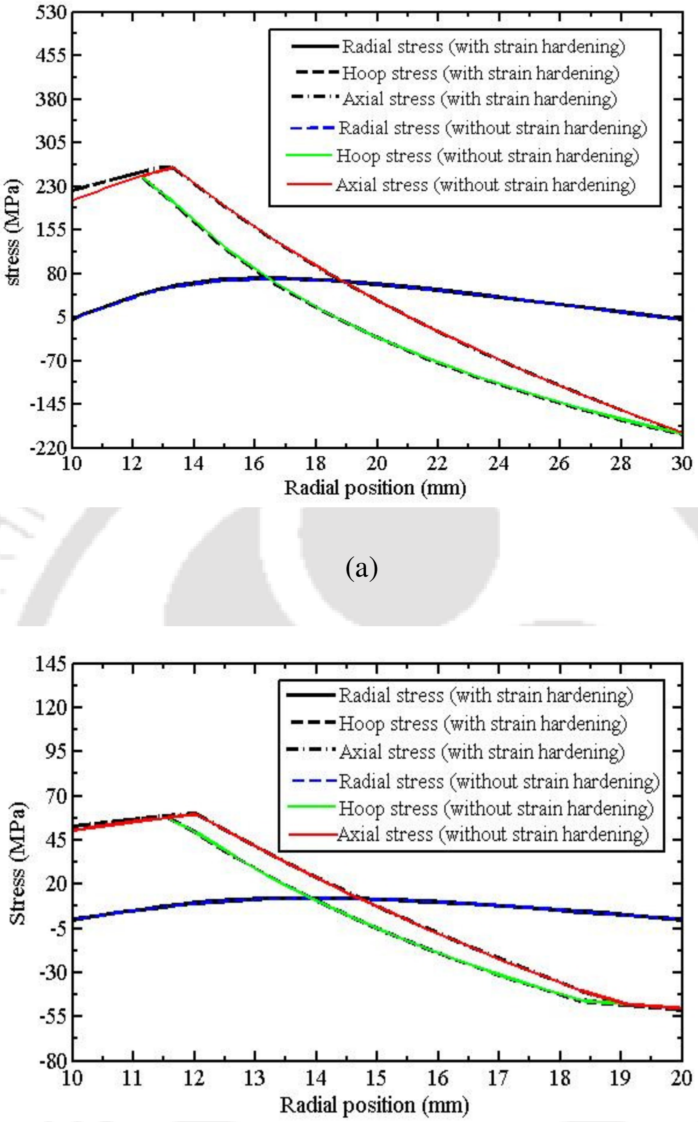

(a)

(b)

Figure 4.9 Elasto-plastic stress distributions with and without strain hardening in (a) SS304 and (b) aluminum cylinders

4.6 Summary

In this chapter, the thermal autofrettage process is analyzed theoretically using generalized plane strain condition for thick-walled cylinders. The analysis is carried out considering Tresca yield criterion and its associated flow rule. Numerical simulations are carried out for the feasibility of the thermal autofrettage of aluminum and SS304 cylinders using the developed analytical closed form solutions for non-hardening case. The simulation results reveal encouraging trends of the residual stresses in the cylinders, which is similar as in the case of hydraulic autofrettage. The effect of strain hardening is also incorporated in the solutions using Ludwik's hardening law. A numerical comparison of the elasto-plastic stresses under thermal gradient is carried out for SS304 and aluminum cylinders. The comparison shows that the effect of strain hardening is not very significant.

Chapter 5

Three-Dimensional Finite Element Analysis of Thermal Autofrettage and its Comparison with Plane Stress and Generalized Plane Strain Models

5.1 Introduction

The thick-walled cylinders subjected to pressures and temperatures find several applications in many industries, for example, oil, chemical, artillery and nuclear power plant industries. In most of the cases, the design attempts to keep the stresses in the cylinders within elastic limits. However, it is always better to carry out an elasto-plastic analysis in order to get an idea about safety in case of untoward situations. Moreover, in an autofrettage process, the plastic deformation is deliberately produced to induce compressive stresses in the inner side of the cylinder. There are also examples where plastic deformation is permitted by design. Thus, the elasto-plastic analysis of the thick-walled cylinders is an attractive research area.

The elasto-plastic behaviour of cylinders in hydraulic autofrettage due to internal pressure loading is well-recognized. There are only a few papers analysing the elasto-plastic behaviour of cylinders under thermal loading. Orçan and Gamer (1991), Orçan (1994) and Orçan (1995) analyzed the thermo-elasto-plastic behaviour of solid cylinders. The thermo-elasto-plastic behaviour of internal heat generating tubes has been studied by Wong and Simionescu (1996), Orçan and Gulgec (2000) and Orçan and Eraslan (2001). No study has been found treating the thermo-elasto-plastic analysis of hollow thick-walled cylinders due to radial thermal gradient. The thermo-elasto-plastic analysis of thick-walled cylinders under radial thermal gradient across the cylinder wall thickness has been carried out in Chapters 3 and 4 assuming plane stress and generalized plane strain conditions, respectively. It is suggested that the plane stress analysis is suitable for the thermal autofrettage of thin circular hollow disks (very short cylinders) and the generalized plane strain analysis provides reasonable solutions for the thermal autofrettage of long cylinders. However, there is no quantification for the length of the cylinder upto which these analyses are applicable. Therefore, this work attempts to develop a criterion on the basis of length to wall thickness ratio of the cylinders for the applicability of the analytical models.

In this chapter, a three-dimensional finite element method (3-D FEM) thermo-elasto-plastic analysis of thick-walled cylinders in thermal autofrettage is carried out. The FEM simulations are carried out in finite element based ABAQUS package. The FEM simulations of elasto-plastic as well as the residual stresses generated during the thermal autofrettage of cylinders are carried out considering strain hardening. Further, FEM simulations are carried out without strain hardening to assess the effect of strain hardening. The results of the FEM analysis are compared with the analytical plane stress and generalized plane strain models. The main objective of the FEM analysis is to develop a dividing line between the analytical models on the basis of the length to wall thickness ratio, $L/(b-a)$ of the cylinder.

5.2 Problem definition

A homogeneous thick-walled hollow cylinder with inner radius, a and outer radius, b is considered. The inner wall is subjected to a temperature T_a and the outer wall is subjected to a temperature T_b such that $T_b>T_a$. The problem is solved using ABAQUS standard code. Under the radial temperature difference, (T_b-T_a), the steady state condition is assumed in ABAQUS standard simulation. The temperature distribution in the cylinder is given by Eq. (3.1). The temperature difference required for initial yielding is decided using either Eq. (3.15) or Eq. (4.19). Thus, the cylinder is subjected to a temperature difference greater than the temperature difference required for initial yielding for achieving thermal autofrettage. In the present analysis, the strain hardening of the material during plastic deformation is considered. For comparison of the FEM results with the plane stress and the generalized plane strain model, the closed form analytical solutions developed in Chapters 3 and 4 are used.

5.3 Three-Dimensional Finite Element Modelling

A 3-D finite element model has been developed to simulate the elasto-plastic and residual stresses in thermal autofrettage using commercial finite element package ABAQUS 6.10. The model is a 3-D solid extruded cylindrical geometry made of aluminum shown in Figure 5.1. The inner and outer radii of the cylinder are taken as 10 mm and 20 mm, respectively. The temperature difference across the wall thickness of the cylinder is considered as 75 °C for achieving thermal autofrettage. The thermal stress analysis during the thermal autofrettage of aluminum cylinder for different lengths is carried out.

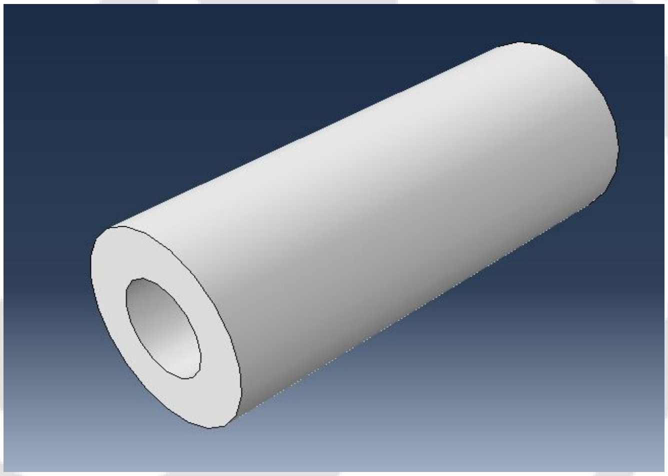

Figure 5.1 The 3-D cylindrical geometry in ABAQUS

A coupled thermo-mechanical approach is used to obtain the steady-state thermal stress solutions in ABAQUS/Standard. A coupled thermal-stress analysis is needed when the stress analysis is dependent on the temperature distribution. In thermal autofrettage process, the cylinder is subjected to non-homogeneous elasto-plastic deformation due to radial thermal gradient between the outer and inner wall of the cylinder. Thus, for the stress solution in thermal autofrettage process, coupled temperature-displacement elements should be provided in ABAQUS/Standard.

The ABAQUS/standard solver is based on the implicit method of solving a non-linear problem. In thermal stress analysis, ABAQUS/Standard uses a backwarddifference scheme to integrate the temperatures and solves the nonlinear coupled system using Newton's method. An exact implementation of Newton's method is used for solving the present problem in ABAQUS/standard. The method involves a non-symmetric Jacobian matrix representation of the coupled equations given by (ABAQUS user's manual, 2007)

$$\begin{bmatrix} K_{uu} & K_{u\theta} \\ K_{\theta u} & K_{\theta\theta} \end{bmatrix} \begin{Bmatrix} \Delta u \\ \Delta\theta \end{Bmatrix} = \begin{Bmatrix} R_u \\ R_\theta \end{Bmatrix}, \tag{5.1}$$

where Δu and $\Delta\theta$ are the respective corrections to the incremental displacement and temperature, K_{ij} are submatrices of the fully coupled Jacobian matrix, and R_u and R_θ are the mechanical and thermal residual vectors, respectively. The system of mechanical and thermal equations is solved simultaneously. This requires the use of the unsymmetric matrix storage and solution scheme. The method provides quadratic convergence when the solution estimate is within the radius of convergence of the algorithm.

5.3.1 Material Properties

The material properties of aluminum are taken as presented in Table 5.1. In plasticity, the hardening model is defined as isotropic hardening. The strain hardening of the material during plastic deformation is taken into account. To define the plastic behaviour of the cylinder during plastic deformation, Ludwik's hardening law is used (Eq. 3.20), where the hardening coefficient, K and strain hardening exponent, n are taken as 58.18 MPa and 0.48, respectively.

Table 5.1 Material properties of aluminum

Yield stress, σ_Y (MPa)	Modulus of elasticity, E (GPa)	Poisson's ratio, v	Coefficient of thermal expansion, α (/°C)	Mass density, ρ (kg/m^3)	Thermal conductivity, k (W/mK)	Specific heat, c_p (J/kgK)
50.3	69	0.30	22.2×10^{-6}	2700	205	900

5.3.2 Boundary Conditions and Mesh Generation

The thermal stresses in the cylinder are due to the radial thermal gradient across the wall thickness. For analyzing the thermal stress, the Dirichlet temperature boundary conditions are specified at the inner and outer surfaces of the cylinder. The temperature of the inner surface is prescribed as 25 °C and that of the outer surface is prescribed as 100 °C. During the analysis, the rotation vector in the circumferential direction is constrained, but the cylinder is free to expand axially. An eight noded continuum C3D8T thermally coupled brick, trilinear displacement and temperature element is used to generate the mesh on the cylinder. The cylinder with typical C3D8T elements is shown in Figure 5.2

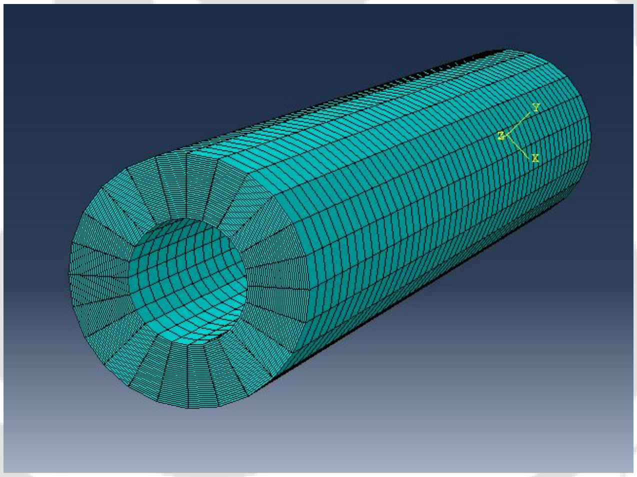

Figure 5.2 The cylindrical geometry with typical C3D8T element

5.3.3 Mesh Sensitivity Analysis

A mesh sensitivity analysis is carried out in order to select an appropriate mesh size. The mesh sensitivity analysis is presented in Table 5.2 based on the maximum values of radial, hoop and axial stresses generated in the cylinder. The length of the cylinder was taken as 100 mm. It is observed from Table 2 that the Mesh 9 with 24 elements in the radial direction, 32 elements in the circumferential direction and 50 elements in the axial direction leads to the convergent mesh. Thus, there are total 38,400 elements. This mesh is expected to provide less than 1% error in solution.

The thermo-elasto-plastic stresses generated in the cylinder are analyzed varying the length of the cylinder. A comparative study with the plane stress and generalized plain strain models is presented for different length to wall-thickness ratio of the cylinder in Section 5.3.4.

Table 5.2 Mesh sensitivity analysis

Mesh	Number of elements in			Maximum value of			Screen time (s)
	Radial direction	Circumferential direction	Axial direction	Radial stress (MPa)	Hoop stress (MPa)	Axial stress (MPa)	
Mesh 1	6	4	25	20.61	48.71	58.20	2
Mesh 2	12	4	25	11.45	59.50	58.04	5
Mesh 3	24	4	25	10.48	62.40	58.00	16
Mesh 4	48	4	25	10.58	63.14	57.99	34
Mesh 5	24	8	25	12.39	59.71	58.34	35
Mesh 6	24	16	25	12.63	61.07	59.18	247
Mesh 7	24	32	25	12.74	62.24	61.28	926
Mesh 8	24	64	25	12.90	62.90	62.29	2959
Mesh 9	**24**	**32**	**50**	**12.74**	**62.76**	**61.21**	**3664**
Mesh 10	24	32	100	12.73	62.93	61.19	4346

5.3.4 Comparison of 3-D Finite Element Elasto-plastic Thermal Stresses with the Plane Stress and Generalized Plane Strain Models for Different Length to Wall Thickness Ratios of the Cylinder

The 3-D FEM simulations were carried out for different length to wall thickness ratios of the cylinder and the results were compared with analytical plane stress and generalized plane strain model. The analytical solutions for plane stress are presented in Chapter 3 and the analytical generalized plane strain solutions are presented in Chapter 4. The present FEM analysis is carried out in 2.40-GHz processor and 2.60-GB random-access memory (RAM) ACER PC and it takes about 1 h of screen time. However, the analytical models provide the solution in less than 10 minutes. The comparison of radial, hoop and axial stresses between 3-D FEM and analytical models along the radial path for different length to wall thickness ratio is shown in Table 5.3 using L_2 norm of error in stresses. The stresses along a radial path from the 3-D ABAQUS finite element model are obtained considering a radial path at the mid length of the cylinder. The stresses along a radial path at the edges become sufficiently low in FEM model and are not taken into account for the analysis.

Table 5.3 Comparison of stresses between 3-D FEM and analytical models

$L/(b-a)$	L_2 norm of error in stresses between FEM and plane stress (MPa)			L_2 norm of error in stresses between FEM and generalized plane strain (MPa)		
	σ_r	σ_θ	σ_z	σ_r	σ_θ	σ_z
10	5.5849	26.7094	134.5956	**2.4418**	**4.3992**	**2.5369**
8	5.5148	27.3775	136.0487	**2.5578**	**4.7597**	**2.7440**
6	5.9687	29.4939	137.3141	2.4754	7.6960	4.1740
5	7.4358	28.3009	133.9557	4.9296	8.7777	11.7016
4	7.8224	40.6167	112.6305	3.8787	31.2258	24.3158
2	4.6443	36.8936	30.4968	4.9293	43.5744	110.0771
1	**3.4278**	**5.1446**	**3.6140**	8.2861	33.3531	135.7536
0.5	**2.7080**	**3.7979**	**1.3881**	7.1190	33.2992	136.0458

It is observed from Table 1 that L_2 norm of error in stresses between 3-D FEM and generalized plane strain are reasonably small when the length to wall thickness ratio of the cylinder is greater than or equal to 6. Thus, the generalized plane strain model is well established for $L/\,(b-a) \geq 6$. It is also observed from Table 1 that when $L/\,(b-a) \leq 1$, the L_2 norm of error between 3-D FEM and plane stress becomes smaller. This shows that the plane stress analytical model is valid for length to wall thickness ratio, $L/\,(b-a) \leq 1$. The comparison of 3-D finite element solutions with the generalized plane strain model for $L/\,(b-a) = 10$ is shown in Figure 5.3 (a). Figure 5.3 (b) shows the comparison of 3-D finite element results with the plane stress model for $L/\,(b-a) = 0.5$ in aluminum cylinder.

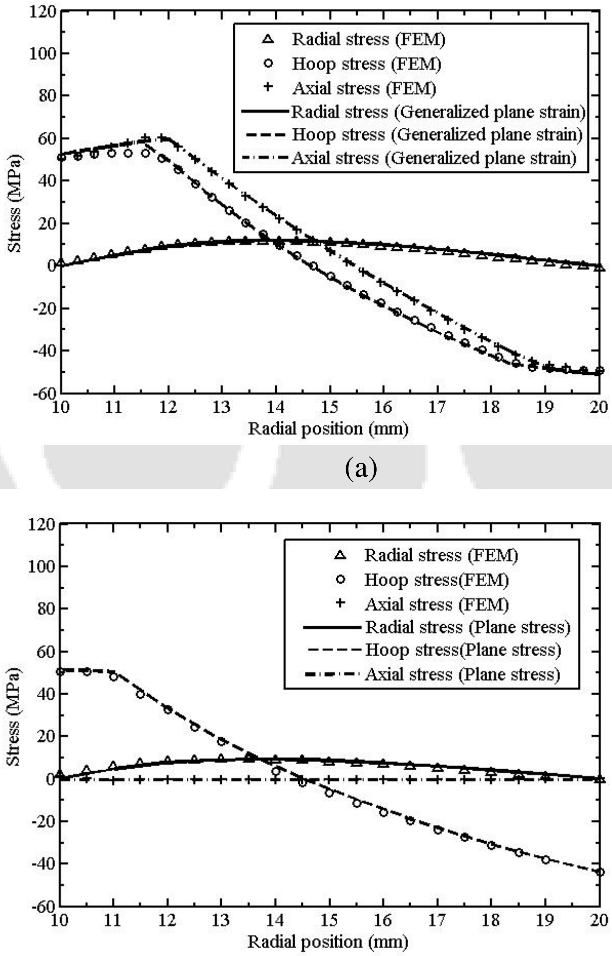

(a)

(b)

Figure 5.3 Comparison of elasto-plastic stresses between 3-D FEM and (a) generalized plane strain for $L/(b-a) = 10$, (b) plane stress for $L/(b-a) = 0.5$ in aluminum cylinder

It is to be noted that ABAQUS uses von Mises yield criterion to solve metal plasticity problems. The analytical solutions are based on Tresca yield criterion. Therefore, a slight deviation is observed between the FEM and analytical solutions in Figure 5.3.

5.4 Finite Element Residual Thermal Stress solutions

The whole cylinder is cooled to room temperature (25 °C) by imposing the cooling boundary condition in ABAQUS/Standard. This generates the residual thermal stresses in the cylinder. The finite element residual thermal stresses in the cylinder are obtained along a radial path at the mid length.

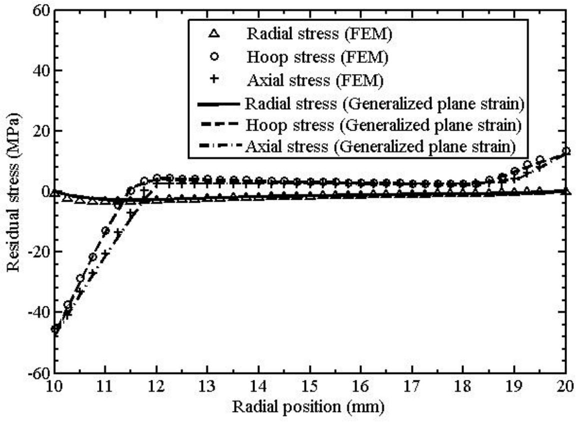

(a)

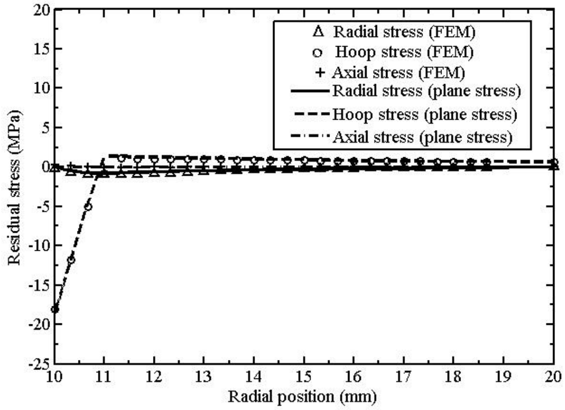

(b)

Figure 5.4 Comparison of residual stresses between 3-D FEM and (a) generalized plane strain for $L/(b-a) = 10$, (b) plane stress for $L/(b-a) = 0.5$ in aluminum cylinder

The results are shown in Figure 5.4 along with the predictions of generalized plane strain model for $L/(b-a)$=10 and plane stress model for $L/(b-a)$=0. 5. It is observed that the finite element predictions of the residual stresses are in close agreement with the analytical models for the respective $L/(b-a)$ ratio of the cylinders. The analytical predictions of the residual stresses are obtained assuming the unloading process to be completely elastic as presented in Chapters 3 and 4.

5.5 Effect of Strain Hardening

The effect of strain hardening in thermal autofrettage is studied for both generalized plane strain and plane stress case using 3-D finite element method. To study the effect of strain hardening in generalized plane strain, the analytical results of elastic-plastic thermal stresses for non-hardening aluminum and SS304 cylinder presented in Subsections 4.4.1.1 & 4.4.2.1 are compared with the finite element results. The finite element results are obtained with and without strain hardening for the cylinders. The length of the cylinder is taken as 200 mm to ensure generalized plane strain condition. Thus, $L/(b-a)$ is 20 for aluminum cylinder and for SS304 cylinder this ratio is 10. For carrying out the 3-D FEM simulation of SS304 cylinder an appropriate mesh size (48 elements in the circumferential direction, 48 elements in the radial direction and 100 elements in the axial direction) was considered. The results of finite element simulations with and without strain hardening are plotted together with the analytical results predicted by the generalized plane strain model for both aluminum and SS304 cylinder are shown in Figures 5.5 and 5.6, respectively. It is observed that there is negligible difference between the stresses obtained by generalized plane strain closed form expressions and 3-D finite element simulations with and without strain hardening. A maximum of only ±5% variation among the stresses between the analytical and finite element results is observed. It is worth noting that the finite element results with and without strain-hardening are in good agreement with the generalized plane strain analytical results. This shows that the effect of strain-hardening is not very significant in the present analysis.

For the case of plane stress, the same cylinders are considered under the same temperature difference between the outer and inner wall of the cylinders as considered for the generalized plane strain case. Only the length of the cylinders is taken as 10 mm to ensure the plane stress condition. Thus, the length to wall thickness ratio, $L/(b-a)$ is 1 for the aluminum cylinder and it is 0.5 for the SS304 cylinder. The non-hardening analytical results are obtained by using the plane stress equations developed in Chapter 3, where the hardening coefficient, K=0. The 3-D finite element simulations are carried out with and without strain hardening and they

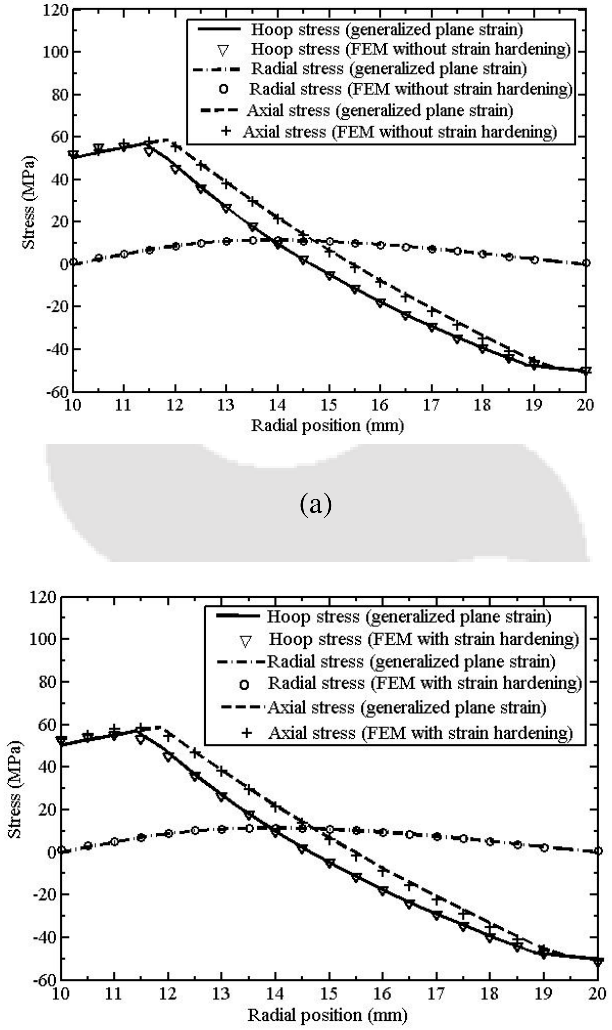

(a)

(b)

Figure 5.5 Comparison of 3-D FEM stresses with generalized plane strain model: (a) without strain hardening, (b) with strain hardening in aluminum cylinder for $L/(b-a)$=20 are compared with the analytical results to study the effect of strain hardening. The comparisons are shown in Figures 5.7 and 5.8 for aluminum and SS304 cylinder, respectively. It is observed that the effect of strain hardening is negligible. The stresses in the strain hardened cylinders deviate by less than 5% as compared to the stresses in the cylinders without strain hardening.

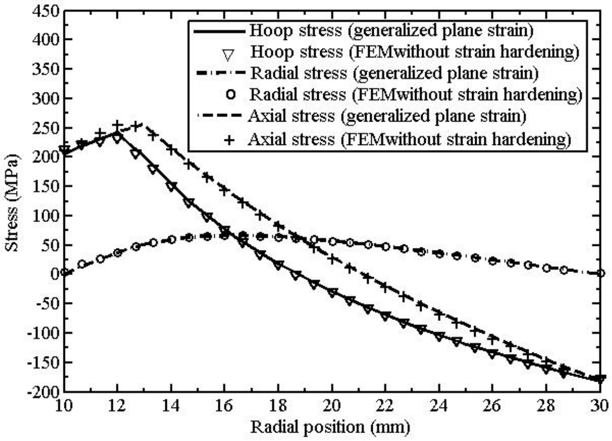

(a)

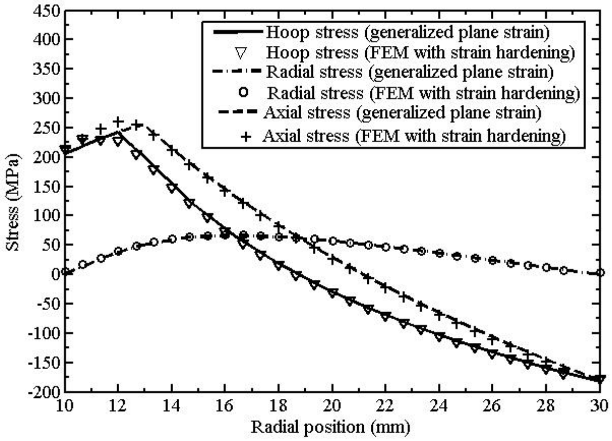

(b)

Figure 5.6 Comparison of 3-D FEM stresses with generalized plane strain model: (a) without strain hardening, (b) with strain hardening in SS304 cylinder for $L/(b-a)=10$

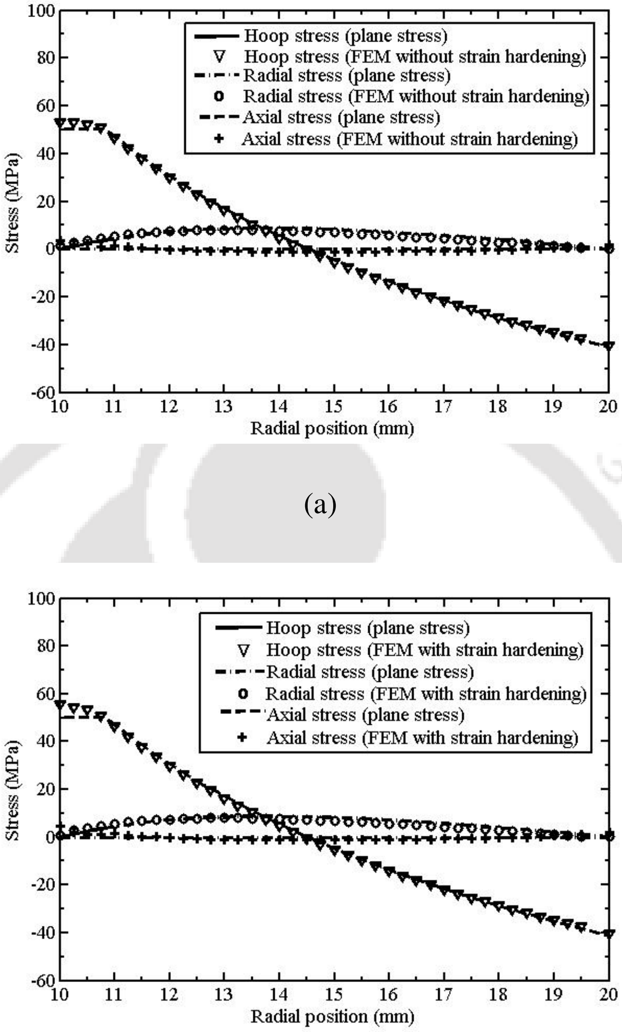

(a)

(b)

Figure 5.7 Comparison of 3-D FEM stresses with plane stress model: (a) without strain hardening, (b) with strain hardening in aluminum cylinder for *L*/(*b*–*a*)=1

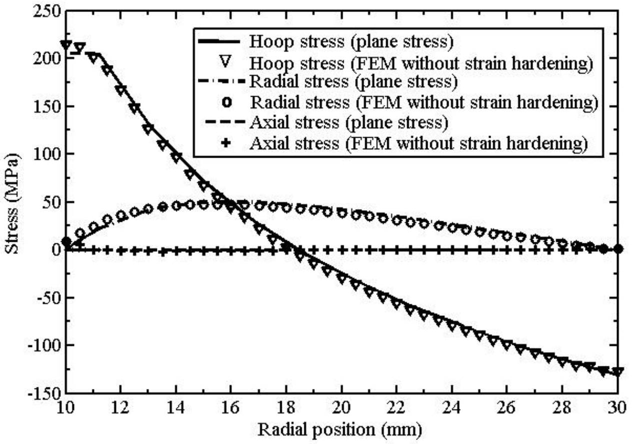

(a)

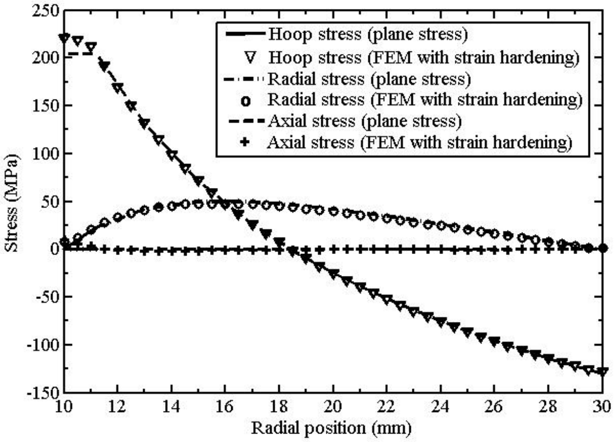

(b)

Figure 5.8 Comparison of 3-D FEM stresses with plane stress model: (a) without strain hardening, (b) with strain hardening in aluminum cylinder for *L*/(*b*–*a*)=0.5

5.6 Summary

In this chapter the three-dimensional finite element elasto-plastic deformation of thick-walled cylinder under radial temperature gradient is carried out. The 3-D FEM results are compared with the plane stress and the generalized plane strain models for different length to wall thickness ratio, *L*/(*b*–*a*) of the cylinder. The comparison suggests the applicability of the developed analytical models on the basis of *L*/(*b*–*a*) ratio of the cylinder. The generalized plane strain analytical model provides realistic solution for $L/(b-a)\geq 6$. Thus, this model is suitable for the thermal autofrettage of long cylinders such as gun barrels, pressure vessels and thick pipes. The plane stress analytical model provides good results for very short cylinders such as thin disks with $L/(b-a)\leq 1$. A typical comparison of FEM elasto-plastic stresses in aluminum cylinder with the generalized plane strain and plane stress models is shown for $L/(b-a) = 10$ and 0.5, respectively. The unloading of temperature difference across the wall thickness of the cylinder is also simulated in ABAQUS and the resulting residual stresses are compared with the generalized plane strain and plane stress models. The comparisons shows a very good agreement with the analytical models for the appropriate $L/(b-a)$ ratios. The finite element simulations are also carried out for aluminum and SS304 cylinders with and without strain hardening taking appropriate lengths corresponding to generalized plane strain and plane stress condition. The FEM results with and without strain hardening are compared with the respective analytical results without considering strain hardening. The comparisons reveal that the effect of strain hardening in the present cases is not very significant. There is only a deviation of about 5% in the stresses due to strain hardening for all the cases.

Chapter 6

An Experimental Study of Thermal Autofrettage Process

6.1 Introduction

The thermal autofrettage is a potential process for generating beneficial compressive residual stresses at and around the inner wall of a thick-walled cylinder or disk. It is accomplished by the removal of the radial thermal gradient that was applied to cause the non-homogenous elasto-plastic deformation within the wall. The compressive residual stresses reduce the effect of the working stress in the cylinder, when subjected to high pressure. This enhances the pressure carrying capacity of the cylinder as well as increases its fatigue strength. Due to the influence of the compressive residual stresses on enhancing the pressure carrying capacity and lifetime, the determination of the residual stresses in any autofrettage process is important for the practical reliability of the process. The theoretical determination of residual stresses in thermal autofrettage process is carried out in Chapter 3 using plane stress assumption and in Chapter 4 using generalized plane strain condition. It is shown in Chapter 5 that the generalized plane strain model is suitable for the thermal autofrettage of thick-walled long cylinders which has the most practical significance in industries. The present chapter investigates the thermal autofrettage of thick-walled cylinders experimentally. An experimental setup has been developed to carry out thermal autofrettage of thick-walled cylinders by creating a radial thermal gradient.

The experimental determination of the residual stress distribution is necessary in order to get confidence in the analytical and numerical model of the process. Researchers have used various well-established techniques for evaluating the residual stresses experimentally such as the Sachs boring method, deep hole drilling method, compliance method, neutron diffraction method and X-rays diffraction

(XRD) method (Stacey *et al*., 1985; Stacey and Webster, 1988; Venter *et al*., 2000; George and Smith, 2000; Jahed *et al*., 2012). In this work, the residual stress field in the thermally autofrettaged cylinders is measured experimentally using Sachs boring technique. Further, the measured residual stresses are compared with the generalized plane strain analytical model presented in Chapter 4.

Many researchers showed that the compressive residual stresses increase the surface hardness whilst the tensile residual stresses decrease the surface hardness (Kokubo, 1932; Pharr *et al*., 1994; Tosha, 2002). The present work also establishes the generation of residual stresses in the thermally autofrettaged cylinders on the basis of Vickers microhardness test. Parker *et al*. (1983), Parker and Underwood (1998) reported that the presence of residual stresses can be detected by making a single radial cut in the autofrettaged cylinder and measuring the opening angle due to the released pure bending moment 'locked-in' by the residual hoop stresses. In the present work, the presence of residual stresses is also confirmed by measuring the opening angle after cutting thermally autofrettaged cylinder along a radius and comparing it with the theoretical opening angle based on the residual hoop stress distribution predicted by the generalized plane strain model. Thus, the objective of the present chapter is to carry out an experimental study of the thermal autofrettage of thick-walled cylinders. Three different experimental techniques have been used and the results have been compared with the theoretical results quantitatively and qualitatively.

The chapter is organized in the following manner. In Section 6.2, the experimental setup for achieving thermal autofrettage is briefly described followed by a brief introduction of the Sachs boring method in Section 6.3. Section 6.4 presents the determination of the residual stresses by Sachs boring method and its comparison with the generalized plane strain model. In Section 6.5, the residual stresses in the cylinder are inferred on the basis of the Vickers microhardness test. In Section 6.6, the method of the measurement of opening angle is presented in order to verify the presence of residual stresses in the cylinder. Section 6.7 summarizes the chapter.

6.2 The Experimental Setup for Achieving Thermal Autofrettage

The thermal autofrettage process utilizes a certain amount of steady state radial temperature gradient across the wall of a thick cylinder to produce beneficial residual stresses at the inner side. The outer wall is subjected to a higher temperature than the inner wall. This can be achieved by heating the outer wall and cooling the inner wall simultaneously. The physical description of the process is provided in Section 1.6. On the basis of this, an experimental setup for achieving thermal autofrettage by creating desired thermal gradient between the outer and inner wall of the cylinder is developed. The setup consists of a ceramic jacketed heater, a cold water storage tank, 0.5 horsepower (HP) water pump, poly vinyl chloride (PVC) pipe, ceramic tube sections, variac, ammeter and digital temperature controllers. The setup is shown in Figure 6.1.

As shown in the figure 6.1, a well-insulated ceramic jacketed heater is employed for heating the outer wall of the cylinder to be autofrettaged. The heater is connected through a variac, an ammeter and a digital temperature controller in series to control the outer wall temperature. *K*-type thermocouples are attached on the outer and inner surfaces and connected to temperature controllers and display to read the corresponding temperatures. Simultaneously, the inner wall is cooled continuously by flowing cold water through the bore. The cold water is stored in a 200 litre capacity tank and is pumped through a poly vinyl chloride (PVC) pipeline using a household 0.5 horsepower (HP) water pump. At the inlet and outlet, the cylinder to be heated is connected to the PVC pipeline using ceramic tube. The ceramic tube is the good insulator of heat and electricity and prevents the heating of PVC pipe. The joint between the cylinder and the ceramic tube section is sealed by using Dow Corning or Anabond RTV silicone high temperature sealant. When the desired temperature difference is achieved, the power is switched off and cold water is forced through the bore till the cylinder cools to the room temperature. This generates beneficial compressive residual stresses at and around the inner wall of the cylinder.

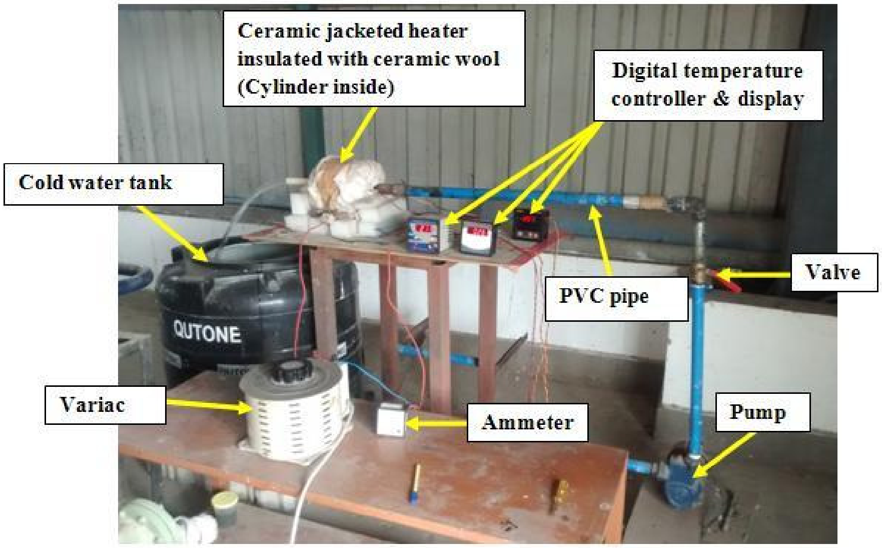

(a)

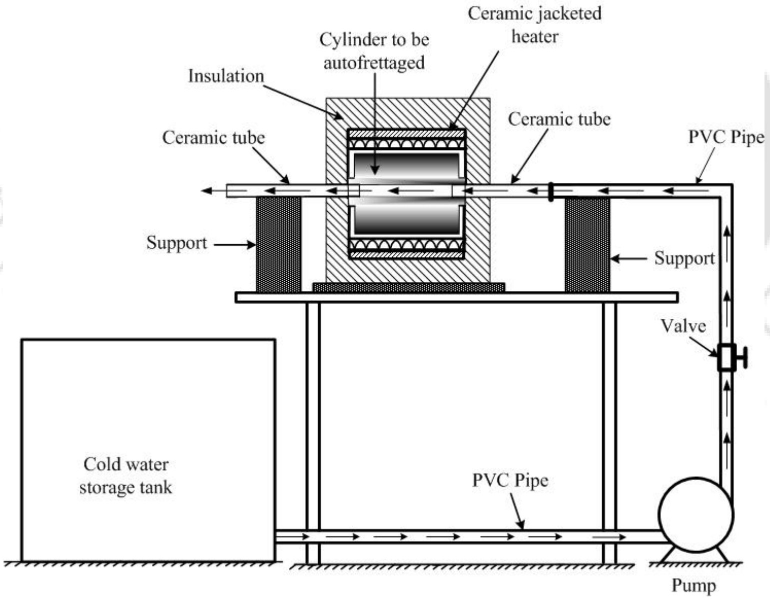

(b)

Figure 6.1 Experimental setup for thermal autofrettage: (a) photograph and (b) schematic diagram

The desired temperature difference across the wall thickness of the cylinder can be created easily in the developed setup. The does not involve any costly equipment. Thus, the process is simple and inexpensive. Also, there is no danger in operating the setup for achieving the thermal autofrettage. This provides an additional advantage from the safety point of view compared to the hydraulic autofrettage process. The process involves flow of cold water, the leakage of which is not harmful to the environment. Due to this, the thermal autofrettage is a greener manufacturing procedure.

6.3 A Brief Description of the Sachs Boring Method

The Sachs boring method is one of the most popular techniques for measuring the residual stresses. The method was first developed by G. Sachs (Sachs, 1927). Traditionally, this method is used for measuring the axisymmetric residual stresses in cylindrical components such as autofrettaged tubes. Researchers have also employed this technique for measuring the residual stress distribution in the cold worked holes of aluminum alloy plates (ÖGzdemir and Edwards, 1996; Smith *et al.*, 1998). In that case, an axisymmetric hollow cylindrical specimen was cut from the plate. The specimen contained the cold worked hole and was subjected to the standard Sachs boring procedure. Garica-Granada (2000) applied the Sachs boring test for measuring non-axisymmetric residual stresses. In the present work, the Sachs boring method is employed for measuring the axisymmetric residual stresses set up in the thermally autofrettaged cylinders.

The method of Sachs boring is destructive in nature. The method involves progressively removing incremental layers from the inside of the cylinder. Strain gauges aligned in the hoop and axial directions are pasted on the outer circumference of the cylinder and are used for measuring the strains on the outer radius while removing the material from the inner diameter in a series of increments. The measured strains are then used for analyzing the residual stress distribution in the cylinder using the equations developed by Sachs (Sachs, 1927). If a cylinder with inner radius a and outer radius b is considered, the residual hoop (σ_θ), axial (σ_z) and radial (σ_r) stresses in the removed layer of any radius r_i are given by

$$\sigma_\theta = \frac{E}{1-\nu^2}\left\{\left(F_b - F_r\right)\frac{\mathrm{d}\theta}{\mathrm{d}F_r} - \frac{\left(F_b + F_r\right)}{2F_r}\theta\right\}, \tag{6.1}$$

$$\sigma_z = \frac{E}{1-\nu^2}\left\{\left(F_b - F_r\right)\frac{\mathrm{d}\Lambda}{\mathrm{d}F_r} - \Lambda\right\}, \tag{6.2}$$

$$\sigma_r = \frac{E}{1-\nu^2}\left\{\frac{\left(F_b - F_r\right)}{2F_r}\theta\right\}, \tag{6.3}$$

where E is the Young’s modulus and ν is the Poisson’s ratio of the material. The strain parameters θ and Λ are given by

$$\theta = \varepsilon_\theta + \nu\varepsilon_z, \tag{6.4}$$

$$\Lambda = \varepsilon_z + \nu\varepsilon_\theta, \tag{6.5}$$

ε_θ, ε_z being the measured cumulative hoop and axial strains on the outer radius after removing an inner incremental layer. F_b, F_r are the cross-sections of the original cylinder and the bored out cylinder respectively given by

$$F_b = \pi b^2, \tag{6.6}$$

$$F_r = \pi r_i^2. \tag{6.7}$$

The derivation of Sachs boring equations (Eqs. 6.1, 6.2 and 6.3) are provided in Appendix E.

6.4 Results of Sachs Boring Method Along With Comparison with the Generalized Plane Strain Model of Thermal Autofrettage

The thermal autofrettage of steel cylinders were carried out using the setup shown in Figure 6.1. It is to be mentioned that during thermal autofrettage, the temperature variation was observed to be less than 3 °C along the length of the cylinder. The residual thermal stresses generated in the cylinders were evaluated experimentally using standard Sachs boring procedure. The experimental results are compared with the generalized plane strain model of thermal autofrettage.

6.4.1 Materials

The materials of the cylinders subjected to thermal autofrettage were SS202, SS304 stainless steel and mild steel. The material properties of SS304 steel and mild steel are summarized in Table 6.1. The detailed dimensions of the specimen are presented in Table 6.2.

Table 6.1 Material properties of specimens

Material	Yield stress, σ_Y (MPa)	Modulus of elasticity, E (GPa)	Poisson's ratio, v	Coefficient of thermal expansion, α (/°C)
SS202	275	207	0.30	17.5×10^{-6}
SS304	215	200	0.29	17.8×10^{-6}
Mild steel	352	219	0.30	13×10^{-6}

Table 6.2 Geometry and autofrettage temperature difference of specimens

Material	Inner radius a (mm)	Outer radius b (mm)	Length L (mm)	Autofrettage temperature difference (T_b–T_a) (°C)
SS202	8.15	24	95	152
SS304	10	20	60	130
SS304	10	25	90	120
Mild steel	12.65	25.30	75	230

6.4.2 Measurement of Sachs Boring

The strain gauges on the outer periphery of the autofrettaged cylinders were pasted such that one strain gauge is aligned in the circumferential direction and the other aligned in the longitudinal direction. The positions of the strain gauges on the outer periphery of the cylinders along with the layers to be removed in each incremental boring are shown schematically in Figure 6.2. The strain gauges used were of type 10/120LG11 (make HBM) with 120 ohm gauge resistance and gauge factor of 2.04. The lead wires connected to the strain gages is a four-wired system. The four-wired system helps in eliminating the temperature effect in the lead wires as well as in eliminating any measurement error due to gauge factor correction and contact resistance. The strain gauges were sealed using Anabond 666 RTV silicon sealant to prevent the gauges from moisture and any other environmental factor such as liquid coolant during machining.

The removal of the layers from the inside diameter of the cylinders was performed in lathe machine. The arrangement for Sachs boring in lathe is shown in Figure 6.3. The boring was carried out at a low spindle speed of 145 RPM using a sharp boring tool. The depth of cut was varied from 0.1 mm to 0.5 mm during the machining at the feed rate of 0.04 mm/rev. The sharp tool and low RPM during boring minimizes vibration and reduces the possibility of generating residual stresses in the component due to machining (Smith *et al.*, 1998). A liquid coolant was employed continuously on the cylindrical specimen during the boring operation to minimize the generation of heat.

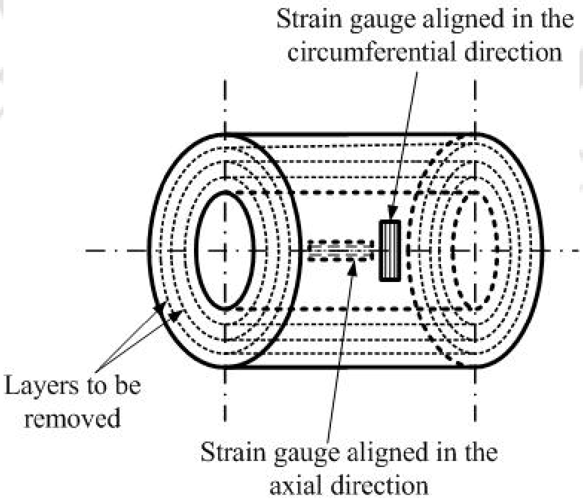

Figure 6.2 Position of the strain gauges on the outer periphery of the cylinder

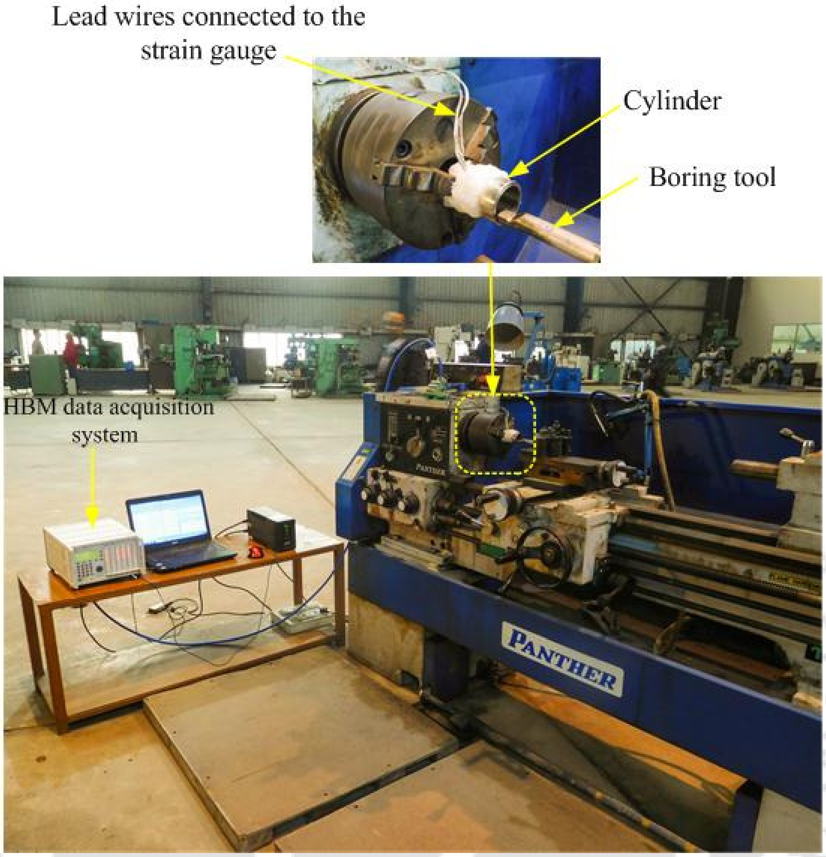

Figure 6.3 The Sachs boring arrangement in lathe machine

The released hoop and axial strains, after boring out of each layer of material, measured on the outer radius of the cylinder were recorded and stored using HBM data acquisition system with CATMAN software. During machining, the lead wires from the strain gauges were wound around the circumference of the chuck of the lathe machine and fixed on the circumference with the help of adhesive tape. This enabled the wires to rotate with the chuck during the material removal process. All the strains were set to zero before the boring was carried out. When one layer of material was removed completely from the cylinder, the machine was stopped and lead wires were taken out from the chuck by removing the adhesive tape. The lead wires were then plugged into the data acquisition system for recording strain data. After recording the strain data, the lead wires were disconnected and again fixed on the circumference of the chuck. Then the machine was started and removal of the next layer of material was carried out. The strain readings were recorded 15 minutes after boring. This was to allow the specimen to cool to room temperature. The procedure was repeated till about 80% of the thickness got removed from the cylinder.

The cumulative hoop and axial strains measured in Sachs boring of autofrettaged SS202, SS304 and mild steel cylinders are given in Tables 6.3, 6.4, 6.5 and 6.6. The strain parameters θ and Λ are evaluated using Eqs. (6.4) and (6.5). It is observed that the strains increased from zero to certain value in compression and then gradually tends to approach towards tension.

Table 6.3 Measured hoop and axial strain in Sachs boring of SS202 with b/a =2.94

Radius, r_i (mm)	Area, F_r (mm^2)	Hoop strain, ε_θ	Axial strain, ε_z	θ	Λ
8.15	208.67	0	0	0	0
8.40	221.67	-6.63257×10^{-6}	-7.66823×10^{-6}	-8.93304×10^{-6}	-9.658×10^{-6}
8.60	232.35	-9.4266×10^{-6}	-1.11468×10^{-5}	-1.27706×10^{-5}	-1.39748×10^{-5}
8.85	246.06	-1.39762×10^{-5}	-1.679×10^{-5}	-1.90132×10^{-5}	-2.09829×10^{-5}
9.10	260.16	-1.65665×10^{-5}	-1.98333×10^{-5}	-2.25165×10^{-5}	-2.48032×10^{-5}
9.50	283.53	-1.74113×10^{-5}	−2.61776E-05	-2.52646×10^{-5}	-3.1401×10^{-5}
9.80	301.72	-1.84048×10^{-5}	-2.76812×10^{-5}	-2.67091×10^{-5}	-3.32026×10^{-5}
10.30	333.29	-1.6686×10^{-5}	-2.99798×10^{-5}	-2.568×10^{-5}	-3.49856×10^{-5}
10.80	366.43	-1.51734×10^{-5}	-3.2117×10^{-5}	-2.48085×10^{-5}	-3.6669×10^{-5}
11.30	401.15	-1.30775×10^{-5}	-3.06151×10^{-5}	-2.2262×10^{-5}	-3.45383×10^{-5}
11.70	430.05	-1.21099×10^{-5}	-3.2769×10^{-5}	-2.19406×10^{-5}	-3.64019×10^{-5}
12.50	490.87	-1.03765×10^{-5}	-3.09742×10^{-5}	-1.96688×10^{-5}	-3.40871×10^{-5}
13.10	539.13	-1.15717×10^{-5}	-3.2385×10^{-5}	-2.12872×10^{-5}	-3.58565×10^{-5}
14.05	620.16	-1.0211×10^{-5}	-3.07002×10^{-5}	-1.94211×10^{-5}	-3.37635×10^{-5}
15.05	711.58	-1.08076×10^{-5}	-3.13859×10^{-5}	-2.02234×10^{-5}	-3.46282×10^{-5}
16.05	809.28	-1.23829×10^{-5}	-2.85776×10^{-5}	-2.09562×10^{-5}	-3.22925×10^{-5}

Table 6.4 Measured hoop and axial strain in Sachs boring of SS304 with b/a =2

Radius, r_i (mm)	Area, F_r (mm^2)	Hoop strain, ε_θ	Axial strain, ε_z	θ	Λ
10.00	314.16	0	0	0	0
10.30	333.29	-9.59904×10^{-6}	-1.06843×10^{-5}	-1.28043×10^{-5}	-1.3564×10^{-5}
10.60	352.98	-1.76466×10^{-5}	-1.87362×10^{-5}	-2.32675×10^{-5}	-2.40302×10^{-5}
10.90	373.25	-2.6142×10^{-5}	-2.8964×10^{-5}	-3.48312×10^{-5}	-3.68066×10^{-5}
11.20	394.08	-2.51799×10^{-5}	-2.7756×10^{-5}	-3.35067×10^{-5}	-3.53099×10^{-5}
11.50	415.47	-2.39738×10^{-5}	-2.6735×10^{-5}	-3.19943×10^{-5}	-3.39271×10^{-5}
11.95	448.63	-2.31968×10^{-5}	-2.4951×10^{-5}	-3.06821×10^{-5}	-3.19101×10^{-5}
12.45	486.95	-2.0276×10^{-5}	-2.2224×10^{-5}	-2.69432×10^{-5}	-2.83069×10^{-5}
12.95	526.85	-1.89257×10^{-5}	-2.098×10^{-5}	-2.52197×10^{-5}	-2.66577×10^{-5}
13.25	551.54	-1.67629×10^{-5}	-1.90245×10^{-5}	-2.24702×10^{-5}	-2.40534×10^{-5}
13.75	593.95	-1.38597×10^{-5}	-1.53539×10^{-5}	-1.84659×10^{-5}	-1.95118×10^{-5}
14.25	673.94	-6.23119×10^{-6}	-8.14101×10^{-6}	-8.6735×10^{-6}	-1.00104×10^{-5}
14.75	683.49	-2.51949×10^{-6}	-3.21732×10^{-6}	-3.48469×10^{-6}	-3.97317×10^{-6}
15.25	730.62	2.1795×10^{-6}	-1.187×10^{-6}	1.8234×10^{-6}	-5.33154×10^{-7}
15.75	779.31	8.8745×10^{-6}	7.1431×10^{-6}	1.10174×10^{-5}	9.80545×10^{-6}
16.25	829.58	1.514×10^{-5}	1.312×10^{-5}	1.9076×10^{-5}	1.7662×10^{-5}

Table 6.5 Measured hoop and axial strain in Sachs boring of SS304 with b/a =2.5

Radius, r_i (mm)	Area, F_r (mm^2)	Hoop strain, ε_θ	Axial strain, ε_z	θ	Λ
10.00	314.16	0	0	0	0
10.10	320.47	-1.70017×10^{-6}	-2.78439×10^{-6}	-2.53549×10^{-6}	-3.29444×10^{-6}
10.26	330.71	-4.85328×10^{-6}	-5.54351×10^{-6}	-6.51634×10^{-6}	-6.99949×10^{-6}
10.45	343.07	-8.11881×10^{-6}	-9.89501×10^{-6}	-1.10873×10^{-5}	-1.23307×10^{-5}
10.65	356.33	-1.121×10^{-5}	-1.23175×10^{-5}	-1.49052×10^{-5}	-1.56805×10^{-5}
10.95	376.68	-1.64348×10^{-5}	-1.7536×10^{-5}	-2.16956×10^{-5}	-2.24664×10^{-5}
11.40	408.28	-2.10368×10^{-5}	-2.21871×10^{-5}	-2.76929×10^{-5}	-2.84982×10^{-5}
11.90	444.88	-1.91763×10^{-5}	-2.3162×10^{-5}	-2.61249×10^{-5}	-2.89149×10^{-5}
12.40	483.05	-1.81351×10^{-5}	-2.012×10^{-5}	-2.41711×10^{-5}	-2.55605×10^{-5}
12.90	522.79	-1.68411×10^{-5}	-1.83046×10^{-5}	-2.23324×10^{-5}	-2.33569×10^{-5}
13.40	564.1	-1.41709×10^{-5}	-1.6673×10^{-5}	-1.91728×10^{-5}	-2.09243×10^{-5}
13.90	606.99	-1.2974×10^{-5}	-1.39649×10^{-5}	-1.71635×10^{-5}	-1.78571×10^{-5}
14.40	651.44	-1.03193×10^{-5}	-9.81728×10^{-6}	-1.32645×10^{-5}	-1.29131×10^{-5}
14.75	683.49	-7.98942×10^{-6}	-8.16942×10^{-6}	-1.04402×10^{-5}	-1.05663×10^{-5}
15.25	730.62	-3.77444×10^{-6}	-6.10308×10^{-6}	-5.60536×10^{-6}	-7.23541×10^{-6}
15.70	774.37	-1.1402×10^{-6}	-2.4201×10^{-6}	-1.86623×10^{-6}	-2.76216×10^{-6}
16.20	824.48	2.2438×10^{-6}	8.25342×10^{-7}	2.4914×10^{-6}	1.49848×10^{-6}
16.70	876.16	7.19202×10^{-6}	4.15729×10^{-6}	8.43921×10^{-6}	6.31489×10^{-6}
17.20	929.41	1.2517×10^{-5}	8.64956×10^{-6}	1.51119×10^{-5}	1.24047×10^{-5}

Table 6.6 Measured hoop and axial strain in Sachs boring of mild steel with b/a =2

Radius, r_i (mm)	Area, F_r (mm^2)	Hoop strain, ε_θ	Axial strain, ε_z	θ	Λ
12.65	502.72	0	0	0	0
12.85	518.75	-4.47518×10^{-6}	-9.26904×10^{-6}	-7.25589×10^{-6}	-1.06116×10^{-5}
13.15	543.25	-1.22299×10^{-5}	-1.51064×10^{-5}	-1.67618×10^{-5}	-1.87754×10^{-5}
13.40	564.1	-1.3673×10^{-5}	-1.85499×10^{-5}	-1.9238×10^{-5}	-2.26519×10^{-5}
13.70	589.64	-1.47564×10^{-5}	-2.11941×10^{-5}	-2.11146×10^{-5}	-2.5621×10^{-5}
14.00	615.75	-1.31324×10^{-5}	-2.52994×10^{-5}	-2.07222×10^{-5}	-2.92391×10^{-5}
14.45	655.97	-1.01324×10^{-5}	-2.32994×10^{-5}	-1.71222×10^{-5}	-2.63391×10^{-5}
14.95	702.15	-7.07518×10^{-6}	-2.00752×10^{-5}	-1.30977×10^{-5}	-2.21977×10^{-5}
15.45	749.91	-5.3174×10^{-6}	-1.71983×10^{-5}	-1.04769×10^{-5}	-1.87935×10^{-5}
15.95	799.23	-3.28444×10^{-6}	-1.46266×10^{-5}	-7.67242×10^{-6}	-1.56119×10^{-5}
16.45	850.12	-1.72435×10^{-6}	-1.08474×10^{-5}	-4.97858×10^{-6}	-1.13648×10^{-5}
16.95	902.58	1.19935×10^{-6}	-7.03235×10^{-6}	-9.10352×10^{-7}	-6.67254×10^{-6}
17.45	956.62	3.90152×10^{-6}	-3.32948×10^{-6}	2.90267×10^{-6}	-2.15903×10^{-6}
17.95	1012.22	6.55904×10^{-6}	1.43336×10^{-6}	6.98904×10^{-6}	3.40107×10^{-6}
18.45	1069.4	1.07984×10^{-5}	4.34162×10^{-6}	1.21009×10^{-5}	7.58113×10^{-6}
18.95	1128.15	1.38523×10^{-5}	8.54031×10^{-6}	1.64144×10^{-5}	1.2696×10^{-5}
19.45	1188.47	1.55106×10^{-5}	1.22906×10^{-5}	1.91978×10^{-5}	1.69438×10^{-5}
19.95	1250.36	1.97969×10^{-5}	1.66572×10^{-5}	2.4794×10^{-5}	2.25962×10^{-5}

6.4.3 Evaluation of Residual Stresses Using Sachs Boring Data and its Comparison with the Generalized Plane Strain Model

The residual stresses in the thermally autofrettaged cylinders are evaluated using the strain data recorded in the Sachs boring experiments in Eqs. (6.1)–(6.3). The evaluation of residual stresses requires the strain parameters θ & Λ, the original cross-section F_b of the cylinders, the bored out cross-sections after each layer of material removed, F_r and the differentiation of the strain parameters with respect to the bored out radius, *i.e.*, $d\theta/dF_r$ & $d\Lambda/dF_r$. The evaluated values of θ, Λ and F_r are shown in Tables 6.3–6.6 for the respective cylinders. The SS202 cylinder has the original cross-section of 1809.56 mm^2. The original cross-section of the SS304 cylinders with b/a= 2 & 2.5 were evaluated to be 1256.64 mm^2 and 1963.49 mm^2, respectively. The original cross-section of the mild steel cylinder was 2010.90 mm^2. The derivatives $\mathrm{d}\theta/\mathrm{d}F_r$ and $\mathrm{d}\Lambda/\mathrm{d}F_r$ are calculated using the central difference method. For example, considering the second row of values in Table 6.4, the derivative $\mathrm{d}\theta/\mathrm{d}F_r$ is evaluated to be -5.99369×10^{-07}. Similarly, the value of $\mathrm{d}\Lambda/\mathrm{d}F_r$ is evaluated as -6.19017×10^{-07}.

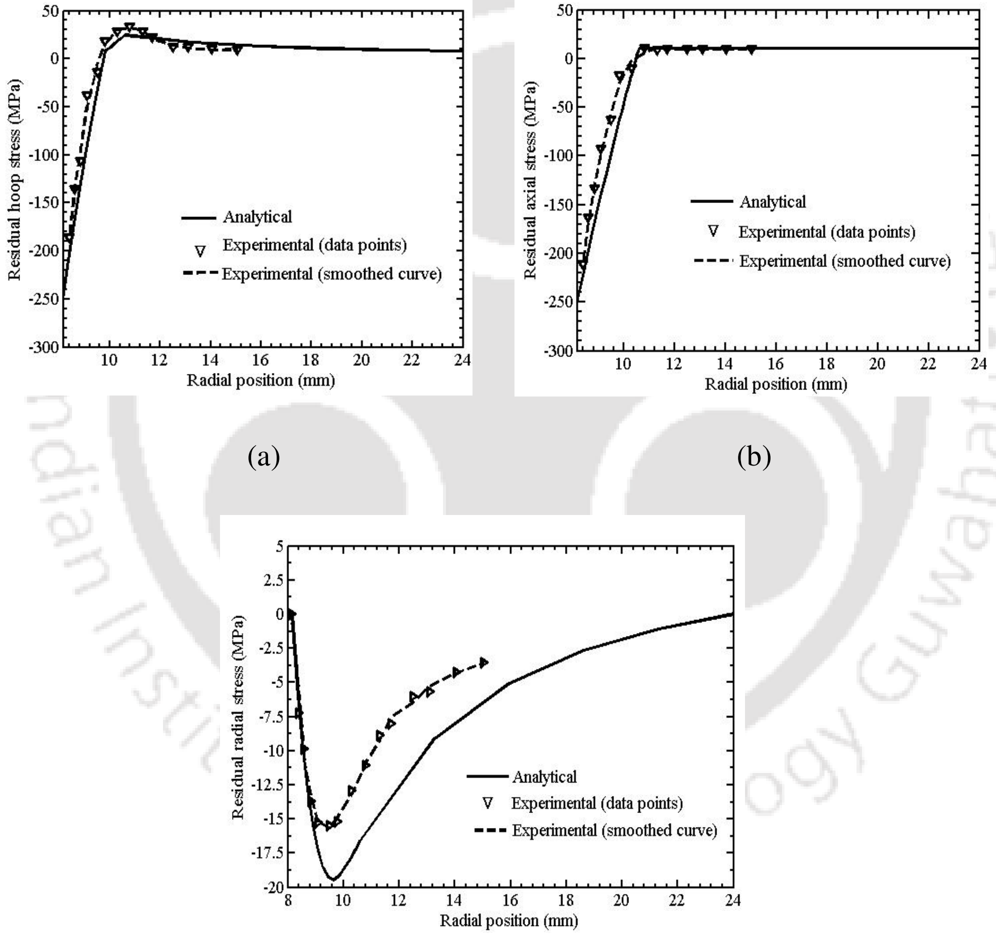

(a) (b)

(c)

Figure 6.4 Residual (a) hoop, (b) axial and (c) radial stress distributions in SS202 cylinder (b/a=2.94)

The residual hoop, axial and radial stresses set up in the SS304 and mild steel cylinders as evaluated from Sachs boring measurement are shown in Figures 6.4, 6.5, 6.6 and 6.7 as a function of bored out radius. The residual stresses are also evaluated using the analytical generalized plane strain model and compared with the experimental results.

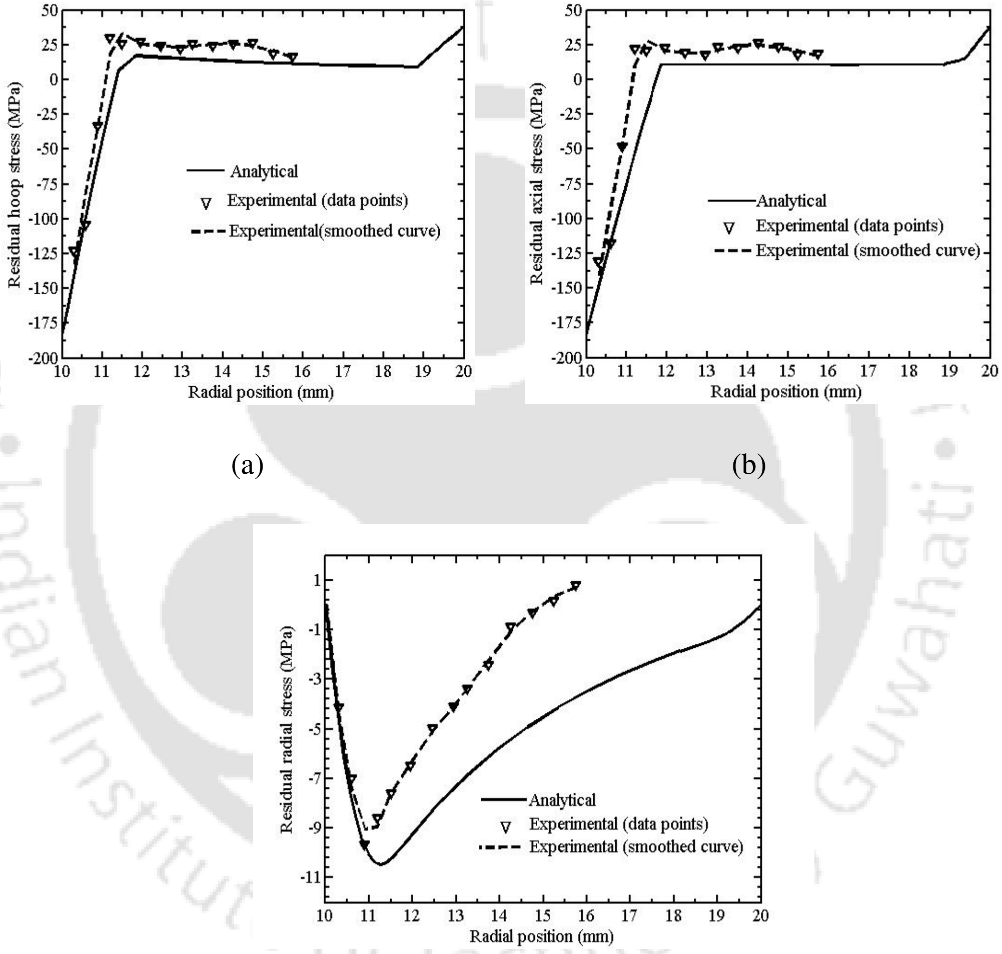

(a)

(b)

(c)

Figure 6.5 Residual (a) hoop, (b) axial and (c) radial stress distributions in SS304 cylinder (*b*/*a*=2)

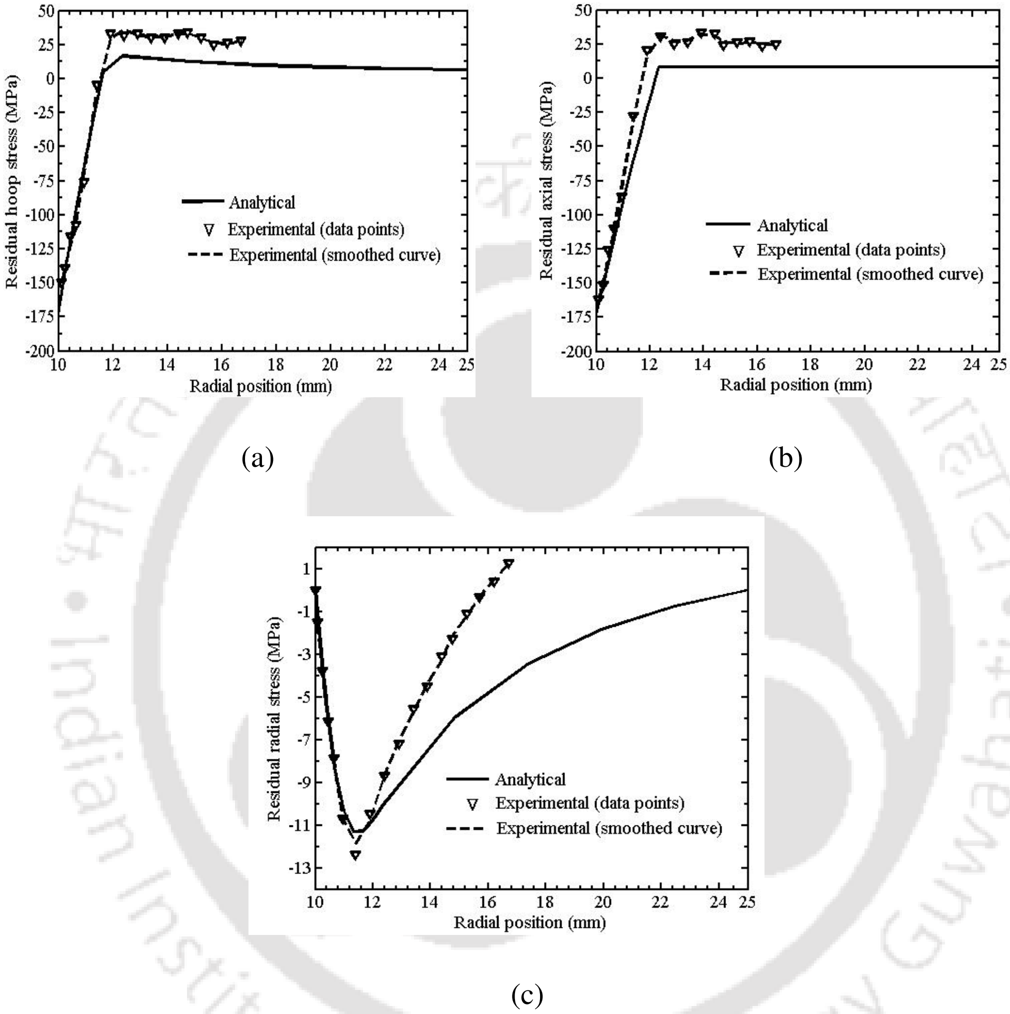

(a)

(b)

(c)

Figure 6.6 Residual (a) hoop, (b) axial and (c) radial stress distributions in SS304 cylinder (*b*/*a*=2.5)

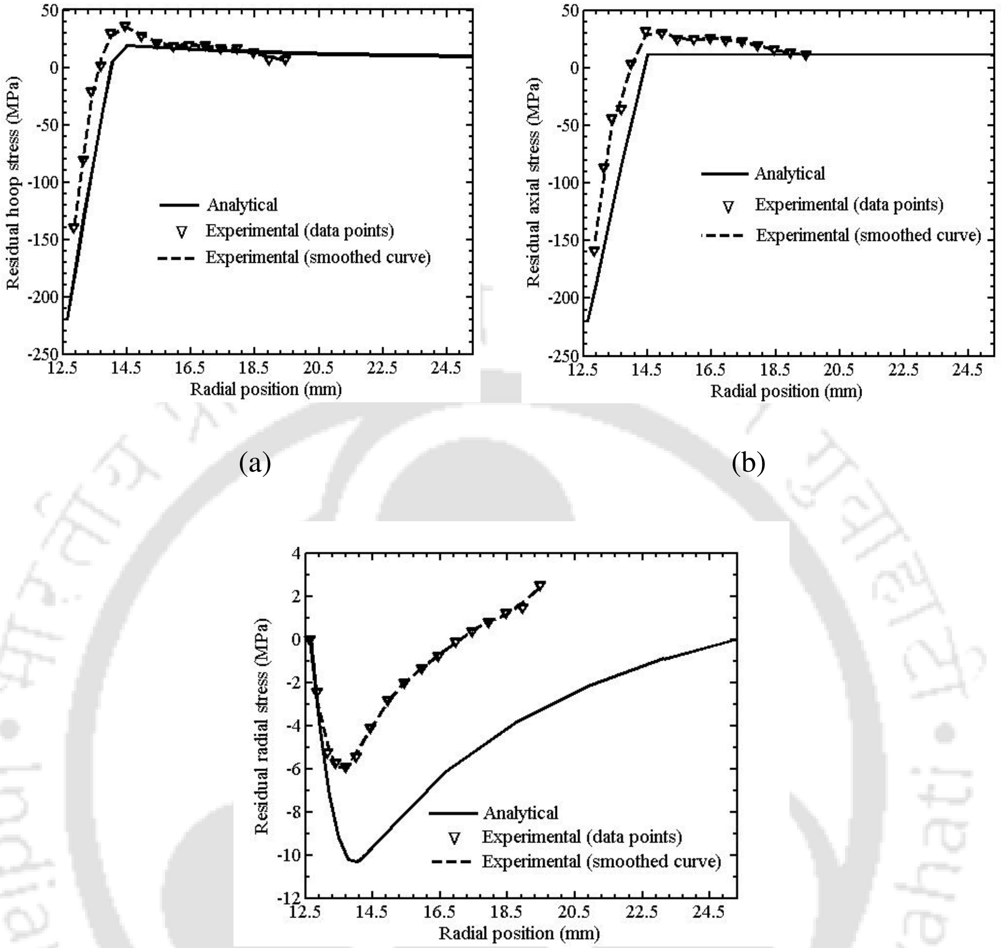

(a)

(b)

(c)

Figure 6.7 Residual (a) hoop, (b) axial and (c) radial stress distributions in mild steel cylinder (*b*/*a*=2)

It is observed from Figures 6.4, 6.5, 6.6 and 6.7 that the experimental Sachs boring residual stresses are in good agreement with the residual stresses predicted by the generalized plane strain model. In all the cases, it is observed that very near to the region of inner surface, the experimental compressive residual stresses very closely match with the analytical residual stresses. The differences between the experimental and analytical stresses may be attributed to the experimental and numerical errors. In the case of SS202 cylinder, the average errors based on L_2 norm (*i.e.*, root mean squared errors) for hoop, axial and radial stresses are observed to be 4.53 MPa, 7.50 MPa and 1.26 MPa, respectively. In SS304 cylinders with *b*/*a*=2, these errors are 6.36 MPa, 10.05 MPa and 1.40 MPa, respectively for hoop, axial and radial stresses. For SS304 cylinder with b/a=2.5, these errors are observed to be 6.12 MPa, 8.28 MPa and 1.15 MPa, respectively. The average errors based on L_2 norm for hoop, axial and radial stresses being 7.52 MPa, 8.55 MPa and 2.27 MPa, respectively in case of the mild steel cylinder.

6.5 Inference of Residual Stresses from Microhardness Test

The residual stresses influence the surface microhardness. The change of hardness of the surface after any metal working process may be interpreted as one of the qualifying test for the presence of residual stresses. Researchers have been using the measurement of hardness as a means to detect the presence of surface residual stresses. For example, Kokubo (1932) reported the change in Vickers hardness values in carbon-steel rolled sheets due to applied stresses under bending load. It was found that the hardness decreases in the presence of tensile stresses whilst in the presence of compressive stresses hardness of the surface increases. The influence of residual stresses on the hardness number during shot peening and sheet bending of medium carbon steel was studied by Tosha (2002), who observed that hardness numbers increase in the compressive stress field and decrease in the tensile stress field. Simes *et al.* (1984) carried out the experimental investigation of the influence of residual stresses on the hardness number obtained in the Vickers indentation test and found that the presence of tensile residual stresses results in a decrease in hardness. In the present analysis, the microhardness on the inner and outer surfaces of the autofrettaged cylinders based on the Vickers diamond indentation test was carried out in order to envisage the generation of thermal residual stresses in the cylinders. To carry out the microhardness test small test samples were extracted from the cylinders by cutting it radially. The Vickers indentation on the inner and outer surfaces of both the autofrettaged and non-autofrettaged samples was carried out at 500 gf. The measured microhardness values on the inner and outer surfaces of the samples shows that the hardness increases on the inner surface of the autofrettaged sample as compared to the non-autofrettaged sample due to the presence of compressive residual stresses. Similarly, due to the presence of tensile residual stresses on the outer surface, a decrease in the measured microhardness was observed. The microhardness test results conducted on the inner and outer surfaces of the SS304 cylinders are presented in Table 6.7.

It is found from Table 6.7 that in the case of SS304 cylinder with *b*/*a*=2, the average microhardness on the inner surface increases from 256.94 HV with standard deviation of 3.03 to 279.36 HV with standard deviation of 4.49. However, on the outer surface, the average microhardness decreases from 283.18 HV with standard deviation of 3.21 to 224.79 HV with standard deviation of 3.50. In the case of SS304 cylinder with *b*/*a*=2.5, the average microhardness on inner surface increased to 290.95 HV with standard deviation of 3.02 and that on the outer surface decreased to 236.22 HV with standard deviation of 3.19. These results indicate that the inner surface of the cylinder is in compression and the outer surface is in tension.

Another cylinder made of mild steel with inner radius 5 mm and outer radius 20 mm is thermally autofrettaged inducing a temperature difference of 260 °C. The Vickers microhardness tests were also conducted for this cylinder on its outer and inner surfaces at a load of 500 gf. The microhardness tests on the outer and inner surfaces of the non-autofrettaged cylinder were also conducted as well. The results are summarized in Table 6.8. A similar trend has been observed as observed in the case of SS304 cylinders. The average microhardness of the non-autofrettaged cylinder on the outer surface is 170.64 HV with standard deviation 5.25. On the inner surface of the non-autofrettaged cylinder, the average microhardness is 174.69 HV with standard deviation 4.13. The average hardness of the outer surface of the autofrettaged cylinder is 157.28 HV with standard deviation 7.32. On the inner surface of the autofrettaged cylinder, the average hardness is 219.52 HV with a standard deviation of 12.84.

Table 6.7 Vickers micro hardness on the surfaces of SS304 cylinders

Non-autofrettaged cylinder (*b*/*a*=2)		Autofrettaged cylinder (*b*/*a*=2)		Autofrettaged cylinder (*b*/*a*=2.5)	
Hardness on the outer surface (HV)	Hardness on the inner surface (HV)	Hardness on the outer surface (HV)	Hardness on the inner surface (HV)	Hardness on the outer surface (HV)	Hardness on the inner surface (HV)
284.8	262.3	223.9	277.1	234.1	286.9
287.9	257.1	225.4	278.8	237.0	288.3
277.5	261.5	221.7	280.1	230.3	285.6
282.8	254.1	229.3	272.8	233.2	288.4
282.3	257.9	218.7	276.8	239.2	295.1
286.8	254.1	226.1	279.2	239.9	289.4
281.9	257.5	219.7	282.8	232.4	295.1
278.4	261.4	224.8	280.8	230.6	291.4
285.8	255.8	228.0	287.7	238.4	289.9
280.4	260.5	220.1	282.7	235.2	297.7
288.4	253.3	219.7	271.9	237.6	290.4
280.4	252.4	227.2	279.3	233.5	290.4
286.8	253.5	227.7	272.7	238.9	294.9
284.3	256.6	225.6	276.8	234.6	290.1
285.8	253.7	227.4	274.9	240.1	287.3
278.4	260.1	229.9	281.7	239.6	293.1
279.9	259.2	230.3	288.3	235.9	289.9
284.8	253.7	223.9	277.1	241.7	292.0
281.9	256.2	221.4	280.3	237.5	292.5
284.3	257.9	225.1	285.4	234.8	290.7

Table 6.8 Vickers micro hardness on the surfaces of mild steel cylinder

Non-autofrettaged cylinder		Autofrettaged cylinder	
Hardness on the outer surface (HV)	Hardness on the inner surface (HV)	Hardness on the outer surface (HV)	Hardness on the inner surface (HV)
172.1	169.7	149.3	208.1
178.3	173.4	144.3	210.2
170.7	172.1	165.2	221.2
167.9	179.3	171.8	200.6
162.4	169.5	163.5	215.2
171.1	172.8	156.3	232.3
167.2	180.2	151.4	201.9
166.6	178.5	155.3	226.7
170.2	170.1	157.8	215.2
170.4	172.6	157.6	234.8
181.8	176.7	155.9	230.7
169.0	181.4	159.0	237.3

6.6 Demonstration of Residual Stresses by the Measurement of Opening Angle of Radial Cut through the Wall Thickness

The angle of opening is a measure of the pure bending moment ‘locked in’ to the cylinder during autofrettage. When the autofrettaged cylinders are cut radially, the cylinders open by an angle β as shown in Figure 6.8. The measurement of this opening angle can be used as a means to demonstrate that the residual stresses are set up in the cylinder (Parker *et al*., 1983).

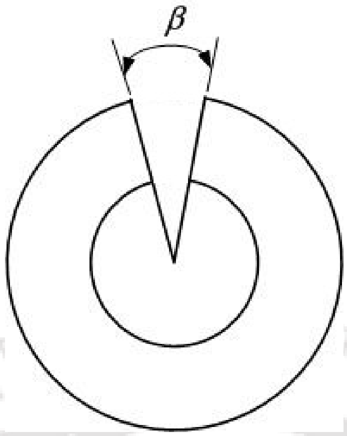

Figure 6.8 Opening angle in thick-walled autofrettaged cylinder with single radial cut

In the thermally autofrettaged cylinders, the pure bending moment 'locked in' the cylinders is calculated based on the residual stress distribution predicted by the generalized plane strain model presented in Chapter 4. In an autofrettaged cylinder of unit length with inner radius *a* and outer radius *b*, the total bending moment acting over any radial cut is given by (Parker *et al*. 1982)

$$M = \int_a^b \sigma_\theta r \mathrm{d}r, \tag{6.8}$$

where σ_θ is the net residual hoop stress set up in the cylinder by autofrettage. When the cylinder has undergone first stage of elasto-plastic deformation during thermal autofrettage, the total bending moment released for a cylinder of unit length due to any single radial cut can be given by

$$M = \int_a^c \sigma_\theta^{(\text{plastic zone I})} r\mathrm{d}r + \int_c^d \sigma_\theta^{(\text{plastic zone II})} r\mathrm{d}r + \int_d^b \sigma_\theta^{(\text{elastic zone})} r\mathrm{d}r. \tag{6.9}$$

Similarly, the total bending moment released in the thermally autofrettaged cylinder of unit length due to a radial cut when the cylinder has undergone second stage of elasto-plastic deformation is given by

$$M = \int_a^c \sigma_\theta^{(\text{plastic zone I})} r\mathrm{d}r + \int_c^d \sigma_\theta^{(\text{plastic zone II})} r\mathrm{d}r + \int_d^e \sigma_\theta^{(\text{elastic zone})} r\mathrm{d}r + \int_e^f \sigma_\theta^{(\text{plastic zone IV})} r\mathrm{d}r + \int_f^b \sigma_\theta^{(\text{plastic zone III})} r\mathrm{d}r. \tag{6.10}$$

In Eqs. (6.9) and (6.10), σ_θ refers to the residual thermal hoop stresses in the respective zones in the cylinder. The variables c, d, e and f refer to the limits of the various zones. These can be determined by satisfying the continuity of stresses as detailed in Chapter 4. The evaluations of the integrals in Eqs. (6.9) and (6.10) are provided in Appendix F.

The opening angle β due to the released bending moment M 'locked in' to the cylinder can be evaluated by using the following equation (Parker and Farrow, 1980):

$$\beta = -\frac{4\pi M}{E}\frac{4\left(b^2-a^2\right)}{N}, \tag{6.11}$$

where E is the Young's modulus of elasticity and N is given by

$$N = \left(b^2-a^2\right)^2 - 4a^2b^2\left\{\ln\left(\frac{b}{a}\right)\right\}^2. \tag{6.12}$$

Here, the thermal autofrettage of SS304 cylinders is considered to measure the opening angles in order to illustrate the existence of residual stresses in the cylinders. The theoretical angle of opening for the cylinders is calculated using Eq. (6.11). Eq. (6.11) requires the value of M, which is evaluated either from Eq. (6.9) or Eq. (6.10) depending on whether the cylinder has undergone first stage or second stage of elasto-plastic deformation. For experimental determination of the opening angle, a disk of 15 mm thickness was extracted from each of the autofrettaged cylinders. A radial cut was made in each disk and the opening angle was measured using profile projector. The experimentally measured opening angles in SS304 cylinders are compared with the theoretical opening angles and are presented in Table 6.9.

Table 6.9 Comparison of experimental opening angle with the theoretical opening angle

Sl. No.	Material	b/a	$(T_b - T_a)$ (°C)	Theoretical opening angle (β_{th})	Experimental opening angle (β_{exp})	% variation
1	SS304	2	130	1.69°	1.98°	14.64
2	SS304	2.5	120	0.91°	1.05°	13.33

The comparison of theoretical and experimental measurement of opening angles in the cylinder shows that the experimentally determined opening angles are slightly greater than the theoretically predicted opening angles. The percentage variation between the experimental and theoretical opening angles is observed to be less than 15%. Thus, it is confirmed that the residual stresses are set up in the thermally autofrettaged cylinders.

6.7 Summary

In this chapter an experimental study of the thermal autofrettage of thick-walled cylinders is carried out. The thermal autofrettage of SS202, SS304 and mild steel with different wall thickness ratios was conducted by creating a thermal gradient between the outer and inner wall of the cylinders. On removal of the thermal gradient, the residual thermal stresses generated in the cylinders were evaluated experimentally using traditional Sachs boring method. The experimentally determined residual stresses are compared with the residual stresses predicted by the generalized plane strain model of thermal autofrettage. The comparison shows that the experimental results are in close agreement with the analytical results. Thus, the generalized plane strain model can be used to analyse the residual stresses generated in the cylinders during thermal autofrettage. The Vickers microhardness test on the inner and outer surfaces of the autofrettaged cylinders was also conducted to infer the presence of residual stresses. It was found that the microhardness increases on the inner surface due to the residual compressive stresses at the inner surface and the microhardness decreases on the outer surface due to the presence of tensile residual stresses at the outer surface. To envisage the presence of residual stresses, the method of measuring the opening angle when the thermally autofrettaged cylinders were cut along radial direction to release the ‘locked in’ bending moment was also carried out. It was found that the experimentally measured opening angles are in good agreement with the theoretically predicted opening angles based on the stress analysis of generalized plane strain model. Among the three experimental methods, the method of measuring the opening angle is the easiest to conduct. Although it does not directly provide the distribution of residual stress along the thickness, it can be used for the quick verification of a theoretically predicted distribution. Given a reliable theoretical model, microhardness measurement can be an excellent destructive method for the determination of residual stresses.

The overall experimental results reveal that the thermal autofrettage process can be used as a potential manufacturing procedure in the industries to generate the beneficial compressive residual stresses at the inner wall. Due to the simplicity in the procedure of thermal autofrettage, the process has some edge over the existing hydraulic and swage autofrettage processes. A good agreement between experimental results with the generalized plane strain theoretical model indicates that the behaviour of thermal autofrettage is easily predictable, a positive feature towards its industrial adaptation.

Chapter 7

A Comparative Study of Thermal and Hydraulic Autofrettage

7.1 Introduction

The hydraulic autofrettage is a widely adopted process for strengthening thick-walled cylinders in industries. The process employs enormous amount of hydraulic oil to create the ultra-high pressure for achieving autofrettage. This requires the highly expensive hydraulic power pack. The high pressure during autofrettage may be dangerous at times. The leakage of hydraulic oil during operation also harms the environment. The thermal autofrettage proposed in this thesis is a potential process to generate beneficial compressive residual stresses at and around the inner wall of a thick-walled cylinder for increasing its pressure carrying capacity. Due to its simplicity and inexpensive arrangement, it can compete with the conventional hydraulic autofrettage process. The process requires only a certain amount of temperature difference between the outer and inner wall of the cylinder for achieving autofrettage.

The residual stresses generated in the cylinder after the release of the temperature difference between the outer and inner wall of the cylinder are analyzed theoretically in Chapter 4 using generalized plane strain condition. The experimental validation of the closed form residual stress expressions using Sachs boring technique has been presented in Chapter 6 for SS202, SS304 and mild steel cylinders. The experimental results match well with theoretical predictions. For example, based on the L_2 error norm, the percentage error in the hoop stress prediction in the case of SS202 is about 2.5% of the maximum hoop stress. The error is about 5% of the maximum hoop stress for the mild steel.

In the present work, a comparative study of thermal and hydraulic autofrettage is carried out for different materials. A comparison is made for assessing the maximum pressure carrying capacity of typical cylinders undergoing hydraulic and thermal autofrettage. A parametric study of both the processes is carried out for high pressure application. There are many situations where the thick-walled cylindrical pressure vessels are subjected to high thermal gradient instead of pressure loading. In this case, vessels may fail due to the generation of high thermal stresses in the wall of the vessel. Sometimes they may be subjected to both thermal gradient and pressure loading. The effect of autofrettage for such situations is also studied in the present work. It is shown that the thermal autofrettage is highly effective for the pressure vessels that are subjected to high thermal gradient.

7.2 Comparison of the Maximum Pressure Carrying Capacity of Cylinders in Thermal Autofrettage with Hydraulic Autofrettage

A quantitative comparison of thermal autofrettage with the conventional hydraulic autofrettage is carried out in terms of the maximum pressure carrying capacity for the case of aluminum and SS304 cylinders as considered in Section 4.4. For comparison the thermal autofrettage is simulated by using the relevant equations developed in Chapter 4. The theoretical expressions (neglecting strain-hardening and Bauschinger effect) for hydraulic autofrettage are available in the standard textbooks, *e.g.*, Chakrabarty (2006). These expressions have been validated by Stacey *et al.* (1985) for 4333 M4, high strength low-alloy steel cylinder with inner radius 15 mm and outer radius 31 mm. Except at the inner surface of the cylinder, the matching between experimental and analytical results was good (about 7.6% of the maximum hoop stress). Bauschinger effect is not significant in all materials. A good matching between theoretical prediction and experimental results of thermal autofrettage for SS202, SS304 and mild steel without considering strain hardening and Bauschinger effect has been observed as discussed in Section 6.4.3. Hence, it is appropriate to use analytical expressions for hydraulic autofrettage also without these effects for proper comparison.

For both the autofrettage, it is considered that the magnitude of generated compressive residual stresses is such that it will not cause the yielding of the cylinders. It is found that in case of aluminum cylinder, the maximum temperature difference in the cylinder is limited to 75 °C for the thermal autofrettage and the maximum autofrettage pressure is limited to about 36 MPa for hydraulic autofrettage to avoid yielding by generated residual stresses. The residual stress distribution in the cylinder for both thermal and hydraulic autofrettage is shown in Figure 7.1. It is observed that the maximum compressive residual stress generated in the cylinder at the inner radius is almost same for both thermal and hydraulic autofrettage.

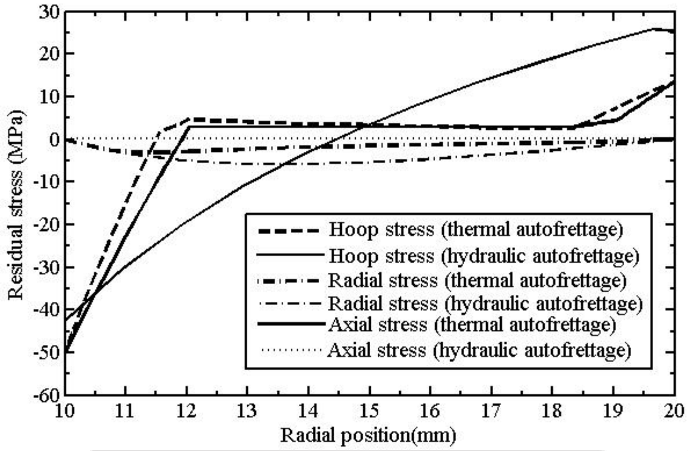

Figure 7.1 Residual stresses in aluminum cylinder for both thermal and hydraulic autofrettage

When the autofrettaged cylinder is pressurized by internal pressure, it is found that the cylinder autofrettaged by thermal gradient can withstand a maximum of 23.4 MPa pressure without causing yielding of the cylinder, whilst hydraulically autofrettaged cylinder can withstand the pressure of about 36 MPa. However, the non-autofrettaged cylinder can withstand only 18.8 MPa pressure. Thus, it is observed that in the present case, the thermal autofrettage increases the maximum pressure carrying capacity of the cylinder by 24.47%, lesser than in hydraulic autofrettage.

Similar simulation of thermal and hydraulic autofrettage is also carried out for SS304 cylinder. The maximum temperature difference across the wall thickness is limited to 129 °C for thermal autofrettage of SS304 cylinder in order to avoid yielding by residual stresses. For the hydraulic autofrettage, to avoid yielding by residual stresses the SS304 cylinder is subjected to a maximum autofrettage pressure of 182 MPa. Simulating the residual stresses for these conditions, it is observed that the same amount of compressive residual stress is generated at the inner radius of the cylinder by means of thermal gradient and hydraulic pressure and is shown in Figure 7.2.

When the cylinder is pressurized after autofrettage, it is found that the thermally autofrettaged cylinder can carry a maximum pressure of 120 MPa. The non-autofrettaged cylinder can withstand only 91 MPa without causing yielding within the cylinder wall. Thus, the maximum pressure carrying capacity of the SS304 cylinder is increased by 31.87%, more than that in the case of aluminum. The hydraulically autofrettaged cylinder can withstand about 182 MPa, an increase of about 100%.

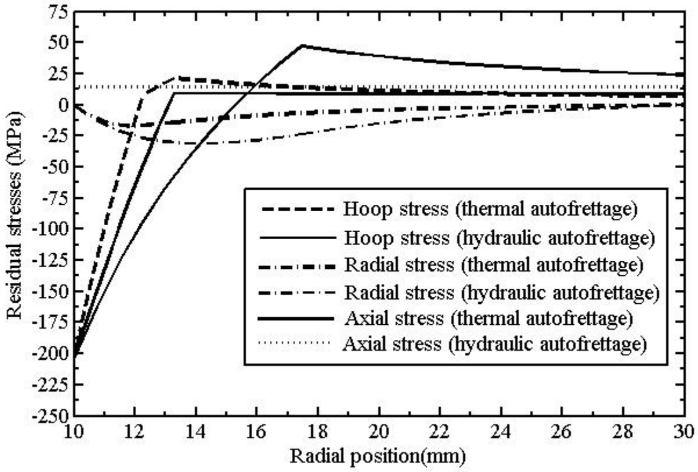

Figure 7.2 Residual stresses in SS304 cylinder for both thermal and hydraulic autofrettage

It is inferred from the above discussion that although the maximum compressive residual stress generated at the inner radius of the cylinder in thermal autofrettage is of the same order as in the case of hydraulic autofrettage, the maximum achievable pressure carrying capacity is less. Nevertheless, the thermal autofrettage has the potential to increase the pressure carrying capacity of the cylinders significantly. The pressure carrying capacity in thermal as well as in hydraulic autofrettage depends on various parameters responsible for the non-homogeneous plastic deformation in the wall of the cylinder. In order to compare the thermal autofrettage both qualitatively and quantitatively with the hydraulic autofrettage, a detailed parametric study is carried out for high pressure application in the following section.

7.3 Parametric Study of Thermal and Hydraulic Autofrettage

The thermal autofrettage process is a potential process to compete with the conventional hydraulic autofrettage process. The process does not require the hydraulic power pack, but the achievable level of autofrettage is limited by the allowable temperature limits on the material of the cylinder. The wall thickness ratio (*b*/*a*) of the cylinder plays an important role in the load requirement for achieving autofrettage. The autofrettage of cylinders is also influenced by the yield strength (σ_Y) and the product of Young's modulus (*E*) & coefficient of thermal expansion (α) of the material. In the following subsections, a detailed comparison of the thermal autofrettage with the conventional hydraulic autofrettage is carried out considering all these aspects.

7.3.1 Effect of Wall Thickness Ratio (*b*/*a*)

The wall thickness ratio (*b*/*a*) is an important parameter in the autofrettage of thick-walled cylinders. In both the hydraulic and thermal autofrettage, the extent of load requirement for achieving the desired elasto-plastic deformation within the wall of the cylinder depends on the wall thickness ratio. Using Tresca yield criterion, the thermal gradient required for initial yielding at the inner wall is given by Eq. (4.19). Defining the non-dimensional thermal gradient to cause yielding as $\theta_Y = E\alpha(T_b - T_a)_\mathrm{Y}/\,(1-\nu)\sigma_Y$, Eq. (4.19) can be expressed as

$$\theta_Y = \frac{2}{\left\{-\dfrac{1}{\ln\left(\dfrac{b}{a}\right)} + \dfrac{2\left(\dfrac{b}{a}\right)^2}{\left(\dfrac{b}{a}\right)^2 - 1}\right\}}. \tag{7.1}$$

When the cylinder is subjected to the pressure loading, the pressure required for initial yielding at the inner wall is given by Tresca criterion (Chakrabarty, 2006)

$$p_Y = \frac{\sigma_Y}{2}\left(1 - \frac{a^2}{b^2}\right). \tag{7.2}$$

The non-dimensional pressure required for initial yielding can be expressed as

$$\overline{p}_Y = \frac{p_Y}{\sigma_Y} = \frac{1}{2}\left(1 - \frac{a^2}{b^2}\right). \tag{7.3}$$

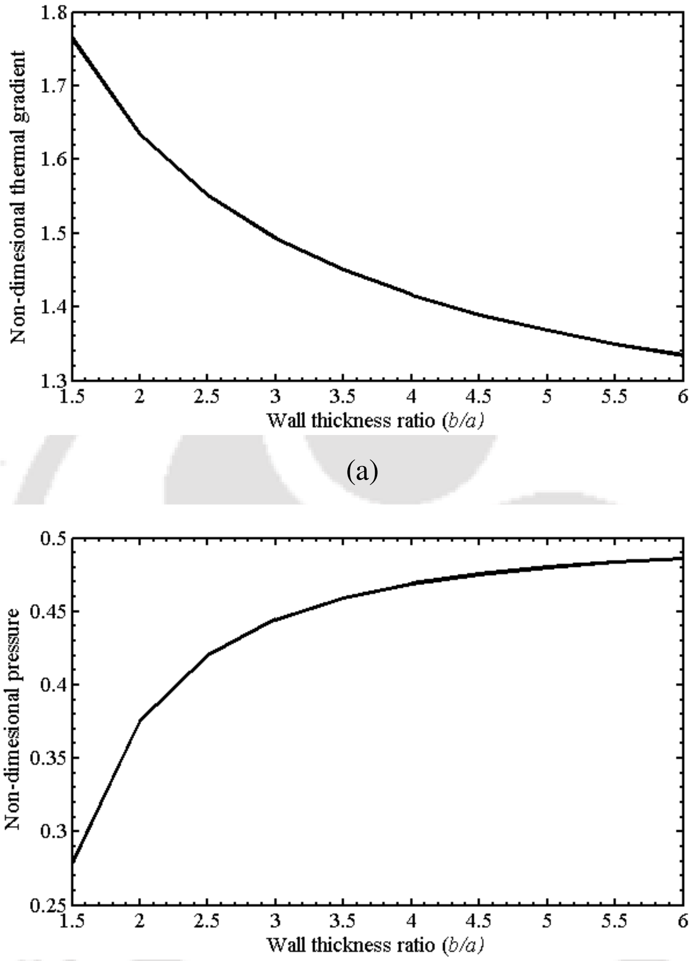

(a)

(b)

Figure 7.3 Variation of required non-dimensional loads with wall thickness ratio for initial yielding in (a) thermal autofrettage (b) hydraulic autofrettage

Figure 7.3 shows the variation of θ_Y versus *b*/*a* and $\overline{p}_Y$ versus *b*/*a* for the case of initial yielding under the thermal gradient and the pressure loading, respectively. It is observed that the required non-dimensional thermal gradient θ_Y decreases as *b*/*a* of the cylinder increases. However, reverse is the case when the cylinder is subjected to hydraulic pressure, *i.e.*, the dimensionless pressure required for initial yielding increases with *b*/*a*. This indicates that in the thermal autofrettage, the maximum thermal gradient required to cause the desired elasto-plastic deformation in the wall of the cylinder decreases with b/a. On the other hand, the maximum pressure required for achieving hydraulic autofrettage increases with b/a. Hence, for high b/a cylinders, the thermal autofrettage may be more convenient than the hydraulic autofrettage.

The maximum equivalent Tresca stress occurs at the inner wall of the cylinder both in the case of hydraulic and thermal autofrettage after unloading. Thus, the reyielding may occur at the inner wall when the autofrettage load is increased. In hydraulic autofrettage, the yielding will restart if the autofrettage pressure (p) is two times the pressure required for initial yielding (p_Y), ignoring the Bauschinger effect. The smallest wall thickness ratio for which the reyielding can occur on unloading is $b/a \approx 2.22$ and the corresponding pressure ($p=2p_Y$) is equal to the collapse pressure. The collapse pressure in the hydraulic autofrettage is $p_o=\sigma_Y \ln(b/a)$ (Chakrabarty, 2006). For $b/a \geq 2.22$, the cylinders can be autofrettaged by applying the maximum pressure, $p=2p_Y$. When $b/a<2.22$, the cylinder collapses at a pressure $p<2p_Y$. Thus, the maximum pressure carrying capacity of a nonhardening cylinder can be increased by 100% compared to the non-autofrettaged one for $b/a \geq 2.22$ in the case of the hydraulic autofrettage. In the case of thermal autofrettage, the achievable level of autofrettage is influenced by the temperature gradient between the outer and inner wall of the cylinder. The increase of the maximum pressure carrying capacity of the cylinder is more in the case of hydraulic autofrettage than the thermal autofrettage. Nevertheless, the thermal autofrettage also increases the maximum pressure carrying capacity of the cylinder significantly.

In order to observe the effect of wall thickness ratio in terms of the increase of the maximum pressure carrying capacity of cylinders, numerical simulations were conducted for Al6061-O and SS316 materials with different wall thickness ratios. The mechanical and thermal properties of Al 6061-O and SS316 are given in Table 7.1. Both the hydraulic and thermal autofrettage for these cylinders are simulated considering the maximum load that does not cause reyielding after unloading. The simulation results are presented in Table 7.2. As expected, it is observed that for the materials with $b/a>2.22$, the maximum pressure carrying capacity of the cylinders is increased by 100% in the case of hydraulic autofrettage. When $b/a<2.22$, the maximum pressure carrying capacity of the cylinders can not be increased by 100%, *e.g.*, for *b*/*a*=2, it is about 85%. It is observed that for the thermal autofrettage, the increase of the maximum pressure carrying capacity, although significant, is lesser than that for the hydraulic autofrettage for the same wall thickness ratio. The percentage increase of the maximum pressure carrying capacity increases with the increase of the wall thickness ratio for the thermal autofrettage.

Table 7.1 Mechanical and thermal properties of Al6061-O and SS316

Material	E (GPa)	σ_Y (MPa)	α (/°C)	v
Al 6061-O	68.9	55.2	25.2×10^{-6}	0.33
SS316	193	290	16.2×10^{-6}	0.30

Table 7.2 Simulation results of hydraulic and thermal autofrettage of cylinders with different wall thickness ratio (*b*/*a*)

Cylinder materials	*b*/*a*	Maximum (T_b-T_a) required in thermal autofrettage (°C)	Maximum pressure required in hydraulic autofrettage (MPa)	% increase of maximum pressure carrying capacity in autofrettage	
				Thermal	Hydraulic
Al 6061-O	2	69	38.25	21.84	84.76
	3	63	49.06	32.54	100
	4	60	51.74	40.37	100
	5	58	52.98	45.02	100
SS316	2	212	200.93	23.41	84.76
	3	193.8	257.78	31.91	100
	4	183.9	271.88	39.41	100
	5	177.6	278.40	44.19	100

It is to be noted that although the maximum pressure carrying capacity of cylinders is more in the hydraulic autofrettage compared to the thermal autofrettage, the requirement of pressure is increased with the increase in the wall thickness ratio. This makes the process expensive due to costly hydraulic power pack. Also, the application of high pressure needs extra care. On the contrary, the thermal autofrettage requires comparatively lower thermal gradient for cylinders with higher wall thickness ratios, making the process an easy-handling.

7.3.2 Effect of $E\alpha$ and σ_Y

The thermal autofrettage is influenced by the $E\alpha$ and σ_Y of the material. Even in hydraulic autofrettage, the load required is dependent on σ_Y. In the Subsections 7.3.2.1 and 7.3.2.2, the thermal and hydraulic autofrettage processes for the materials with different values of $E\alpha$ and σ_Y are discussed.

7.3.2.1 Autofrettage of cylinders for low $\sigma_Y/(E\alpha)$ materials

It is evident From Eq. (4.19) that for materials with low value of $\sigma_Y/(E\alpha)$, a small thermal gradient can cause the yielding at the inner wall. Thus, cylinders made of materials with low value of $\sigma_Y/(E\alpha)$ are very much suitable for the thermal autofrettage. The small thermal gradient can be easily established. Normal cold water can be employed as a flowing fluid through the inner surface of the cylinder in order to keep it at a colder state. The outer wall need not be exposed to a high temperature for such cylinders. As a result recrystallization and other microstructural changes in the materials are avoided. In hydraulic autofrettage, materials with low value of σ_Y require low pressure for initial yielding. Some of the materials with low $\sigma_Y/(E\alpha)$ are listed in Table 7.3. The simulation of thermal autofrettage for the cylinders made of these materials is carried out using the analytical generalized plane strain solutions. To compare with the thermal autofrettage, simulation of hydraulic autofrettage is also conducted. For all simulations, cylinders with fixed b/a=3 is considered.

Table 7.3 Properties of Materials with low $\sigma_Y/(E\alpha)$

Materials	E (GPa)	σ_Y (MPa)	α (/°C)	ν
ASTM 128 grade B2	200	145	21.5×10^{-6}	0.30
muntz metal	110	345	20.8×10^{-6}	0.34
constantan	163	74	18.8×10^{-6}	0.33
gun metal	103	152	19.8×10^{-6}	0.34

The ease of autofrettage depends on the load required to cause the necessary elasto-plastic deformation within the wall of the cylinder. Table 7.4 presents the maximum load required for achieving the autofrettage both by the thermal gradient and the hydraulic pressure. The maximum load is the largest value of the load that does not cause the reverse yielding of the cylinder at the inner radius after its removal. Corresponding to the maximum load, the extent of plastic deformation in the thermal autofrettage is smaller than in the hydraulic autofrettage. Thus, the maximum achievable level of autofrettage in the thermal autofrettage is smaller than in the hydraulic autofrettage. The level of autofrettage is defined as the percentage of the cylinder's wall undergoing plastic deformation. In the present case, the maximum achievable level of autofrettage is about 16% in the thermal autofrettage and about 37% in the hydraulic autofrettage. The maximum percentage increase of pressure carrying capacity of the cylinders due to both thermal and hydraulic autofrettage is also presented in Table 7.4. As the wall thickness ratio of all cylinders is more than 2.22 (b/a=3), the hydraulically autofrettaged cylinder can increase the pressure carrying capacity upto 100% as discussed in Subsection 7.3.1. By employing the thermal autofrettage, the maximum pressure carrying capacity of the cylinders can be increased to about 32–34%. This does not need a high thermal gradient and thus the material properties do not change significantly. In the hydraulic autofrettage, the required maximum pressure for achieving autofrettage increases with the increase of σ_Y. As the maximum pressure increases, the cost of hydraulic power pack increases exponentially. On the other hand, the heater cost increases almost linearly with the power of the heater. Thus, the thermal autofrettage of cylinders is more economical for the materials with low $\sigma_Y/(E\alpha)$ materials than the hydraulic autofrettage.

Table 7.4 Maximum load required in thermal and hydraulic autofrettage for achieving maximum level of autofrettage

Cylinder materials	Maximum load required in		% increase in pressure in	
	thermal autofrettage, $(T_b - T_a)$ (°C)	hydraulic autofrettage, pressure (p) (MPa)	thermal autofrettage	hydraulic autofrettage
ASTM 128 grade B2	184.70	128.88	32	100
muntz metal	124.80	306.67	33.24	100
constantan	47.58	65.77	33.54	100
gun metal	146.80	135.11	33.33	100

7.3.2.2 Autofrettage of cylinders for high $\sigma_Y/(E\alpha)$ materials

Some materials possessing high $\sigma_Y/(E\alpha)$ require comparatively higher thermal gradient. For thermal autofrettage either the inner wall of the cylinder can be subjected to a low temperature by cryogenic cooling or the outer wall to a high temperature. There are practical limitations on the temperatures that the materials can sustain. The hydraulic autofrettage of cylinders also requires high pressure as the σ_Y is high for high $\sigma_Y/(E\alpha)$ materials.

To create a high thermal gradient in the thermal autofrettage, subjecting the outer wall to a temperature more than the recrystallization temperature is undesirable. One alternative is to cool the inner wall to a very low temperature and exposing the outer wall to a temperature much below the recrystallization temperature. However, low temperature also affects the engineering properties of materials. The hardness, yield strength, tensile strength, modulus of elasticity and fatigue resistance of almost all metals and alloys increase as the temperature is lowered (Hurlich, 1968). Materials like nickel, copper, silver, aluminum, titanium including their alloys and some of the stainless steel grades can retain good ductility and toughness down to very low temperature. The material properties such as Young's modulus and yield strength of these materials do not deviate much at low temperature from their properties at room temperature. Thus, these materials can be subjected to a low temperature to create desired thermal gradient for achieving thermal autofrettage. For example, Al6061-T6 alloy and 17-4 PH stainless steel (condition H1150-M), which possess high $\sigma_Y/(E\alpha)$ are suitable for thermal autofrettage. The properties of Al6061-T6 and 17-4 PH stainless steel (condition H1150-M) are listed in Table 7.5.

Table 7.5 Material properties of Al6061-T6 and 17-4 PH stainless steel (condition H1150-M)

Materials	Young's modulus (GPa)	Yield strength (MPa)	Coefficient of thermal expansion (/°C)	Poisson's ratio (v)
Al6061-T6	68.9	276	25.2×10^{-6}	0.33
17-4 PH stainless steel (condition H1150-M)	196	517	7.1×10^{-6}	0.30

For the cylinders made of Al6061-T6 and 17-4 PH stainless steel with wall thickness ratio of 3, the cylinders start yielding at thermal gradients of 158.98 °C and 388.21 °C respectively. The numerical simulation of the thermal autofrettage shows that the maximum temperature difference of 318 °C is required for achieving the maximum increase in the pressure carrying capacity, which is about 33%, in the Al6061-T6 cylinder. The required temperature difference of 318 °C can be achieved by exposing the inner wall to cryogenic temperature using liquid hydrogen or liquid nitrogen and keeping the outer wall below its recrystallization temperature.

The maximum temperature difference of 776 °C is needed for achieving the maximum increase in the pressure carrying capacity of the cylinder made of 17-4 PH stainless steel. However, it is difficult to create such high thermal gradient in this cylinder due to the temperature limits on the inner and outer wall. The 17-4 PH stainless steel retains its good mechanical and thermal properties upto 316 °C and down to −196 °C (liquid nitrogen temperature). Thus, the maximum temperature difference that can be created across the wall thickness is only 512 °C. The simulation shows the maximum increase of 16.94% in pressure carrying capacity in 17-4 PH stainless steel for a temperature difference of 512 °C. Thus, the thermal autofrettage of 17-4 PH steel is not very useful. Using hydraulic autofrettage, the pressure carrying capacity can be increased by two times compared to the non-autofrettaged cylinders. This can be achieved by inducing a maximum pressure of 258.74 MPa in Al6061-T6 and 459.54 MPa in 17-4 PH steel. The materials like nickel, copper, Al6061-O, SS304, SS316 and some titanium alloys can be exposed to a very low temperature; however, due to their low $\sigma_Y/(E\alpha)$ ratios, the use of cryogenic fluids are not required for thermal autofrettage.

It is observed that for high $\sigma_Y/(E\alpha)$ materials, the hydraulic autofrettage requires enormous amount of pressure and the thermal autofrettage requires cryogenic fluids. The use of cryogenic fluids in thermal autofrettage of cylinders makes the process expensive; albeit it is less expensive than the hydraulic autofrettage. Moreover, cryogenic cooling of inner wall of the cylinders for achieving the thermal autofrettage is a lot safer than applying a high pressure in the hydraulic autofrettage. The most common cryogenic coolants such as liquid nitrogen and liquid hydrogen are not harmful to the environment. On the other hand, for creating hydraulic pressures, hydraulic power pack utilizes a large amount of hydraulic oil that is harmful to the environment. Thus, the thermal autofrettage is a greener manufacturing process, although for some materials, *e.g.*, 17-4 PH stainless steel, the maximum increase of pressure carrying capacity is limited due to allowable temperature limits on the material.

7.4 Thermal Autofrettage of Cylinders Subjected to High Thermal Gradient without Pressure and its Comparison with Hydraulic Autofrettage

In general, the thick-walled cylindrical vessels are autofrettaged for high pressure applications. However, there are many applications in industries, where thick-walled cylinders are subjected to high thermal gradient such as cryogenic storage tanks. For example, Shuttle program requires very large cryogenic ground storage tanks to store liquid oxygen and hydrogen (Arens *et al*., 2010). There are other examples in chemical and oil industries where thick-walled pipes are used to carry hot fluids. In such cases, the inner wall of the pipe is subjected to higher temperature than the outer wall, which may create a large thermal gradient across the wall of the pipe. Due to such large thermal gradient in the wall of the thick-walled cylinders, they are subjected to large thermal stresses. The cylinders may fail when the generated thermal stresses exceed the yield strength of the material in service condition. Hence, the thermal load carrying capacity should be enhanced. The autofrettage process can be employed to withstand high thermal stresses due to the thermal gradient.

As a way to strengthen the cylinder material to withstand the high thermal stress, the thermal autofrettage is simulated for typical cylinders in this section. Further, it is compared with the conventional hydraulic autofrettage. Typical thick-walled cylinders made of SS316 and Al6061-O with inner radius, a=10 mm and outer radius b=30 mm are considered. The material properties of SS316 and Al6061-O are given in Table 7.1. From the application point of view, there exist two situations for thermal loading. In Subsections 7.4.1 and 7.4.2, these two cases are described and simulations of thermal autofrettage are carried out for the typical cylinders. In Subsection 7.4.3, hydraulic autofrettage of the same cylinders is simulated and they are subjected to high thermal gradient for comparing their performance with thermally autofrettaged cylinders.

7.4.1 Case 1: Cylinders Subjected to Thermal Gradient in which the Inner Wall is at Lower Temperature than the Outer Wall ($T_a<T_b$)

In this case, high tensile thermal stresses are generated at and around the inner wall by the applied thermal gradient. The tensile thermal stresses at and around the inner wall can be reduced by inducing compressive residual stresses. This can be achieved through thermal autofrettage. The thermal autofrettage of SS316 and Al6061-O cylinders for the present case are simulated and the results are presented.

For the thermal autofrettage, the cylinders must be subjected to a thermal gradient greater than the thermal gradient required for the initial yielding. The temperature differences that cause the initial yielding in the SS316 and Al6061-O cylinders are 96.92 °C and 31.79 °C, respectively. The maximum temperature differences for thermal autofrettage in these cylinders are 193.84 °C and 63.58 °C, respectively to avoid reverse yielding after unloading. Both the cylinders undergo first stage of elasto-plastic deformation creating an inner plastic zone in the wall. In the SS316 cylinder, the plastic zone propagates to a radial position d=13.2874 mm. The plastic zone propagates to d=13.2876 mm in the Al6061-O cylinder.

The distribution of the residual thermal stresses after elastic unloading of the induced thermal gradients in the SS316 and Al6061-O cylinders are shown in Figure 7.4. The distribution shows that substantial amount of compressive residual hoop and axial thermal stresses are generated at and around the inner wall. The residual hoop and axial thermal stresses at and around the outer wall are tensile, but the magnitude is small. The residual radial thermal stresses are very small and compressive throughout the thickness. The compressive residual thermal stresses offset the tensile thermal stresses at and around the inner wall when the cylinders are subjected to the thermal gradient in the next phase of loading. Hence, the cylinders will be able to withstand larger thermal gradient than the non-autofrettaged cylinders.

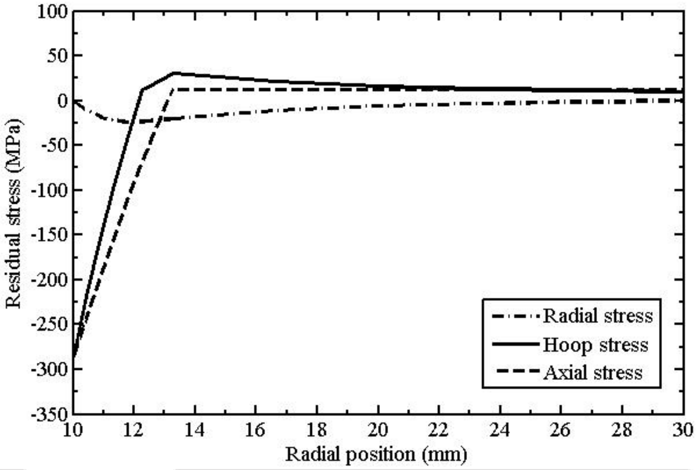

(a)

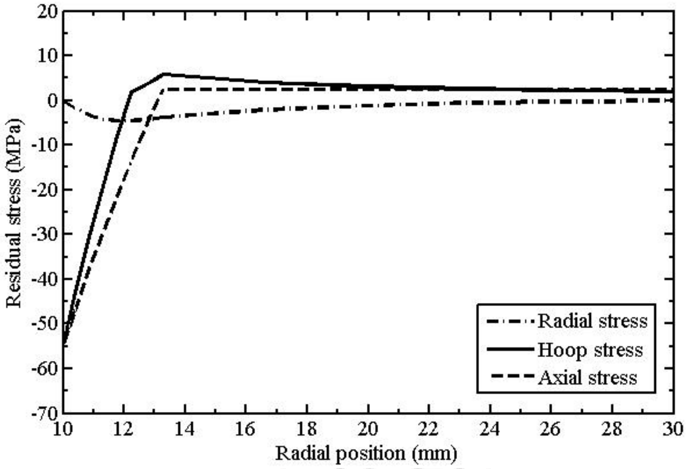

(b)

Figure 7.4 Residual stress distribution in (a) SS316 and (b) Al6061-O cylinders for $T_a<T_b$

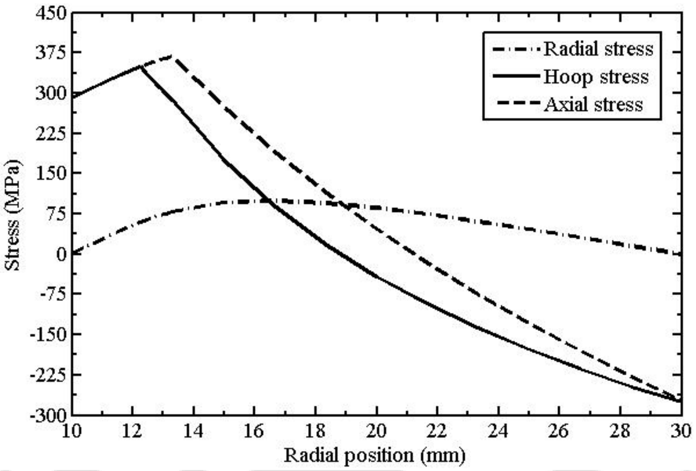

(a)

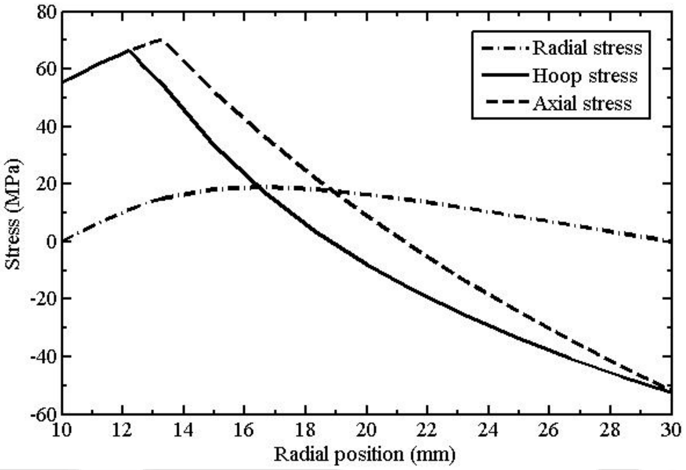

(b)

Figure 7.5 Net stress distribution in the thermally autofrettaged (a) SS316 and (b) Al6061-O cylinders when subjected to thermal gradients for $T_a<T_b$

The SS316 and Al6061-O cylinders can withstand the maximum temperature differences of 193.84 °C and 63.58 °C, respectively without yielding. The net stresses in the walls of the autofrettaged cylinders are obtained by adding the stresses due to working thermal gradient to the residual thermal stresses and are shown in Figure 7.5. The thermal stresses under the working thermal gradient are given by Eqs. (4.11), (4.12) and (4.16). The maximum thermal stress in the autofrettaged cylinders is significantly reduced due to the compressive residual thermal stresses. The non-autofrettaged SS316 and Al6061-O cylinders can withstand the maximum temperature differences of 96.92 °C and 31.79, °C respectively. Thus, the maximum thermal gradient that the autofrettaged cylinders can withstand is increased by 100% as compared to the non-autofrettaged cylinders.

7.4.2 Case 2: Cylinders Subjected to Thermal Gradient in which the Inner Wall is at Higher Temperature than the Outer Wall (T_a>T_b)

When the inner wall of the cylinder is at a higher temperature than the outer wall, compressive stresses are generated at and around the inner wall. In this case, generation of tensile residual thermal stresses at and around the inner wall will help in reducing the magnitude of compressive thermal stresses. The cylinders may be autofrettaged by cooling the outer wall and heating the inner wall continuously till the desired thermal gradient is achieved. The analytical expressions developed in Chapter 4 are used for the simulation where the value of the sign factor 'k_1' is -1. The thermal autofrettage simulations of the SS316 and Al6061-O cylinders for $T_a>T_b$ are carried out.

The outer wall of the cylinder may be subjected to room temperature or even lower by circulating compressed air or any other cold fluid. The surface of the inner wall may be heated electrically using a heating element. Thus, a negative thermal gradient (T_b-T_a) is produced to achieve the desired elasto-plastic deformation within the wall of the cylinder. Here, all the thermal gradients involved are same as in Section 7.4.1, but with a negative sign. The distribution of the residual thermal stresses in the cylinders is shown in Figure 7.6. It is observed that the stress distribution is exactly opposite to that observed for Case 1. At and around the inner wall, large amount of tensile residual stresses is generated. On the other hand, small amount of compressive residual stresses is produced at and around the outer wall. Thus, when the cylinders are subjected to thermal gradients such that $T_a>T_b$, in the next loading stage, the tensile residual thermal stresses at and around the inner wall offset the compressive thermal stresses.

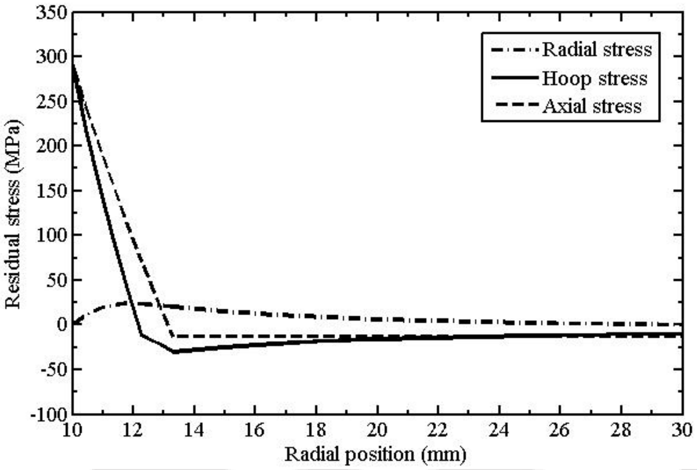

(a)

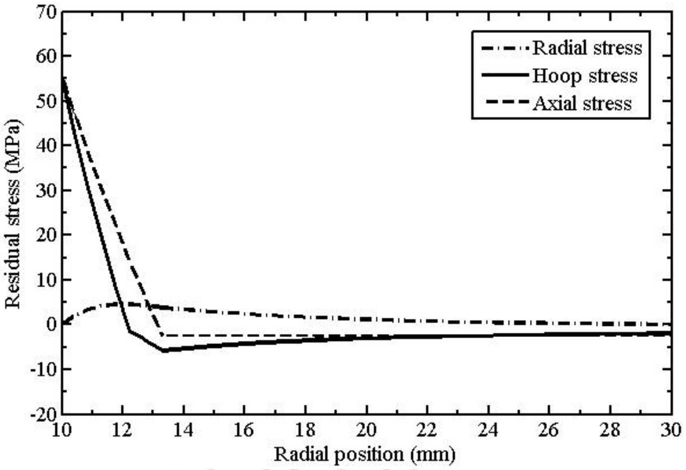

(b)

Figure 7.6 Residual stress distribution in (a) SS316 and (b) Al6061-O cylinders for $T_a>T_b$

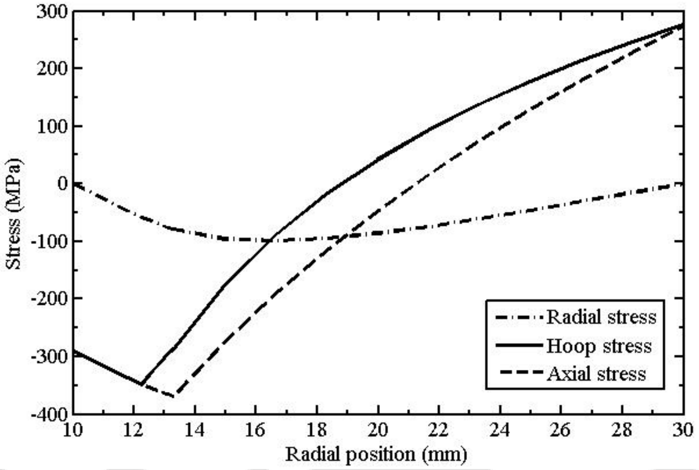

(a)

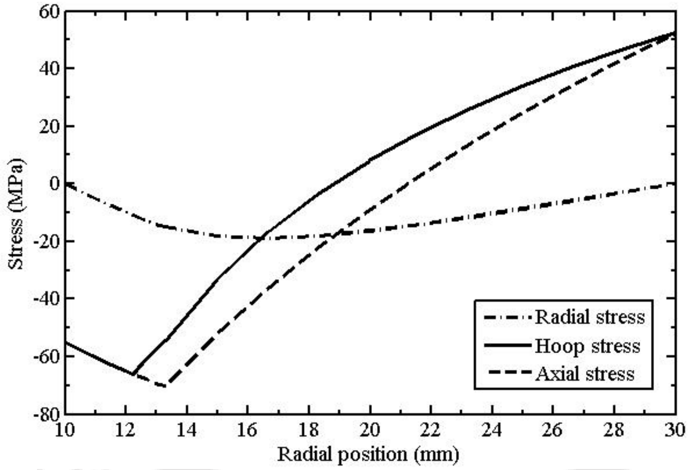

(b)

Figure 7.7 Net stress distribution in the thermally autofrettaged (a) SS316 and (b) Al6061-O cylinders subjected to thermal gradients for $T_a > T_b$

By subjecting the thermally autofrettaged cylinders to thermal gradients, it is found that the SS316 and Al6061-O cylinders can withstand the maximum of −193.84 °C and −63.58 °C temperature differences respectively. Thus, the maximum thermal gradient that the autofrettaged cylinders can withstand is increased by 100%. The net stress distribution in the autofrettaged cylinders for the present case is shown in Figure

7.7. It is observed that the net thermal stresses in the cylinders are compressive at and around the inner wall and tensile at and around the outer wall. The compressive thermal stresses are greater than the tensile thermal stresses. This shows that the autofrettaged cylinders may withstand some internal pressure loading along with the thermal gradient. This aspect will be discussed in Section 7.5.

7.4.3 Hydraulic Autofrettage of Cylinders Subjected to Thermal Gradient without Pressure

The hydraulic autofrettage of thick-walled cylinders subjected to thermal gradient is simulated in order to compare it with the thermal autofrettage. The cylinders are same as in Subsection 7.4.2. In hydraulic autofrettage, the cylinders may have closed-end or open-end and the axial strain, ε_z, is assumed to be constant (Chakrabarty, 2006). The cylinders are subjected to hydraulic autofrettage by inducing the maximum pressure as given in Table 7.2 for $b/a = 3$. The residual stresses set up in the cylinders after removal of the induced pressure are shown in Figure 7.8 both for closed-end and open-end cylinders. Sufficiently high compressive residual hoop stresses are induced at and around the inner wall of the cylinders.

If the hydraulically autofrettagedSS316 cylinder is subjected to thermal gradient such that $T_a<T_b$, instead of internal pressure, it can withstand the maximum thermal gradient of 126 °C. Thus, the maximum thermal gradient that the cylinder can withstand is increased by 30% as compared to the non-autofrettaged one. The maximum temperature difference that the autofrettaged Al6061-O cylinder can withstand is 42.27 °C. Thus, the maximum thermal gradient capacity of the Al6061-O cylinder is increased by 33%. The net stress distribution in the cylinders for the present case is shown in Figure 7.9. The hydraulically autofrettaged cylinders cannot be subjected to high thermal gradient such that $T_a>T_b$. In this case, the compressive thermal stresses due to the thermal gradient will add to the compressive residual stresses already produced by the hydraulic autofrettage. This leads to the increase of overall stress causing the failure of the cylinders.

Contrary to the hydraulically autofrettaged cylinders, the thermally autofrettaged cylinders can withstand double the thermal gradient that anon-autofrettaged cylinder can withstand, as shown in Subsection 7.4.2. It can be concluded that for the cylinders subjected to high thermal gradient without pressure, the thermal autofrettage is superior to the hydraulic autofrettage.

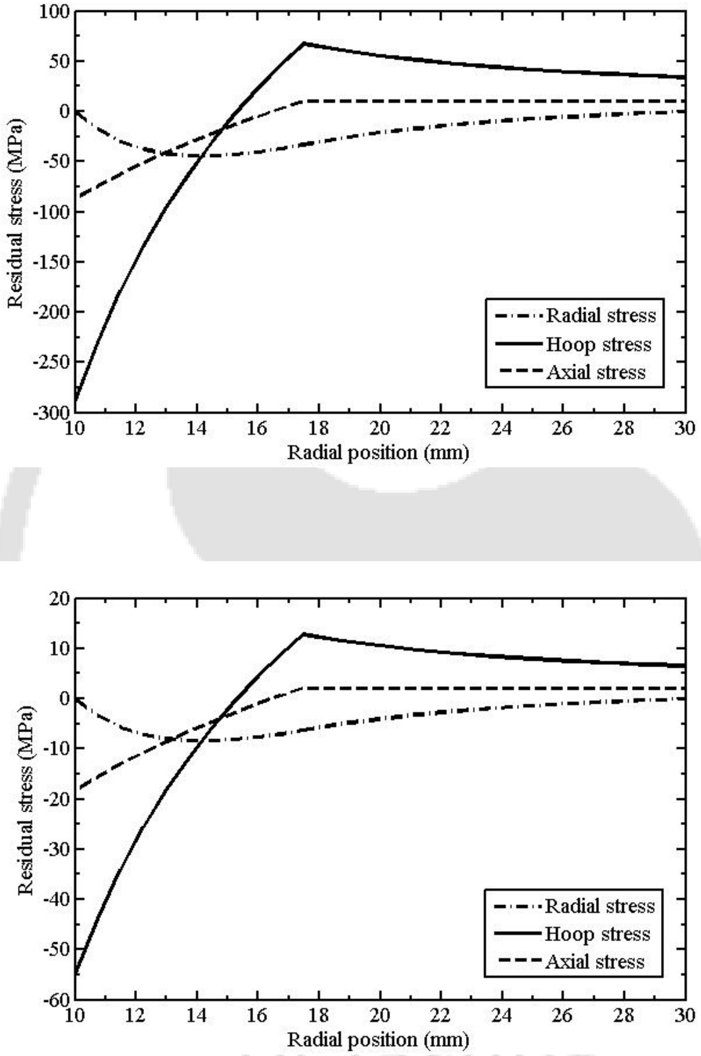

(b)

Figure 7.8 Residual stresses in (a) SS316 and (b) Al6061-O cylinders due to hydraulic autofrettage

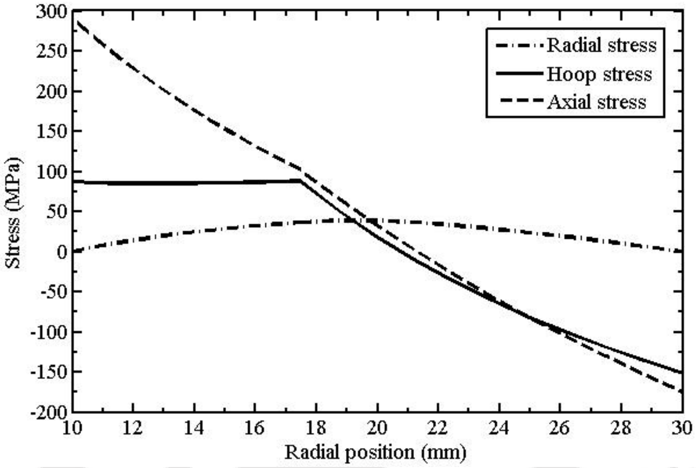

(a)

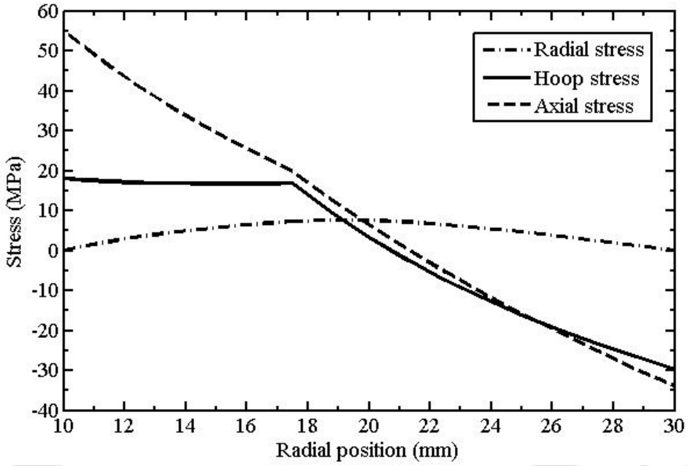

(b)

Figure 7.9 Net stress distributions in hydraulically autofrettaged (a) SS316, (b) Al6061-O cylinders when subjected to thermal gradient (T_a<T_b)

7.5 Thermal Autofrettage of Cylinders Subjected to Thermal Gradient with Pressure and its Comparison with Hydraulic Autofrettage

There are situations where thick-walled cylindrical vessels are subjected to high pressure as well as thermal gradients. Typical examples are thick-walled pipes carrying hot fluid under pressure in oil or chemical industries. This needs the special attention of the vessel designers to increase the load carrying capability of the cylinders subjected to the thermal gradient with internal pressure. In this section, both the hydraulic and the thermal autofrettage of the cylinders subjected to the thermal gradient with internal pressure are studied and comparison is made.

As shown in Figure 7.7, in the thermally autofrettaged cylinders subjected to thermal gradients, the net compressive stresses of sufficiently high magnitude are produced at and around the inner wall. If the cylinders are now subjected to some internal pressure, it can offset the net compressive stresses at and around the inner wall as the application of pressure generates tensile stresses at and around the inner wall. Thus, the thermal autofrettage is useful for cylinders subjected to thermal gradient along with internal pressure. Numerical simulation of the thermally autofrettaged SS316 cylinder is carried out by subjecting it to various thermal gradient and pressure combinations. The combination for which the cylinder is safe is shown in Figure 7.10. The maximum equivalent Tresca stress occurs at the inner wall as the pressure is increased upto the temperature difference of 165 °C. After that the safe pressure decreases with increasing thermal gradient because the maximum equivalent Tresca stress exists at the outer wall.

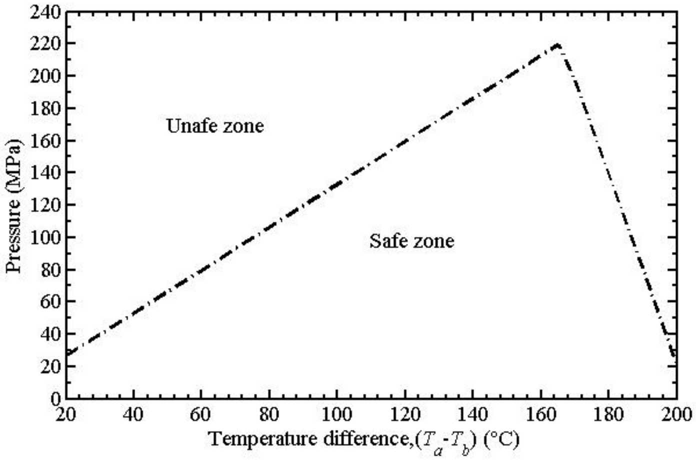

Figure 7.10 Safe and unsafe zones for different combinations of thermal gradient and pressure loading for the thermally autofrettaged SS316 cylinder

The hydraulically autofrettaged cylinders can withstand enhanced pressure in combination with the negative thermal gradient (T_b<T_a). The hydraulically autofrettaged SS316 cylinder is simulated by subjecting it to thermal gradients with pressure loading. The combinations of thermal gradients and pressure loading for which the cylinder is in the safe zone are shown in Figure 7.11. It is observed that as the thermal gradient is increased, the safe pressure decreases. For all combinations, the maximum equivalent Tresca stress occurs at the radius of elastic-plastic interface.

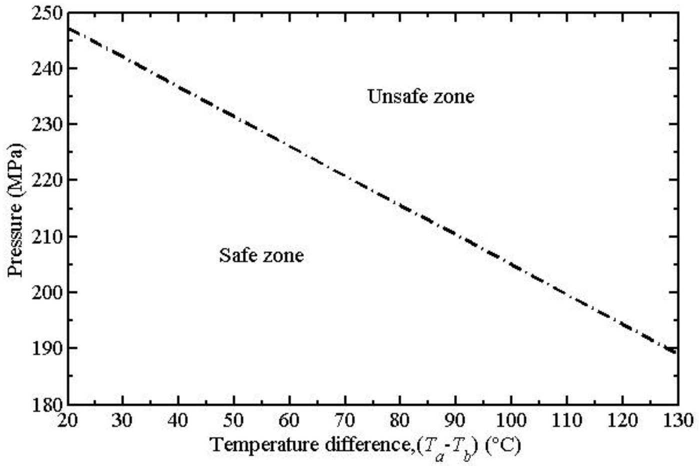

Figure 7.11 Safe and unsafe zones for different combinations of thermal gradient and pressure loading for the hydraulically autofrettaged SS316 cylinder

In short, both the thermal and hydraulic autofrettage can take thermal gradient in combination with internal pressure. In the hydraulic autofrettage, the pressure loading decreases with the thermal gradient. On the other hand, in thermal autofrettage, the pressure loading increases with the thermal gradient up to certain thermal gradient; thereafter it cannot sustain more pressure.

7.6 Summary

In this chapter a comparative study of thermal autofrettage with the conventional hydraulic autofrettage has been carried out considering various aspects. It is observed that in the thermal autofrettage, the maximum possible pressure carrying capacity increases with the wall thickness ratio. In the hydraulic autofrettage, there is 100% increase in pressure carrying capacity for wall thickness ratio $b/a \geq 2.22$. Such a high increase in the maximum possible pressure carrying capacity cannot be achieved by thermal autofrettage. For low $\sigma_Y/(E\alpha)$ materials, the thermal autofrettage requires a thermal gradient that can be easily created by cooling the inner wall using cold water.

Hence, the thermal autofrettage is more economical than the hydraulic autofrettage as the hydraulic power pack for applying pressure in the hydraulic autofrettage is costlier than the heater used for thermal autofrettage. Materials with high $\sigma_Y/(E\alpha)$ require cryogenic fluids for achieving thermal autofrettage which are more economical and a lot safer than a high pressure hydraulic power system. The thermal autofrettage of cylinders subjected to large thermal gradient is investigated and compared with the hydraulic autofrettage. It is observed that the thermally autofrettaged cylinders can bear more thermal gradient than the hydraulically autofrettaged cylinders. Autofrettage of cylinders subjected to combined thermal gradient and pressure loading simultaneously is also studied. The analysis shows that both the thermal and hydraulic autofrettage can be used for cylinders subjected to combined thermal gradient and pressure loading, but the stress-response is different for both the cases. The suitability of one process over the other will depend on the actual magnitudes of thermal gradient and pressure.

Chapter 8

A Study on Enhancing the Performance of Thermally Autofrettaged Cylinder through Shrink-Fitting

8.1 Introduction

Autofrettage is one of the most popular metal working processes used to strengthen the high pressure cylindrical components in terms of their pressure carrying capacity and fatigue lifetime. In order to achieve the further increase in the pressure carrying capacity and at the same time to achieve maximum fatigue life, the shrink-fit is often combined with the autofrettage process. In autofrettage process the Bauschinger effect puts a limit on the maximum compressive residual stress at the inner radius. The shrink-fit of cylinders alone cannot generate compressive residual stresses as large as in the autofrettage process. Therefore, a combination of autofrettage and shrink-fit happens to be advantageous that helps in keeping the inner autofrettaged cylinder in compression with maximum compressive residual stress at the inner radius without further yielding. Researchers have studied the combined effect of hydraulic autofrettage and shrink-fit in order to increase the maximum fatigue life of cylinders (Kapp *et al*., 1998; Parker, 2001; Parker and Kendall, 2003; Jahed *et al*., 2006; Lee *et al*., 2009).

Although the conventional hydraulic autofrettage process is widely employed to increase the pressure carrying capacity and is also combined with the shrink-fit to enhance the fatigue life, the hydraulic autofrettage process is not cost-effective at times. Moreover, sometimes there are concerns of health and safety due to high pressure and noise generated by hydraulic power pack. Compared to the hydraulic autofrettage process, the thermal autofrettage process proposed in this thesis is simple and less expensive. The process can potentially increase the pressure carrying capacity of the cylinder. However, the maximum increase in pressure carrying capacity is less as compared to the conventional hydraulic autofrettage. The present work studies the possibilities of enhancing the pressure carrying capacity in the thermally autofrettaged cylinder by shrink-fit. It is considered that the cylinder is first subjected to thermal autofrettage and then an outer cylindrical layer is shrink-fitted to it. This also puts the main cylinder under compression, which enhances its fatigue strength. The thermal autofrettage is analysed using the stress analysis presented in Chapter 4 assuming elastic-perfectly plastic material and devoid of Bauschinger effect, where the effect of strain hardening was shown to be insignificant. The analysis provided reasonably good agreement with the experimental results presented in Chapter 6.

8.2 Shrink fitting of an outer cylindrical layer to the thermally autofrettaged cylinder

An outer cylindrical layer of inner radius less than the outer radius, b of the thermally autofrettaged cylinder by δ, *i.e.*, $(b-\delta)$ is considered, where δ is the shrink-fit allowance. The inner radius of the thermally autofrettaged cylinder is a. The outer radius of the layer is z. A compound cylinder is formed by shrink-fitting the outer layer to the thermally autofrettaged cylinder. The geometry of the compound cylinder is shown in Figure 8.1. The inner thermally autofrettaged cylinder consists of two inner plastic zones (plastic zone I, $a\le r\le c$ and Plastic zone II, $c\le r\le d$), two outer plastic zones (Plastic zone III, $f\le r\le b$ and Plastic zone IV, $e\le r\le f$) and an intermediate elastic zone, $d\le r\le e$ when the cylinder undergoes second stage of plastic deformation. The two outer plastic zones do not appear in the first stage of plastic deformation and the elastic zone spreads from d to outer radius, b. The two adjacent inner plastic zones (and in some cases outer plastic zones as well) in the wall of the cylinder appear due to Tresca yield criterion and correspond to different sides of yield locus. The boundary radii, c, d, e and f between the different zones are evaluated using the stress continuity as detailed in Chapter 4. Due to shrink-fit, the contact pressure p_{sh} between the two cylinders is given by (Lee *et al*., 2009)

$$p_{sh} = \frac{\left(\dfrac{\delta}{b}\right)}{\dfrac{1}{E_1}\left(\dfrac{b^2+a^2}{b^2-a^2}-\nu_1\right)+\dfrac{1}{E_2}\left(\dfrac{z^2+b^2}{z^2-b^2}+\nu_2\right)}, \tag{8.1}$$

where E_1 & E_2 are the Young's modulus of elasticity of the inner and outer cylinder and ν_1 & ν_2 are the Poisson's ratio of the inner and outer cylinder respectively.

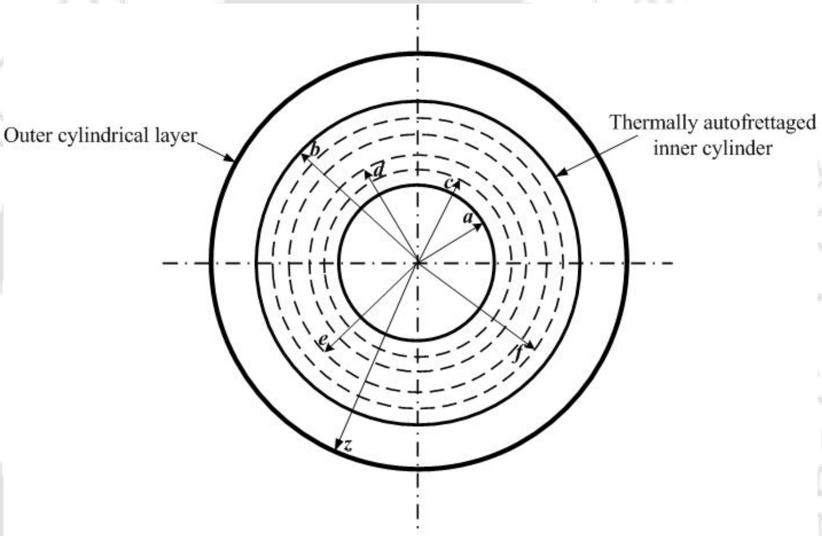

Figure 8.1 Geometry of the compound cylinder with thermally autofrettaged inner cylinder

The contact pressure, p_{sh} acts as an external pressure on the inner thermally autofrettaged cylinder and as an internal pressure on the outer cylindrical layer. The stress distributions in the inner cylinder due to shrink-fit considering open end condition are given by (Lee *et al.*, 2009)

$$\sigma_r^{\mathrm{sh}_i} = -p_{sh}\frac{b^2}{b^2-a^2}\left(1-\frac{a^2}{r^2}\right), \tag{8.2}$$

$$\sigma_\theta^{\mathrm{sh}_i} = -p_{sh}\frac{b^2}{b^2-a^2}\left(1+\frac{a^2}{r^2}\right), \tag{8.3}$$

$$\sigma_z^{\mathrm{sh}_i} = 0. \tag{8.4}$$

The stress distributions in the outer cylindrical layer due to shrink-fit are given by (Lee *et al.*, 2009)

$$\sigma_r^{\mathrm{sh}_o} = p_{sh}\frac{b^2}{z^2-b^2}\left(1-\frac{z^2}{r^2}\right), \tag{8.5}$$

$$\sigma_\theta^{\mathrm{sh}_o} = p_{sh}\frac{b^2}{z^2-b^2}\left(1+\frac{z^2}{r^2}\right), \tag{8.6}$$

$$\sigma_z^{\mathrm{sh}_o} = 0. \tag{8.7}$$

In the compound cylinder, the net residual stress distribution in the thermally autofrettaged inner cylinder is given by the superposition of the shrink-fit stresses to the residual stresses induced by the thermal autofrettage. The expressions for residual stresses in the different zones due to thermal autofrettage are available in Chapter 4. The net residual stresses in the outer cylindrical layers are only due to shrink-fit and are given by Eqs. (8.5), (8.6) and (8.7).

8.3 Numerical Results and Discussion

To see the effect of shrink-fitting to the thermally autofrettaged cylinder, the numerical simulation of the residual stresses in the compound cylinder is carried out. An SS304 cylinder with inner radius, a = 10 mm and outer radius, b = 30 mm is first considered for thermal autofrettage. Then, an outer layer of 10 mm thickness, *i.e.*, with outer radius z = 40 mm made of the same material is considered to be shrink-fitted. The material properties of SS304 are as follows: Young's modulus of elasticity, E = 193 GPa, yield stress, σ_Y =205 MPa, Poisson's ratio, ν = 0.3, coefficient of thermal expansion, $\alpha = 17.2\times10^{-6}$/ºC.

It is assumed that after shrink-fitting, the net residual stresses at the inner radius of the compound cylinder will not cause further yielding of the material. As the shrink-fit stresses are superimposed to the residual stresses due to thermal autofrettage to achieve the net maximum residual stress at the inner radius, the temperature difference required for thermal autofrettage of the inner cylinder is reduced. The thermal autofrettage need not produce large residual stresses alone. This will inhibit the possible Bauschinger effect during elastic unloading of temperature difference in thermal autofrettage. Bauschinger effect is significant only when the level of overstrain is large (Huang and Cui, 2006). For a temperature difference (T_b–T_a) employed to achieve the thermal autofrettage in the inner cylinder, the shrink-fit allowance δ is suitably chosen such that the net maximum residual stresses will not cause yielding at the inner radius. For each combination of (T_b–T_a) and δ, the simulations are carried out for finding out the increase in the maximum pressure carrying capacity corresponding to the yield onset pressure. The yield onset pressure of the non-autofrettaged single/monobloc cylinder of inner radius 10 mm and outer radius of 40 mm is 96.09 MPa. The simulation results are presented in Table 8.1.

Table 8.1 Pressure carrying capacity for various combinations of (T_b–T_a) and shrink-fit allowance

Geometry of the autofrettaged cylinder (mm)	Thickness of the outer cylindrical layer (mm)	(T_b–T_a) (°C)	Shrink fit allowance, δ (mm)	Maximum pressure capacity of the compound cylinder (MPa)	% change in pressure carrying capacity
a=10 b = 30	10	110	0.020	151.88	58.06
		109	0.021	153.00	59.22
		108	0.022	154.10	60.37
		107	0.023	155.20	61.51
		106	0.024	156.29	62.65
		105	0.025	157.34	63.74
		104	0.026	158.36	64.80
		103	0.027	159.40	65.88
		102	0.028	144.20	50.06
		101	0.029	118.50	23.32
		100	0.030	92.80	–3.40

It is observed from Table 8.1 that as the shrink fit allowance δ is increased, the temperature difference, $(T_b{-}T_a)$, required for thermal autofrettage of the inner cylinder decreases in order to produce the net maximum residual stresses at the inner radius. The maximum pressure carrying capacity of the cylinder is increased up to a certain combination of $(T_b{-}T_a)$ and δ and thereafter it starts decreasing. The maximum pressure carrying capacity of the compound cylinder is the maximum for $(T_b{-}T_a) = 103$ °C and $\delta = 0.027$ mm. The net residual stress distribution and overall stress distribution for the maximum internal working pressure (159.40 MPa) in this case is shown in Figures 8.2 and 8.3, respectively. It is to be noted that the overstrain level in the autofrettaged cylinder is only 10.8%. The maximum compressive residual stress generated due to unloading is 122.21 MPa at the inner radius, which is much lower than the yield strength of SS304. Thus, the Bauschinger effect is not very significant in the present case, as also supported by the experiments in Section 6.4.3.

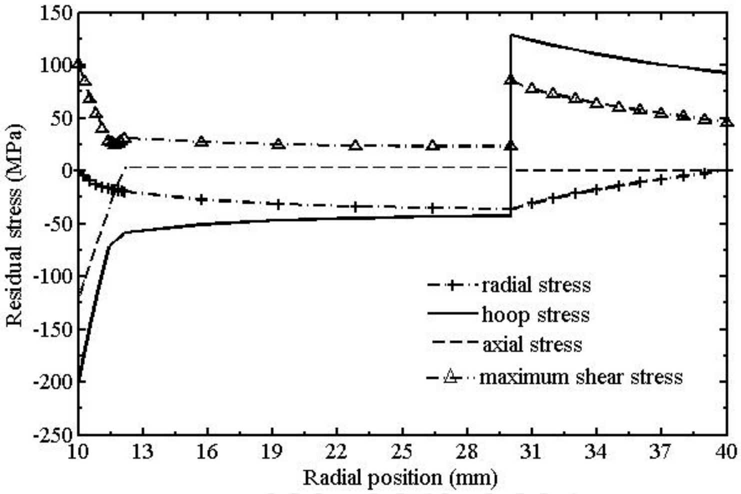

Figure 8.2 Residual stress distributions in the compound cylinder where the inner cylinder is thermally autofrettaged

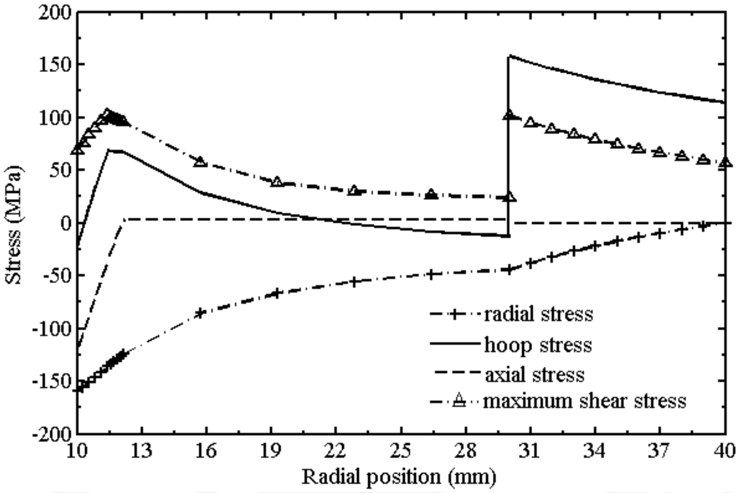

Figure 8.3 Overall stress distribution in the pressurized compound cylinder (for p = 159.40 MPa) where the inner cylinder is thermally autofrettaged

The maximum pressure carrying capacity of the cylinder starts reducing drastically from the combination (T_b–T_a) = 102 °C and δ = 0.028 mm (with increasing δ) as shown in Table 8.1. The compound cylinder cannot withstand the pressure equal to the corresponding non-autofrettaged single cylinder for the combination (T_b–T_a) = 100 °C and δ = 0.030 mm. This is due to the fact that as the shrink-fit allowance, δ increases beyond a limit with the corresponding reduction in (T_b–T_a), the maximum equivalent Tresca stress condition exists at the inner radius of the outer cylindrical layer. Thus, it is observed that the combination of (T_b–T_a) and δ plays a significant role in increasing the pressure carrying capacity of the shrink-fitted compound cylinder. In the present case, choosing the proper combination of (T_b–T_a) and δ, the maximum pressure carrying capacity of the compound cylinder can be increased to the maximum of 65.88% as compared to the corresponding non-autofrettaged single cylinder. However, if a corresponding single cylinder is considered only under thermal autofrettage without shrink-fitting, the cylinder can withstand the maximum internal working pressure of 133.90 MPa which is only 39.34% greater than the non-autofrettaged one. Thus, in the present case, the shrink-fitting of an outer layer to a thermally autofrettaged cylinder provides a greater increase in the pressure carrying capacity than the corresponding thermally autofrettaged single cylinder. It is also important to notice that due to shrink-fit, the net residual hoop stresses in the inner cylinder is compressive throughout the wall thickness. Due to this, the fatigue life of the cylinder increases when it is subjected to cyclic pressure loading.

The thermally autofrettaged cylinder which is combined with shrink-fit may undergo dimensional change in the inner diameter during the processing of thermal autofrettage. It is expected that the dimensional change in the inner diameter of the cylinder is within the permitted tolerance zone. A discussion on the dimensional change in the cylinder due to thermal autofrettage is provided in Appendix G.

8.4 A Comparison of the Effect of Shrink-fit on Hydraulic and Thermal Autofrettage

In this section a comparison of the effect of the shrink-fit on thermal and hydraulic autofrettage is carried out. The inner cylinder as considered in Section 8.3 is replaced with the one which is hydraulically autofrettaged prior to shrink-fitting. The residual stresses due to hydraulic autofrettage in the inner cylinder are evaluated using the equations given in ref (Chakrabarty, 2006). As the outer cylinder is shrink-fitted, these stresses are superimposed to the shrink-fit stresses to give the net residual stresses in the inner cylinder. The different combination of autofrettage pressure, p_a and shrink-fit allowance, δ are considered in order to obtain the net maximum residual stresses at the inner radius of the compound cylinder such that the cylinder will not re-yield by Tresca yield criterion. The compound cylinder with inner cylinder hydraulically autofrettaged is subjected to internal working pressure to assess the maximum pressure carrying capability of the cylinder. The different combinations of p_a and δ with maximum pressure carrying capacity are presented in Table 8.2.

It is observed from Table 8.2 that by shrink-fitting an outer cylindrical layer to a hydraulically autofrettaged cylinder, the pressure carrying capacity of the cylinder can be increased to the maximum of 100% as compared to the corresponding non-autofrettaged single cylinder. In the present case this is achieved up to the shrink-fit allowance, δ = 0.026 mm, with a proper combination of autofrettage pressure. On the other hand, the shrink-fit to the thermally autofrettaged cylinder provides the maximum increase of 65.88% pressure carrying capacity with proper combination of (T_b–T_a) and δ which is also very significant as in this case the pressure carrying capacity becomes about 1.7 times of the pressure carrying capacity of non-autofrettaged case. The thermal autofrettage with shrink-fit appears to be a greener manufacturing procedure as the process utilizes only cold water for cooling the inner surface of the cylinder during autofrettage. The leakage of cold water during the operation of the process is not harmful to the environment. On the other hand, the hydraulic autofrettage utilizes hydraulic oil, the exposure of which to the environment is harmful. Moreover, most of the high pressure hydraulic power packs produce a lot of noise in the shop floor, which is harmful to operators. Therefore, the thermal autofrettage can be a preferred technique for increasing the pressure carrying capacity of high pressure components, although its maximum achievable pressure carrying capacity is lesser than the hydraulically autofrettaged cylinder with shrink-fit. Apart from avoiding environmental pollution, energy saving is also an important attribute of green manufacturing. The detailed estimation of energy budgets in hydraulic and thermal autofrettage process is left for future work. Apparently, raising the temperature of the workpiece requires more energy than simply deforming it. However, some measures can be adopted for minimizing the energy consumption in the thermal autofrettage. For example, the heat gained during cooling can be utilized for reducing the overall heating load. Heating can also be carried out by a waste heat recovery system. In high pressure hydraulic power packs, invariably a refrigerating system is used to cool the oil, which consumes a lot of energy. Moreover, maintenance and consumables (primarily hydraulic oil) needed for a hydraulic system will also enter into the energy budget.

It is also observed from Table 8.2 that after $\delta = 0.026$ mm, as the shrink-fit allowance is increased with suitable combination of p_a, the percentage increase of the maximum pressure carrying capacity significantly starts decreasing. As δ becomes 0.03 mm, the cylinder is not able to withstand the pressure equal to the non-autofrettaged single cylinder as in the case of thermal autofrettage with shrink-fit. The residual stress distribution and overall stress distribution for p_a= 147.50 MPa, $\delta = 0.026$ mm are shown in Figures 8.4 and 8.5, respectively.

The lesser increase of the maximum pressure carrying capacity in the shrink-fitted thermally autofrettaged cylinder than the shrink-fitted hydraulically autofrettaged cylinder may be attributed to the net residual hoop stress profile in the compound cylinder. The net residual hoop stress profile in the inner plastic zone, in the thermally autofrettaged inner cylinder (Figure 8.2) is much steeper than in the hydraulically autofrettaged inner cylinder (Figure 8.4). In the case of thermal autofrettage, it results in the maximum equivalent Tresca stress to occur first at the inner plastic boundary, *c*, during the application of working pressure (Figure 8.3). On the other hand, in the case of hydraulic autofrettage, the maximum equivalent Tresca stress exists first at the inner radius, *a* (Figure 8.5).

Table 8.2 Pressure carrying capacity for various combinations of autofrettage pressure, p_a and shrink-fit allowance

Geometry of the autofrettaged cylinder (mm)	Thickness of the outer layer (mm)	Autofrettage pressure, p_a (MPa)	Shrink fit allowance, δ (mm)	Maximum pressure capacity of the compound cylinder (MPa)	% change in pressure carrying capacity
$a = 10$ $b = 30$	10	155.54	0.020	192.18	100
		154.20	0.021	192.18	100
		152.85	0.022	192.18	100
		151.53	0.023	192.18	100
		150.18	0.024	192.18	100
		148.85	0.025	192.18	100
		147.50	0.026	192.18	100
		146.2	0.027	170.00	76.91
		144.80	0.028	144.20	50.06
		144.80	0.029	118.50	23.32
		142.20	0.030	92.80	–3.42

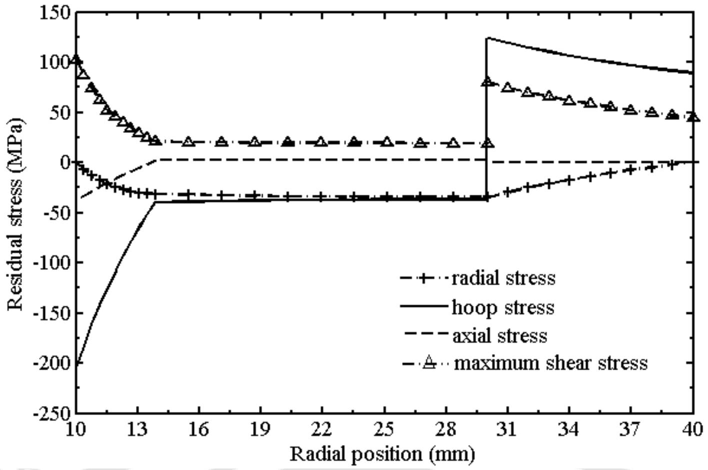

Figure 8.4 Residual stress distribution in the compound cylinder where the inner cylinder is hydraulically autofrettaged

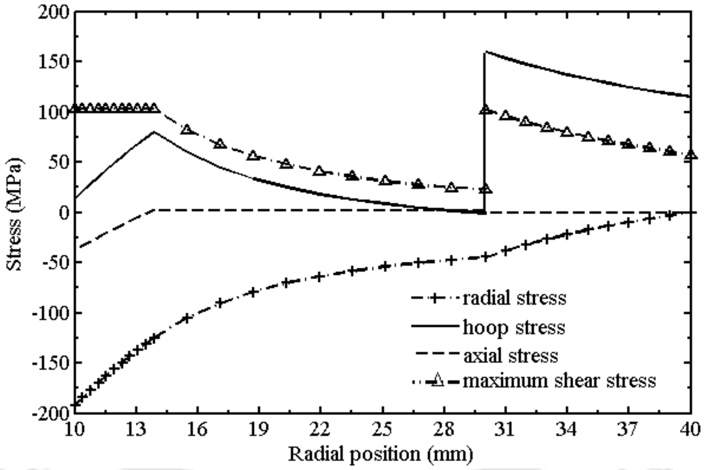

Figure 8.5 Overall stress distribution in the re-pressurized compound cylinder for (p=192.18 MPa) where the inner cylinder is hydraulically autofrettaged

8.5 Fatigue Life Analysis

The thick-walled cylinders are subjected to autofrettage in order to enhance their fatigue life. Shrink-fit is often performed on autofrettaged cylinders for further enhancement in the fatigue life. In this section, the fatigue life of thermally autofrettaged cylinder with shrink-fit is analyzed. Further, it is compared with the fatigue lives of single/monobloc thermally autofrettaged as well as non-autofrettaged cylinders. For the estimation of fatigue life, the stress intensity factor given by Underwood (1972) for straight-fronted, longitudinal crack is employed. The fatigue lives for each case is calculated using Paris law.

8.5.1 Calculation of Stress Intensity Factor

The first mode of stress intensity factor for a straight-fronted longitudinal crack of $l/w<0.25$ (l is the crack depth and w is the wall thickness) under pressure p is given by (Underwood, 1972)

$$K_{\mathrm{I}} = 1.12\sigma_{\theta}\sqrt{\pi l} + 1.13p\sqrt{\pi l} + 1.12\sigma_{\theta \mathrm{R}}\sqrt{\pi l}, \tag{8.8}$$

where σ_{θ} is the Lamé hoop stress and $\sigma_{\theta \mathrm{R}}$ is the residual hoop stress. The crack geometry is shown in Figure 8.6. Under a cyclic pressure, the range of stress intensity, ΔK_{I} is

$$\Delta K_{\mathrm{I}} = K_{\mathrm{Imax}} - K_{\mathrm{Imin}}, \tag{8.9}$$

where from Eq. (8.8), K_{Imax} and K_{Imin} are given by

$$K_{\mathrm{Imax}} = 1.12\sigma_{\theta \max}\sqrt{\pi l} + 1.13p_{\max}\sqrt{\pi l} + 1.12\sigma_{\theta \mathrm{R}}\sqrt{\pi l}, \tag{8.10}$$

$$K_{\mathrm{Imin}} = 1.12\sigma_{\theta \min}\sqrt{\pi l} + 1.13p_{\min}\sqrt{\pi l} + 1.12\sigma_{\theta \mathrm{R}}\sqrt{\pi l} \tag{8.11}$$

In Eqs. (8.10) and (8.11), $p_{\max}$ and $p_{\min}$ are the maximum and minimum pressure in the cycle. For large compressive residual stresses, K_{Imin} may results into negative value. In that case, K_{Imin} is set to zero providing $\Delta K_{\mathrm{I}} = K_{\mathrm{Imax}}$. Then,

$$\Delta K_{\mathrm{I}} = 1.12\Delta\sigma_{\theta}\sqrt{\pi l} + 1.13\Delta p\sqrt{\pi l} + 1.12\sigma_{\theta \mathrm{R}}\sqrt{\pi l}. \tag{8.12}$$

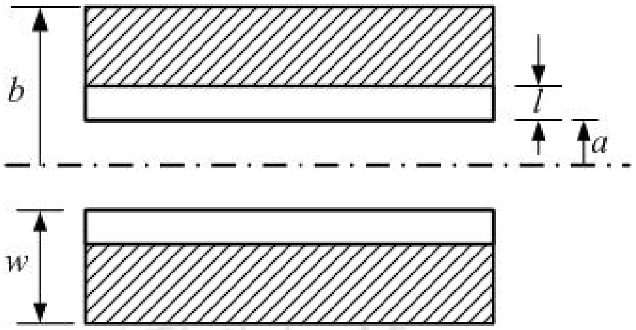

Figure 8.6 A straight-fronted longitudinal crack emanating from the inner wall of a thick cylinder showing crack geometry parameters

The range of hoop stress at any radius *r*, is given by the Lame hoop stress distribution as

$$\Delta\sigma_\theta = \frac{\Delta p\left(1+\frac{b^2}{r^2}\right)}{\left(W^2-1\right)}, \tag{8.13}$$

where *b* is the outer radius of the cylinder and *W* is the wall thickness ratio given by *b*/*a*, where *a* is the inner radius of the cylinder. Inserting Eq. (8.13) into Eq. (8.12), the stress intensity factor in non-dimensional form is given by

$$\frac{\Delta K_\mathrm{I}}{\Delta K_o} = 1.12\left\{\frac{\left(1+\frac{b^2}{r^2}\right)}{\left(W^2-1\right)} + 1.009 + \frac{\sigma_{\theta\mathrm{R}}}{\Delta p}\right\}, \tag{8.14}$$

where $\Delta K_o = \Delta p\sqrt{\pi l}$. For non-autofrettaged cylinder, $\sigma_{\theta\mathrm{R}}$ is zero in Eq. (8.14).

The stress intensity factor is calculated as a function of crack depth ratio (*l*/*w*). The crack depth ratio is defined as

$$\frac{l}{w} = \frac{r-a}{b-a} \tag{8.15}$$

Corresponding to a particular value of l/w, the radial position, r can be obtained from Eq. (8.15), which substituted in Eq. (8.14). In the following subsections the stress intensity factor is calculated for different cases.

8.5.1.1 Thermally autofrettaged cylinder with shrink-fit

The non-dimensional stress intensity factor for the thermally autofrettaged cylinder with shrink-fit presented in Section 8.3 is calculated for four different pressures– 96.09 MPa (the yield onset pressure of the non-autofrettaged monobloc cylinder), 110 MPa (an intermediate arbitrary pressure value), 133.90 MPa (the yield onset pressure of the thermally autofrettaged monobloc cylinder) and 159.40 MPa (the yield onset pressure of the thermally autofrettaged cylinder with shrink-fit). It is considered that the minimum pressure in the cylinder during operation is zero. The thermal autofrettage and shrink-fit parameters are provided in Section 8.3. The residual stress distribution was shown in Figure 8.2. A straight-fronted longitudinal crack is considered at the inner wall of the compound cylinder. The crack geometry is shown in Figure 8.6. The thickness of inner cylinder is 20 mm. The allowable final crack depth is taken as 25% of the inner layer thickness, *i.e*., 5 mm as per ASME pressure vessel code (2007). The wall thickness ratio of the compound cylinder to be used in Eq. (8.14) is defined as, $W=z/a=4$ with reference to Figure 8.1. The stress intensity factor for the compound cylinder is calculated using Eq. (8.14) for the different pressures and is shown in Figure 8.7 as a function of (l/w). It is observed that the stress intensity factor increases to the radius of elastic-plastic interface and thereafter it starts decreasing gradually. Also, the stress intensity factor increases with the working pressure following the same trend.

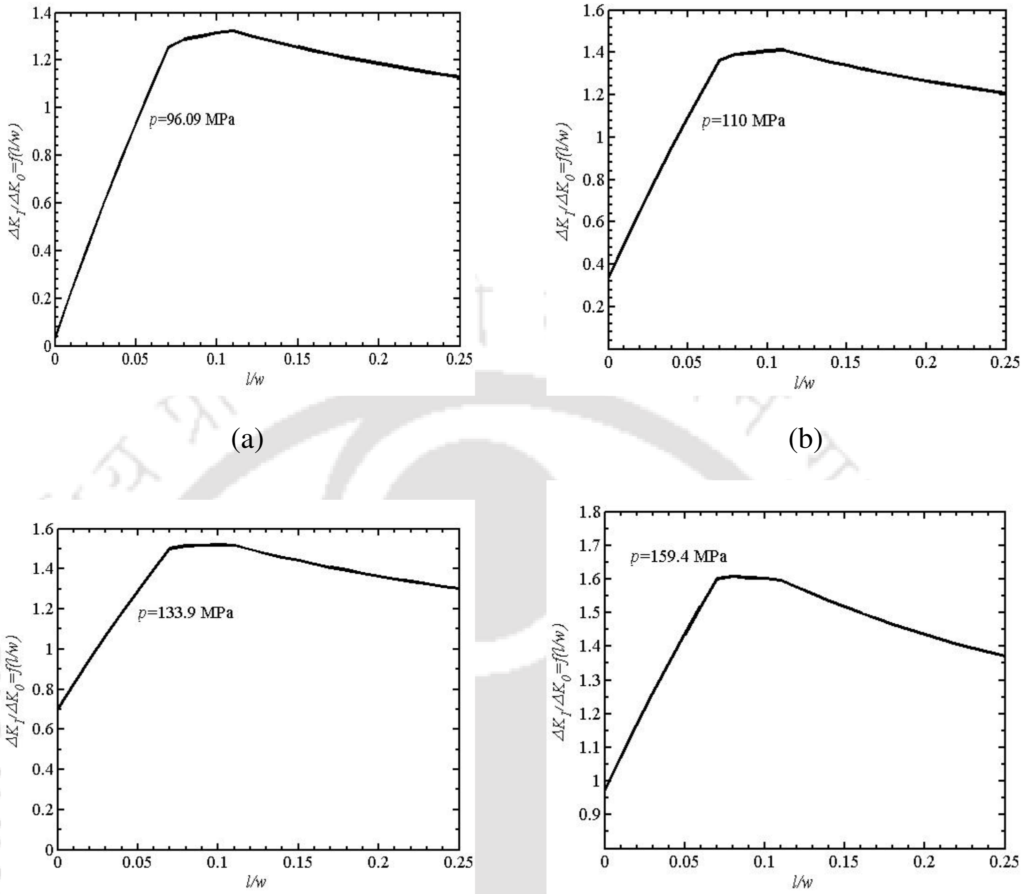

(a) (b)

(c) (d)

Figure 8.7 Stress intensity factors for a straight-fronted longitudinal crack in the autofrettaged cylinder with shrink-fit for different working pressures: (a) *p*=96.09 MPa, (b) *p*=110 MPa, (c) *p*=133.90 MPa, (d) *p*=159.40 MPa

8.5.1.2 Thermally autofrettaged monobloc cylinder

A monobloc SS304 cylinder is considered for thermal autofrettage inducing a temperature difference of 122 °C across the wall thickness for achieving maximum pressure carrying capacity (133.9 MPa).The residual stress distribution in the thermally autofrettaged cylinder can be evaluated from the expressions presented in Section 4.2.4. The crack geometry parameters for this cylinder correspond to Figure 8.6. The non-dimensional stress intensity factor for this cylinder is calculated using Eq. (8.14) for three different pressures– 96 MPa, 110 MPa and 133.9 MPa and is shown in Figure 8.8 as a function of (l/w). Similar trend is observed for this case as in Subsection 8.5.1.1.

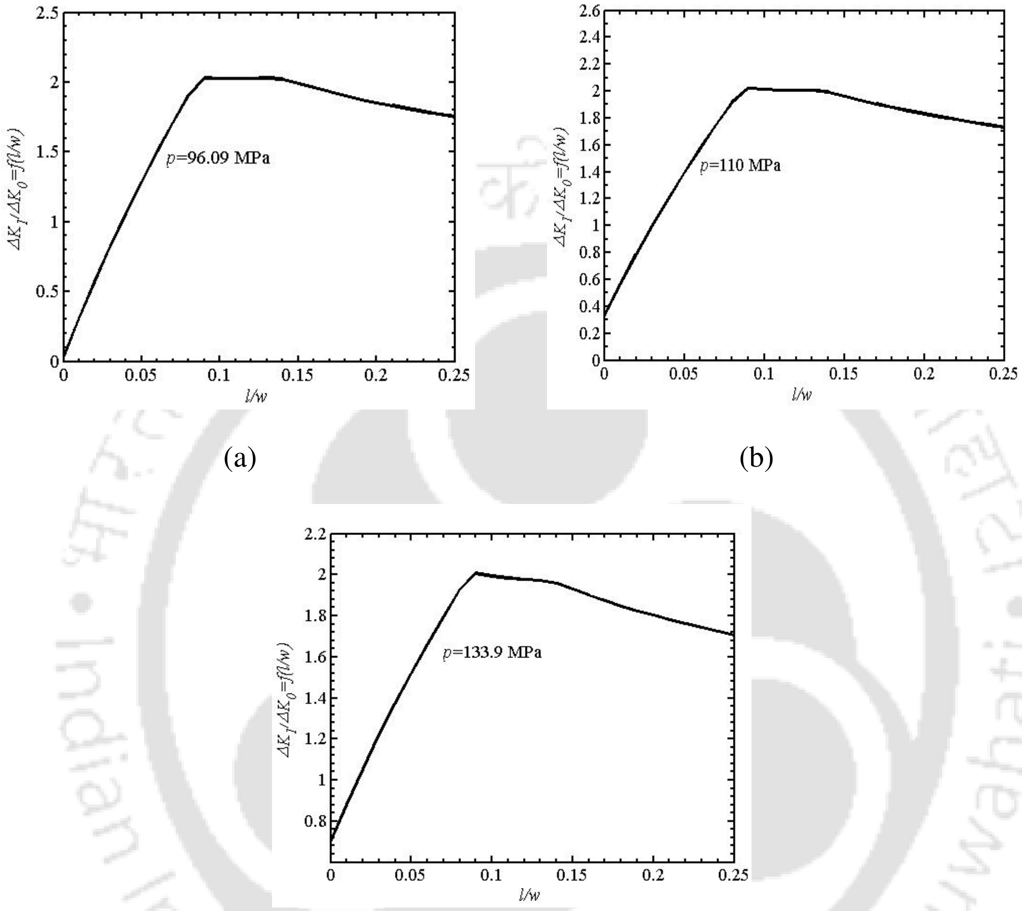

(a) (b)

(c)

Figure 8.8 Stress intensity factors for a straight-fronted longitudinal crack in thermally autofrettaged SS304 monobloc cylinder for different working pressures: (a) p=96.09 MPa, (b) p=110 MPa, (c) p=133.90 MPa

8.5.1.3 Non-autofrettaged monobloc cylinder

The non-autofrettaged cylinder can withstand the maximum pressure of 96.09 MPa. The non-dimensional stress intensity factors for this cylinder at the maximum pressure carrying capacity are calculated from Eq. (8.14) putting $\sigma_{\theta \mathrm{R}}$ =0. The distribution is shown in Figure 8.9 as a function of (l/w) for the crack geometry shown in Figure 8.6. It is observed that the stress intensity factor becomes the maximum at the inner radius and then decreases gradually.

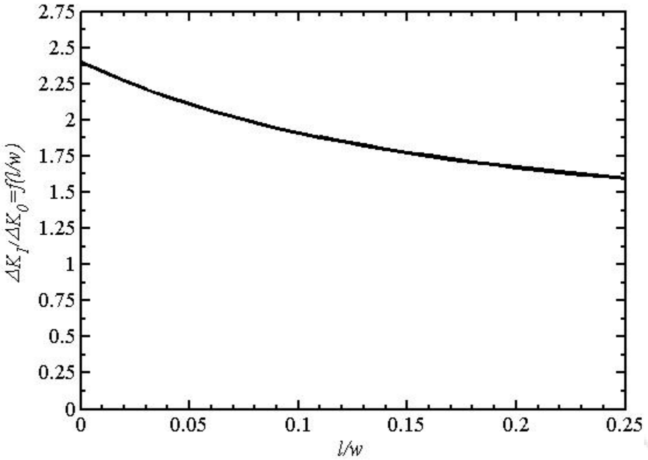

Figure 8.9 Stress intensity factors for a straight-fronted longitudinal crack in the non-autofrettaged monobloc SS304 cylinder for 96.09 MPa

8.5.2 Calculation of Fatigue Life

The fatigue life of cylinders is calculated using Paris law given by (Paris and Erdogan, 1963)

$$\frac{\mathrm{d}l}{\mathrm{d}N}=A\left(\Delta K_{\mathrm{I}}\right)^{m}, \tag{8.16}$$

where A and m are material constants. As $\Delta K_{\mathrm{I}}/\Delta K_o = f\left(l/w\right)$,

$$\Delta K_{\mathrm{I}}=\Delta K_o f\left(\frac{l}{w}\right)=\Delta p\sqrt{\pi l}\,f\left(\frac{l}{w}\right) \tag{8.17}$$

Using Eq. (8.17) in Eq. (8.16),

$$\frac{\mathrm{d}l}{\mathrm{d}N}=A\left(\pi\right)^{\frac{m}{2}}\left(\Delta p\right)^{m}\left(l\right)^{\frac{m}{2}}\left\{f\left(l/w\right)\right\}^{m} \tag{8.18}$$

Dividing both sides of Eq. (8.18) by w, provides

$$\frac{\mathrm{d}\left(l/w\right)}{\mathrm{d}N}=A\left(\pi\right)^{\frac{m}{2}}\left(\Delta p\right)^{m}\left(l/w\right)^{\frac{m}{2}}w^{\frac{m}{2}-1}\left\{f\left(l/w\right)\right\}^{m} \tag{8.19}$$

Integrating Eq. (8.19), the fatigue life is obtained as

$$\int_{0}^{N_f} \mathrm{d}N = \int_{(l/w)_i}^{(l/w)_f} \frac{\mathrm{d}\left(l/w\right)}{A\left(\pi\right)^{\frac{m}{2}}\left(\Delta p\right)^{m}\left(l/w\right)^{\frac{m}{2}} w^{\frac{m}{2}-1}\left\{f\left(l/w\right)\right\}^{m}}$$

$$N_f = \frac{w^{1-\frac{m}{2}}}{A\left(\pi\right)^{\frac{m}{2}}\left(\Delta p\right)^{m}} \int_{(l/w)_i}^{(l/w)_f} \frac{\mathrm{d}(l/w)}{(l/w)^{\frac{m}{2}}\left[f(l/w)\right]^{m}}. \tag{8.20}$$

The lower limit of the integration $(l/w)_i$ is the initial crack depth ratio and the upper limit of the integration $(l/w)_f$ is the final crack depth ratio in Eq. (8.20). The integral can be evaluated numerically using Simpson's 1/3rd rule.

The fatigue life of the cylinder for different cases is calculated using Eq. (8.20). The initial crack depth ratio is taken as 0.001 (Rees, 1991) and the final crack depth ratio is taken as 0.25 as per the ASME pressure vessel code (2007). For SS304 (austenitic steel) the material constants in Eq. (8.20) are taken as A=5.5×10^{-12} and m=3.25 (Barsom and Rolfe, 1987). In evaluating the integrand of Eq. (8.20), the values of $f(l/w)$ are calculated from Figures 8.7, 8.8 and 8.9 for the respective cases fitting polynomial curves. The summary of the results are presented in Table 8.3.

It is observed from Table 8.3 that the fatigue life of the thermally autofrettaged cylinder is significantly increased by performing shrink-fit. The fatigue of the cylinders is dependant on the working pressures. As the working pressure increases the fatigue life is reduced. For the working pressure of 96.09 MPa, the fatigue life of the thermally autofrettaged cylinder with shrink-fit is increased by 241,38,41,152 cycles than the non-autofrettaged monobloc cylinder and by 17,69,593 cycles than the thermally autofrettaged monobloc cylinder. For 110 MPa, this enhancement is 57,422 cycles than the thermally autofrettaged monobloc cylinder. The fatigue life of the thermally autofrettaged cylinder with shrink-fit is increased by 3,571 cycles than the thermally autofrettaged monobloc cylinder when the cylinder is under the working pressure of 133.9 MPa. Thus, the thermally autofrettaged cylinder with shrink-fit has the maximum fatigue life for a fixed safe working pressure. At its maximum pressure carrying capacity, the fatigue life of this cylinder is 39,674 cycles which is 2.9 times the fatigue life of the non-autofrettaged monobloc cylinder operating at the maximum working pressure.

Table 8.3 Fatigue lives of cylinders for different range of working pressures

Working pressure (MPa)	Fatigue lives (Cycles)		
	Thermally autofrettaged cylinder with shrink-fit	Thermally autofrettaged monobloc cylinder	Non-autofrettaged monobloc cylinder
96.09	241,38,54,831	241,20, 85,238	13,679
110	33,63,670	33,06,248	–
133.90	1,88,934	1,85,362	–
159.40	39,674	–	–

8.6 Summary

In this work, a methodology for enhancing the performance of a thermally autofrettaged cylinder in terms of the maximum pressure carrying capacity through shrink-fit is proposed. The pressure carrying capacity of the thermally autofrettaged cylinder cannot be increased more than about 40% for cylinders up to wall thickness ratio of 4. Therefore, an outer cylindrical layer is shrink-fitted to the thermally autofrettaged cylinder and the advantage is highlighted through a numerical example. The maximum increase of pressure carrying capacity of about 66% is achieved by shrink-fitting the thermally autofrettaged cylinder. A comparison of the effect of shrink-fit on the thermal and hydraulic autofrettage is also carried out. It is found that the hydraulic autofrettage with shrink-fitting provides 100% increase in the maximum pressure carrying capacity with proper selection of shrink-fit allowance and autofrettage pressure. Nevertheless, the thermal autofrettage with shrink-fit also provides a significant increase in the pressure carrying capacity. The fatigue life of the thermally autofrettaged cylinder with shrink-fit is also studied for different working pressures and compared with the fatigue lives of corresponding single/monobloc thermally autofrettaged as well as non-autofrettaged cylinders. The results show that the thermally autofrettaged cylinder with shrink-fit provides improved fatigue life for a particular safe working pressure. Moreover, prima facie, thermal autofrettage with shrink-fit is a greener and cheaper manufacturing process compared to hydraulic autofrettage. The hydraulic autofrettage is a well-established industrial process. The thermal autofrettage has yet to make its entry in industry. The degree of its superiority in terms of economy and environment can be more clearly assessed after its use in industry.

Chapter 9

Conclusions and Scope for Future Work

9.1 Conclusions

In this thesis, a thermal autofrettage process has been proposed based on the generation of beneficial compressive residual stresses at and around the inner wall of a thick-walled cylinder/disk due to radial thermal gradient. The created radial thermal gradient across the wall thickness of the cylinders/disks causes the non-homogeneous plastic deformation; the removal of which generates beneficial residual stresses. A theoretical and experimental study of the proposed thermal autofrettage process has been carried out for exploring its feasibility.

For the theoretical analysis of the process, two analytical models— plane stress (σ_z=0) and generalized plane strain (ε_z= constant) models have been developed. The plane stress model is suitable for the thermal autofrettage of very short cylinders (thin disks) such as fastener holes. The generalized plane strain model is applicable in general for thermal autofrettage of long cylinders such as pressure vessels. The models are based on the Tresca yield criterion and its associated flow rule. The numerical simulations of the models for typical cylinders/disks have been carried and are found to be encouraging. The analyses show a significant increase in the maximum pressure carrying capacity of the cylinders/disks. From the numerical simulation it has been observed that the level of overstrain is usually small in thermal autofrettage. The effect of strain hardening is also studied during plastic deformation by thermal gradient using Ludwik's hardening law. It has been shown that the effect of strain hardening is negligible for the typical cases presented in this thesis.

A three-dimensional finite element method (3-D FEM) modelling of the thermal stresses generated in the cylinder due to thermal autofrettage is also carried out using finite element based ABAQUS package. The 3-D FEM stresses are compared with the stresses predicted by the plane stress and the generalized plane strain model of thermal autofrettage. The comparison suggests the applicability of the developed models on the basis of the length to wall thickness ratio of the cylinders. It has been found that the generalized plane strain model is valid for the cylinders with length to wall thickness ratio, $L/(b-a)\geq 6$. The plane stress model provides realistic solution for cylinders with $L/(b-a)\leq 1$.

A rigorous experimental study of the proposed process is carried out for the practical realization of the theoretical study. An experimental setup has been developed to achieve thermal autofrettage by creating the desired thermal gradient in the thick-walled cylinders. Thermal autofrettage of cylinders made of different materials (SS202, SS304 stainless steels and mild steel) was conducted in the developed setup. A qualitative and quantitative experimental assessment of the residual stresses induced in the thermally autofrettaged cylinders have been carried out using three different techniques— Sachs boring, microhardness test and the measurement of opening angle due to single radial cut through the wall thickness of the cylinders. The experimentally measured Sachs boring residual stresses closely match with the theoretical results predicted by the generalized plane strain model. For example, the average errors based on L_2 norm (*i.e.*, root mean squared errors) for hoop, axial and radial stresses in the case of SS202 cylinder (b/a=2.94) are observed to be 4.53 MPa, 7.50 MPa and 1.26 MPa, respectively. The other two experimental methods provide a qualitative assessment for the presence of residual stresses in the thermally autofrettaged cylinders. It has been observed that the Vickers microhardness increases on the inner surface of the autofrettaged cylinders compared to the corresponding non-autofrettaged cylinders due to the existence of compressive residual stresses. The Vickers microhardness on the outer surface of the autofrettaged cylinders is lesser than that on the outer surface of non-autofrettaged cylinders due to the presence of tensile residual stresses. The experimentally measured opening angles due to the single radial cut through the wall thickness are in good agreement with the theoretically evaluated opening angles with a deviation of less than 15%. This also confirms the presence of residual stresses in the thermally autofrettaged cylinders. The overall experimental results indicate that the proposed thermal autofrettage process is a practically feasible process. The behaviour of the process is easily predictable. This aspect is important for its industrial adaptation.

A comparative study of the proposed thermal autofrettage with the conventional hydraulic autofrettage has been carried out in this thesis. A detailed parametric study has been carried out for both thermal and hydraulic autofrettage. It has been observed that in the thermal autofrettage, the maximum possible pressure carrying capacity increases with the wall thickness ratio. In the hydraulic autofrettage, there is 100% increase in pressure carrying capacity for wall thickness ratio $b/a \geq 2.22$. Such a high increase in the maximum possible pressure carrying capacity cannot be achieved by thermal autofrettage due the limited overstrain level in the wall of the cylinder. The thermal autofrettage process is likely to be more economical than the hydraulic autofrettage as the process does not require expensive hydraulic power pack. The thermal autofrettage process has also been studied for the thick-walled cylinders subjected to high thermal gradient with or without pressure. The results are compared with the hydraulic autofrettage. The comparison shows that for cylinders subjected to high thermal gradient without pressure, the thermal autofrettage is superior to the hydraulic autofrettage. The thermal as well as the hydraulic autofrettage can be subjected to combined thermal gradient and pressure. As the stress-response is different for both the cases, the actual magnitudes of working thermal gradient and pressure suggests the suitability of one process over the other. The thermal autofrettage process can be considered a greener manufacturing procedure compared to the hydraulic autofrettage process due to elimination of hydraulic oil.

A methodology has been proposed in order to enhance the performance of thermally autofrettaged cylinders through shrink-fit. The pressure carrying capacity as well as the fatigue life of the thermally autofrettaged cylinders have been increased further by performing shrink-fit. Through shrink-fit over the thermally autofrettaged cylinder, it has been shown that the maximum pressure carrying capacity of the compound cylinder can be increased to about 66% for wall thickness ratio of 4. It is to be noted that the pressure carrying capacity of the corresponding thermally autofrettaged single/monobloc cylinders can be increased to about only 40%. The fatigue life analyses of the thermally autofrettaged cylinder with shrink-fit has been carried out and compared with the corresponding single/monobloc thermally autofrettaged as well as non-autofrettaged cylinders. It has been observed that the thermally autofrettaged cylinders provide larger fatigue life for a fixed safe working pressure as compared to the corresponding single/monobloc thermally autofrettaged as well as non-autofrettaged cylinders.

The contributions of the thesis may be summarized as follows:

- A process of achieving autofrettage by means of thermal stresses is proposed. An experimental setup has been developed and it has been observed that it is possible to generate beneficial compressive residual stresses on the inner surface of a cylinder.
- The analytical models have been developed for obtaining the residual stresses as a result of radial thermal gradient for plane stress and generalized plane strain thermal autofrettage cases.
- A three-dimensional finite element model is also developed using ABAQUS package. A criterion is developed to assess the plane stress as well as generalized plane strain assumptions.
- The generalized plane strain model is validated by carrying out in-house experiments.
- A detailed comparative study of thermal autofrettage and hydraulic autofrettage is carried out. It is noted that the thermal autofrettage has a clear cut edge over hydraulic autofrettage when the cylinder has to face thermal gradient during working. In the other cases, its suitability may be justified with respect to ease and economy.
- It has been theoretically studied that shrink-fitting on a thermally autofrettaged cylinder enhances its pressure carrying capacity and fatigue life.

9.2 Scope for Future Work

In the present thesis, a thermal autofrettage process is proposed which has been studied both theoretically and experimentally for the first time. The process appears to be a commercially viable and useful process. This is the first rigorous study on thermal autofrettage process. The works can be further extended both on the theoretical and experimental front in order to establish it as a potential industrial process. Some areas are described below.

- **Refinement of analytical modelling:** In the present thesis, the theoretical modelling of the thermal autofrettage process is carried out using the Tresca yield criterion and its associated flow rule. The modelling can be extended to incorporate von Mises yield criterion and can be compared with the present models. In the theoretical modelling, the Bauschinger effect during unloading is not taken into account. Many researchers have shown this effect to affect the bore residual stresses in case of hydraulic autofrettage, where the level of overstrain is large. The present work reveals that the level of overstrain is usually small in thermal autofrettage and thus, the Bauschinger effect appears to be insignificant. In future the Bauschinger effect can be incorporated in the modelling of thermal autofrettage to quantify its effect in terms of percentage reduction in bore residual hoop stresses. For some materials, there may be a requirement of using temperature dependent thermal and mechanical parameters in the mathematical model. The process can also be modeled for anisotropic materials.
- **Development of analytical model for short cylinder:** The 3-D FEM modelling of thermal autofrettage presented in this thesis suggests that for the cylinders with length to wall thickness ratios between 1 and 6, *i.e.* $1<L/(b-a)<6$, the plane stress and generalized plane strain models do not provide realistic solution. Thus, there is scope to develop a realistic analytical model for this transition range of $L/(b-a)$, *i.e.*, for short cylinders.
- **Experimental study:** The experimental assessment of the residual stresses induced by thermal autofrettage is carried out using Sachs boring technique, microhardness test and measuring the opening angle due to radial cut through the wall thickness. Researchers can also use other popular alternative methods such as neutron diffraction, hole-drilling methods to quantify the residual stresses in thermal autofrettage and make a comparison among various techniques. In applying the experimental methods, printed strain sensors may be used to assess the residual stresses in the cylinder. There is

also a scope to develop a model for quantifying the residual stresses based on the measurement of microhardness.

- **Enhancing the applicability of thermal autofrettage process:** The thermal autofrettage process may be a very suitable process for the autofrettage of miniature sized component. For these components induction heating may be employed. Moreover, the process can be studied for different geometries such as rifled cylinder, tapered cylindrical geometries and cylinders with valves and radial holes. In the present work, the thermal gradient in the experimental setup is created by heating the outer surface and cooling the inner surface by circulating cold water. There is also the scope to explore creating thermal gradient by cryogenic cooling of the inner surface instead of heating the outer surface. A combination of heating the outer surface as well as cryogenic cooling may be employed. There is a scope to explore the possibility of combining mechanical load with thermal gradient for achieving autofrettage. Further, the process can also be explored for functionally graded materials. There is also scope to carry out the heat treatment and autofrettage simultaneously.
- **Other manufacturing aspects:** To study the microstructural effect at the grain level, the crystal plasticity model can be incorporated in order to account for the changes in shape and orientation of the crystal lattice. Moreover, the variation of surface hardening and edge effect due to heating and cooling during thermal autofrettage can be investigated. The energy budget and economic analysis of the process can also be carried out in future.
- **Experimental study on shrink-fitted thermally autofrettaged cylinders:** The theoretical study of thermal autofrettage with shrink-fit carried out in the present work predicts improved pressure carrying capacity as well as enhanced fatigue life. The future research can be a rigorous experimental study on this aspect for its realistic assessment. The theoretical works presented in this thesis will provide a basis in performing the experiments. Finally, there is a scope for proper optimization of the process.

References

- ABAQUS User's Manual, (2007), Version 6.7, Dassault Systèmes Simulia Corp., Providence, RI, USA.
- Abdelsalam, O.R. and Sedaghati, R., (2013), Design optimization of compound cylinders subjected to autofrettage and shrink-fitting processes, ASME Journal of Pressure Vessel Technology, **135**, pp. 021209-1– 021209-11.
- Alegre, J.M., Bravo, P. and Preciado, M., (2006), Design of an autofrettaged high-pressure vessel, considering the Bauschinger effect, Proceedings of the Institution of Mechanical Engineers, Part E: Process Mechanical Engineering, **220**, pp. 7–16.
- Alexandrov, S., Jeong, W. and Chung. K., (2016), Descriptions of reversed yielding in internally pressurized tubes, ASME Journal of Pressure Vessel Technology, **138**, pp. 011204-1–011204-10.
- Ali, A.R.M., Ali, Ghosh, N.C. and Alam, T.E., (2010), Optimum design of pressure vessel subjected to autofrettage process, World Academy of Science, Engineering and Technology, **46**, pp. 667–672.
- Aliakbari, K. and Farhangdoost, K., (2014), Plastic deformation influence on material properties of autofrettaged tubes used in diesel engines injection system, ASME Journal of Pressure Vessel Technology, **136**, pp. 041402-1–041402-6.
- Alinezhad, P. and Bihamta, R., (2012), A study on the tool geometry effects in the swage autofrettage process, Advanced Materials Research, **433–440**, pp. 2206–2211.

- Allen, A., Andreani, C., Hutchings, M.T. and Windsor, C.G., (1981), Measurement of internal stress within bulk materials using neutron diffraction, NDT International, **14(5)**, pp. 249–254.
- Allen, D.N. and Sopwith, D.G., (1951), The stresses and strains in a partially thick tube under internal pressure and end load, Proceedings of the Royal Society, London, Series A, **205**, pp. 69–82.
- Arens, E., Youngquist, R., McFall, J., Simmons, S. and Cox, R., (2010), Developing NDE techniques for large cryogenic tanks, NASA technical report, Report/Patent Number: KSC-2010-251.
- ASME Pressure Vessel and Piping Design Code, (1997), Design Using Autofrettage, Division 3, Section 8, Article KD-5, pp. 71–73.
- ASME Boiler and Pressure Vessel Code, (2004), Section VIII, Division 3, Article KD-510–530, pp. 104–105.
- ASME Boiler and Pressure Vessel Code, (2007), Rules for Construction of High Pressure Vessels, Section VIII, Division 3, Article KD-4, pp. 74–76.
- ASTM E 837-08, (2008), Standard test method for determining residual stresses by the hole-drilling strain gauge method, American Society for Testing and Materials.
- Avitzur, B., (1994), Autofrettage–stress distribution under load and retained stresses after depressurization, International Journal of Pressure Vessel and Piping, **57**, pp. 271–287.
- Ayob, A.B., Tamin, M.N. and Elbasheer, M.K., (2009), Pressure limits of thick-walled cylinders. Proceedings of the International Multi Conference of Engineers and Computer Scientists 2, Hong Kong, March 18–20.
- Badr, E.A., Sorem, J.R. and Tipton, S.M., (1999), Residual stress estimation in crossbores with Bauschinger effect inclusion using FEM and strain energy density, ASME Journal of Pressure Vessel Technology, **121**, pp. 358– 363.

- Baishya, N.J., Sharma, D. and Dixit, U.S., (2014), Optimization of pressure vessel under thermo-elastic condition, Journal of the Institution of Engineers (India): Series C, **95(4)**, pp. 389–400.

- Bähre, D. and Brünnet, H., (2011), Simulation of removing autofrettage-induced residual stress loaded layers by finite element analysis, 1st CIRP Conference on Surface Integrity, Procedia Engineering, **19**, pp. 9−15.

- Banks-Sills, L. and Marmur, I., (1989), Influence of autofrettage on fracture toughness, International Journal of Fracture, **40**, pp. 143-155.

- Barbáchano, H., Alegre, J.M. and Cuesta, I.I., (2011), FEM simulation of the swage tube forming (STF) in cylinders subjected to internal pressure, Anales de Mecánica de la Fractura **28(2)**, pp. 481−486.

- Barbero, E.J. and Wen E.W., (2002), Coefficient of thermal expansion compatibility through mechanical and thermal autofrettage in metal lined composite pipes, ASTM STP 1436, C. E. Bakis, Ed., American society for Testing and Materials, West Conshohocken, PA.

- Barsom, J.M. and Rolfe, S.T, (1987), Fracture and Fatigue Control in Structures−Applications of Fracture Mechanics, Prentice-Hall, Inc., Englewood Cliffs, New Jersey.

- Bastable, M.J., (1992), From breechloaders to monster guns: Sir William Armstrong and the invention of modern artillery, 1854−1880, Technology and Culture **33(2)**, pp. 213–247.

- Beaney, E.M. and Procter, E., (1974), A critical evaluation of the centre hole technique for the measurement of residual stresses, Strain, **10(1)**, pp. 7−14.

- Bhatnagar, R.M., (2013), Modelling, validation and design of autofrettage and compound cylinder, European Journal of Mechanics A/Solids, **39**, 17−25.

- Bihamta, R., Movahhedy, M.R. and Mashreghi, A.R., (2007), A numerical study of swage autofrettage of thick-walled tubes, Materials and Design, **28**, pp. 804−815.

- Bland, D.R., (1956), Elastoplastic thick-walled tubes of work-hardening material subject to internal and external pressures and to temperature gradients, Journal of the Mechanics and Physics of Solids, **4**, pp. 209−229.
- Bowie, O.L. and Freese, C.E., (1972), Elastic analysis for a radial crack in a circular ring, Engineering Fracture Mechanics, **4**, pp. 315-321.
- Bueckner, H.F., (1970), A novel principle for the computation of stress intensity factors, Zeitschrift fuer Angewandte Mathematik & Mechanik, **50**, pp. 529–546.
- Chakrabarty, J., (2006), Theory of Plasticity, 3rd edition, Butterworth-Heinemann, Burlington.
- Chang, L., Pan, Y. and Ma, X., (2013), Residual Stress Calculation of Swage Autofrettage Gun Barrel, IJCSI International Journal of Computer Science, **10(2)**, pp. 52−59.
- Chen, P.C.T., (1972), The finite element analysis of elastic-plastic thick-walled tubes, Proceedings of Army Symposium on Solid Mechanics, The Role of Mechanics in Design-Ballistic Problems, pp. 243-253.
- Chen, P.C.T., (1980), Generalized plane-strain problems in an elastic-plastic thick-walled cylinder, Technical Report ARLCB-TR-80028, US Army Armament Research and Development Command, Large Caliber Weapon Systems Laboratory, Benét Weapons Laboratory, Watervliet, N. Y. 12189.
- Chen, P.C.T., (1986), The Bauschinger and hardening effect on residual stresses in an autofrettaged thick-walled cylinder, ASME Journal of Pressure Vessel Technology, **108(1)**, pp. 108−112.
- Chen, P.C.T., (1988a), A simple analysis of the swage autofrettage process, Technical Report ARCCB-TR-88030, US Army Armament Research, Development and Engineering Center, Close Combat Armaments Center, Benét Laboratories, Watervliet, N.Y. 12189−4050.
- Chen, P.C.T., (1988b), Finite element analysis of the swage autofrettage process, Technical report ARCCB-TR-88037, U. S. Army Armament

Research Development and Engineering Center, Benét Laboratories, Watervliet, N.Y. 12189–4050.

- Cheng, W. and Fannie, I., (1986), Measurement of residual hoop stresses in cylinders using the compliance method, ASME Journal of Engineering Materials and Technology, **108(2)**, pp. 87–92.
- Clark, G., (1982), Residual stresses in swage-autofrettaged thick-walled cylinders, Department of Defence Support, Materials Research Laboratories, Report MRL-R-847, Melbourne, Victoria.
- Clark, G., (1984), Fatigue crack growth through residual stress fields-theoretical and experimental studies on thick-walled cylinders, Theoretical and Applied Fracture Mechanics, **2**, pp. 111-125.
- Cowper, G.R., (1960), The elastoplastic thick-walled sphere subjected to a radial temperature gradient, ASME Journal of Applied Mechanics, **27(3)**, pp. 496–500.
- Darijani, H., Kargarnovin, M.H. and Naghdabadi, R., (2009), Design of thick-walled cylindrical vessels under internal pressure based on elasto-plastic approach, Materials and Design, **30**, pp. 3537–3544.
- Darijani, H., Kargarnovin, M.H. and Naghdabadi, R., (2009), Design of spherical vessels under steady-state thermal loading using thermo-elasto–plastic concept, International Journal of Pressure Vessel and Piping, **86**, pp. 143–52.
- Davidson, T.E., Barton, C.S., Reiner, A.N. and Kendall, D.P., (1962), New approach to the autofrettage of high-strength cylinders, Experimental Mechanics, **2**, pp. 33–40.
- Davidson, T.E., Barton, C.S., Reiner, A.N. and Kendall, D.P., (1963), Overstrain of high-strength open-end cylinders of intermediate diameter ratio, In Proceedings of the first international congress on experimental mechanics, Pergamon Press, New York, pp. 335–352.

- Davidson, T.E., Kendall, D.P. and Reiner, A.N., (1963), Residual stresses in thick-walled cylinders resulting from mechanically induced overstrain, Experimental Mechanics, **3**, pp. 253–262.

- Dewangan, M.K. and Panigrahi, S.K., (2015), Residual stress analysis of swage autofrettaged gun barrel via finite element method, Journal of Mechanical Science and Technology, **29(7)**, pp. 2933−2938.

- Dixit, P.M. and Dixit, U.S., (2008), Modeling of Metal Forming and Machining Processes: By Finite Element and Soft Computing Methods, Springer, London.

- Dixit U.S., (2009), Finite Element Methods for Engineers, Cengage Learning, New Delhi.

- Durban, D., (1979), Large strain solution for pressurized elasto/plastic tubes, ASME Journal of Applied Mechanics, **46**, pp.228-230.

- Durban, D., (1981), Thermoplastic behavior of a thick-walled sphere, AIAA Journal, **19(6)**, pp. 826-828.

- Durban, D., (1983), Thermo-elastic/plastic behaviour of a strain-hardening thick-walled sphere, International Journal of Solids and Structures, **19(7)**, pp. 643-652.

- Durban, D. and Kubi, M., (1992), A General Solution for the Pressurized Elastoplastic Tube, ASME Journal of Applied Mechanics, **59(1)**, pp. 20–26.

- Ezra, A., Glick, H., Howell, W. and Kaplan, M., (1973), Method and apparatus for explosive autofrettage. U.S. Patent No. 3,751,954.

- Farhangdoost, K. and Aliakbari, K., (2011), Comparison between fatigue life of autofrettage and nonautofrettage cylinders using stress intensity factor (KI), Key Engineering Materials, **452−453**, pp. 201−204.

- Faupel, J.H., (1955), Residual stresses in heavy-wall cylinders, Journal of the Franklin Institute, **259(5)**, pp. 405−419.

- Feng, H., Mughrabi, H. and Donth, B., (1998), Finite element modeling of low temperature autofrettage of thick-walled tubes of the austenitic stainless steel AISI304L: Part I. Smooth thick walled tubes, Modelling and Simulation in Material Science and Engineering, **6(1)**, pp. 54–69.

- Franklin, G.J. and Morrison, J.L.M., (1960), Autofrettage of cylinders: prediction of pressure/external expansion curves and calculation of residual stresses, Proceedings of the Institution of Mechanical Engineers, **174**, pp. 947–974.

- Gangling, L., Xiaoying, Z., Jinxiang, L. and Liwen, H., (1988), Elastoplastic analysis of an open-ended cylinder from the twelve polygon yield condition, International Journal of Pressure Vessel and Piping, **33**, pp. 143–152.

- Gao, X.-L., (1992), An exact elasto-plastic solution for an open-ended thick-walled cylinder of a strain hardening material, International Journal of Pressure Vessel and Piping, **52**, pp. 129–144.

- Gao, X.-L., (1993), An exact elasto-plastic solution for a closed-end thick-walled cylinder of elastic linear-hardening material with large strains, International Journal of Pressure Vessel and Piping, **56**, pp. 331–350.

- Gao, X.-L., (2003) Elasto-plastic analysis of an internally pressurized thick-walled cylinder using a strain gradient plasticity theory, International Journal of Solids and Structures, **40**, pp. 6445–6455.

- Gao, X.-L., (2007), Strain gradient plasticity solution for an internally pressurized thick-walled cylinder of an elastic linear-hardening material, Zeitschrift für angewandte Mathematik und Physik, **58(1)**, pp. 161–173.

- Gao, X.-L., Wen, J.-F., Xuan, F.-Z. and Tu, S.-T., (2015), Autofrettage and shakedown analyses of an internally pressurized thick-walled cylinder based on strain gradient plasticity solutions, ASME Journal of Pressure Vessel Technology, **82**, pp. 041010-1– 041010-12.

- Garcia-Granada, A.A., Smith, D.J. and Pavier, M.J., (2000), A new procedure based on Sachs' boring for measuring non-axisymmetric residual stresses, International Journal of Mechanical Sciences, **42**, pp. 1027−1047.

- George, D. and Smith, D.J., (2000), The application of the deep hole technique for measuring residual stresses in an autofrettaged tube, Proceedings of PVP 2000, ASME Pressure Vessel and Piping, July 23−27, Seattle, Washington.

- Gerald, C.F. and Wheatley, P.O., (1994), Applied Numerical Analysis, fifth edition, Addison-Wesley, England.

- Gexia, Y. and Hongzhao, L., (2012), An analytical solution of residual stresses for shrink-fit two-layer cylinders after autofrettage based on actual material behavior, ASME Journal of Pressure Vessel Technology, **134**, pp. 061209-1− 061209-8.

- Gibson, M.C., Hameed, A., Parker, A.P. and Hetherington, J.G., (2006), A comparison of methods for predicting residual stresses in strain-hardening, autofrettaged thick cylinders, including the Bauschinger effect, ASME Journal of Pressure Vessel Technology, **128**, pp. 217− 222.

- Gibson, M.C., (2008), Determination of residual stress distributions in autofrettaged thick-walled cylinders, Ph.D. Thesis, Defence College of Management and Technology, Cranfield University, U.K.

- Gibson, M.C., Hameed, A. and Hetherington, J.G., (2012), investigation of driving force variation during swage autofrettage, using finite element analysis, ASME Journal of Pressure Vessel Technology, **134**, pp. 051203-1−051203-7.

- Gibson, M.C., Hameed, A. and Hetherington, J.G., (2014), investigation of residual stress development during swage autofrettage, using finite element analysis, ASME Journal of Pressure Vessel Technology, **136**, pp. 021206-1−021206-7.

- Hameed, A., Brown, R.D. and Hetherington, J.G., (2003), Numerical analysis of the effect of machining on the depth of yield, maximum firing pressure and residual stress profile in an autofrettaged gun tube, ASME Journal of Pressure Vessel Technology, **125**, pp. 342– 346.

- Hameed, A., Brown, R.D. and Hetherington, J., (2004), A study of the residual stress distribution in an autofrettaged, thick-walled cylinder with cross-bore, ASME Journal of Pressure Vessel Technology, **126**, pp. 497–503.

- Hamilton, N.R., Wood, J., Easton, D., Robbie, M.B.O., Zhang, Y. and Galloway, A., (2015), Thermal autofrettage of dissimilar material brazed joints, Materials and Design, **67**, pp. 405–412.

- Hill, R., Lee, E.H. and Tupper, S.J., (1947), The theory of combined plastic and elastic deformation with particular reference to a thick tube under internal pressure, Proceedings of the Royal Society of London, Series A, Mathematical and Physical Sciences, **191**, pp. 278–303.

- Hill, R., (1950), The Mathematical Theory of Plasticity, Clarendon Press, Oxford, UK.

- Hill, R.E., Lee, H., and Tupper, S.J., (1951), Plastic flow in a closed-end tube with internal pressure, Proc. First US Nat. Cong. Applied Mechanics.

- Hojjati, M.H. and Hassani, A., (2007), Theoritical and finite element modeling of autofrettage process in strain hardening thick-walled cylinders, International Journal of Pressure Vessels and Piping, **84**, pp. 310–319.

- Hosseinian, E., Farrahi, G.H. and Movahhedy, M.R., (2009), An analytical framework for the solution of autofrettaged tubes under constant axial strain condition, ASME Journal of Pressure Vessel Technology, **131**, pp. 061201-1– 061201-8.

- Hu, Z. and Penumarthy, C., (2014), Computer modeling and optimization of swage autofrettage process of a thick-walled cylinder incorporating

Bauschinger effect, American Transactions on Engineering & Applied Sciences, **3(1)**, pp. 31−63.

- Huang, X.P., (2005), A general autofrettage model of a thick-walled cylinder based on tensile-compressive stress-strain curve of a material, Journal of Strain Analysis for Engineering Design, **40(6)**, pp. 599–608.
- Huang, X.P. and Cui, W.C., (2006), Effect of Bauschinger effect and yield criterion on residual stress distribution of autofrettaged tube, ASME Journal of Pressure Vessel Technology, **128**, pp. 212–216.
- Huang, X. and Moan, T., (2009), Residual stress in an autofrettaged tube taking Bauschinger effect as a function of the prior plastic strain, ASME Journal of Pressure Vessel Technology, **131**, pp. 021207-1– 021207-7.
- Hughes, H., (1967) X-Ray techniques for residual stress measurement, Strain, **3(3)**, pp. 26–31.
- Hurlich, A., (1968), Low temperature metals, Proceedings of the 1968 Summer Study on Superconducting Devices and Accelerators, pp. 311–325.
- Incropera, F.P. and Dewitt, D.P., (1996), Fundamentals of Heat and Mass Transfer, 4th edition, John Wiley & Sons, New York.
- Iremonger, M.J. and Kalsi, G.S., (2003), A numerical study of swage autofrettage, ASME Journal of Pressure Vessel Technology, **125**, pp. 347–351.
- Jacob, L., (1907), La Résistance et L'équilibre Elastique des Tubes Frettés, Mémoire de L'artillerie Navale, **1(5)**, pp. 43–155 (in French).
- Jahed, H. and Dubey, R.N., (1997), An axisymmetric method of elastic-plastic analysis capable of predicting residual stress field, ASME Journal of Pressure Vessel Technology, **119**, pp. 264– 273.
- Jahed, H., Farshi, B. and Hosseini, M., (2006a), Fatigue life prediction of autofrettage tubes using actual material behaviour, International Journal of Pressure Vessel and Piping, **83**, pp. 749–755.

- Jahed, H., Farshi, B. and Karimi, M., (2006b), Optimum autofrettage and shrink-fit combination in multi-layer cylinders, ASME Journal of Pressure Vessel Technology, **128**, pp.196–200.

- Jahed, H., Faritus, M.R. and Jahed, Z., (2012), Residual stress measurements in an autofrettage tube using hole drilling method, ASME Journal of Pressure Vessel Technology, **134**, pp. 051501-1– 051501-7.

- Johnson, W. and Mellor, P.B., (1962), Elastic-plastic behaviour of thick-walled spheres of non-work-hardening material subject to a steady-state radial temperature gradient, International Journal of Mechanical Sciences, **4**, pp. 147–58.

- Kammash, T.B., Murch, S.A. and Naghdi, P.M., (1960), The elastic-plastic cylinder subjected to radially distributed heat source, lateral pressure and axial force with application to nuclear reactor fuel elements, Journal of the Mechanics and Physics of Solids, **8(1)**, pp. 1–25.

- Kandil, A., El-Kady, A.A. and El-Kafrawy, A., (1995), Transient thermal stress analysis of thick-walled cylinders, International journal of mechanical sciences, **37(7)**, pp. 721–732.

- Kapp, J.A., Brown, B., LaBombard, E.J. and Lorenz, H.A., (1998), On the design of high durability high pressure vessels, Proceedings of ASME PVP Conference, **371**, pp. 85–91.

- Kargarnovin, M.H., Zarei, A.R., and Darijani, H., (2005), Wall thickness optimization of thick-walled spherical vessel using thermo-elasto-plastic concept, International Journal of Pressure Vessel and Piping, **82**, pp. 379–385.

- Koh, S.K., (1996), Fatigue life simulation and estimation of an autofrettaged thick-walled pressure vessel with an external groove, International Journal of Fatigue, **18(1)**, pp. 49–56.

- Koh, S.K., Lee, S.I., Chung, S.H. and Lee, K.Y., (1997), Fatigue design of an autofrettaged thick-walled pressure vessel using CAE techniques, International Journal of Pressure Vessel and Piping, **74**, pp. 19–32.
- Koh, S.K., (2000), Elastic-plastic stress analysis and fatigue lifetime prediction of cross-bores in autofrettaged pressure vessels, KSME International Journal, **14(9)**, pp. 935–946.
- Koiter, W.T., (1953), On partially plastic thick-walled tubes, Biezeno Anniversary Volume, H. Stain, Haarlem-Antwerpen, pp.232-251.
- Kokubo, S., (1932), Changes in hardness of a plate caused by bending. Sci. Rep. Tohoku, Imperial University, Japan, Series I, **21**, pp. 256–267.
- Lambert, J.W., (1953), A method of deriving residual stress equations, Proceedings of the Society of Experimental Stress Analysis, **XII(1)**, pp. 91–96.
- Lamé, G., (1852), Leçons sur la Théorie Mathématique de l'Élasticité des Corps Solides, Gauthier-Villars, Paris.
- Lee, S.L., O'Hara, G.P., Olmstead, V. and Capsimalis, G., (1992), Characterization of residual stresses in an eccentric swage autofrettaged thick-walled steel cylinders, Technical report ARCCB-TR-92017, U.S. Army Armament Research development and engineering Center, Benét Laboratories, Watervliet, N.Y. 12189–4050.
- Lee, E.Y., Lee, Y.S., Yang, Q.M., Kim, J.H., Cha, K.U. and Hong, S.K., (2009), Autofrettage process analysis of a compound cylinder based on the elastic-perfectly plastic and strain hardening stress-strain curve, Journal of Mechanical Science and Technology, **23**, pp. 3153–3160.
- Lee, Z.Y., Chen, C.K. and Hung, C.I., (2001), Transient thermal stress analysis of multilayered hollow cylinder, Acta Mechanica, **151(1-2)**, pp. 75–88.
- Ma, Q., Levy, C. and Perl, M., (2015), The Bauschinger effect's influence on the stress intensity factors of a semi-elliptical crack emanating from an

erosion at the bore of a fully autofrettaged pressurized cylinder, ASME Journal of Pressure Vessel Technology, **137**, pp. 041403-1– 041403-7.

- MacGregor, C.W., Coffin Jr., L.F. and Fisher, J.C., (1948), Partially plastic thick-tubes, Journal of the Franklin Institute, **245(1)**, pp. 135−158.
- Macrae, A.E., (1930), Overstrain of metals, His Majesty's Stationery Office, London.
- Majzoobi, G.H., Farrahi, G.H. and Mahmoudi, A.H., (2003), A finite element simulation and an experimental study of autofrettage for strain hardened thick-walled cylinders, Materials Science and Engineering A, **359**, pp. 326–331.
- Majzoobi, G.H. Farrahi, G.H. Pipelzadeh, M.K. and Akbari, A., (2004), Experimental and finite element prediction of bursting pressure in compound cylinder, International Journal of Pressure Vessels and Piping, **81**, pp. 889–896.
- Majzoobi, G.H. and Ghomi, A., (2006), Optimization of autofrettage in thick-walled cylinders, Journal of Achievements in Materials and Manufacturing Engineering, **16(1−2)**, pp. 124−131.
- Marcal, P.V., (1965), A stiffness method for elastic-plastic problems, International Journal of Mechanical Sciences, **7(4)**, pp. 229-238.
- Mathar, J., (1934), Determination of initial stresses by measuring the deformation around drilled holes, Transactions of ASME, **56(4)**, pp. 249–254.
- Megahed, M.M. and Abbas, A.T., (1991), Influence of reverse yielding on residual stresses induced by autofrettage, International Journal of Mechanical Sciences, **33**, pp. 139−150.
- Milligan, R.P., Hoo, W.H., and Davidson, T.E., (1966), The Bauschinger Effect in a High-Strength Steel, Journal of Basic Engineering, **88(2)**, pp. 480-488.

- Mote, J.D., Ching, L.K.W., Knight, R.E., Fay, R.J. and Kaplan, M.A., (1971), Explosive autofrettage of cannon barrels, AMMRC CR 70-25, Army Materials and Mechanics Research Center, Watertown, Massachusetts 02172.

- Nádai, A., (1931), Plasticity, McGraw-Hill Book Company, Inc. New York.

- Noda, N., Hetnarski, R.B. and Tanigawa, Y., (2003), Thermal stresses, 2nd edition, Taylor and Francis, New York.

- Obata, Y. and Noda, N., (1994), Steady thermal stresses in a hollow circular cylinder and a hollow sphere of a functionally gradient material, Journal of Thermal stresses, **17(3)**, pp. 471–487.

- O'Hara, G.P., (1992), Analysis of the swage autofrettage process, Technical report ARCCB-TR-92016, U. S. Army Armament Research development and engineering Center, Benét Laboratories, Watervliet, N.Y. 12189–4050.

- ÖGzdemir A.T. and Edwards, L., (1996), Measurements of the three-dimensional residual stress distribution around split-sleeve cold-expanded holes, Journal of Strain Analysis for Engineering Design, **31**, pp. 413–421.

- Ootao, Y., Tanigawa, Y. and Fukuda, T., (1991), Axisymmetric transient thermal stress analysis of a multilayered composite hollow cylinder, Journal of thermal stresses, **14(2)**, pp. 201–213.

- Orçan, Y. and Gamer, U., (1991), Elastic-plastic deformation of a centrally heated cylinder, Acta Mechanica, **90**, pp. 61–80.

- Orçan, Y., (1994), Thermal stresses in a heat generating elastic-plastic cylinder with free ends, International Journal of Engineering Science, **32(6)**, pp. 883–98.

- Orçan, Y., (1995), Residual stresses and secondary plastic flow in a heat generating elastic-plastic cylinder with free ends, International Journal of Engineering Science, **33(12)**, pp. 1689–1698.

- Orçan, Y. and Gulgec, M., (2000), Influence of the temperature dependence of the yield stress on the stress distribution in a heat-generating tube with free ends, Journal of Thermal Stresses, **23**, pp. 529–547.
- Orçan, Y. and Eraslan, A.N., (2001), Thermal stresses in elastic-plastic tubes with temperature-dependent mechanical and thermal properties, Journal of Thermal Stresses, **24**, pp. 1097–113.
- Paris, P.C. and Erdogan, F., (1963), A critical analysis of the crack propagation laws, ASME Journal of Basic Engineering, **85**, pp. 528–534.
- Parker, A.P. and Farrow, J.R., (1980), Technical note: On the equivalence of axisymmetric bending, thermal, and autofrettage residual stress fields, Journal of Strain Analysis for Engineering Design, **15(1)**, pp. 51–52.
- Parker, A.P. and Farrow, J.R., (1981), Stress intensity factors for multiple radial cracks emanating from the bore of an autofrettaged or thermally stressed, thick cylinder, Engineering Fracture Mechanics, **14**, pp. 237–241.
- Parker, A.P., Underwood, J.H., Throop, J.F. and Andrasic, C.P., (1982), Stress intensity and fatigue crack growth in a pressurized, autofrettaged thick cylinder, Technical report ARLCB-TR-82027, US Army Armament Research And Development Command, Large Caliber Weapon Systems Laboratory, Benét Weapons Laboratory, Watervliet, N.Y. 12189–4050.
- Parker, A.P, Underwood, J.H., Throop, J.F. and Andrasic, C.P., (1983), Stress intensity and fatigue crack growth in a pressurized, autofrettaged thick cylinder, American Society for Testing and Materials 14th National Symposium on Fracture Mechanics, UCLA, ASTM STP 791, pp. 216–237.
- Parker, A.P. and Underwood, J.H., (1998), Influence of the Bauschinger effect on residual stress and fatigue lifetimes in autofrettaged thick walled cylinders, In: T.L. Panontin and S.D. Sheppard (eds), Fatigue and fracture mechanics: 29th volume (ASTM STP1321), West Conshohocken, PA: American Society for Testing and Materials, pp.565–583.

- Parker, A.P., Underwood, J.H. and Kendall, D.P., (1999), Bauschinger Effect Design Procedures for Autofrettaged Tubes Including Material Removal and Sachs' Method, ASME Journal of Pressure Vessel Technology, **121**, pp. 430–437.

- Parker, A.P., (2001a), Autofrettage of open end tubes— Pressures, stresses, strains and code comparisons, ASME Journal of Pressure Vessel Technology, **123**, pp. 271–281.

- Parker, A.P., (2001b), Bauschinger effect design procedures for compound tubes containing an autofrettaged layer, ASME Journal of Pressure Vessel Technology, **123**, pp. 203–206.

- Parker, A.P. and Kendall, D.P., (2003), Residual stresses and lifetimes of tubes subjected to shrink-fit prior to autofrettage, ASME Journal of Pressure Vessel Technology, **125(3)**, pp. 282–286.

- Parker, A.P., O'Hara, G.P. and Underwood, J.H., (2003), Hydraulic versus swage autofrettage and implications of the Bauschinger effect, ASME Journal of Pressure Vessel Technology, **125(3)**, pp. 309–314.

- Parker, A.P., (2005), Assessment and Extension of an Analytical Formulation for Prediction of Residual Stress in Autofrettaged Thick Cylinders, ASME Pressure Vessels and Piping Conference, Denver, CO, July 17–21.

- Parker, A.P., Gibson, M.C., Hameed, A. and Troiano, E., (2012), Material Modeling for autofrettage stress analysis including "single effective material". ASME Journal of Pressure Vessel Technology, **134**, pp. 041004-1–041004-7.

- Perl, M. and Aroné, R., (1988), Stress intensity factors for a radial multi-jacketed partially autofrettaged pressurized thick-walled cylinder, ASME Journal of Pressure Vessel Technology, **110**, pp. 147–154.

- Perl, M. (2000), The change in overstrain level resulting from machining of an autofrettaged thick-walled cylinder, Journal of Pressure Vessel Technology, **122**, pp. 9−14.

- Perl, M. and Perry, J., (2006), An experimental-numerical determination of the three-dimensional autofrettage residual stress field incorporating Bauschinger effects, ASME Journal of Pressure Vessel Technology, **128**, pp. 173−178.

- Perry, J. and Aboudi, J. (2003), Elasto-plastic stresses in thick walled cylinders, ASME Journal of Pressure Vessel Technology, **125**, pp. 248−252.

- Perry, J. and Perl, M. (2008), A 3-D model for evaluating the residual stress field due to swage autofrettage, ASME Journal of Pressure Vessel Technology, **130**, pp. 041211-1− 041211-6.

- Pharr, G.M., Tsui, T.Y., Bolshakov, A. and Oliver, W.C., (1994), Effects of residual stress on the measurement of hardness and elastic modulus using nanoindentation. MRS Proceedings, **338**, doi:10.1557/PROC-338-127.

- Poritsky, H., (1934), Analysis of thermal stresses in sealed cylinders and the effect of viscous flow during anneal, Journal of Applied Physics, **5(12)**, pp. 406–411.

- Pu, S.O. and Hussain, M.A., (1979), Stress intensity factors for a circular ring with a uniform array of radial cracks using cubic isoparametric singular elements, ASTM STP 667, pp. 685−699.

- Rees, D.W.A., (1987), A theory of autofrettage with applications to creep and fatigue. International Journal of Pressure Vessel and Piping **30**, pp. 57−76.

- Rees, D.W.A., (1990), Autofrettage theory and fatigue life of open-ended cylinders, Journal of Strain Analysis for Engineering Design, **25**, pp. 109−121.

- Rees, D.W.A., (1991a), The fatigue life of thick-walled autofrettaged cylinders with closed ends, Fatigue and Fracture of Engineering Materials and Structures, **14(1)**, pp. 51–68.

- Rees, D.W.A., (1991b), A bounding method for predicting the fatigue life of plain and autofrettaged thick-walled cylinders, International Journal of Fatigue, **13(1)**, pp. 59–67.

- Rees, D.W.A., (2011), A theory for swaging of discs and lugs, Meccanica, **46**, pp. 1213–1237.

- Ren-rui, Z., Chun-da, T. and Guo-zhen, Z., (1999) Elasto-plastical dynamic analysis of explosive autofrettage, Southwest Petroleum University (Natural Science), **21(4)**, pp. 82–85.

- Rice, J.R., (1972), Some remarks on elastic crack-tip stress field. International Journal of Solids and Structures, **8**, pp. 751–758.

- Rogan, J., (1975), Fatigue strength and mode of fracture of high pressure tubing made from low-alloy high strength steels, High Pressure Engineering, I. Mech E., London, UK. pp. 287–295.

- Sachs, G., (1927), Der Nachweiss immerer spannungen in stangen und rohren, Z. Metallkunde, **19**, pp. 352–357.

- Sadeghian, M. and Toussi, H.E., (2012), Elasto-plastic axisymmetric thermal stress analysis of functionally graded cylindrical vessel, Journal of Basic and Applied Scientific Research, **2**, pp. 10246–57.

- Sadeghian, M. and Toussi, H.E., (2014), Axisymmetric elastoplasticity of a temperature-sensitive functionally graded cylindrical vessel, ASME Journal of Pressure Vessel Technology, **136**, pp. 061203-1– 061203-8.

- Shim, W.S., Kim, J.H., Lee, Y.S., Cha, K.U. and Hong, S.K., (2010), Hydraulic autofrettage of thick-walled cylinders incorporating Bauschinger effect, Experimental Mechanics, **50**, 621–626.

- Simes, T.R., Mellor, S.G. and Hills, D.A., (1984), Research Note: A note on the influence of residual stress on measured hardness, Journal of Strain Analysis for Engineering Design, **19(2)**, pp. 135−137.
- Sinha, R.N., (1978), Thermal stress analysis of a hollow thick cylinder by the finite element method, Journal of the Institution of Engineers (India), Mechanical Engineering Division, **59**, pp.131−133.
- Smith, D.J., Pavier, M.J. and Poussard, C.P., (1998), An assessment of Sachs method for measuring residual stresses in cold worked fastener holes, Journal of Strain Analysis for Engineering Design, **33**, pp. 263–274.
- Stacey, A., MacGillivary, H.J., Webster, G.A., Webster, P.J. and Ziebeck, K.R.A., (1985), Measurement of residual stresses by neutron diffraction, Journal of Strain Analysis for Engineering Design, **20(2)**, pp. 93−100.
- Stacey, A. and Webster, G.A., (1988), Determination of residual stress distributions in autofrettaged tubing, International Journal of Pressure Vessel and Piping, **31**, pp. 205–220.
- Steele, M.C., (1952), Partially plastic thick-walled cylinder theory, ASME Journal of Applied Mechanics, **19**, 133−140.
- Taylor, D.J., Watkins, T.R., Hubbard, C.R., Hill, M.R. and Meith, W.A., (2012), Residual stress measurements of explosive clad cylindrical pressure vessels, ASME Journal of Pressure Vessel Technology, **134**, pp. 011501-1– 011501-8.
- Thomas, D.G.B., (1953), The autofrettage of thick tubes with free ends, Journal of Mechanics and Physics of Solids, **1**, pp. 124−133.
- Throop, J.F., (1970), Fatigue crack tolerance in thick walled cylinders, WVT Technical Report 7035.
- Thumser, R., Bergmann, J.W., and Vormwald, M., (2002), Residual stress fields and fatigue analysis of autofrettaged parts, Journal of Pressure Vessel and Piping, **79**, pp. 113−117.

- Till., E.T. and Rammerstorfer, F.G., (1983), Nonlinear finite element analysis of an autofrettage process, Computers and Structures, **17(5-6)**, pp. 857−864.

- Tosha, K., (2002), Influence of residual stresses on the hardness number in the affected layer produced by shot peening, Proceedings of the Second Asia-Pacific Forum on Precision Surface Finishing and Deburring Technology, Seoul, Korea, July 22–24, pp. 48–54.

- Troiano, E., Parker, A.P., Underwood, J.H. and Mossey, C., (2003), Experimental data, numerical fit and fatigue life calculations relating to the Bauschinger effect in high-strength armament steels, Technical report ARCCB-TR-03006, U.S. Army Armament Research Development and Engineering Center, Close Combat Armaments Center, Benét Laboratories, Watervliet, N.Y. 12189–4050.

- Underwood, J.H., (1972), Stress intensity factors for internally pressurized thick-walled cylinders, ASTM STP 513, Part 1, pp. 59−70.

- Underwood, J.H. and Miller, J.J., (1988), Stress corrosion cracking of A723 steel pressure vessels: two case studies, Technical Report ARCCB-TR-88002, US Army ARSEC, Benét Laboratories, Watervliet, NY 12189−4050.

- Underwood, J.H. and Parker, A.P., (1995), Fatigue life analyses and tests for thick-walled cylinders including effects of overstrain and axial grooves, ASME Journal of Pressure Vessel Technology, **117(3)**, pp. 222-226.

- Underwood, J.H., DeSwardt, R.R., Venter, A.M., Troiano, E., Hyland, E.J. and Parker, A.P., (2007), Hill Stress Calculations for Autofrettaged Tubes Compared With Neutron Diffraction Residual Stresses and Measured Yield Pressure and Fatigue Life, ASME Proceedings of Pressure Vessels Piping Conference, San Antonio, Texas, USA, July 22–26, Vol. 5, pp. 47–52.

- Vaidyanathan, S.S., Finnie, I., (1971), Determination of residual stresses from stress intensity factor measurements, ASME Journal of Basic Engineering, **93(2)**, pp. 242-246.

- Venter, A.M., de Swardt, R.R. and Kyriacou, S., (2000), Comparative measurements on autofrettaged cylinders with large Bauschinger reverse yielding zones, Journal of Strain Analysis for Engineering Design, **35**, pp. 459–469.

- Wahi, N., Ayob, A. and Elbasheer, M.K., (2011), Effect of autofrettage on allowable pressure of thick-walled cylinders, Proceedings of International Conference on Environmental and Agricultural Engineering, IACSIT Press, Singapore, IPCBEE 15, pp. 14–18.

- Wong, H. and Simionescu, O., (1996), An analytical solution of thermoplastic thick-walled tube subject to internal heating and variable pressure, taking into account corner flow and nonzero initial stress, International Journal of Engineering Science, **34**, pp. 1259–69.

- Xiaoying, Z. and Gangling, L., (1984), Autofrettaged calculative method of a thick-walled cylinder for the open-ended case, In Proceedings of the 5th International Conference on Pressure Vessel Technology, Vol. 1, ASME United Engineering Center, New York, pp. 85–95.

- Zerari, N., Saidouni, T. and Benretem, A., (2013), Determination of residual stresses induced by the autofrettage treatment by the X-rays diffraction method, Modern Mechanical Engineering, **3**, pp. 121–126.

- Zhu, R. and Yang, J., (1998), Autofrettage of thick cylinders, International Journal of Pressure Vessels and Piping, **75**, pp. 443–446.

Appendix

Appendix A

Bisection Method (Gerald and Wheatley, 1994)

The bisection method is one of the important numerical methods to find out the root of an equation. The method is based on bisecting an interval repeatedly where the root lies. Suppose that $f(x)$ is a continuous function of real variable x defined on an interval $[a, b]$. The problem can be defined as to find out the root of the equation $f(x)=0$. By intermediate value theorem $f(x)$ has atleast one root in the interval $[a, b]$ if the product of the function values at a and b is negative, *i.e.*, $f(a)f(b)<0$.

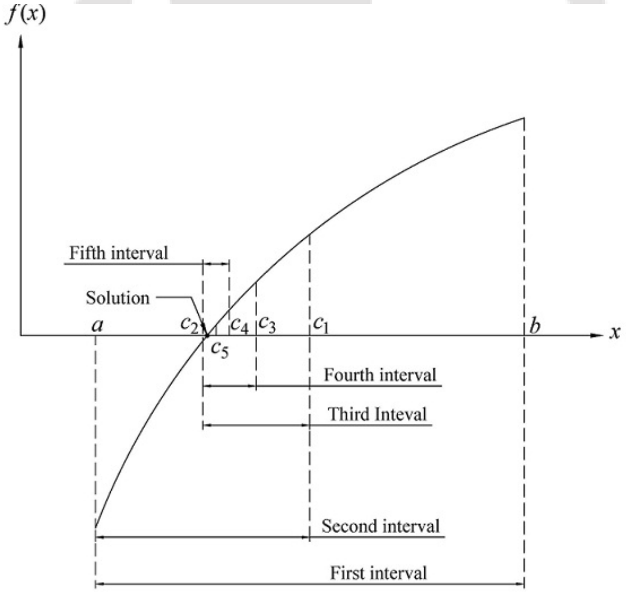

Figure A.1 Graphical representation of bisection method

To find out the root, the interval $[a, b]$ is divided into two subintervals by computing the midpoint $c= (a+b)/2$. The function value at c is then evaluated. If $f(c)=0$, c is a root of the equation. Otherwise, it is further decided in which subinterval $[a, c]$ or $[c, b]$ the root lies based on either $f(\mathrm{a})f(c)<0$ or $f(\mathrm{c})f(b)<0$. Suppose $f(a)f(c)<0$, a root lies in $[a, c]$. In that case, c is set to b and bisection of the interval is carried out in a similar way. If $f(\mathrm{c})f(b)<0$, c is set to a and the interval is bisected further. The root now lies in an interval whose length is half of the original interval. The process is repeated until $f(c)=0$ or the interval $[a, b]$ becomes very small to a desired degree of tolerance accuracy. The bisection method is schematically shown in Figure A.1 using an x-y sketch with y-axis being the function. A flow chart describing the working of bisection method is shown in Figure A.2.

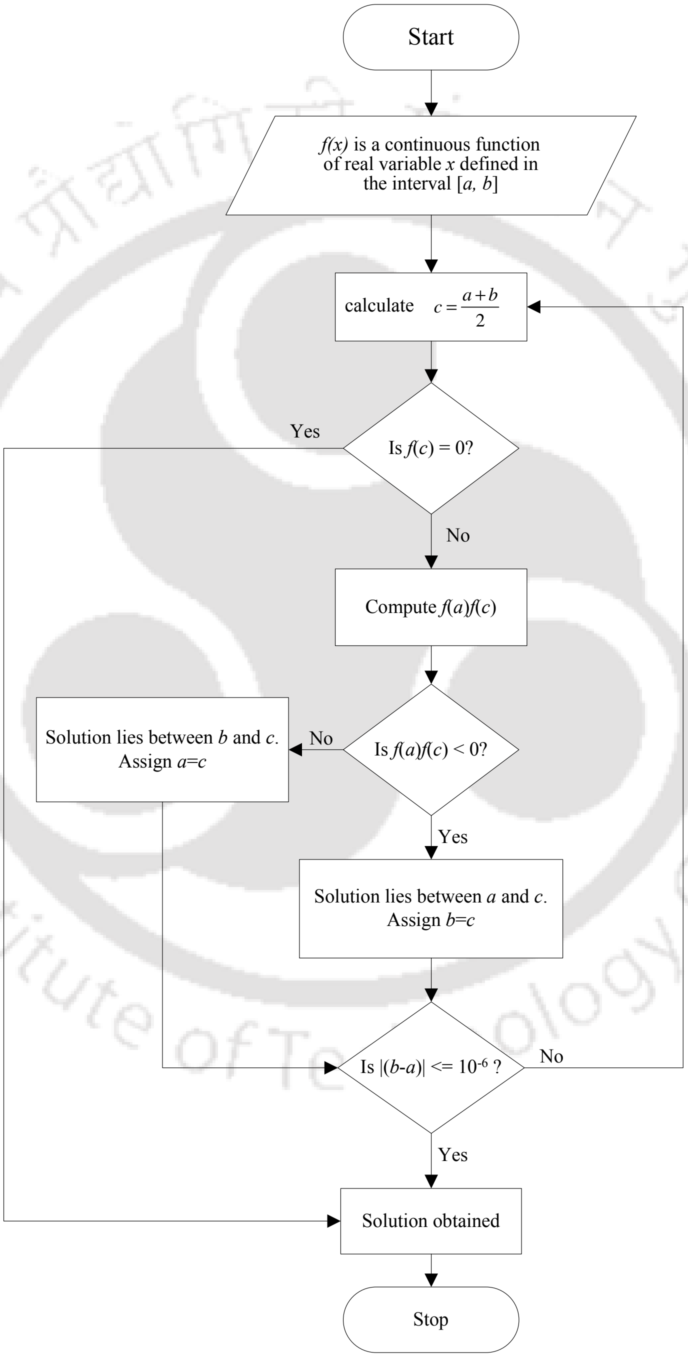

Figure A.2 Flowchart of bisection method

Appendix B

Effect of wall thickness ratio and temperature difference in plane stress case of thermal autofrettage:

Consider the typical aluminum disk as presented in Subsection 3.6.1. The effect of wall thickness ratio b/a and temperature difference (T_b–T_a) have been analyzed during the thermal autofrettage of this disk for different conditions using the equations presented in Chapter 3. In the first case, the wall thickness ratio of the disk is kept constant and the temperature difference across the wall thickness is varied. The simulated results for this case are presented in Table B.1. In the second case, the temperature difference across the wall thickness is kept constant and the wall thickness ratio is varied. The simulated results are presented in Table B.2. It is observed from Table B.1 that as the temperature difference across the wall thickness is increased, the value of the radius of elastic-plastic interface also increases. As a result, the corresponding pressure carrying capacity is also increased gradually. Table B.2 shows that increase of b/a increases the extent of the plastic zone and the corresponding pressure carrying capacity also increases. It has been observed that the increase of b/a contributes more in the pressure carrying capacity of the disk.

Table B.1 Effect of (T_b–T_a) for b/a =2 in aluminum disk

(T_b–T_a) (°C)	Radius of elastic-plastic interface, c (mm)	Pressure carrying capacity (MPa)	% increase in pressure
60	10.33	20.1	6.5
70	10.81	21.4	13.47
80	11.21	22.2	17.71
87.4	11.49	22.4	18.77

Table B.2 Effect of b/a for $(T_b - T_a)$=80 °C in aluminum disk

b/a	Radius of elastic-plastic interface, c (mm)	Pressure carrying capacity (MPa)	% increase in pressure
2	11.21	22.2	17.71
2.5	11.79	26.6	25.95
3	12.32	30	34.23
3.5	12.79	32.7	41.62
4	13.23	35.1	48.92

Appendix C

Solution of Differential Equation (4.41)

The second order linear non-homogeneous differential equation (Eq. 4.41) with varying coefficients in σ_r is

$$\frac{r^2}{E}\frac{\mathrm{d}^2\sigma_r}{\mathrm{d}r^2}+\frac{3r}{E}\frac{\mathrm{d}\sigma_r}{\mathrm{d}r}-\frac{1-2\nu}{E}\sigma_r=\frac{1}{E}k_1\sigma_Y+\alpha T_a+\alpha\left(T_b-T_a\right)\frac{\ln\left(\frac{r}{a}\right)}{\ln\left(\frac{b}{a}\right)}-\alpha\frac{\left(T_b-T_a\right)}{\ln\left(\frac{b}{a}\right)}-\varepsilon_0. \tag{C.1}$$

The homogeneous part of the Eq. (C.1) can be written as

$$r^2\frac{\mathrm{d}^2\sigma_r}{\mathrm{d}r^2}+3r\frac{\mathrm{d}\sigma_r}{\mathrm{d}r}-\left(1-2\nu\right)\sigma_r=0, \tag{C.2}$$

which is a Euler-Cauchy equation. Taking $\sigma_r = r^m$, the corresponding auxiliary equation can be written as

$$m^2+\left(3-1\right)m-\left(1-2\nu\right)=0 \tag{C.3}$$

The roots of Eq. (80) are

$$m_1=-1+\sqrt{2\left(1-\nu\right)},\qquad m_2=-1-\sqrt{2\left(1-\nu\right)} \tag{C.4}$$

Therefore, the basis of solutions is

$$\left(\sigma_r\right)_1=r^{m_1}=r^{-1+\sqrt{2(1-\nu)}},\qquad \left(\sigma_r\right)_2=r^{m_2}=r^{-1-\sqrt{2(1-\nu)}} \tag{C.5}$$

Thus, the general solution of the homogeneous part of the Eq. (C.1) is

$$\left(\sigma_r\right)_h=C_5r^{m_1}+C_6r^{m_2}=C_5r^{-1+\sqrt{2(1-\nu)}}+C_6r^{-1-\sqrt{2(1-\nu)}} \tag{C.6}$$

To find out the particular solution, Eq. (C.1) is written in standard form as

$$\frac{\mathrm{d}^2\sigma_r}{\mathrm{d}r^2}+\frac{3}{r}\frac{\mathrm{d}\sigma_r}{\mathrm{d}r}-\frac{1-2\nu}{r^2}\sigma_r=\frac{1}{r^2}k_1\sigma_Y+\frac{E}{r^2}\alpha T_a+\frac{E}{r^2}\alpha\left(T_b-T_a\right)\frac{\ln\left(\frac{r}{a}\right)}{\ln\left(\frac{b}{a}\right)}-\frac{E}{r^2}\alpha\frac{\left(T_b-T_a\right)}{\ln\left(\frac{b}{a}\right)}-\frac{E}{r^2}\varepsilon_0. \tag{C.7}$$

The particular solution is given by

$$\left(\sigma_r\right)_p=-\left(\sigma_r\right)_1\int\frac{\left(\sigma_r\right)_2 g(r)}{W}\mathrm{d}r+\left(\sigma_r\right)_2\int\frac{\left(\sigma_r\right)_1 g(r)}{W}\mathrm{d}r, \tag{C.8}$$

where

$$g\left(r\right)=\frac{1}{r^{2}}k_{1}\sigma_{Y}+\frac{E}{r^{2}}\alpha T_{a}+\frac{E}{r^{2}}\alpha\left(T_{b}-T_{a}\right)\frac{\ln\left(\frac{r}{a}\right)}{\ln\left(\frac{b}{a}\right)}-\frac{E}{r^{2}}\alpha\frac{\left(T_{b}-T_{a}\right)}{\ln\left(\frac{b}{a}\right)}-\frac{E}{r^{2}}\varepsilon_{0}. \tag{C.9}$$

and W is the Wronskian given by

$$W=\left(\sigma_{r}\right)_{1}\left(\sigma_{r}\right)_{2}'-\left(\sigma_{r}\right)_{2}\left(\sigma_{r}\right)_{1}'$$

$$W=r^{-1+\sqrt{2(1-\nu)}}\left\{-1-\sqrt{2\left(1-\nu\right)}\right\}r^{-2-\sqrt{2(1-\nu)}}-r^{-1-\sqrt{2(1-\nu)}}\left\{-1+\sqrt{2\left(1-\nu\right)}\right\}r^{-2+\sqrt{2(1-\nu)}}$$

$$W=-2r^{-3}\sqrt{2\left(1-\nu\right)} \tag{C.10}$$

Inserting Eqs. (C.9) and (C.10), the first term of Eq. (C.8) becomes

$$=-r^{-1+\sqrt{2(1-\nu)}}\int\frac{r^{-1-\sqrt{2(1-\nu)}}\left\{\frac{1}{r^{2}}k_{1}\sigma_{Y}+\frac{E}{r^{2}}\alpha T_{a}+\frac{E}{r^{2}}\alpha\left(T_{b}-T_{a}\right)\frac{\ln\left(\frac{r}{a}\right)}{\ln\left(\frac{b}{a}\right)}-\frac{E}{r^{2}}\alpha\frac{\left(T_{b}-T_{a}\right)}{\ln\left(\frac{b}{a}\right)}-\frac{E}{r^{2}}\varepsilon_{0}\right\}}{-2r^{-3}\sqrt{2\left(1-\nu\right)}}\mathrm{d}r$$

$$=-r^{-1+\sqrt{2(1-\nu)}}\left[\begin{array}{l}\frac{k_{1}\sigma_{Y}}{\left\{-2\sqrt{2\left(1-\nu\right)}\right\}}\int r^{-\sqrt{2(1-\nu)}}\mathrm{d}r+\frac{E\alpha T_{a}}{\left\{-2\sqrt{2\left(1-\nu\right)}\right\}}\int r^{-\sqrt{2(1-\nu)}}\mathrm{d}r+\frac{E\alpha\left(T_{b}-T_{a}\right)}{\left\{-2\sqrt{2\left(1-\nu\right)}\right\}\ln\left(\frac{b}{a}\right)}\int\ln\left(\frac{r}{a}\right)r^{-\sqrt{2(1-\nu)}}\mathrm{d}r\\+\frac{E\alpha\left(T_{b}-T_{a}\right)}{\left\{-2\sqrt{2\left(1-\nu\right)}\right\}\ln\left(\frac{b}{a}\right)}\int r^{-\sqrt{2(1-\nu)}}\mathrm{d}r+\frac{E\varepsilon_{0}}{\left\{-2\sqrt{2\left(1-\nu\right)}\right\}}\int r^{-\sqrt{2(1-\nu)}}\mathrm{d}r\end{array}\right]$$

$$=\frac{-r^{-1+\sqrt{2(1-\nu)}}}{\left\{-2\sqrt{2\left(1-\nu\right)}\right\}}\left[k_{1}\sigma_{Y}\int r^{-\sqrt{2(1-\nu)}}\mathrm{d}r+E\alpha T_{a}\int r^{-\sqrt{2(1-\nu)}}\mathrm{d}r+\frac{E\alpha\left(T_{b}-T_{a}\right)}{\ln\left(\frac{b}{a}\right)}\int\ln\left(\frac{r}{a}\right)r^{-\sqrt{2(1-\nu)}}\mathrm{d}r+\frac{E\alpha\left(T_{b}-T_{a}\right)}{\ln\left(\frac{b}{a}\right)}\int r^{-\sqrt{2(1-\nu)}}\mathrm{d}r+E\varepsilon_{0}\int r^{-\sqrt{2(1-\nu)}}\mathrm{d}r\right]$$

$$=\frac{-r^{-1+\sqrt{2(1-\nu)}}}{\left\{-2\sqrt{2\left(1-\nu\right)}\right\}}\left[\begin{array}{l}k_{1}\sigma_{Y}\frac{r^{-\sqrt{2(1-\nu)}+1}}{\left\{-\sqrt{2\left(1-\nu\right)}+1\right\}}+E\alpha T_{a}\frac{r^{-\sqrt{2(1-\nu)}+1}}{\left\{-\sqrt{2\left(1-\nu\right)}+1\right\}}+\frac{E\alpha\left(T_{b}-T_{a}\right)}{\ln\left(\frac{b}{a}\right)}\left\{\ln\left(\frac{r}{a}\right)\frac{r^{-\sqrt{2(1-\nu)}+1}}{\left\{-\sqrt{2\left(1-\nu\right)}+1\right\}}-\int\frac{r^{-\sqrt{2(1-\nu)}}}{\left\{-\sqrt{2\left(1-\nu\right)}+1\right\}}\mathrm{d}r\right\}\\+\frac{E\alpha\left(T_{b}-T_{a}\right)}{\ln\left(\frac{b}{a}\right)}\frac{r^{-\sqrt{2(1-\nu)}+1}}{\left\{-\sqrt{2\left(1-\nu\right)}+1\right\}}+E\varepsilon_{0}\frac{r^{-\sqrt{2(1-\nu)}+1}}{\left\{-\sqrt{2\left(1-\nu\right)}+1\right\}}\end{array}\right]$$

$$=\frac{-r^{-1+\sqrt{2(1-\nu)}}}{\left\{-2\sqrt{2(1-\nu)}\right\}}\left[\begin{array}{l} k_1\sigma_Y\dfrac{r^{-\sqrt{2(1-\nu)}+1}}{\left\{-\sqrt{2(1-\nu)}+1\right\}}+E\alpha T_a\dfrac{r^{-\sqrt{2(1-\nu)}+1}}{\left\{-\sqrt{2(1-\nu)}+1\right\}}+\dfrac{E\alpha\left(T_b-T_a\right)}{\ln\left(\dfrac{b}{a}\right)}\left\{\ln\left(\dfrac{r}{a}\right)\dfrac{r^{-\sqrt{2(1-\nu)}+1}}{\left\{-\sqrt{2(1-\nu)}+1\right\}}-\dfrac{r^{-\sqrt{2(1-\nu)}+1}}{\left\{-\sqrt{2(1-\nu)}+1\right\}^2}\right\} \\ +\dfrac{E\alpha\left(T_b-T_a\right)}{\ln\left(\dfrac{b}{a}\right)}\dfrac{r^{-\sqrt{2(1-\nu)}+1}}{\left\{-\sqrt{2(1-\nu)}+1\right\}}+E\varepsilon_0\dfrac{r^{-\sqrt{2(1-\nu)}+1}}{\left\{-\sqrt{2(1-\nu)}+1\right\}} \end{array}\right]$$

$$\begin{aligned}=&\frac{k_1\sigma_Y}{\left\{2\sqrt{2(1-\nu)}\right\}\left\{1-\sqrt{2(1-\nu)}\right\}}+\frac{E\alpha T_a}{\left\{2\sqrt{2(1-\nu)}\right\}\left\{1-\sqrt{2(1-\nu)}\right\}}+\frac{E\alpha\left(T_b-T_a\right)}{\left\{2\sqrt{2(1-\nu)}\right\}\left\{1-\sqrt{2(1-\nu)}\right\}}\frac{\ln\left(\frac{r}{a}\right)}{\ln\left(\frac{b}{a}\right)} \\ &-\frac{E\alpha\left(T_b-T_a\right)}{\left\{2\sqrt{2(1-\nu)}\right\}\left\{1-\sqrt{2(1-\nu)}\right\}^2\ln\left(\frac{b}{a}\right)}-\frac{E\alpha\left(T_b-T_a\right)}{\left\{2\sqrt{2(1-\nu)}\right\}\left\{1-\sqrt{2(1-\nu)}\right\}\ln\left(\frac{b}{a}\right)}-\frac{E\varepsilon_0}{\left\{2\sqrt{2(1-\nu)}\right\}\left\{1-\sqrt{2(1-\nu)}\right\}}.\end{aligned} \tag{C.11}$$

Similarly, the second term of Eq. (C.8) is evaluated as

$$=r^{-1-\sqrt{2(1-\nu)}}\int\frac{r^{-1+\sqrt{2(1-\nu)}}\left\{\dfrac{1}{r^2}k_1\sigma_Y+\dfrac{E}{r^2}\alpha T_a+\dfrac{E}{r^2}\alpha\left(T_b-T_a\right)\dfrac{\ln\left(\dfrac{r}{a}\right)}{\ln\left(\dfrac{b}{a}\right)}-\dfrac{E}{r^2}\alpha\dfrac{\left(T_b-T_a\right)}{\ln\left(\dfrac{b}{a}\right)}-\dfrac{E}{r^2}\varepsilon_0\right\}}{-2r^{-3}\sqrt{2\left(1-\nu\right)}}\,dr$$

$$\begin{aligned}=&-\frac{k_1\sigma_Y}{\left\{2\sqrt{2(1-\nu)}\right\}\left\{1+\sqrt{2(1-\nu)}\right\}}-\frac{E\alpha T_a}{\left\{2\sqrt{2(1-\nu)}\right\}\left\{1+\sqrt{2(1-\nu)}\right\}}-\frac{E\alpha\left(T_b-T_a\right)}{\left\{2\sqrt{2(1-\nu)}\right\}\left\{1+\sqrt{2(1-\nu)}\right\}}\frac{\ln\left(\frac{r}{a}\right)}{\ln\left(\frac{b}{a}\right)} \\ &+\frac{E\alpha\left(T_b-T_a\right)}{\left\{2\sqrt{2(1-\nu)}\right\}\left\{1+\sqrt{2(1-\nu)}\right\}^2\ln\left(\frac{b}{a}\right)}+\frac{E\alpha\left(T_b-T_a\right)}{\left\{2\sqrt{2(1-\nu)}\right\}\left\{1+\sqrt{2(1-\nu)}\right\}\ln\left(\frac{b}{a}\right)}+\frac{E\varepsilon_0}{\left\{2\sqrt{2(1-\nu)}\right\}\left\{1+\sqrt{2(1-\nu)}\right\}}.\end{aligned} \tag{C.12}$$

Thus, adding the expressions (C.11) and (C.12), the particular solution is obtained as

$$\left(\sigma_r\right)_p=\frac{k_1\sigma_Y}{(2\nu-1)}+\frac{E\alpha T_a}{(2\nu-1)}+\frac{E\alpha\left(T_b-T_a\right)}{(2\nu-1)}\frac{\ln\left(\frac{r}{a}\right)}{\ln\left(\frac{b}{a}\right)}-\frac{2E\alpha\left(T_b-T_a\right)}{(2\nu-1)^2\ln\left(\frac{b}{a}\right)}-\frac{E\alpha\left(T_b-T_a\right)}{(2\nu-1)\ln\left(\frac{b}{a}\right)}-\frac{E\varepsilon_0}{(2\nu-1)}. \tag{C.13}$$

Thus, the complete solution of the differential equation (C.1) is

$$\sigma_r=\left(\sigma_r\right)_h+\left(\sigma_r\right)_p \tag{C.14}$$

Substituting Eqs. (C.6) and (C.13) into Eq. (C.14), the complete solution of Eq. (C.1) is obtained as

$$\sigma_r = C_5 r^{-1+\sqrt{2(1-\nu)}} + C_6 r^{-1-\sqrt{2(1-\nu)}} + \frac{k_1\sigma_Y}{(2\nu-1)} + \frac{E\alpha T_a}{(2\nu-1)} + \frac{E\alpha(T_b-T_a)}{(2\nu-1)} \frac{\ln\left(\frac{r}{a}\right)}{\ln\left(\frac{b}{a}\right)}$$

$$-\frac{2E\alpha(T_b-T_a)}{(2\nu-1)^2\ln\left(\frac{b}{a}\right)} - \frac{E\alpha(T_b-T_a)}{(2\nu-1)\ln\left(\frac{b}{a}\right)} - \frac{E\varepsilon_0}{(2\nu-1)}.$$

$$\sigma_r = C_5 r^{-1+\sqrt{2(1-\nu)}} + C_6 r^{-1-\sqrt{2(1-\nu)}} + \frac{k_1\sigma_Y}{(2\nu-1)} + \frac{E\alpha T_a}{(2\nu-1)} + \frac{E\alpha(T_b-T_a)}{(2\nu-1)\ln\left(\frac{b}{a}\right)}\left\{\ln\left(\frac{r}{a}\right) - \frac{2\nu+1}{2\nu-1}\right\} - \frac{E\varepsilon_0}{(2\nu-1)}. \tag{C.15}$$

Eq. (C.15) corresponds to Eq. (4.42), which is the resulting solution of Eq. (4.41).

Appendix D

Two-Gauss-point formula (Dixit, 2009):

The general form of the two-Gauss-point integration formula can be expressed as

$$\int_{-1}^{+1} f\left(\xi\right)\mathrm{d}\xi = w_1 f\left(\xi_1\right) + w_2 f\left(\xi_2\right), \tag{D.1}$$

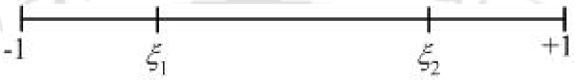

Figure D.1 Limits of integration and sampling points in two-Gauss-point formula

where w_1, w_2 weights and ξ_1, ξ_2 are sampling points. If the limits of the integrations are different, they can be transformed to lie from −1 to +1 with the help of linear transformation of variables. If x varies from a to b, the relation

$$x = \frac{a+b}{2} + \frac{b-a}{2}\xi \tag{D.2}$$

can be used to ensure that ξ varies from −1 to +1. Eq. (D.2) provides

$$\mathrm{d}x = \frac{b-a}{2}\mathrm{d}\xi \tag{D.3}$$

There are four unknowns– w_1, w_2, ξ_1 and ξ_2 in Eq. (D.1). These unknowns can be evaluated by fitting a third degree polynomial exactly. Consider

$$f\left(\xi\right) = a + b\xi + c\xi^2 + d\xi^3 \tag{D.4}$$

Substitution of $f(\xi)$ in Eq. (D.1) provides

$$\int_{-1}^{+1}\left(a + b\xi + c\xi^2 + d\xi^3\right)\mathrm{d}\xi = w_1 f\left(a + b\xi_1 + c\xi_1^{\,2} + d\xi_1^{\,3}\right) + w_2 f\left(a + b\xi_2 + c\xi_2^{\,2} + d\xi_2^{\,3}\right), \tag{D.5}$$

$$2a + \frac{2c}{3} = \left(w_1 + w_2\right)a + \left(w_1\xi_1 + w_2\xi_2\right)b + \left(w_1\xi_1^{\,2} + w_2\xi_2^{\,2}\right)c + \left(w_1\xi_1^{\,3} + w_2\xi_2^{\,3}\right)d \tag{D.6}$$

As a, b, c and d are arbitrary, equating the coefficients on both sides, one obtains

$$w_1 + w_2 = 2 \tag{D.7}$$

$$w_1\xi_1 + w_2\xi_2 = 0 \tag{D.8}$$

$$w_1\xi_1^{\,2} + w_2\xi_2^{\,2} = \frac{2}{3} \tag{D.9}$$

$$w_1\xi_1^{\ 3} + w_2\xi_2^{\ 3} = 0 \tag{D.10}$$

Solving Eqs. (D.7)–(D.10), the values of w_1, w_2, ξ_1 and ξ_2 are obtained as

$$\xi_1 = -\frac{1}{\sqrt{3}}, \quad \xi_2 = \frac{1}{\sqrt{3}}, \quad w_1 = 1, \quad w_2 = 1.$$

Appendix E

Derivation of Sachs Equations (Lambert, 1953)

The Sachs equations can be derived by using the equations from the theory of elasticity. A cylindrical specimen with inner radius, *a* and outer radius, *b* is considered. When the cylinder is progressively bored out from the inside, it is assumed that it possesses a radial position, *r*. Hoop stress (σ_θ) at the outer surface of a thick-walled cylinder due a uniform internal pressure, p_i is given by

$$\sigma_\theta = \frac{2r^2 p_i}{b^2 - r^2}, \tag{E.1}$$

The generalized Hook's law provides the axial (σ_a) and hoop (σ_θ) stress components as

$$\sigma_z = \frac{E}{1-\nu^2}(\varepsilon_z + \nu\varepsilon_\theta) = \frac{E}{1-\nu^2}\Lambda, \tag{E.2}$$

$$\sigma_\theta = \frac{E}{1-\nu^2}(\varepsilon_\theta + \nu\varepsilon_a) = \frac{E}{1-\nu^2}\theta. \tag{E.3}$$

The above relations are to be applied on the surface of the cylinder where the radial stress, σ_r =0. The terms, $\varepsilon_\theta + \nu\varepsilon_a$ is defined as θ and $\varepsilon_z + \nu\varepsilon_\theta$ is defined as Λ.

Now, consider that the cylinder has been bored out to an arbitrary radius *r*. A uniform pressure p_i has been removed from the inside boundary due to the removal of material containing polar symmetric residual stresses. At radius, *r*, the pressure, p_i removed is equal to the original radial stress at that point before boring started. Thus,

$$\sigma_r = p_i \tag{E.4}$$

Substituting p_i from Eq. (E.1) in Eq. (E.4) and then using Eq. (E.3), the expression for residual radial stress is obtained as

$$\sigma_r = \frac{b^2 - r^2}{2r^2}\sigma'_\theta = \frac{b^2 - r^2}{2r^2}\frac{E}{1-\nu^2}\theta. \tag{E.5}$$

Multiplying the numerator and denominator by π, the above equation can be expressed in the form as given by Sachs as

$$\sigma_r = \frac{E}{1-\nu^2}\left\{\frac{\left(F_b - F_r\right)}{2F_r}\theta\right\}, \tag{E.6}$$

where

$$F_b = \pi b^2, \quad F_r = \pi r^2. \tag{E.7}$$

Eq. (E.6) provides the radial residual stress as a function of r and the strains measured at various stages of boring.

To derive the expression for residual hoop stress, consider a thin cylindrical layer of material of radius, r, which has been bored out. This layer was also subjected to a uniform pressure, p_i. The relationship between the hoop stress and the external pressure, p_i on the outer periphery of the removed layer can be obtained from a free body diagram of the half of the cylindrical layer. If the layer is split by a plane through its axis and any diameter, the equilibrium of the forces acting provides

$$rp_i = \int_0^r \sigma_\theta\left(\rho\right)\mathrm{d}\rho \tag{E.8}$$

Substituting p_i from Eq. (E.1) and σ_θ from Eq. (E.3)

$$\int_0^r \sigma_\theta\left(\rho\right)\mathrm{d}\rho = \frac{E}{1-\nu^2}\frac{b^2 - r^2}{2r}\theta. \tag{E.9}$$

Differentiating both sides of Eq. (E.9) with respect to r, the following equation is obtained:

$$\sigma_\theta\left(r\right) = \frac{E}{1-\nu^2}\left\{\left(-\frac{b^2}{2r^2} - \frac{1}{2}\right)\theta + \frac{b^2 - r^2}{2r}\frac{\mathrm{d}\theta}{\mathrm{d}r}\right\},$$

$$\sigma_\theta\left(r\right) = \frac{E}{1-\nu^2}\left(\frac{-b^2 - r^2}{2r^2}\theta + \frac{b^2 - r^2}{2r}\frac{\mathrm{d}\theta}{\mathrm{d}r}\right). \tag{E.10}$$

Using chain rule, the term $\frac{\mathrm{d}\theta}{\mathrm{d}r}$ can be expressed as

$$\frac{\mathrm{d}\theta}{\mathrm{d}r} = \frac{\mathrm{d}\theta}{\mathrm{d}F_r}\frac{\mathrm{d}F_r}{\mathrm{d}r} = 2\pi r\frac{\mathrm{d}\theta}{\mathrm{d}F_r}. \tag{E.11}$$

Thus, Eq. (E.10) becomes

$$\sigma_\theta = \frac{E}{1-\nu^2}\left\{\frac{-b^2 - r^2}{2r^2}\theta + \left(\pi b^2 - \pi r^2\right)\frac{\mathrm{d}\theta}{\mathrm{d}F_r}\right\}. \tag{E.12}$$

Multiplying the numerator and denominator of the term, $\frac{-b^2-r^2}{2r^2}$, by π, Eq. (E.12) can be expressed as

$$\sigma_\theta = \frac{E}{1-\nu^2}\left\{\left(F_b - F_r\right)\frac{\mathrm{d}\theta}{\mathrm{d}F_r} - \frac{\left(F_b + F_r\right)}{2F_r}\theta\right\}. \tag{E.13}$$

Eq. (E.13) provides the residual hoop stress as given by Sachs.

For the axial residual stress, it is assumed that the specimen is long enough so that the plane strain conditions are valid. When the specimen is bored out to a radius, r, a longitudinal boundary force, F is removed from the inside of the remaining hollow cylinder.

Considering the removed cylindrical layer of radius, r, F is given by

$$F = \int_0^r \sigma_z\left(\rho\right)\mathrm{d}F_\rho = 2\pi\int_0^r \sigma_z\left(\rho\right)\rho\,\mathrm{d}\rho. \tag{E.14}$$

The axial stress due to F is given by

$$\sigma_z = \frac{F}{\pi\left(b^2 - r^2\right)}. \tag{E.15}$$

From Eqs. (E.2) and (E.15),

$$\frac{F}{\pi\left(b^2 - r^2\right)} = \frac{E}{1-\nu^2}\Lambda. \tag{E.16}$$

Substituting Eq. (E.14) in Eq. (E.16):

$$2\int_0^r \sigma_z\left(\rho\right)\rho\,\mathrm{d}\rho = \frac{E}{1-\nu^2}\left(b^2 - r^2\right)\Lambda. \tag{E.17}$$

Differentiating Eq. (E.17) on both sides, the following equation is obtained:

$$2r\sigma_z\left(r\right) = \frac{E}{1-\nu^2}\left\{-2r\Lambda + \left(b^2 - r^2\right)\frac{\mathrm{d}\Lambda}{\mathrm{d}r}\right\},$$

$$\sigma_z = \frac{E}{1-\nu^2}\left(-\Lambda + \frac{\left(b^2 - r^2\right)}{2r}\frac{\mathrm{d}\Lambda}{\mathrm{d}r}\right). \tag{E.18}$$

The term $\frac{\mathrm{d}\Lambda}{\mathrm{d}r}$ can be expresses similar way as in Eq. (E.11) as

$$\frac{\mathrm{d}\Lambda}{\mathrm{d}r} = 2\pi r\frac{\mathrm{d}\Lambda}{\mathrm{d}F_r}. \tag{E.19}$$

Using Eq. (E.19) in Eq. (E.18), the expression of Sachs residual axial stress is obtained as

$$\sigma_z = \frac{E}{1-\nu^2}\left\{\left(F_b - F_r\right)\frac{\mathrm{d}\Lambda}{\mathrm{d}r} - \Lambda\right\}. \tag{E.20}$$

Appendix F

Evaluation of integrals in Eq. (6.9)

The integrals in Eq. (6.9) are evaluated by using the values of residual hoop stresses from Eqs. (4.58), (4.61) and (4.55) and are given as follows:

$$\int_a^c \sigma_\theta^{(\text{plasticzone I})} r\mathrm{d}r$$

$$=k_1\sigma_Y\left(\frac{c^2-a^2}{4}\right)+k_1\sigma_Y\left\{\ln c\left(\frac{c^2}{2}\right)-\ln a\left(\frac{a^2}{2}\right)\right\}+C_3\left(\frac{c^2-a^2}{2}\right) \tag{F.1}$$

$$+\frac{E\alpha(T_b-T_a)}{2(1-\nu)\ln\left(\frac{b}{a}\right)}\left[\left(\frac{c^2-a^2}{2}\right)+\left\{\ln\left(\frac{c}{a}\right)\frac{c^2}{2}-\left(\frac{c^2-a^2}{4}\right)\right\}-\ln\left(\frac{b}{a}\right)\left(\frac{b^2}{b^2-a^2}\right)\left\{\left(\frac{c^2-a^2}{2}\right)+a^2\ln\left(\frac{c}{a}\right)\right\}\right].$$

$$\int_c^d \sigma_\theta^{(\text{plasticzone II})} r\mathrm{d}r$$

$$=\frac{C_5\sqrt{2(1-\nu)}}{1+\sqrt{2(1-\nu)}}\left(d^{1+\sqrt{2(1-\nu)}}-c^{1+\sqrt{2(1-\nu)}}\right)-\frac{C_6\sqrt{2(1-\nu)}}{1-\sqrt{2(1-\nu)}}\left(d^{1-\sqrt{2(1-\nu)}}-c^{1-\sqrt{2(1-\nu)}}\right)+\frac{k_1\sigma_Y}{(2\nu-1)}\left(\frac{d^2-c^2}{2}\right)$$

$$+\frac{E\alpha T_a}{(2\nu-1)}\left(\frac{d^2-c^2}{2}\right)+\frac{E\alpha(T_b-T_a)}{(2\nu-1)\ln\left(\frac{b}{a}\right)}\left\{\ln\left(\frac{d}{a}\right)\frac{d^2}{2}-\ln\left(\frac{c}{a}\right)\frac{c^2}{2}-\left(\frac{d^2-c^2}{4}\right)-\left(\frac{d^2-c^2}{2\nu-1}\right)\right\}-\frac{E\varepsilon_0}{(2\nu-1)}\left(\frac{d^2-c^2}{2}\right) \tag{F.2}$$

$$+\frac{E\alpha(T_b-T_a)}{2(1-\nu)\ln\left(\frac{b}{a}\right)}\left[\left(\frac{d^2-c^2}{2}\right)+\ln\left(\frac{d}{a}\right)\frac{d^2}{2}-\ln\left(\frac{c}{a}\right)\frac{c^2}{2}-\left(\frac{d^2-c^2}{4}\right)-\ln\left(\frac{b}{a}\right)\left(\frac{b^2}{b^2-a^2}\right)\left\{\left(\frac{d^2-c^2}{2}\right)+a^2\ln\left(\frac{d}{c}\right)\right\}\right].$$

$$\int_d^b \sigma_\theta^{(\text{elasticzone})} r\mathrm{d}r$$

$$=\frac{E\alpha}{2(1-\nu)}\frac{(T_b-T_a)}{\ln\left(\frac{b}{a}\right)}\left[\begin{array}{l}\ln\left(\frac{b}{a}\right)\left(\frac{b^2-d^2}{2}\right)-\ln\left(\frac{b}{a}\right)\left(\frac{b^2}{b^2-a^2}\right)\left\{\left(\frac{b^2-d^2}{2}\right)+a^2\ln\left(\frac{b}{d}\right)\right\}\\ -\left\{\frac{d^2}{b^2+d^2(2\nu-1)}\right\}\left\{\ln\left(\frac{b}{a}\right)(2\nu-1)-\nu-\ln\left(\frac{d}{a}\right)\right\}\left\{\left(\frac{b^2-d^2}{2}\right)+b^2\ln\left(\frac{b}{d}\right)\right\}\end{array}\right] \tag{F.3}$$

$$-\left\{\frac{d^2}{b^2+d^2(2\nu-1)}\right\}\left\{\left(\frac{b^2-d^2}{2}\right)+b^2\ln\left(\frac{b}{d}\right)\right\}\left(k_1\sigma_Y+E\alpha T_a-E\varepsilon_0\right).$$

Evaluation of integrals in Eq. (6.10)

The first two integrals in Eq. (6.10) are same as in Eqs (F.1) and (F.2). The remaining integrals are evaluated as follows using Eqs. (4.103), (4.106) and (4.109):

$$\int_{d}^{e} \sigma_{\theta}^{(\text{elastic zone})} r\mathrm{d}r$$

$$= \frac{E\alpha}{(2\nu-1)} T_a \left(\frac{e^2-d^2}{2}\right) + \frac{E\alpha(T_b-T_a)}{2(1-\nu)\ln\left(\frac{b}{a}\right)} \left[\begin{aligned} &\frac{1}{(2\nu-1)}\left\{\ln\left(\frac{d}{a}\right)+\frac{1}{2}-\frac{e^2}{2d^2}\right\}\left(\frac{e^2-d^2}{2}\right)+\left(\frac{e^2-d^2}{4}\right) \\ &+\frac{e^2}{2}\ln\left(\frac{e}{d}\right)-\ln\left(\frac{b}{a}\right)\left(\frac{b^2}{b^2-a^2}\right)\left\{\left(\frac{e^2-d^2}{2}\right)+a^2\ln\left(\frac{e}{d}\right)\right\} \end{aligned} \right] \tag{F.4}$$

$$+\frac{k_1\sigma_Y}{2\nu-1}\left(1+\frac{e^2}{2d^2}\right)\left(\frac{e^2-d^2}{2}\right)-k_1\sigma_Y\left(\frac{e^2}{2}\right)\ln\left(\frac{e}{d}\right)+\frac{E\varepsilon_0}{(1-2\nu)}\left(\frac{e^2-d^2}{2}\right).$$

$$\int_{e}^{f} \sigma_{\theta}^{(\text{plastic zone IV})} r\mathrm{d}r$$

$$= \frac{E\alpha}{(2\nu-1)} T_a \left(\frac{f^2-e^2}{2}\right) + \frac{E\alpha(T_b-T_a)}{2(1-\nu)\ln\left(\frac{b}{a}\right)} \left[\begin{aligned} &\frac{1}{(2\nu-1)}\left\{\ln\left(\frac{d}{a}\right)+\frac{1}{2}-\frac{e^2}{2d^2}\right\}\left(\frac{f^2-e^2}{2}\right)+\left(\frac{f^2-e^2}{4}\right) \\ &+\left(\frac{f^2}{2}\right)\ln\left(\frac{f}{e}\right)-\ln\left(\frac{b}{a}\right)\left(\frac{b^2}{b^2-a^2}\right)\left\{\left(\frac{f^2-e^2}{2}\right)+a^2\ln\left(\frac{f}{e}\right)\right\} \end{aligned} \right] \tag{F.5}$$

$$+k_1\sigma_Y\left\{\frac{1}{2\nu-1}\left(1+\frac{e^2}{2d^2}\right)\left(\frac{f^2-e^2}{2}\right)-\left(\frac{f^2}{2}\right)\ln\left(\frac{f}{e}\right)\right\}+\frac{E\varepsilon_0}{(1-2\nu)}\left(\frac{f^2-e^2}{2}\right).$$

$$\int_{f}^{b} \sigma_{\theta}^{(\text{plastic zone III})} r\mathrm{d}r$$

$$= -k_1\sigma_Y\left\{\left(\frac{b^2-f^2}{4}\right)+\left(\frac{b^2}{2}\right)\ln b-\left(\frac{f^2}{2}\right)\ln f\right\}+C_7\left(\frac{b^2-f^2}{2}\right) \tag{F.6}$$

$$+\frac{E\alpha(T_b-T_a)}{2(1-\nu)\ln\left(\frac{b}{a}\right)}\left[\begin{aligned} &\left(\frac{b^2-f^2}{4}\right)+\left(\frac{b^2}{2}\right)\ln\left(\frac{b}{a}\right)-\left(\frac{f^2}{2}\right)\ln\left(\frac{f}{a}\right) \\ &-\ln\left(\frac{b}{a}\right)\left(\frac{b^2}{b^2-a^2}\right)\left\{\left(\frac{b^2-f^2}{2}\right)+a^2\ln\left(\frac{b}{f}\right)\right\} \end{aligned} \right].$$

Appendix G

Dimensional change in thermally autofrettaged cylinder

The inner diameter of the cylinder is changed during thermal autofrettage. From the point of view of engineering application, the change in dimension of the inner diameter needs to be taken care of. The change in dimension should be in the permitted tolerance zone. The change in inner diameter of the cylinder can be evaluated by measuring the radial displacement at the inner radius after the removal of induced thermal gradient. The displacement after removal of the thermal gradient can be evaluated by subtracting the elastic displacement during unloading given by Eq. (4.17) from the displacement due to loading given by Eq. (4.27).

Consider an SS304 cylinder with inner radius a=10 mm, outer radius b=30 mm and is subjected to a temperature difference (T_b–T_a) =103 °C for achieving thermal autofrettage as in Section 8.3. The value of the displacement at the inner radius due to temperature difference of 103 °C is evaluated using Eq. (4.27) as

$$u_{\text{loading}} = 0.0053\,\text{mm}$$

The elastic displacement at the inner radius during unloading is evaluated using Eq. (4.17) as

$$u_{\text{elastic}} = 0.0038\,\text{mm}$$

Thus, the value of the net displacement at the inner radius after the removal of the temperature difference is evaluated as

$$u_{\text{net}} = u_{\text{loading}} - u_{\text{elastic}} = 0.0015\,\text{mm}.$$

Hence the change in the inner diameter in the cylinder due to thermal autofrettage is =2×0.0015=0.003 mm. As the change in dimension in the inner diameter is very small, this does not cause any problem in application.

There are many applications in automobile or aerospace industries where the change in dimensions is permitted by specifying a tolerance zone in the manufacturing of components. Suppose that we need to design a hole for fitting an axle in automobile industry. Consider a hole of basic size 20 mm in H7 system. In this case, the size of the hole dimension deviates by maximum 0.021 mm and minimum 0.00 mm. Thus, the maximum permitted tolerance is 0.021 mm. In the present example of thermally autofrettaged cylinder, the basic size of the inner diameter is 20 mm and a maximum change in dimension is obtained as 0.003 mm, which is smaller than the maximum permitted tolerance in H7 system. Thus, the product does not cause any problem if it has to be manufactured by thermal autofrettage for fitting axles in automobile industry. The change in dimension of the inner diameter of thermally autofrettaged cylinder can be controlled by limiting the maximum temperature difference during thermal autofrettage. Thus, it is possible to keep the change in the inner diameter of thermally autofrettaged cylinder within the permitted tolerance zone.

Publications from the Present Thesis

International Journals

1. S. M. Kamal and U. S. Dixit, (2015), Feasibility study of thermal autofrettage of thick-walled cylinders, *ASME Journal of Pressure Vessel Technology*, 137(6), pp. 061207-1–061207-18. DOI:10.1115/1.4030025.
2. S. M. Kamal, A. Ch. Borsaikia and U. S. Dixit, (2016), Experimental assessment of residual stresses induced by the thermal autofrettage of thick-walled cylinder, *Journal of Strain Analysis*, 51(2), pp. 144–160, DOI: 10.1177/0309324715616005.
3. S. M. Kamal and U. S. Dixit, (2016), A comparative study of thermal and hydraulic autofrettage, *Journal of Mechanical Science and Technology*, 30(6), pp. 2483–2496, DOI:10.1007/s12206-016-0508-8.
4. S. M. Kamal and U. S. Dixit, (2016), A study on enhancing the performance of thermally autofrettaged cylinder through shrink-fitting, *ASME Journal of Manufacturing Science and Engineering*, 138(9), pp. 094501-1–094501-5, DOI:10.1115/1.4033083.

Book Chapter

S.M. Kamal and U.S. Dixit (2015), Feasibility Study of Thermal Autofrettage Process, , in Advances in Material Forming and Joining, 5th International and 26th All India Manufacturing Technology, Design and Research Conference, AIMTDR 2014, edited by R. G. Narayanan and U. S. Dixit, Springer, New Delhi.

International/National Conferences

1. S. M. Kamal and U.S. Dixit, (2014), Feasibility study of thermal autofrettage process, Proceedings of 5th International and 26th All India Manufacturing Technology, Design and Research Conference, December 12-14, IIT Guwahati (Enhanced version of this paper is published as book chapter).

2. S. M. Kamal, A. Ch. Borsaikia and U. S. Dixit, (2015), Measurement of Residual Stresses in Thermally Autofrettaged Thick-walled Cylinders, Proceedings of the 30th National Convention of Production Engineers, July 18th and 19th, NIT Agartala.
3. S. M. Kamal, U. S. Dixit, Q. Liu, Vadim V. Silberschmidt and A. Roy, (2016), Thermo-Elasto-Plastic Finite Element Stress Analysis of Thick-Walled Cylinder and its Comparison with Plane Stress and Plane Strain Analyses, The 12th World Congress on Computational Mechanics, July 24−29, Seoul, Korea (accepted).
4. S. M. Kamal and U. S. Dixit, Fatigue life enhancement of thermally autofrettaged cylinders through shrink-fit, 6th International and 27th All India Manufacturing Technology, Design and Research Conference, December 16−18, 2016; to be held at College of Engineering Pune (abstract accepted).